TU Delft

Delft University of Technology

Document Version
Final published version

Citation (APA)
Möller-Gulland, R. (2024). *3D Electrodes for an Integrated Battery-Electrolyser*. [Dissertation (TU Delft), Delft University of Technology]. https://doi.org/10.4233/uuid:77342826-462d-49ae-bbe2-4806538e9d96

Important note
To cite this publication, please use the final published version (if applicable).
Please check the document version above.

Copyright
In case the licence states “Dutch Copyright Act (Article 25fa)”, this publication was made available Green Open Access via the TU Delft Institutional Repository pursuant to Dutch Copyright Act (Article 25fa, the Taverne amendment). This provision does not affect copyright ownership.
Unless copyright is transferred by contract or statute, it remains with the copyright holder.

Sharing and reuse
Other than for strictly personal use, it is not permitted to download, forward or distribute the text or part of it, without the consent of the author(s) and/or copyright holder(s), unless the work is under an open content license such as Creative Commons.

Takedown policy
Please contact us and provide details if you believe this document breaches copyrights.
We will remove access to the work immediately and investigate your claim.

This work is downloaded from Delft University of Technology.

3D Electrodes for an Integrated Battery-Electrolyser

Robin Möller-Gulland

3D Electrodes for an Integrated Battery-Electrolyser

Robin Möller-Gulland

3D Electrodes for an Integrated Battery-Electrolyser

Dissertation

for the purpose of obtaining the degree of doctor
at Delft University of Technology,
by the authority of the Rector Magnificus
prof. dr. ir. T.H.J.J. van der Hagen,
chair of the Board of Doctorates,
to be defended publicly on
Monday 11 November 2024 at 17:30 o'clock

by

Robin MÖLLER-GULLAND

Master of Science in Chemical Engineering,
RWTH Aachen University, Germany,

born in Cuxhaven, Germany.

This dissertation has been approved by the promotors.

Composition of the doctoral committee:

Rector Magnificus	chairperson
Prof. dr. F.M. Mulder	Delft University of Technology, promotor
Prof. dr. ir. J.R. van Ommen	Delft University of Technology, promotor
Independent members:	
Prof. dr. J.J.C. Geerlings	Delft University of Technology
Dr. R. Kortlever	Delft University of Technology
Prof. dr. M. Tromp	University of Groningen
Dr. ir. M.T.D. de Groot	Eindhoven University of Technology
Dr. A. Anastasopol	TNO
Prof. dr. B. Dam	Delft University of Technology, reserve member

The work described in this thesis has been carried out in the Materials for Energy Conversion and Storage (MECS) group, Department of Chemical Engineering, Faculty of Applied Sciences, Delft University of Technology. This work is part of the Open Technology research program with Project Number 15169, which is (partly) financed by The Netherlands Organization for Scientific Research (NWO).

Printed by:	Ridderprint | www.ridderprint.nl
Cover artwork:	Robin Möller-Gulland. Style transfer from Claude Monet's "Saint-Georges majeur au crépuscule" to a 3D electrode drawing using the AI image generation program Stable Diffusion.

Copyright © 2024 by R. Möller-Gulland

ISBN: 978-94-6506-385-0

An electronic version of this dissertation is available at
http://repository.tudelft.nl/.

Contents

Summary **ix**

Samenvatting **xiii**

1 Introduction **1**
1.1 The imperative of climate change mitigation 2
1.2 The battolyser™ – an integrated Ni-Fe battery and electrolyser 3
1.3 3D electrodes 7
1.4 Electrochemical CO_2 reduction to value-added chemicals 9
1.5 This thesis 10
References 13

2 3D hybrid battery-electrolyser nickel electrodes: A theoretical analysis **19**
2.1 Introduction 20
2.2 Mathematical models 23
2.2.1 Oxygen evolution 23
2.2.2 Battery charging and oxygen evolution in parallel. . . . 27
2.3 Results and discussion 31
2.3.1 Current and potential distribution in porous 3D electrodes during oxygen evolution 31
2.3.2 Hybrid 3D battery and electrolysis electrodes 44
2.4 Conclusions 53
References 56

3 3D nickel electrodes for hybrid battery and electrolysis devices **61**
3.1 Introduction 62
3.2 Results and discussion 67
3.2.1 A general statistical model for a dual function battery-electrolyser electrode. 67
3.2.2 Indirect 3D printing of nickel electrodes 69
3.2.3 Electrode activation and battery charging efficiency . . 69

3.2.4 High rate battery performance . . . 75
3.2.5 Electrolysis . . . 81
3.2.6 Energy Efficiency . . . 85
3.3 Conclusions . . . 87
References . . . 88

4 3D iron electrodes for hybrid battery and electrolysis application 95
4.1 Introduction . . . 96
4.2 A method for indirect 3D printing of sintered iron electrodes . 98
4.3 Results and discussion . . . 102
4.3.1 Impact of electrode void fraction and channel size . . . 102
4.3.2 Addition of carbon black . . . 118
4.3.3 Electrode stability . . . 123
4.3.4 Comparison of discharge capacities with literature. . . . 125
4.4 Scaling for industrial manufacturing . . . 130
4.5 Conclusions . . . 131
References . . . 132

5 Eliminating redox-mediated electron transfer mechanisms on a supported molecular catalyst enables CO_2 conversion to ethanol 139
5.1 Introduction . . . 141
5.2 Results and discussion . . . 142
5.3 Summary and conclusion . . . 153
5.4 Methods . . . 155
References . . . 168

6 Outlook: A flow-through battery-electrolyser 175
6.1 Introduction . . . 176
6.2 Cell design for 3D flow-through electrodes . . . 177
6.3 Preliminary results . . . 179
6.4 Conclusions . . . 182
References . . . 183

A 3D hybrid battery-electrolyser nickel electrodes: A theoretical analysis 185
A.1 Derivation of $\kappa_{eff,3D}$ . . . 186
A.2 Calculation of $\Delta\Phi(0)$ . . . 187
A.3 Approximation of the reaction penetration depth . . . 188

A.4 Model implementation . . . 189
A.5 Modeling parameters . . . 189
References . . . 190

B 3D nickel electrodes for hybrid battery and electrolysis devices 191
B.1 Chemicals . . . 192
B.2 Electrode preparation . . . 192
B.3 Measuring the electrode porosity and void fraction . . . 196
B.4 Electrochemical testing . . . 198
B.5 Electrochemically active surface area (ECSA) . . . 199
B.6 Electrochemical impedance spectroscopy (EIS) . . . 202
B.7 Modelling Results . . . 204
B.8 Scanning Electron Microscopy (SEM) and X-ray diffraction (XRD) . . . 205
B.9 Supporting Figures . . . 210
References . . . 212

C 3D iron electrodes for hybrid battery and electrolysis application 215
C.1 Materials and equipment . . . 216
C.2 Electrochemical testing . . . 216
C.3 Electrode properties . . . 218
C.4 Supporting results . . . 218

D Eliminating redox-mediated electron transfer mechanisms on a supported molecular catalyst enables CO_2 conversion to ethanol 225
References . . . 258

Acknowledgements 263

Curriculum Vitae 267

List of Publications 269

Summary

The battolyser™, which is based on a nickel iron battery, functions both as a battery, and when overcharged, as an alkaline water electrolyser for the production of H_2. In times of renewable energy oversupply, i.e. low energy prices, the battery electrodes are charged and subsequently produce H_2 and O_2. Conversely, in times of undersupply of renewables, i.e. high energy prices, energy stored in the battery electrodes can be discharged back to the grid. This flexibility in operation results in a high utilisation factor despite the fluctuating energy output of renewables. However, the electrodes employed in conventional nickel-iron batteries are not designed for this dual application. The goal of this thesis is the development of hybrid battery-electrolyser nickel and iron electrodes that provide both a high areal battery storage capacity and allow for efficient electrolysis at industrially relevant current densities.

In Chapter 2, we introduce the concept of 3D battolyser™ electrodes. In contrast to conventional planar (Non-3D) electrodes, 3D electrodes include open structures such as channels that improve electrolyte access, i.e. the ionic conductivity, and facilitate bubble removal during electrolysis. To understand the impact of the open channel volume, or void fraction, we first develop a simplified 1D model of a porous sintered nickel electrode that allows for the modelling of the current and potential distribution in porous 3D electrodes. Based on this model, we find relationships between dimensionless parameters that describe the impact of the current density and structural properties such as porosity, void fraction, and surface area on electrode utilisation and polarisation. We then develop a method to determine the optimal void fraction that maximizes the reactive surface area for oxygen evolution and discuss in which cases 3D electrodes are most beneficial. Finally, we demonstrate how the higher ionic conductivity of 3D electrodes also improves battery charging efficiency at high current densities as a result of the more homogeneous current distribution across the electrode depth.

In Chapter 3, we develop 3D battolyser™ nickel electrodes. To this end, we introduce an indirect 3D printing technique that uses easy to 3D print and low-cost moulds made of polylactic acid (PLA). A paste consisting of nickel powder, epoxy resin and carboxymethylcellulose (CMC) is injected into the PLA mould. Dissolving the mould in an aqueous solution of potassium hydroxide and sintering the green part yields a porous 3D nickel substrate. Following $Ni(OH)_2$ loading, the 3D electrode has a high areal battery capacity of 140 mAh/cm^2. In order to determine the impact of the 3D geometry, we compare the electrochemical performance of the 3D electrode with that of a conventional Non-3D electrode. The 3D electrode exhibits significantly enhanced charging efficiency and (dis)charge rate capability. In addition, material utilisation during oxygen evolution is increased by a factor of 2.5 resulting in a reduction in overpotential while also reducing the amount of nickel in the sintered substrate by around 44 %. Even after prolonged electrolysis and electrolysis current densities of up to 800 mA/cm^2, the tested electrodes can still be fully discharged. Furthermore, we show that the results obtained from the porous electrode model in Chapter 2 are in good agreement with the experimental results shown presented in this Chapter.

In Chapter 4, we develop 3D battolyser™ iron electrodes via indirect 3D printing. Here, we replace the carboxymethylcellulose and epoxy resin used in Chapter 3 with an agar-based binder system adapted from metal injection moulding (MIM). This facilitates manufacturing, reduces the number of process steps and allows for scaling of 3D electrodes using industrially established techniques such as MIM and material extrusion additive manufacturing (MEX). We manufacture and test three 3D electrodes with varying void fractions and channel dimensions as well as a planar Non-3D electrode as control. As already shown for the nickel electrodes discussed in Chapter 3, the improved ionic conductivity of the open 3D structures results in increased material utilisation and (dis)charge rate capability. However, we find that a too high void fraction is detrimental for battery performance. All tested iron electrodes exhibit efficient hydrogen evolution at current densities comparable to those of industrial alkaline electrolysers. Even though the tested electrodes can withstand electrolysis current densities exceeding 1000 mA/cm^2 prior to initial battery cycling, we find that prolonged cycling in combination with high electrolysis current densities (>1000 mA/cm^2) can affect electrode stability. Finally, we

find that the addition of the conductive additive carbon black to a Non-3D electrode leads to increased material utilisation and discharge capacities of up to 651 mAh/cm^2 or 1330 mAh/cm^3 at 30 °C. Together the work shows flexible, hour duration charge storage capabilities at alkaline electrolyser current densities. Efficient electricity storage and conversion in one integrated device without compromising either application is thus brought a significant step forward.

In Chapter 5, we expand the use of 3D electrodes to the electrochemical reduction of CO_2. To this end, we first manufacture a porous 3D nickel scaffold via indirect 3D printing. Instead of a PLA mould as used in Chapters 3 and 4, we employ a resin mould printed via stereolithographic (SLA) 3D printing. The higher resolution of SLA 3D printing has the potential to significantly increase electrode detail, allowing for more intricate geometries. On this 3D nickel electrode, we deposit the molecular catalyst iron tetraphenylporphyrin (Fe-TPP). In a specifically designed 3D printed cell in which a mixed phase flow of CO_2 and electrolyte flows trough the 3D electrode structure, we reduce CO_2 to ethanol with a Faradaic efficiency of 68 % +/- 3.2 % at -0.3 V vs. RHE and a partial current density of 21 mA/cm^2. Such reliable reduction of CO_2 to ethanol is typically restricted to copper-based catalysts. Here, we find that the combination of Fe-TPP and nickel fixes the iron oxidation state during electrocatalytic CO_2 reduction, which facilitates further reductions and the coupling of *CO intermediates. In addition, the electrode and cell design facilitate mixing of CO_2 with the electrolyte and access to the Fe-TPP catalyst within the electrode pores. We demonstrate ethanol production for up to 60 hours of operation.

In Chapter 6, we present a 3D printed cell concept for a flow-through battery-electrolyser employing the 3D electrodes developed in Chapter 3 and Chapter 4. The 3D geometry of the electrodes allows for a reduced inter-electrode gap, and thus reduced ohmic losses, without sacrificing effective bubble removal. For a first proof of concept, we install a 3D nickel electrode loaded with $Ni(OH)_2$ as anode and a bare 3D nickel electrode as cathode. With this set-up, we demonstrate electrolysis at 60 °C with a thermal efficiency of 83 % (1.78 V) at a current density of 400 mA/cm^2. Despite electrolysis current densities as high as 1000 mA/cm^2, the anode discharge performance is not affected. The presented flow cell set-up can serve as a platform for future studies on the impact of electrolyte flow

speed, temperature and electrode geometry.

Samenvatting

De battolyser™, die elektroden gebruikt, die gebaseerd zijn op een nikkel-ijzer batterij, functioneert zowel als een batterij, als, wanneer hij wordt overladen, als een alkalische water elektrolyser voor de productie van H_2. In tijden van overschot aan hernieuwbare energie, d.w.z. lage energieprijzen, worden de batterij-elektroden opgeladen en produceren vervolgens H_2 en O_2. Omgekeerd, in tijden van tekort aan hernieuwbare energie, d.w.z. hoge energieprijzen, kan de in de batterij-elektroden opgeslagen energie terug naar het net worden ontladen. Deze flexibiliteit resulteert in een hoge gebruiksfactor ondanks de fluctuerende energie-output van hernieuwbare energiebronnen. De elektroden die in conventionele nikkel-ijzer batterijen worden gebruikt, zijn echter niet ontworpen voor deze dubbele toepassing. Het doel van deze thesis is de ontwikkeling van hybride batterij-elektrolyser nikkel- en ijzeren elektroden die zowel een hoge batterijopslagcapaciteit per elektrode oppervlakte eenheid bieden als efficiënte elektrolyse mogelijk maken bij industrieel relevante stroomdichtheden.

In Hoofdstuk 2 introduceren we het concept van 3D battolyser™-elektroden. In tegenstelling tot conventionele vlakke (niet-3D) elektroden, omvatten 3D-elektroden open structuren zoals kanalen die de toegankelijkheid van elektrolyt verbeteren, oftewel de ionische geleidbaarheid, en die van bellen tijdens elektrolyse vergemakkelijken. Om de impact van het open kanaalvolume, of de holtefractie, te begrijpen, ontwikkelen we eerst een vereenvoudigd 1D-model van een poreuze gesinterde nikkelelektrode die het modelleren van de stroom- en potentiaalverdeling in poreuze 3D-elektroden mogelijk maakt. Op basis van dit model vinden we relaties tussen dimensieloze parameters die de impact van de stroomdichtheid en structurele eigenschappen zoals porositeit, holtefractie en oppervlakte beschrijven op elektrodebenutting en polarisatie. Vervolgens ontwikkelen we een methode om de optimale holtefractie te bepalen die het reactieve oppervlak voor zuurstofontwikkeling maximaliseert en bespreken in welke gevallen 3D-elektroden het meest voordelig zijn. Tenslotte tonen we aan hoe de hogere ionische geleidbaarheid van 3D-elektroden ook de oplaad-

efficiëntie van de batterij verbetert bij hoge stroomdichtheden als gevolg van de meer homogene stroomverdeling over de elektrodendiepte.

In Hoofdstuk 3 ontwikkelen we 3D battolyser™ nikkelelektroden. Hiervoor introduceren we een indirecte 3D-printtechniek die gebruik maakt van gemakkelijk te printen en goedkope mallen gemaakt van polylactidezuur (PLA). Een pasta bestaande uit nikkel poeder, epoxyhars en carboxymethylcellulose (CMC) wordt in de PLA-mal geïnjecteerd. Het oplossen van de mal in een waterige oplossing van kaliumhydroxide en het sinteren van het onderdeel levert een poreus 3D-reale batterijcapaciteit per cm^2 van 140 mAh/cm^2. Om de impact van de 3D-geometrie te bepalen, vergelijken we de elektrochemische prestaties van de 3D-elektrode met die van een conventionele niet-3D-elektrode. De 3D-elektrode vertoont aanzienlijk verbeterde laadefficiëntie en (ont)laadvermogen. Daarnaast wordt het materiaalgebruik tijdens zuurstofontwikkeling verhoogd met een factor 2,5 wat resulteert in een vermindering van de overpotentiaal en tegelijkertijd een vermindering van de hoeveelheid nikkel in het gesinterde substraat met ongeveer 44%. Zelfs na langdurige elektrolyse en elektrolysestroomdichtheden tot 800 mA/cm^2 kunnen de geteste elektroden nog volledig worden ontladen. Verder tonen we aan dat de resultaten verkregen uit het poreuze elektrode model in Hoofdstuk 2 goed overeenkomen met de experimentele resultaten die in dit hoofdstuk worden gepresenteerd.

In Hoofdstuk 4 ontwikkelen we 3D battolyser™ ijzerelektroden via indirect 3D-printen. Hier vervangen we de carboxymethylcellulose en epoxyhars gebruikt in Hoofdstuk 3 door een agar-gebaseerd bindmiddelsysteem, aangepast vanuit metal injection moulding (MIM). Dit vergemakkelijkt de productie, vermindert het aantal processtappen en maakt het mogelijk om 3D-elektroden op te schalen met behulp van industrieel gevestigde technieken zoals MIM en materiaalextrusie additieve productie (MEX). We vervaardigen en testen drie 3D-elektroden met verschillende holtefracties en kanaalafmetingen alsook een vlakke niet-3D-elektrode als controle. Zoals reeds aangetoond voor de nikkelen elektroden besproken in Hoofdstuk 3 , leidt de verbeterde ionische geleidbaarheid van de open 3D-structuren tot een verhoogd materiaalgebruik en (ont)laadvermogen. Echter, we vinden dat een te hoge holtefractie nadelig is voor de batterijprestaties. Alle geteste ijzerelektroden vertonen efficiënte waterstofontwikkeling bij stroomdichtheden vergelijkbaar met die van industriële alkalische elektrolyzers. Hoewel de geteste elektroden elektrolyse stroomdichtheden kunnen weer-

staan die meer dan 1000 mA/cm^2 bedragen voor de initiële batterijcyclus, stellen we vast dat langdurige cycli in combinatie met hoge elektrolysestroomdichtheden (>1000 mA/cm^2) de stabiliteit van de elektrode kunnen aantasten. Tenslotte, vinden we dat de toevoeging van een geleidend koolstof additief aan een zeer poreuze niet-3D ijzer elektrode leidt tot een verhoogd materiaalgebruik en ontladingscapaciteiten tot 651 mAh/cm^2 of 1330 mAh/cm^3 bij 30 °C. Samen met de nikkelelektrode toont het werk flexibele, uur-durende oplaadcapaciteiten bij stroomdichtheden van alkalische elektrolysers. Efficiënte elektriciteitsopslag en -conversie in één geïntegreerd apparaat zonder afbreuk te doen aan een van de toepassingen afzonderlijk wordt hiermee aanzienlijk vooruitgeholpen.

In Hoofdstuk 5 breiden we het gebruik van 3D-elektroden uit naar de elektrochemische reductie van CO_2. Hiervoor vervaardigen we eerst een poreus 3D-nikkelsubstraat via indirect 3D-printen. In plaats van een PLA-mal zoals gebruikt in Hoofdstukken 3 en 4, gebruiken we een harsmal geprint via stereolithografische (SLA) 3D-printing. De hogere resolutie van SLA 3D-printen heeft de potentie om de detaillering van de elektrode aanzienlijk te verhogen, wat mogelijkheden biedt voor meer ingewikkelde geometrieën. Op deze 3D-nikkelelektrode deponeren we de moleculaire katalysator ijzertetrafenylporfyrine (Fe-TPP). In een specifiek ontworpen 3D-geprinte cel, waarin een gemengde fase van CO_2 en elektrolyt door de 3D-elektrodestructuur stroomt, reduceren we CO_2 tot ethanol met een Faraday-efficiëntie van 68 % ± 3.2 % bij -0.3 V vs. RHE en een partiële stroomdichtheid van 21 mA/cm^2. Zo'n betrouwbare reductie van CO_2 tot ethanol is doorgaans beperkt tot op koper gebaseerde katalysatoren. Hier ontdekken we dat de combinatie van Fe-TPP en nikkel de ijzeroxidatietoestand fixeert tijdens de elektrokatalytische CO_2-reductie, wat verdere reducties en de koppeling van $*$CO-intermediairen vergemakkelijkt. Bovendien faciliteren het elektrode- en celontwerp het mengen van CO_2 met het elektrolyt en de toegang tot de Fe-TPP-katalysator in de elektrodeporiën. We demonstreren de productie van ethanol voor 60 uur bedrijfstijd.

In Hoofdstuk 6 presenteren we een 3D-geprint celconcept voor een doorstroom batterij-elektrolyser die gebruik maakt van de 3D-elektroden ontwikkeld in Hoofdstuk 3 en Hoofdstuk 4. De 3D-geometrie van de elektroden maakt een verkleinde elektrode afstand mogelijk, wat leidt tot verminderde ohmse verliezen, zonder dat dit ten koste gaat van de effectieve verwijdering het transport van bellen. Als eerste concept, installeren we

een 3D-nikkelelektrode beladen met $Ni(OH)_2$ als anode en een pure 3D-nikkelelektrode als kathode. Met deze opstelling demonstreren we elektrolyse bij 60 °C met een thermische efficiëntie van 83 % (1.78 V) bij een stroomdichtheid van 400 mA/cm^2. Ondanks elektrolysestroomdichtheden tot 1000 mA/cm^2, wordt de ontlaadprestatie van de $Ni(OH)_2$ in de anode niet beïnvloed. De gepresenteerde flowcelopstelling kan dienen als platform voor toekomstige studies naar het effect van elektrolytstroomsnelheid, temperatuur en elektrodegeometrie.

1

Introduction

1

1.1. The imperative of climate change mitigation

Climate change presents a significant threat to ecosystems and modern society. Its main driver is the anthropogenic emission of green house gases (GHG) such as carbon dioxide (CO_2) and methane (CH_4) leading to the rise of the global average temperature. Without intervention, this rise in temperature will increase the frequency and severity of extreme weather events and droughts, cause a rise in sea-levels, decimate biodiversity and increase the risk of dangerous climate feedback loops [1]. Health issues such as heat stress, respiratory problems and the spread of infectious diseases such as dengue, malaria and lyme disease are all exacerbated by climate change [2]. The effects of climate change disproportionally affect vulnerable populations due to factors like socio-economic status and geographical location, resulting in mass migration [3, 4].

In 2015, the Paris Agreement was adopted by 196 nations with the goal of limiting the global temperature increase to ideally 1.5 °C, but well below 2 °C above pre-industrial levels [5]. However, as shown in Figure 1.1, in 2023 the 1.5 °C threshold has already been exceeded on almost 50 % of all days, raising concerns for faster than expected global warming with unpredictable consequences [6, 7]. Policies implemented for climate change mitigation by the end of 2020 are expected to only limit warming to 2.2 to 3.5 °C by the end of the century. As a result, GHG emissions of sectors such as energy supply, industry and transportation must be immediately and rapidly reduced with the goal of eventually reaching net-zero CO_2 emissions by 2050 in order to limit warming to 1.5 °C [1].

The transition to renewable energy sources such as wind and solar is central to strategies for mitigating climate change. In 2023, significant growth in wind and solar pushed the share of renewables in the global electricity mix above 30 % for the first time, with wind and solar together accounting for a record 13.4 % share [8]. However, the energy output of wind and solar depends not only on the geographic location but also varies with the time of day and season. Compensating for this intermittency with short- and long-term energy storage solutions will be essential for the future growth of wind and solar. Besides transitioning to renewable energy sources, a net-zero future also requires the development of alternative, cost-effective and CO_2-neutral technologies for carbon-intensive industries such as the steel, chemical and heavy transport industry [9–11].

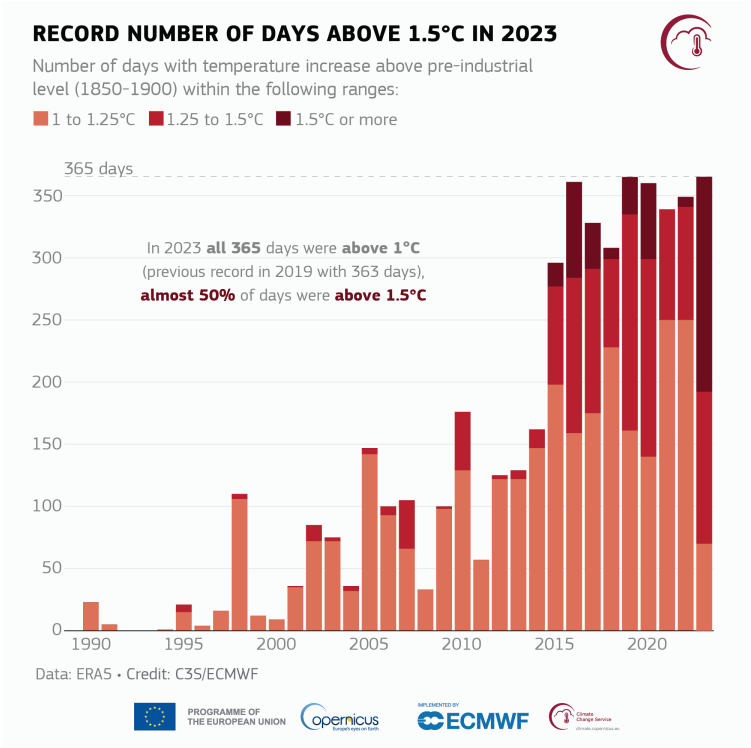

Figure 1.1: Number of days from 1990 to 2023 during which the global average temperature exceeded pre-industrial values (1850-1900) by 1 to 1.25 °C (orange), 1.25 to 1.5 °C (red) and 1.5 °C or more (crimson). Figure reprinted from Ref. [6].

1.2. The battolyser™ – an integrated Ni-Fe battery and electrolyser

Given their high energy density, flexibility in location, and rapid response time, batteries are a promising energy storage technology to mitigate the intermittency of renewables. However, their application is mostly limited to short durations on the scale of hours to days due to their high self-discharge rate, low energy density and cost. Green hydrogen, i.e. hydrogen generated from renewables, and hydrogen derived synthetic fuels such as methane and ammonia (power-to-gas/liquid) can be generated from surplus energy and used for seasonal energy storage [12, 13]. As hydrogen, methane and ammonia are also a common feedstock for numerous

1

chemical processes, generating these using renewable energy would also facilitate the decarbonisation of the chemical industry. In the steel industry, hydrogen can substitute carbon (coke) in the reduction process of iron ore, hereby effectively eliminating CO_2 emissions from this process step [9]. In addition, hydrogen-powered fuel cells can replace internal combustion engines that can be used to decarbonise the heavy transportation industry [11]. Overall, both batteries and hydrogen will play a central role in a renewable energy future.

In 2017, Mulder et al. [14] introduced the battolyser™, an integrated battery and alkaline electrolyser (Figure 1.2). It is based on the Ni-Fe battery developed by Jungner and Edison that is known for its robustness and longevity, lasting up to 25 years [15, 16]. Due to the availability and low cost of the main electrode materials, Ni and Fe, Ni-Fe batteries have gained renewed interest for large-scale grid energy storage [17, 18]. However, unlike a conventional Ni-Fe battery, the battolyser™ is overcharged to efficiently produce hydrogen via alkaline electrolysis when the battery capacity is reached.

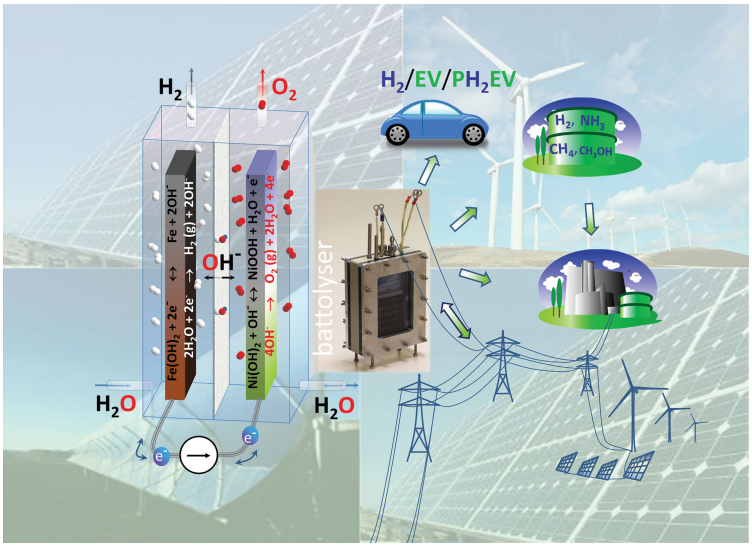

Figure 1.2: (left) Principle of the battolyser™ as an integrated Ni-Fe battery and alkaline electrolyser. (right) Use cases for electricity grid stabilization, supply of fuel for e.g. plug-in hybrid electric and hydrogen vehicles (PH_2EV) and H_2 production as a chemical feedstock. Figure reprinted from Ref. [14].

During charging, $Ni(OH)_2$ in the positive electrode is oxidized to NiOOH, while $Fe(OH)_2$ in the negative electrode is reduced to Fe:

$$Ni(OH)_2 + OH^- \underset{\text{discharge}}{\overset{\text{charge}}{\rightleftharpoons}} NiOOH + H_2O + e^- \quad +0.49 \text{ V vs. SHE} \tag{1.1}$$

$$Fe(OH)_2 + 2\,e^- \underset{\text{discharge}}{\overset{\text{charge}}{\rightleftharpoons}} Fe + 2\,OH^- \quad \text{-0.88 V vs. SHE} \tag{1.2}$$

Fe and NiOOH formed in the charging process function as efficient catalysts for the hydrogen evolution (HER) and oxygen evolution reaction (OER), respectively. Thus, a charged battolyser™ operates as an alkaline electrolyser generating oxygen at the Ni electrode:

$$4\,OH^- \xrightarrow{\text{overcharging}} O_2(g) + 2\,H_2O + 4\,e^- \tag{1.3}$$

(1.23 V - 0.059 V × pH vs. SHE) and hydrogen at the Fe electrode:

$$2\,H_2O + 2\,e^- \xrightarrow{\text{overcharging}} H_2(g) + 2\,OH^- \tag{1.4}$$

(0.00 V - 0.059 V × pH vs. SHE). The OH^- ions are conducted via a highly concentrated aqueous KOH electrolyte. As shown in Figure 1.2, a diaphragm that is permeable for OH^- separates the electrodes and prevents mixing of H_2 and O_2. When discharged, the HER and OER catalysts, Fe and NiOOH, are fully converted back to $Fe(OH)_2$ and $Ni(OH)_2$, respectively. Remarkably, these transformations are fully reversible with no apparent loss in functionality even after numerous cycles of charging, electrolysis and discharging [14].

This integration of a battery and an alkaline electrolyser in a single device, using the same electrodes, reduces the amount of materials required, reduces the footprint and significantly increases the utilisation factor. Generally, conventional electrolysers are designed for continuous operation and not for a variable power load as is the case for wind and solar. Gas purity decreases for lower loads as gas cross-over is less diluted at lower current densities, thereby increasing the risk of explosion of combustible H_2/O_2 mixtures [19]. Thus, for safety reasons, too high

impurities necessitate a shut-down. However, alkaline electrolyser systems are particularly susceptible to electrode degradation when operated with an intermittent power supply such as wind and solar. This is due to reverse currents originating from the catalysts reverting back to their original state following oxidation and reduction at the anode and cathode, respectively [20]. As a result, conventional alkaline electrolysers must either operate at a minimum load even when electricity prices are high, i.e. when renewables are less available, or include protection mechanisms such as a separate power supply that applies a low protective current to prevent electrode degradation during shut-down [21]. The battolyser™, on the other hand, can stop electrolysis when electricity prices are high and instead reversibly discharge the energy stored in the battery back into the grid without any adverse effects to the electrodes.

When energy prices are low, i.e. when there is an oversupply in renewable energy, the battery is first charged and then seamlessly transitions into hydrogen production. In contrast to conventional batteries, such as Li-ion, Ni-Cd, or Ni-MH, the battolyser™ can store energy in the form of hydrogen in excess of its battery capacity which eliminates the need to curtail an oversupply of renewable energy. In addition, unlike Ni-Cd or Ni-MH batteries, Ni-Fe batteries are not susceptible to memory effects when partially discharged [22]. Therefore, the battolyser™ can also be used to mitigate short-term fluctuations of over- and undersupply in the electricity grid by partially charging and discharging the battery capacity.

However, the electrodes in conventional Ni-Fe batteries are not designed for electrolysis. On the contrary, as electrolysis reduces the battery charging efficiency, it has been considered an unwanted side reaction. Therefore, the reduction of hydrogen and oxygen evolution has been a central topic of research in the development of Fe and Ni battery electrodes [17, 23–26]. In addition, battery and electrolysis electrodes differ in structural properties such as porosity, catalyst loading and geometry. Bubbles generated during electrolysis reduce the ionic conductivity of the electrolyte and cover catalytically active sites resulting in increased cell potentials [27, 28]. Therefore, electrodes in alkaline electrolysers typically have an open structure including slits or holes to facilitate bubble removal. For instance, such open electrode structures include louvered, slotted, perforated, finned or mesh designs to prevent bubble trapping [29–31]. As OER and HER occur only at the catalyst surface, these struc-

tures are coated with a thin porous layer of electrocatalyst. For battery electrodes, on the other hand, the energy storage capacity depends on the mass of active material. Thus, in order to reach a high capacity per superficial electrode area (mAh/cm^2), battery electrodes typically have a lower porosity, a higher thickness and no open geometry compared to electrolysis electrodes. As a result, new types of electrodes must be developed that are tailored towards the dual functionality of electrolysis and battery operation.

1.3. 3D electrodes

In recent years, 3D structured non-planar electrodes have gained significant interest for applications in various types of batteries, supercapacitors, electrolysers and electrochemical reactors [32–35]. Thanks to advances in 3D printing technologies, complex electrode geometries tailored to a specific application can be realized [36]. Hereijgers et al. [37, 38] demonstrated how the geometry of an electrode can be designed to improve mass transfer with a low pressure drop in a flow-through configuration. In addition, the open structure (e.g. channels) of 3D electrodes increases the electrolyte accessibility and thus the ionic conductivity. Saleh et al. [39] showed how this improvement in ionic conductivity can increase the areal capacity, i.e. material utilisation, and rate capability in Li-ion batteries. For electrolysis, a 3D structure including periodically ordered interconnected channels facilitates bubble removal for both HER and OER [40, 41]. Compared to stochastically structured electrode substrates such as nickel foam, such an ordered channel configuration prevents bubble trapping and agglomeration [40].

Due to the proven advantages for both electrolysis and battery electrodes, 3D electrodes are an attractive option for an integrated battery-electrolyser. In this thesis, we define the void fraction as the ratio of the open channel volume to the overall electrode volume. Per this definition, conventional electrolysis electrodes such as catalyst coated meshes have a high void fraction, while conventional battery electrodes have a void fraction of zero. Thus, in first approximation, the void fraction can serve as a parameter to design battery-electrolyser electrodes across a spectrum between battery and electrolysis functionality. Figure 1.3 shows a com-

1

monly studied [37, 40, 41] 3D electrode geometry consisting of periodically repeating interconnected channels. Here, the electrode material itself is porous, with pores in the order of μm. The combination of small pores within the material and larger channels in the order of mm gives rise to a hierarchically porous structure. As gas bubbles generated during electrolysis can be effectively removed via the channels, the inter-electrode gap can be significantly reduced. Not only does this reduce ohmic voltage losses, the volume of the cell is also reduced significantly. In addition, electrolyte flowing through, rather than past, the electrodes further enhances bubble and heat removal.

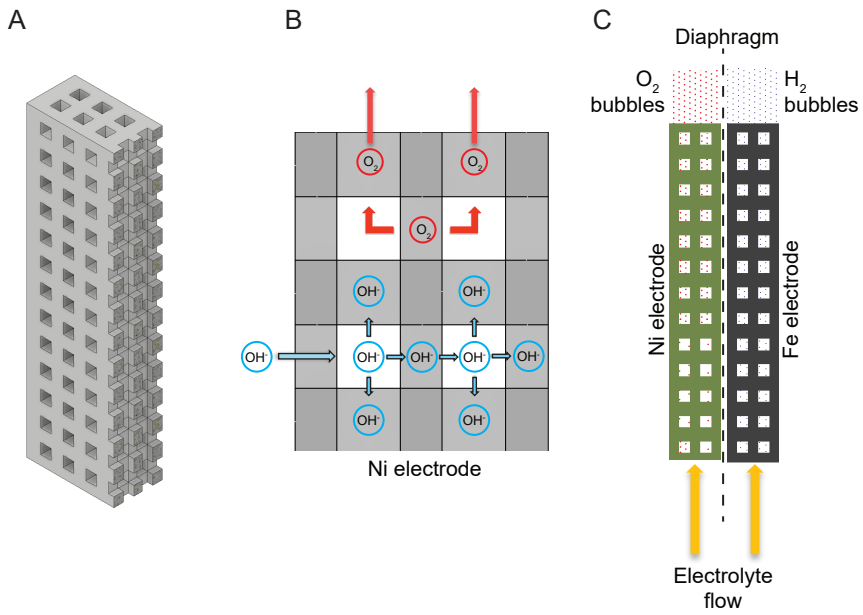

Figure 1.3: Benefits of 3D structured electrodes with hierarchical porosity. (A) Isometric cross section of a 3D mesh electrode with periodically repeating interconnected channels. (B) The interconnected channels improve electrolyte accessibility which increases the ionic conductivity. Such an ordered structure also facilitates bubble removal during electrolysis. (C) As bubbles are removed via the interconnected channels, the inter-electrode gap and can be significantly reduced, resulting in a decrease in ohmic voltage losses. Electrolyte flowing through, rather than past, the electrodes further enhances bubble and heat removal.

Common additive manufacturing techniques for the preparation of 3D electrodes include selective laser melting (SLM) [42], selective laser sintering (SLS) [43] and direct ink writing (DIW) [44]. However, the high cost of SLS and SLM are expensive techniques, with costs typically in the order of hundreds of euros per part. Especially when numerous iterations throughout the design process are necessary, this quickly becomes cost-prohibitive. While DIW is among the simplest and most cost-effective additive manufacturing techniques, the rheological properties of the ink containing the printing material must be carefully adjusted in conjunction with the printing parameters. In addition, due to the diameter of the extruded paste in DIW, there is distinct layering of the printed structure, which can affect the resolution and surface finish.

In 2019, Hereijgers et al. [37] introduced the technique of indirect 3D printing. Here, a mould, i.e. the negative of the electrode geometry, is 3D printed from a polymer using fused deposition modeling (FDM). A metal paste containing a binder and liquefaction agent is then injected into the mould. After solidification, e.g. through curing of the binder, the mould is then removed via a suitable solvent which yields the green part of the electrode. Finally, the green part is sintered to yield a self-supporting, porous all-metal electrode with no layering. FDM printing has a low barrier to entry due to its low price and ease of printing. As a result, indirect 3D printing via FDM allows research groups to manufacture and study 3D electrodes without prohibitive cost. For example, indirect 3D printing of 3D nickel electrodes is in the order of euros per part, a factor 100 lower compared to SLS and SLM [1].

1.4. Electrochemical CO_2 reduction to value-added chemicals

In order to mitigate the increase of CO_2 in the atmosphere, CO_2 can be sequestered directly from air or captured from industrial processes and power plants before it is released [45]. Using electricity produced from renewables, the electrochemical reduction of this waste CO_2 (CO2RR) presents a sustainable CO_2-neutral, or -negative, option to produce value-added chemicals such as alcohols (e.g. methanol and ethanol), organic

[1] Based on quotations received from external 3D printing companies in 2019.

acids (e.g. formic acid), ethylene and syngas (CO + H_2)[46]. Due to their high energy density, alcohols are especially attractive for the use as renewable fuels. For instance, ethanol can be used for the generation of electricity via a direct-ethanol fuel cell or added to gasoline (up to 10 vol%) [47, 48].

To date, only copper-based catalysts can reliably convert CO_2 to C_{2+} products at meaningful current densities to products such as ethanol [49–52]. However, while copper-based electrodes produce an array of products such as ethylene, acetate, ethanol and methanol, the selective production of a target compound is challenging. In recent years, 3D printing of electrodes for CO_2 reduction has gained considerable interest [53, 54]. Besides conventional catalyst development, the 3D geometry of the electrode presents a degree of freedom that could affect mass transfer, selectivity and current density.

1.5. This thesis

The key goal of this thesis is the development of 3D structured nickel and iron electrodes for the use in an integrated battery-electrolyser. Next to the development of manufacturing procedures, we assess the impact of the 3D geometry for both battery functionality and electrolysis. What sets this work apart from previous studies on 3D electrodes for batteries and electrolysers, is the integration of both battery and electrolysis functionality in a single electrode, without compromising the performance of either. Thus, we demonstrate high current densities for electrolysis combined with a significant areal battery capacity. The latter allows for discharge durations of multiple hours, even at high current densities. In a renewable energy future, an integrated battery-electrolyser equipped with such electrodes can fully utilise surplus energy over multiple hours of overproduction through battery charging and electrolysis, while at times of underproduction battery discharging provides energy back to the electricity grid.

Research questions and outline

Chapter 2

"How do electrode thickness, porosity and void fraction affect the current distribution and electrode polarisation? What is the ideal 3D void fraction?"

We first develop a 1D model of a porous sintered nickel electrode for both battery and electrolysis operation. Here, we extend the Bruggeman relation for the ionic conductivity to take the void fraction of a 3D electrode into account. We then introduce a method to determine the optimal void fraction for a given electrode porosity, thickness and current density that maximizes the reactive surface area and minimizes electrode polarisation during electrolysis.

Chapter 3

"After we predicted the benefits of 3D nickel electrodes in Chapter 2, can we confirm this experimentally?"

Here, we develop an indirect 3D printing technique using moulds printed from PLA. The porous sintered nickel electrodes are loaded with $Ni(OH)_2$ and the battery and electrolysis performance are assessed in 3D printed cells. Experimental results are in good agreement with the results obtained from the model developed in Chapter 2. Not only does the increased ionic conductivity of the 3D electrode improve battery charging and electrolysis performance, it also significantly improves the discharge rate capability. Even following oxygen evolution at a current density of 800 mA/cm^2, the nickel electrodes can still be fully discharged.

Chapter 4

"How can we manufacture 3D structured iron electrodes and how does the void fraction affect performance?"

In this Chapter, we first develop an indirect 3D printing technique for iron electrodes using PLA moulds and a cross-linked agar binder. We then study the impact of the void fraction and channel size on battery and electrolysis performance in 3D printed cells. While the high ionic conductivity of the channels in the 3D structure results in an increase in

material utilisation, we also discuss limits to this approach. Further, we report discharge capacities as high as 651 mAh/cm^2 at 30 °C when the conductive additive carbon black is added.

Chapter 5

"Can a 3D nickel electrode be combined with a molecular catalyst to yield C_{2+} products during CO_2 reduction?"

Here, we load a sintered 3D nickel electrode with the molecular catalyst iron-tetraphenylporphyrin (Fe-TPP) to yield an effective CO_2 reduction catalyst. Experiments are conducted in a specifically designed 3D printed flow cell that improves access of CO_2 and electrolyte into the electrode. Remarkably, this combination of Fe-TPP molecular catalyst, 3D nickel electrode and cell design results in the reduction to ethanol with a high Faradaic efficiency of 68% +/- 3.2% at -0.3 V vs. the reversible hydrogen electrode and partial current density of -21 mA/cm^2.

Chapter 6

"How can 3D nickel and iron electrodes be incorporated into a flow-through cell design for an integrated battery-electrolyser?"

We present a 3D printed cell concept and preliminary results for a flow-through battery-electrolyser employing 3D electrodes. Using a 3D nickel electrode loaded with $Ni(OH)_2$ as anode and a bare 3D nickel electrode as cathode, we demonstrate electrolysis at 60 °C with a thermal efficiency of 83% (1.78 V) at a current density of 400 mA/cm^2. Despite electrolysis current densities as high as 1000 mA/cm^2, the anode discharge performance is not affected. The presented flow cell set-up can serve as a platform for future studies on the impact of electrolyte flow speed, temperature and electrode geometry.

References

[1] H. Lee, K. Calvin, D. Dasgupta, G. Krinner, A. Mukherji, P. Thorne, C. Trisos, J. Romero, P. Aldunce, K. Barret, *et al.*, *IPCC, 2023: Climate change 2023: Synthesis report, summary for policymakers. contribution of working groups I, II and III to the sixth assessment report of the intergovernmental panel on climate change [core writing team, H. Lee and J. Romero (eds.)]. IPCC, Geneva, Switzerland.* (2023).

[2] D. V. Parums, *Climate change and the spread of vector-borne diseases, including dengue, malaria, lyme disease, and west nile virus infection,* Medical Science Monitor: International Medical Journal of Experimental and Clinical Research **29**, e943546 (2023).

[3] J. Samson, D. Berteaux, B. J. McGill, and M. M. Humphries, *Geographic disparities and moral hazards in the predicted impacts of climate change on human populations,* Global Ecology and Biogeography **20**, 532 (2011).

[4] M. Burzyńskia, C. Deuster, F. Docquier, and J. De Melo, *Climate Change, Inequality, and Human Migration*, Tech. Rep. (IZA Discussion Papers, 2019).

[5] United Nations Framework Convention on Climate Change, *Paris Agreement,* https://unfccc.int/process-and-meetings/the-paris-agreement/the-paris-agreement (2015), [Online; accessed 12-May-2024].

[6] Copernicus Climate Change Service, *The 2023 Annual Climate Summary: Global Climate Highlights 2023,* https://climate.copernicus.eu/global-climate-highlights-2023 (2024), [Online; accessed 12-May-2024].

[7] W. J. Ripple, C. Wolf, J. W. Gregg, J. Rockström, T. M. Newsome, B. E. Law, L. Marques, T. M. Lenton, C. Xu, S. Huq, *et al.*, *The 2023 state of the climate report: Entering uncharted territory,* BioScience **73**, 841 (2023).

[8] M. Wiatros-Motyka, N. Fulghum, and D. Jones, *Global electricity review 2024,* (2024).

[9] J. Kim, B. K. Sovacool, M. Bazilian, S. Griffiths, J. Lee, M. Yang, and J. Lee, *Decarbonizing the iron and steel industry: A systematic review of sociotechnical systems, technological innovations, and policy options,* Energy Research & Social Science **89**, 102565 (2022).

[10] E. T. Vogt and B. M. Weckhuysen, *The refinery of the future,* Nature **629**, 295 (2024).

[11] S. Gross, *The challenge of decarbonizing heavy transport,* en. In:(Oct. 2022) **28** (2020).

[12] J. J. Brey, *Use of hydrogen as a seasonal energy storage system to manage renewable power deployment in Spain by 2030,* International Journal of Hydrogen Energy **46**, 17447 (2021).

[13] G. Glenk and S. Reichelstein, *Reversible power-to-gas systems for energy conversion and storage,* Nature Communications **13**, 2010 (2022).

[14] F. M. Mulder, B. M. H. Weninger, J. Middelkoop, F. G. B. Ooms, and H. Schreuders, *Efficient electricity storage with a battolyser, an integrated Ni–Fe battery and electrolyser,* Energy & Environmental Science **10**, 756 (2017).

[15] C. Chakkaravarthy, P. Periasamy, S. Jegannathan, and K. I. Vasu, *The nickel/iron battery,* Journal of Power Sources **35**, 21 (1991).

[16] A. K. Shukla, M. K. Ravikumar, and T. S. Balasubramanian, *Nickel/iron batteries,* Journal of Power Sources **51**, 29 (1994).

[17] J. M. E. Abarro, J. N. L. Gavan, D. E. D. Loresca, M. A. A. Ortega, E. A. Esparcia Jr, and J. A. D. Paraggua, *A Tale of Nickel-Iron Batteries: Its Resurgence in the Age of Modern Batteries,* Batteries **9**, 383 (2023).

[18] A. K. Manohar, S. Malkhandi, B. Yang, C. Yang, G. K. S. Prakash, and S. R. Narayanan, *A high-performance rechargeable iron electrode for large-scale battery-based energy storage,* Journal of the Electrochemical Society **159**, A1209 (2012).

[19] P. Trinke, P. Haug, J. Brauns, B. Bensmann, R. Hanke-Rauschenbach, and T. Turek, *Hydrogen crossover in PEM and alkaline water electrolysis: mechanisms, direct comparison and mitigation strategies,* Journal of The Electrochemical Society **165**, F502 (2018).

[20] H. Kojima, K. Nagasawa, N. Todoroki, Y. Ito, T. Matsui, and R. Nakajima, *Influence of renewable energy power fluctuations on water electrolysis for green hydrogen production,* International Journal of Hydrogen Energy **48**, 4572 (2023).

[21] J. Divisek, J. Mergel, and H. Schmitz, *Advanced water electrolysis and catalyst stability under discontinuous operation,* International Journal of Hydrogen Energy **15**, 105 (1990).

[22] C.-n. CAO *et al.*, *The Memory Effect of MH-Ni Battery,* Journal of Electrochemistry **6**, 11 (2000).

[23] K. Shinyama, Y. Magari, A. Funahashi, T. Nohma, and I. Yonezu, *Improvement of high-temperature characteristics of the sintered nickel positive electrode for an alkaline storage battery,* Electrochemistry **71**, 686 (2003).

[24] J. O. G. Posada and P. J. Hall, *Controlling hydrogen evolution on iron electrodes,* International Journal of Hydrogen Energy **41**, 20807 (2016).

[25] Y. Sui and X. Ji, *Anticatalytic strategies to suppress water electrolysis in aqueous batteries,* Chemical Reviews **121**, 6654 (2021).

[26] J. Li, E. Shangguan, D. Guo, Q. Li, Z. Chang, X.-Z. Yuan, and H. Wang, *Calcium metaborate as a cathode additive to improve the high-temperature properties of nickel hydroxide electrodes for nickel–metal hydride batteries,* Journal of Power Sources **263**, 110 (2014).

[27] H. Vogt, *The actual current density of gas-evolving electrodes—notes on the bubble coverage,* Electrochimica Acta **78**, 183 (2012).

[28] B. E. Bongenaar-Schlenter, L. J. J. Janssen, S. J. D. Van Stralen, and E. Barendrecht, *The effect of the gas void distribution on the ohmic resistance during water electrolytes,* Journal of Applied Electrochemistry **15**, 537 (1985).

[29] K. Zeng and D. Zhang, *Recent progress in alkaline water electrolysis for hydrogen production and applications,* Progress in Energy and Combustion Science **36**, 307 (2010).

[30] H. I. Lee, H.-S. Cho, M. Kim, J. H. Lee, C. Lee, S. Lee, S.-K. Kim, C.-H. Kim, K. B. Yi, and W.-C. Cho, *The structural effect of electrode mesh on hydrogen evolution reaction performance for alkaline water electrolysis,* Frontiers in Chemistry **9**, 787787 (2021).

[31] F. Hine and K. Murakami, *Bubble Effects on the Terminal Voltage of a Vertical Cell with Perforated Electrodes,* Journal of The Electrochemical Society **128**, 64 (1981).

[32] X. Xu, Y. H. Tan, J. Ding, and C. Guan, *3D printing of next-generation electrochemical energy storage devices: from multiscale to multimaterial,* Energy & Environmental Materials **5**, 427 (2022).

[33] S. Mooraj, Z. Qi, C. Zhu, J. Ren, S. Peng, L. Liu, S. Zhang, S. Feng, F. Kong, Y. Liu, *et al.*, *3D printing of metal-based materials for renewable energy applications,* Nano Research **14**, 2105 (2021).

[34] N. Fonseca, S. V. Thummalapalli, S. Jambhulkar, D. Ravichandran, Y. Zhu, D. Patil, V. Thippanna, A. Ramanathan, W. Xu, S. Guo, *et al.*, *3D Printing-Enabled Design and Manufacturing Strategies for Batteries: A Review,* Small **19**, 2302718 (2023).

[35] F. C. Walsh, L. F. Arenas, and C. Ponce de León, *Developments in electrode design: structure, decoration and applications of electrodes for electrochemical technology,* Journal of Chemical Technology & Biotechnology **93**, 3073 (2018).

[36] L. Zeng, P. Li, Y. Yao, B. Niu, S. Niu, and B. Xu, *Recent progresses of 3D printing technologies for structural energy storage devices,* Materials Today Nano **12**, 100094 (2020).

[37] J. Hereijgers, J. Schalck, J. Lölsberg, M. Wessling, and T. Breugelmans, *Indirect 3D printed electrode mixers,* ChemElectroChem **6**, 378 (2019).

[38] J. Hereijgers, J. Schalck, and T. Breugelmans, *Mass transfer and hydrodynamic characterization of structured 3D electrodes for electrochemistry,* Chemical Engineering Journal **384**, 123283 (2020).

[39] M. S. Saleh, J. Li, J. Park, and R. Panat, *3D printed hierarchically-porous microlattice electrode materials for exceptionally high specific capacity and areal capacity lithium ion batteries,* Additive Manufacturing **23**, 70 (2018).

[40] T. Kou, S. Wang, R. Shi, T. Zhang, S. Chiovoloni, J. Q. Lu, W. Chen, M. A. Worsley, B. C. Wood, S. E. Baker, *et al.*, *Periodic porous 3D electrodes mitigate gas bubble traffic during alkaline water electrolysis at high current densities,* Advanced Energy Materials **10**, 2002955 (2020).

[41] I. Sullivan, H. Zhang, C. Zhu, M. Wood, A. J. Nelson, S. E. Baker, C. M. Spadaccini, T. Van Buuren, M. Lin, E. B. Duoss, *et al.*, *3D printed nickel–molybdenum-based electrocatalysts for hydrogen evolution at low overpotentials in a flow-through configuration,* ACS Applied Materials & Interfaces **13**, 20260 (2021).

[42] L. F. Arenas, C. P. de León, and F. C. Walsh, *3d-printed porous electrodes for advanced electrochemical flow reactors: A Ni/stainless steel electrode and its mass transport characteristics,* Electrochemistry Communications **77**, 133 (2017).

[43] A. Limper, N. Weber, A. Brodersen, R. Keller, M. Wessling, and J. Linkhorst, *Additive manufacturing of composite porosity mixer electrodes,* Electrochemistry Communications **134**, 107176 (2022).

[44] D. Kong, Y. Wang, S. Huang, B. Zhang, Y. V. Lim, G. J. Sim, P. Valdivia y Alvarado, Q. Ge, and H. Y. Yang, *3d printed compressible quasi-solid-state nickel–iron battery,* ACS Nano **14**, 9675 (2020).

[45] A. Dubey and A. Arora, *Advancements in carbon capture technologies: A review,* Journal of Cleaner Production **373**, 133932 (2022).

[46] M.-Y. Lee, K. T. Park, W. Lee, H. Lim, Y. Kwon, and S. Kang, *Current achievements and the future direction of electrochemical CO2 reduction: A short review,* Critical Reviews in Environmental Science and Technology **50**, 769 (2020).

[47] M. Z. F. Kamarudin, S. K. Kamarudin, M. S. Masdar, and W. R. W. Daud, *Direct ethanol fuel cells,* International Journal of Hydrogen Energy **38**, 9438 (2013).

[48] R. Kunwer, S. R. Pasupuleti, S. S. Bhurat, S. K. Gugulothu, and N. Rathore, *Blending of ethanol with gasoline and diesel fuel–A review,* Materials Today: Proceedings **69**, 560 (2022).

[49] E. Boutin, L. Merakeb, B. Ma, B. Boudy, M. Wang, J. Bonin, E. Anxolabéhère-Mallart, and M. Robert, *Molecular catalysis of CO_2 reduction: Recent advances and perspectives in electrochemical and light-driven processes with selected Fe, Ni and Co aza macrocyclic and polypyridine complexes,* Chemical Society Reviews **49**, 5772 (2020).

[50] S. Nitopi, E. Bertheussen, S. B. Scott, X. Liu, A. K. Engstfeld, S. Horch, B. Seger, I. E. L. Stephens, K. Chan, C. Hahn, J. K. Nørskov, T. F. Jaramillo, and I. Chorkendorff, *Progress and perspectives of electrochemical CO_2 reduction on copper in aqueous electrolyte,* Chemical Reviews **119**, 7610 (2019).

[51] X. Wang, Z. Wang, F. P. García de Arquer, C.-T. Dinh, A. Ozden, Y. C. Li, D.-H. Nam, J. Li, Y.-S. Liu, J. Wicks, *et al.*, *Efficient electrically powered CO_2-to-ethanol via suppression of deoxygenation,* Nature Energy **5**, 478 (2020).

[52] T. Jaster, A. Gawel, D. Siegmund, J. Holzmann, H. Lohmann, E. Klemm, and U.-P. Apfel, *Electrochemical CO2 reduction toward multicarbon alcohols-The microscopic world of catalysts & process conditions,* Iscience **25** (2022).

[53] A. K. K. Padinjareveetil and M. Pumera, *Advances in Designing 3D-Printed Systems for CO2 Reduction,* Advanced Materials Interfaces **10**, 2201734 (2023).

[54] W.-Y. Yan, C. Zhang, and L. Liu, *Hierarchically porous CuAg via 3D printing/dealloying for tunable CO2 reduction to syngas,* ACS Applied Materials & Interfaces **13**, 45385 (2021).

2

3D hybrid battery-electrolyser nickel electrodes: A theoretical analysis

An integrated battery-electrolyser can store renewable energy as a battery and produce hydrogen when overcharged. This dual application requires novel electrode concepts that ideally enhance both battery and electrolysis operation without compromising either. One such concept is 3D structured electrodes including channels that improve the ionic conductivity and material utilisation as well as facilitate bubble removal during electrolysis. However, the benefits of such 3D electrodes must be balanced against the reduction in reactive surface area as a result of the open volume, or void fraction, of the channels. In this work, we first develop a simplified 1D model of a porous sintered nickel electrode that takes the void fraction of the 3D geometry into account and allows for the determination of the current and potential distribution for both battery charging and oxygen evolution. We then introduce a method to determine the optimal void fraction that maximizes the reactive surface area for oxygen evolution and discuss under which circumstances a 3D geometry is beneficial. Finally, we show how the improved ionic conductivity of 3D electrodes also results in more homogenous battery charging and increases the charging efficiency in nickel electrodes.

The results in this chapter have been submitted for publication.

2.1. Introduction

Climate change poses significant risks to modern society, threatening food security [1], disrupting biodiversity [2], exacerbating socio-economic inequalities [3] and causing more frequent and severe weather events [4]. It is widely recognized that anthropogenic CO_2 emissions are the major cause for an increase in average global temperatures since the start of the industrialization. Mitigating climate change by reducing CO_2 emissions calls for the transition to renewable energy sources such as wind and solar. However, their daily and seasonal variability requires the integration of both short- and long-term energy storage [5, 6].

The battolyser™ introduced by Mulder et al. [7] integrates both short- and long-term energy storage in a single device. It is based on a nickel-iron battery in which the nickel and the iron electrodes not only function as battery electrodes, but also generate oxygen and hydrogen, respectively, when fully charged. This integrated battery-electrolyser can compensate for diurnal variations in the energy supply by charging at times of low energy prices (e.g. during oversupply of wind and solar) and discharging when the energy prices are high (e.g. at peak times in the evening). In contrast to designated battery technologies such as Li-ion, the battolyser™ can still store energy in the form of hydrogen even when fully charged. This can then be stored and used for seasonal energy needs, transportation and as a feedstock for the steel and chemical industry.

However, electrodes employed in conventional nickel-iron batteries are not designed for this dual application of battery energy storage and alkaline electrolysis. On the contrary, oxygen and hydrogen evolution have been considered a parasitic side reactions that decrease the battery charging efficiency, deplete water in the electrolyte and pose an explosion hazard. While conventional nickel and iron battery electrodes can perform electrolysis efficiently at low current densities [7], their transport properties become limiting at high current densities. Therefore, new types of hybrid electrodes are required that combine a high battery storage capacity and rate capability with efficient electrolysis at industrially relevant current densities.

Besides the intrinsic activity of an electrocatalyst, structural properties of the electrode such as the thickness, porosity and reactive surface

area play a significant role for the electrode performance. The larger the reactive surface area over which the applied current is distributed, the lower the local current density and thus overpotential is going to be. Thick, porous electrodes made from sintered metals, foams or felts loaded with catalyst and/or active battery material offer a high surface area and battery capacity per cm^2 of superficial electrode area (height x width). However, the utilisation of this surface area, and thus the effectively used electrode thickness, is limited by the ohmic losses incurred by the ionic electrolyte resistance within the electrode.

In order to decrease the ionic resistance of the electrode, channels can be integrated into the structure that enhance electrolyte accessibility. 3D structuring of such porous electrodes allows for the realisation of complex geometries with multi-scale interconnected porosity which can be rationally designed to meet the requirements for a specific application and operating conditions. The benefits of 3D electrodes have been demonstrated both for battery applications [8–11] and water electrolysis [12–15]. For the latter, a well chosen 3D structure facilitates bubble removal compared to, for example, a stochastically structured nickel foam [14]. Bubbles displace the conductive electrolyte and cover catalytically active sites resulting in increased ohmic losses, an inhomogeneous current distribution and higher overpotentials [16, 17]. Therefore, strategies to effectively remove bubbles are essential in increasing the energy efficiency of an electrolyser [18]. Due to the advantages for both battery and electrolysis operation, periodically structured 3D porous electrodes are a promising option for an integrated battery-electrolyser.

On the other hand, the benefits of a 3D geometry must be weighed against the reduction in surface area and battery capacity compared to a planar electrode. Whether or not a 3D geometry is suitable has to be decided under consideration of the electrode porosity, thickness and current density. Modelling the current distribution and overpotential across the electrode thickness can aid in the understanding of how structural electrode properties affect performance. This is key for the optimization of electrode performance. Such models have been covered extensively in literature for planar porous nickel battery electrodes under consideration of (dis)charging kinetics and concentration gradients for both OH^- and O_2 [19–22]. However, none of these models can be applied directly to account for the additional macroscopic 3D geometry.

A key parameter required for modelling the current distribution in electrodes is the ionic conductivity. A planar porous electrode consists of the solid metal phase and the electrolyte within the pores that conducts the ions. A low porosity, i.e. a low electrolyte volume within the electrode, will result in reduced ion mobility, i.e. ionic conductivity, compared to the bulk electrolyte. In addition, ion mobility is affected by the tortuosity of the pores, which is a measure of how convoluted the path of a pore is. A convoluted path through the electrode increases the distance an ion must travel, which effectively reduces the ionic conductivity. However, microscopic properties such as the porosity and tortuosity will vary throughout the electrode resulting in a locally changing ionic conductivity. In effective medium theory, instead of accounting for this microscopic heterogeneity, average values for the porosity and tortuosity are assumed to be homogenous throughout the electrode. With this assumption, an effective ionic conductivity, κ_{eff}, can be defined using the Bruggeman relation[23, 24]:

$$\kappa_{eff} = \kappa\epsilon^{\tau} \tag{2.1}$$

where κ, ϵ and τ are the bulk electrolyte conductivity, the electrode porosity and the tortuosity, respectively.

A 3D structured porous electrode can be considered as hierarchically porous where the pores and 3D features (e.g. channels) constitute a micro- and macroporosity, respectively. Here, we describe the macroporosity with the void fraction Θ, that represents the volume fraction of the electrode occupied by open 3D features such as channels. The void fraction varies across the electrode and is defined by the electrode geometry. For complex electrode geometries, modelling the current distribution then requires computationally expensive 3D models that describe this specific geometry. However, in order to determine limits for the void fraction, a fast method is required that does not have to take the specific electrode geometry into account. To this end, we define an average effective ionic conductivity, $\kappa_{eff,3D}$, throughout the electrode that expands the Bruggeman relation to take the void fraction into account. We then derive a 1D differential equation in dimensionless form that describes the potential and current distribution for the oxygen evolution reaction (OER) and charging reaction (CR) for sintered 3D nickel electrodes. By solving this differential equation numerically for varying current densities, electrode thicknesses

and void fractions, we find a simple relationship between the electrode utilisation and the dimensionless voltage drop for OER. Based on this, we develop a methodology to determine the optimal electrode void fraction that maximizes the reactive surface area and thus minimizes electrode polarisation for OER. Furthermore, we show how the increased effective ionic conductivity in 3D electrodes results in a more homogenous current distribution and how this is beneficial for the charging efficiency of the battery.

2.2. Mathematical models

2.2.1. Oxygen evolution

In order to describe the current and potential distribution for the oxygen evolution reaction (OER) within the porous electrode, we follow the methodology of Daniel-Bek [25] and Posey [26] employed for a one-dimensional electrode model. Here, the electrode is considered as a system of idealized pores filled with electrolyte embedded within a conductive matrix. Material properties such as the specific surface area, porosity, electrolyte conductivity, etc. are considered as uniform throughout the electrode. We assume further that the reactant concentration within the pores remains constant over time and do not take the effects of concentration polarization into account. In practice, this assumption applies for the following cases: (1) The electrolyte is highly concentrated and well-mixed (e.g. in a flow-through configuration) in combination with sufficiently thin electrodes and low current densities; (2) the first moments after OER is started before gradients in reactant concentration can form. Effects of oxygen bubbles such as the reduction of the effective electrolyte conductivity and coverage of electrochemically active surface area are not considered. Note that in this section, we do not yet consider the battery charging reaction (CR), i.e. the active material is considered fully charged. Therefore, the entirety of the applied current i_{ch} goes towards OER, so that $i_{ch} = i_{OER}$ (Figure 2.1).

As shown in Figure 2.1, the applied current flows from the counter electrode across the length of the pores. Due to the limited conductivity of the solution, the ionic current flow results in a gradient in the solution potential $\phi_S(x)$ across the pore length. For a current collector with a

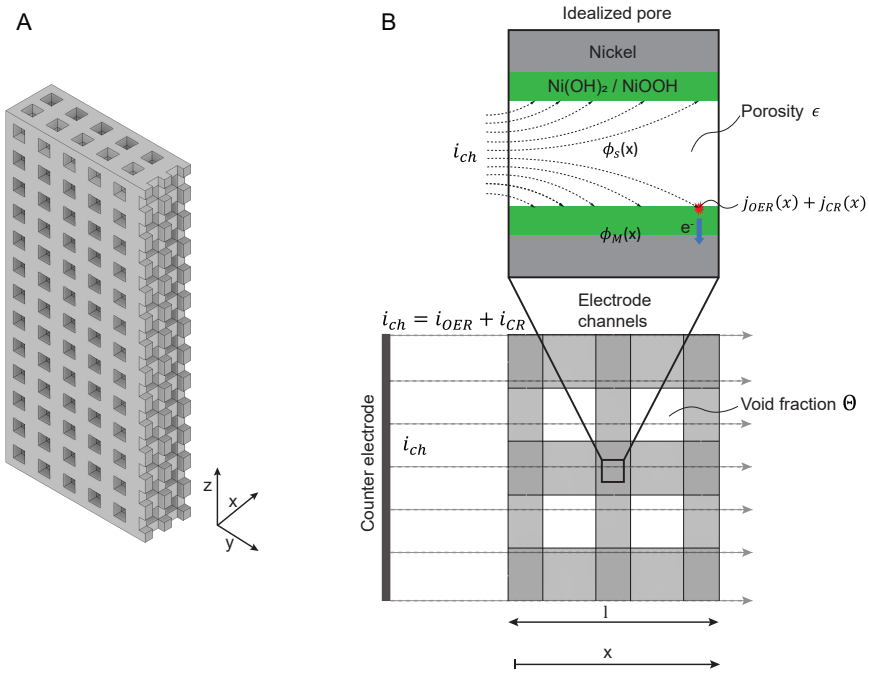

Figure 2.1: (A) Cross-section of a 3D electrode showing channels in x-, y- and z-direction. (B) Schematic of potentials and electrochemical reactions in an idealized porous 3D structured sintered nickel electrode charged at a current i_{ch}. The electrode channels constitute the macroscopic void fraction Θ. At the walls of the micropores, charging of the active material $Ni(OH)_2$/NiOOH (CR) and oxygen evolution (OER) occur with the local partial current densities $j_{CR}(x)$ and $j_{OER}(x)$, respectively. Due to both OER and CR occurring in parallel, the total charging current i_{ch} is split between the respective currents going towards OER (i_{OER}) and CR (i_{CR}). For a fully charged electrode, $i_{ch} = i_{OER}$.

sufficiently low electrical resistivity compared to the ionic resistivity in the solution phase, we can assume that there is no gradient in the potential of the metal phase, ϕ_M. Electrochemical oxygen evolution occurs at the interface between the solution phase and the conductive pore walls and is driven by the difference in their respective potentials, $\Delta\phi(x) = \phi_M - \phi_S(x)$. The rate of oxygen evolution is determined by the overpotential $\eta_{OER}(x)$

with respect to the equilibrium potential $E_{0,OER}$.

$$\eta_{OER}(x) = \phi_M - \phi_S(x) - E_{0,OER} \tag{2.2}$$

Due to the gradient in the solution potential, the overpotential, and therefore the rate of oxygen evolution, decrease across the depth of the pore. In the absence of mass transfer limitations and for high anodic overpotentials the local current density for oxygen evolution, $j_{OER}(x)$, can be described by the simplified Butler-Volmer equation:

$$j_{OER}(x) = j_{0,OER} \ \exp\left(\frac{\alpha_{a,OER}F}{RT}\eta_{OER}(x)\right) \tag{2.3}$$

where $j_{0,OER}$ and $\alpha_{a,OER}$ are the OER exchange current density and anodic transfer coefficient, respectively. As a result of oxygen evolution, the ionic current, i_S, in the electrolyte decreases across the depth of the pore:

$$i_S(x) = i_{OER} - S\int_0^x j_{OER}(x)dx' \tag{2.4}$$

S and i_{OER} represent the electrochemically active surface area per unit length and the applied oxygen evolutin current, respectively. With Ohm's law, assuming a constant electrolyte concentration, the relation between ionic current and the solution potential is given by:

$$\frac{1}{A_{el}}\left[i_{OER} - S\int_0^x j_{OER}(x)dx'\right] = \kappa\frac{d\phi_S}{dx} = -\kappa\frac{d\eta_{OER}}{dx} \tag{2.5}$$

Differentiation of Equation 2.5 yields [25, 26]:

$$\frac{d^2\eta_{OER}}{dx^2} = \frac{S}{\kappa A_{el}}j_{OER}(x) \tag{2.6}$$

where A_{el} describes the average cross-sectional electrolyte area and κ represents the electrolyte conductivity. Compared to a conventional, Non-3D structured electrode, a 3D electrode replaces some of the porous electrode

volume with open structures that are filled with electrolyte. These open structures, such as the channels shown in figure 2.1, can be considered as macroscopic pores. In order to describe this macroscopic porosity, we introduce the void fraction Θ as the ratio of the open volume (e.g.channel volume), V_{ch}, to the total electrode volume, V_{tot}: $\Theta = V_{ch}/V_{tot}$. In practice, the void fraction will vary in all three spatial dimensions depending on the electrode geometry. Instead, we consider the void fraction as an average value which is uniform throughout the electrode, analogous to other electrode parameters such as porosity and surface area. The resulting model allows for more general estimates of the current and potential distribution depending on the void fraction, irrespective of the specific geometry. The average electrolyte cross-sectional area of the porous electrode, A_{el}, is determined by the electrode porosity ϵ and the void fraction Θ of the 3D electrode. By rewriting κA_{el}, we can define an effective electrolyte conductivity for a 3D electrode, $\kappa_{eff,3D}$ (see Appendix A.1):

$$\begin{aligned} \kappa A_{el} &= \kappa \left[(1-\Theta)\epsilon^{\tau} + \Theta\right] A \\ &= \kappa_{eff,3D}\ A \end{aligned} \tag{2.7}$$

wherein A refers to the superficial electrode area, and τ denotes the tortuosity. For a conventional electrode, i.e. for $\Theta = 0$, Equation 2.7 describes the Bruggeman equation for the effective electrolyte conductivity commonly employed for the description of porous electrodes [24, 27, 28]. While the larger open volume of 3D electrodes increases the effective electrolyte conductivity, the resulting reduction in porous electrode material reduces the electrochemically active surface area. With the specific surface area for a conventional electrode S_0, the reduced specific surface area of the 3D electrode is described by $S = S_0(1-\Theta)$. Overall, taking the 3D geometry into account, Equation 2.6 can be rewritten as:

$$\frac{d^2\eta_{OER}}{dx^2} = \frac{S_0(1-\Theta)}{\kappa_{eff,3D}\ A}\ j_{OER}(x) \tag{2.8}$$

The equations above can be simplified by adopting a dimensionless notation as shown by Posey [26]. We define a reduced length $\xi = x/l$, where l is the electrode thickness; a reduced reaction rate $\rho(\xi) = j_{OER}(\xi)/j_{0,OER}$; a reduced total current $I_{OER} = i_{OER}/i_{0,OER}$ with the exchange current

density of the porous electrode $i_{0,OER} = S_0(1-\Theta)lj_{0,OER}$; the resistance parameter $K_{OER} = (i_{0,OER}lF)/(\kappa_{eff,3D}ART)$ and the reduced overpotential $\Phi_{OER}(\xi) = [F\eta_{OER}(\xi)]/RT$. With this dimensionless notation Equation 2.8 can be rewritten as:

$$\frac{d^2\Phi_{OER}(\xi)}{d\xi^2} = K_{OER}\rho_{OER}(\xi) \tag{2.9}$$

with

$$\rho_{OER}(\xi) = e^{\alpha_{a,OER}\ \Phi_{OER}(\xi)} \tag{2.10}$$

The potential and current distribution over the thickness of a porous (3D) electrode can be determined by solving Equation 2.9 for $\Phi(\xi)$ with the following boundary conditions:

$$\left.\frac{d\Phi_{OER}}{d\xi}\right|_{\xi=0} = -K_{OER}I_{OER}, \quad \left.\frac{d\Phi_{OER}}{d\xi}\right|_{\xi=1} = 0 \tag{2.11}$$

2.2.2. Battery charging and oxygen evolution in parallel

In battery-electrolyser nickel electrodes the charging reaction (CR) of the active material and the oxygen evolution reaction (OER) occur simultaneously during charging (Figure 2.1). Equation 2.4 can be extended to include both CR and OER in parallel:

$$i_S(x) = i_{ch} - S\int_0^x [j_{OER}(x) + j_{CR}(x)]\,dx' \tag{2.12}$$

$$\tag{2.13}$$

from which follows:

$$\frac{d^2\eta_{OER}}{dx^2} = \frac{S_0(1-\Theta)}{\kappa_{eff,3D}\ A}\ [j_{OER}(x) + j_{CR}(x)] \tag{2.14}$$

The porosity and electrochemically active surface area are assumed to be constant throughout charging. In order to solve this differential equation, we require terms for the local current densities for both the charging and oxygen evolution reaction. The overall charging reaction of $Ni(OH)_2$ to NiOOH is given by:

$$Ni(OH)_2 + OH^- \xrightarrow{charging} NiOOH + H_2O + e^- \tag{2.15}$$

We assume that the active material loaded into the porous structure of sintered nickel forms a homogeneous film on the pore walls. During charging, protons and electrons are released from the interlamellar sheets of $Ni(OH)_2$ and diffuse through the bulk of the active material to the electrolyte interface and current collector, respectively. Reversely, protons and electrons are intercalated during discharging [29]. The kinetics for both the charging reaction and oxygen evolution are known to vary with the proton concentration at the surface of the active material film contacting the electrolyte [29, 30]. Here, we neglect the diffusive mass transfer resistances of protons and assume that there is no gradient in proton concentration across the thickness of the active material film. Therefore, the surface proton concentration equals that of the bulk. As indicated by Paxton and Newman [23] and Gu et al. [21], this assumption is justified for proton diffusion length scales below 3 μm. Furthermore, we do not take differences in electronic conductivity between the highly conductive nickel scaffold and the active material into account. The state of charge, $soc(x)$, can be expressed using the average proton concentration $c_H(x)$ in the nickel hydroxide film:

$$soc(x) = 1 - \frac{c_H(x)}{c_{H,max}} \tag{2.16}$$

where $c_{H,max}$ denotes the maximum proton concentration, i.e. when the active material is fully discharged. Ta and Newman determined that the exchange current density for oxygen evolution on pure nickel hydroxide films increases linearly with the state of charge and exhibits irreversible Tafel behavior [30]. Therefore, the local current density for oxygen evolution can be expressed as:

$$j_{OER}(x) = j_{0,OER,ref} \left(\frac{c_{OH}}{c_{OH,ref}} \right)^2 soc(x) \ \exp\left(\frac{\alpha_{a,OER} F}{RT} \eta_{OER}(x) \right) \tag{2.17}$$

For the charging reaction, we adapt the kinetic expression used by Fan [20] and De Vidts [19]:

$$\begin{aligned} j_{CR}(x) = 2 \ j_{0,CR,ref} \Bigg[\frac{c_{OH}}{c_{OH,ref}} \ [1 - soc(x)] \exp\left(\frac{\alpha_{a,CR} F}{RT} \eta_{CR}(x) \right) \\ - soc(x) \exp\left(- \frac{\alpha_{c,CR} F}{RT} \eta_{CR}(x) \right) \Bigg] \end{aligned} \tag{2.18}$$

Here, c_{OH} is the electrolyte concentration, and $c_{OH,ref}$ is the reference electrolyte concentration at which the exchange current densities of the charging reaction, $j_{0,CR,ref}$ and oxygen evolution, $j_{0,OER,ref}$, were measured. We assume that there are no changes in reactant concentration over time, so that c_{OH} does not change across the depth of the pores. The overpotential for each reaction is given by:

$$\eta_{OER}(x) = \phi_M - \phi_S(x) - E_{0,OER} \tag{2.19}$$

$$\eta_{CR}(x) = \phi_M - \phi_S(x) - E_{0,CR}(x) \tag{2.20}$$

The equilibrium potential for the battery charging reaction, $E_{0,CR}(x)$, depends on the proton concentration and can be estimated by the Nernst equation [27]:

$$E_{0,CR}(x) = E_{0,1/2} + \frac{RT}{F}\, ln\left(\frac{1 - \frac{c_H(x)}{c_{H,max}}}{\frac{c_H(x)}{c_{H,max}}}\right) \tag{2.21}$$

$$= E_{0,1/2} + \frac{RT}{F}\, ln\left(\frac{soc(x)}{1 - soc(x)}\right) \tag{2.22}$$

where $E_{0,1/2}$ represents the equilibrium potential at 50 % state of charge. In practice, the charging reaction for the nickel electrode has been shown to exhibit a mixed potential due to the OER at higher states of charge [31]. In addition, the equilibrium potential is affected by structural changes and the intercalation of H_2O, and ions such as OH^- and K^+ between the interlamellar sheets. These effects give rise to a hysteresis behavior resulting in different equilibrium potentials for the same state of charge depending on whether the electrode is charging or discharging. Equation 2.21 can be modified to accommodate for the deviation from Nernstian behavior as a result of the above described non-ideal effects [32]. Since this work only considers the charging reaction, and modified Nernstian expressions are often developed for specific conditions and material properties, we employ the unmodified term in Equation 2.21 for the estimate of the equilibrium potential.

Subtracting Equation 2.20 from Equation 2.19 allows for the substitution of η_{CR} in Equation 2.18:

$$\begin{aligned}\eta_{CR}(x) &= \eta_{OER}(x) + E_{0,OER} - E_{0,CR}(x) \\ &= \eta_{OER}(x) + \Delta E_0(x)\end{aligned} \tag{2.23}$$

By inserting Equation 2.23 into Equation 2.18, the differential equation in Equation 2.14 can be solved for $\eta_{OER}(x)$. Rewriting Equation 2.14 in the previously introduced dimensionless notation yields:

$$\frac{d^2\Phi_{OER}}{d\xi^2} = K_{OER}\ \rho_{OER}(\xi, soc) + \ K_{CR}\ \rho_{CR}(\xi, soc) \tag{2.24}$$

$$\Phi_{CR}(\xi) = \Phi_{OER}(\xi) + \Delta\Phi_0(\xi) \tag{2.25}$$

where $\Delta\Phi_0(\xi) = F\Delta E_0(\xi)/RT$. The reduced reaction rates ρ_k, the resistance parameters K_k and the reduced current I_k for OER and CR are defined as:

$$\begin{aligned}\rho_k(\xi, soc) &= \frac{j_k(\xi, soc)}{j_{0,k,ref}} \\ K_k &= \frac{S_0(1-\Theta)l^2 F j_{0,k,ref}}{\kappa_{eff,3D} ART} \quad \text{where } k = \begin{cases}\text{OER} & \text{for oxygen evolution} \\ \text{CR} & \text{for the charging reaction}\end{cases} \\ I_k(SOC) &= \frac{i_k(SOC)}{S_0(1-\Theta)l j_{0,k,ref}}\end{aligned} \tag{2.26}$$

where i_k represents the total current for either OER or CR across the entire electrode. SOC denotes the overall state of charge of the electrode defined as:

$$SOC(t) = \int_0^1 soc(\xi, t)d\xi \tag{2.27}$$

Equation 2.24 is solved with the following boundary conditions:

$$\left.\frac{d\Phi_{OER}(\xi)}{d\xi}\right|_{\xi=0} = -K_{OER}\ I_{OER}(soc) - K_{CR}\ I_{CR}(soc)$$
$$= \frac{lFi_{ch}}{\kappa_{eff,3D}\ ART} \tag{2.28}$$
$$\left.\frac{d\Phi_{OER}}{d\xi}\right|_{\xi=1} = 0$$

The local state of charge, $soc(\xi, t)$, depends not only on the local charging current j_{CR}, but also on the charging duration. Thus, the potential distribution described by Equation 2.24 is implicitly a function of time. If we neglect double-layer charging and assume no gradients in electrolyte composition, the profiles of potential and current are formed instantaneously. We further assume homogenous charging across the thickness of the $Ni(OH)_2$/NiOOH film and neglect mass transfer resistances within. Therefore, Equation 2.24 describes the steady-state potential and current distribution at time t. The local state of charge can then be calculated after a time step Δt as:

$$soc(\xi, t + \Delta t) = soc(\xi, t) + \frac{lS\rho_{CR}\ j_{0,CR,ref}}{C}\Delta t \tag{2.29}$$

where C refers to the battery capacity.

2.3. Results and discussion

2.3.1. Current and potential distribution in porous 3D electrodes during oxygen evolution

The larger reactive surface area of porous electrodes can effectively reduce activation overpotentials and thus increase the energy efficiency of electrochemical reactions such as the OER. Structural properties that affect electrode performance are the thickness and the porosity. While an increase in thickness enhances the overall surface area, its utilisation for the electrochemical reaction is limited by the ionic resistance within the electrode pores. As a result, too thick electrodes can be partially inactive so that the additional surface area does not contribute to a further

reduction in overpotential. Decreasing the ionic resistance, for example by increasing the porosity and operating temperature, increases the utilisation. However, an increase in porosity also decreases the surface area. Furthermore, for the here discussed hybrid electrodes that also function as battery electrodes, porosities are typically low in order to accommodate the loaded active material that determines the energy storage capacity of the electrode. An increase in temperature is limited by the stability of the active material and cell components. While conventional alkaline electrolysers operate at temperatures between 80 and 90°C [33], nickel-iron batteries are typically limited to temperatures below 45°C [34]. The 3D structure of electrodes presents an additional degree of freedom that allows for the adjustment of the ionic resistance, where the void fraction, Θ, is the equivalent of a macroscopic porosity determined by the additional open volume of the 3D features (e.g. channels). Just as the microscopic porosity, ϵ, of the porous electrode material, an increase in void fraction of the 3D structure decreases the ionic resistance at the cost of a reduction in reactive surface area. Therefore, the void fraction must be determined to reduce overpotentials under consideration of the applied current density as well as structural and catalytic parameters of the porous electrode material.

Conventional electrode geometry

Due to the ionic resistance, the solution potential, and therefore the overpotential, decrease across the electrode thickness. As shown in Figure 2.2 C, the reduced overpotential is similar at the front of the electrode, $\Phi(0)$, and the back, $\Phi(l)$, if the electrode is sufficiently thin for a given current density. Accordingly, the reaction occurs over the entire electrode, albeit at a lower magnitude towards the back ($\xi = 1$). Increasing the electrode thickness results in an inhomogeneous distribution of the overpotential shifting the reaction towards the front of the electrode. How effectively an electrode is utilized, can be determined from the relative reaction rate, $\rho(\xi)/\rho(0) = j(\xi)/j(0)$. In areas where $\rho(\xi)/\rho(0)$ approaches zero, the electrode is considered inactive as a result of the too high ionic resistance which prevents the penetration of the reaction deeper into the electrode (Figure 2.2 A). Based on the definition for the electrode utilisation used

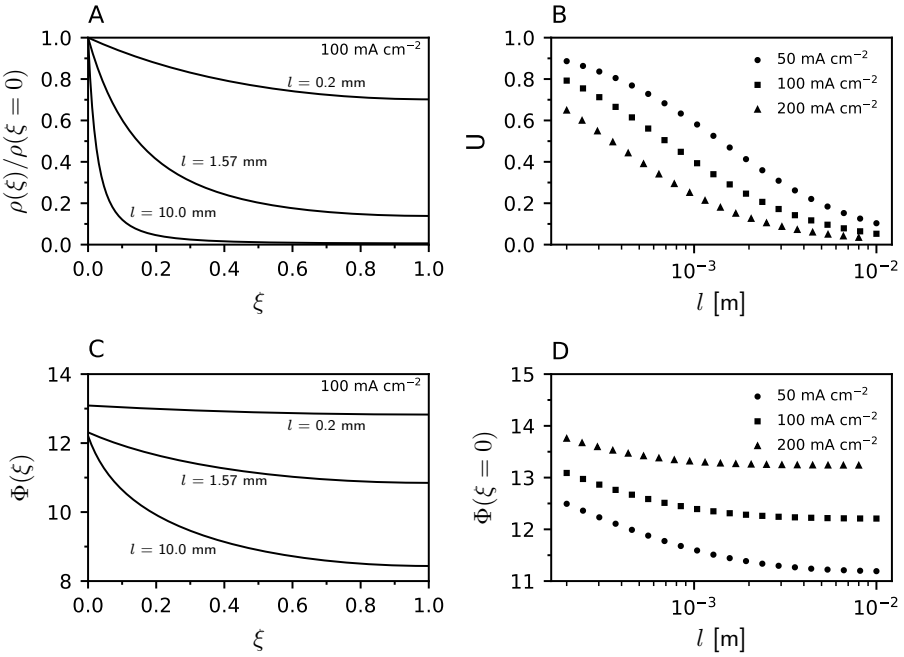

Figure 2.2: (A, C) Current distribution $\rho(\xi)/\rho(0)$ and reduced overpotential $\Phi(\xi)$ over the reduced electrode coordinate $\xi = x/l$ for a superficial current density of 100 mA/cm^2. (B, D) Electrode utilisation U as defined in Equation 2.30 and reduced overpotential at the front of the electrode ($\Phi(\xi) = 0$) for different electrode thicknesses and superficial current densities.

by Rausch and Wendt [35][1], we can define the utilisation of an electrode via the reduced reaction rate $\rho(\xi) = j(\xi)/j(0)$:[2]

$$U = \int_0^1 \frac{\rho(\xi)}{\rho(0)} d\xi = \frac{I}{\rho(0)} \tag{2.30}$$

As shown in Figure 2.2 B, the utilisation not only decreases for thicker electrodes, but also for higher current densities. This is due to the increased voltage drop across the electrode thickness at higher current densities. Up to a limiting thickness, l_{lim}, the electrode polarization, $\Phi(0)$,

[1] $U = l^{-1} \int_0^l j(x)/j(0) dx'$.
[2] $i = S \int_0^x j(x) dx'$, so that $I = \int_0^1 \rho(\xi) d\xi$.

decreases. Beyond this thickness, $\Phi(0)$ does not decrease significantly (Figure 2.2 D). This limiting thickness is commonly referred to as the reaction penetration depth [24, 36, 37]. It describes the thickness at which the utilisation of the additional reactive surface area gained by increasing the electrode thickness is limited by the ionic resistance of the electrode. The reaction penetration depth can be defined as the characteristic length of the exponential decay of the local overpotential in a semi-infinite electrode (Figure A.1) [24, 37]. For higher current densities, the reaction penetration depth, and thus the utilisation, decreases (Figure 2.2 B, D). As a result, the electrode thickness should be chosen close to the reaction penetration depth for a specific current density. Designing electrodes thicker than the reaction penetration depth results in increased material costs with no additional gain in performance. Electrodes below the reaction penetration depth reduce material costs with the caveat of higher operating costs, i.e. higher overpotentials.

Effective surface area enhancement with 3D electrodes

As shown above, in conventional electrodes the thickness and current density are limited by the ionic resistance. Channels filled with electrolyte in a more open 3D structure decrease the ionic resistance within the electrode with the caveat of reducing the total reactive surface area. In order to reduce the activation overpotential and increase the energy efficiency, the applied current must be distributed over as large of a surface area as possible. Thus, when deciding on the void fraction of a 3D electrode, we need to strike a balance between the removal and the overall improved accessibility of surface area. Using the utilisation U as defined in Equation 2.30, the effective electrochemically active surface, $A_{R,eff}$, is given by:

$$A_{R,eff} = US_0l(1-\Theta) \tag{2.31}$$

where S_0 is the surface area per unit length of a conventional electrode. In order to assess a 3D electrode compared to a conventional electrode, we define the 3D surface enhancement Γ, which is the ratio of the respective effective reactive surface areas $A_{R,eff,3D}$ and $A_{R,eff}$:

$$\begin{aligned}\Gamma &= \frac{A_{R,eff,3D}}{A_{R,eff}} \\ &= \frac{U_{3D}}{U_0}(1-\Theta) \not< 1\end{aligned} \tag{2.32}$$

Here, U_{3D} and U_0 represent the utilisation of a 3D electrode and a conventional electrode, respectively. In order for a 3D electrode to be beneficial over a conventional electrode, Γ must be larger than one. The resulting difference in electrode polarization can be derived from Tafel kinetics (see Appendix A.2):

$$\begin{aligned}\Delta\Phi(0) &= \Phi_{3D}(0) - \Phi_0(0) \\ &= \frac{1}{\alpha_{a,OER}} \ln\left(\frac{1}{\Gamma}\right)\end{aligned} \tag{2.33}$$

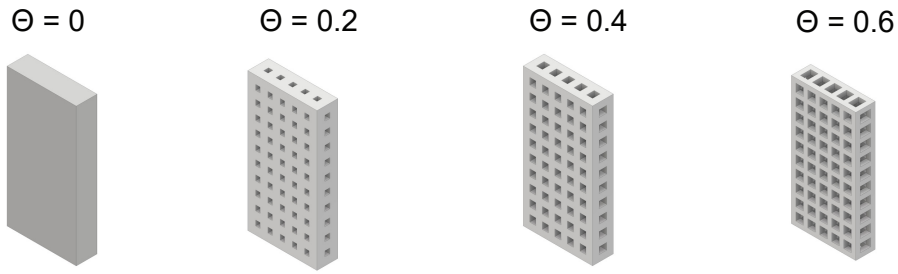

Figure 2.3: Examples for 3D electrodes with varying void fraction Θ.

Figure 2.4 shows the utilisation, 3D surface enhancement and difference in polarization of electrodes with varying void fraction and thickness at a constant superficial current density. For electrodes with a void fraction larger than zero, i.e. 3D electrodes, the utilisation increases with the void fraction for all thicknesses. However, there is a limiting thickness for each void fraction at which the reduced total surface area of the 3D electrode is compensated for by the decreased ionic resistance and enhanced material utilisation (Figure 2.4 B). For lower thicknesses, the effective surface area of a 3D electrode is lower compared to a conventional electrode ($\Gamma < 1$), which results in higher electrode polarization (Figure 2.5 C). For thicknesses where $\Gamma > 1$, the increased effective conductivity results in an

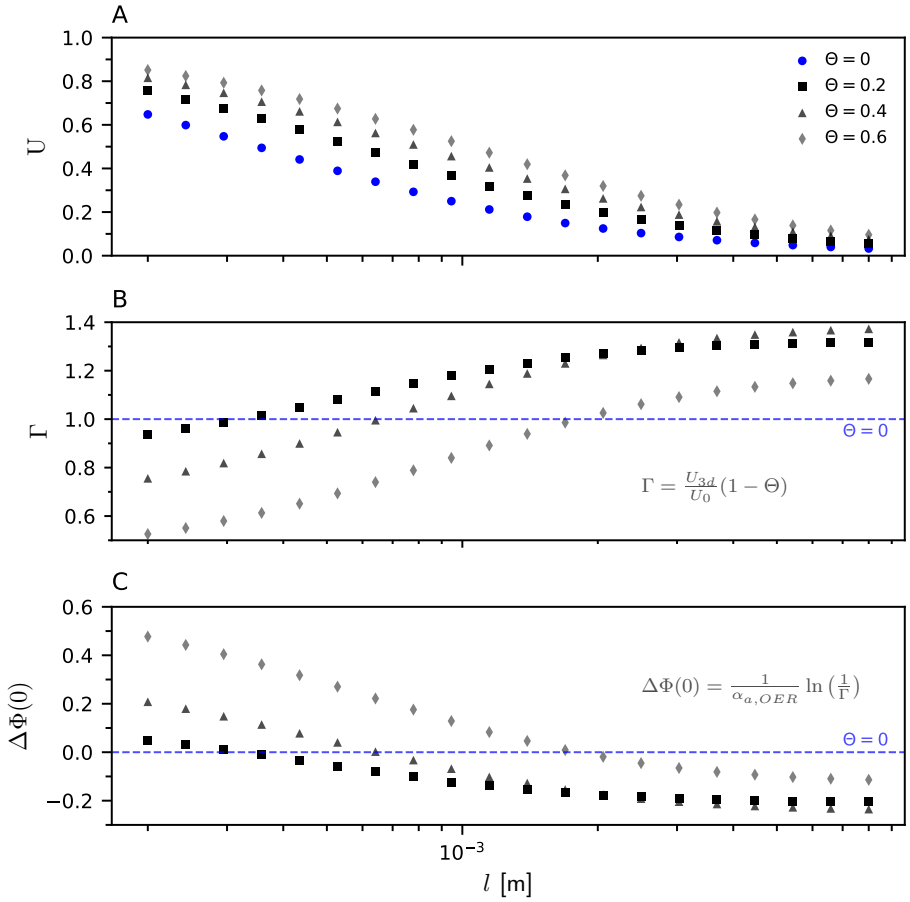

Figure 2.4: Electrode utilisation (A), surface enhancement (B) and difference in reduced overpotential compared to a Non-3D electrode ($\Theta = 0$) at a superficial current density of 200 mA/cm^2 for different electrode thicknesses and void fractions (C). For $\Delta\Phi(0) < 0$, the reduced overpotential is lower compared to a Non-3D electrode.

increase of the effectively utilized surface area, which reduces electrode polarization. We observe a similar limit for the applied current density at a constant electrode thickness (Figure 2.5). It is apparent that higher void fractions are only beneficial for thicker electrodes or higher current densities, i.e. when the voltage drop across the electrode thickness is sig-

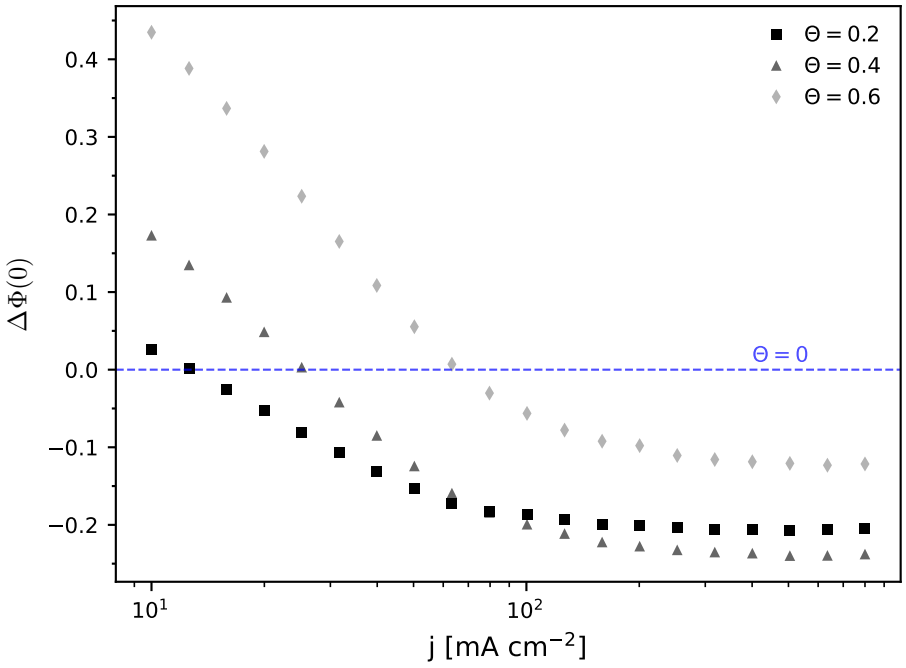

Figure 2.5: Difference in reduced overpotential compared to a Non-3D electrode ($\Theta = 0$) for a 5 mm thick electrode for different superficial current densities j and void fractions Θ. For $\Delta\Phi(0) < 0$, the reduced overpotential is lower compared to a Non-3D electrode.

nificant. However, there appears to be an upper limit to the void fraction. For the conditions shown in Figures 2.4 and 2.5, electrodes with a void fraction of 0.40 outperform those with a void fraction of 0.20 for higher thicknesses and current densities while a void fraction of 0.60 exhibits the lowest reduction in polarization compared to a conventional electrode. Consequently, there is an optimal void fraction depending on the range of operating current density, electrode thickness and material properties of the porous electrode scaffold.

Optimal void fraction for oxygen evolution

The results shown in Figures 2.2 - 2.5 were obtained from solving the differential equation outlined in section 2.2.1 using the finite difference method. Particularly in cases where the gradient of the overpotential is high, i.e. for high superficial current densities and thick electrodes, determining the electrode utilisation and polarization is computationally expensive. Therefore, our goal was to determine simple relationships between the dimensionless numbers introduced in section 2.2.1 that allow for the direct calculation of the utilisation and polarization for a given superficial current density and set of electrode properties. With the definition for the utilization (Equation 2.30), the dimensionless electrode polarization, $\Phi(0)$, is given by:[3]

$$\Phi(0) = \frac{1}{\alpha_a} \ln\left(\rho(0)\right) = \frac{1}{\alpha_a} \ln\left(\frac{I}{U}\right) \tag{2.34}$$

The utilisation decreases both for higher current densities and thicker electrodes (Figures 2.4 and 2.5). This is due to the voltage drop in the electrolyte across the electrode thickness. The product of the resistance parameter K and the reduced current I can be considered a dimensionless voltage drop. Plotting the utilisation over KI for varying current densities, electrode porosities, void fractions and thicknesses results in an inverse sigmoid curve as shown in Figures 2.6 and 2.11. The utilisation as a function of KI can be described using a Hill function [38]:

$$U = \frac{1}{1 + \left(\frac{KI}{m}\right)^k} \tag{2.35}$$

k and m represent the slope and the value of KI, where the utilisation is 50 %, respectively. Such an inverse sigmoid curve is also used to empirically describe the decrease in discharge capacity as a function of discharge rate in Ni-Cd batteries [39]. As shown in Figure 2.6, Equations 2.34 and 2.35 provide a dimensionless framework, integrating data across varying operating conditions and electrode properties. It can be used to rapidly assess when the use of 3D electrodes is the most effective and which values for the void fraction to choose.

[3] $\rho(\xi) = e^{\alpha_a \Phi(\xi)} = j(\xi)/j_0$.

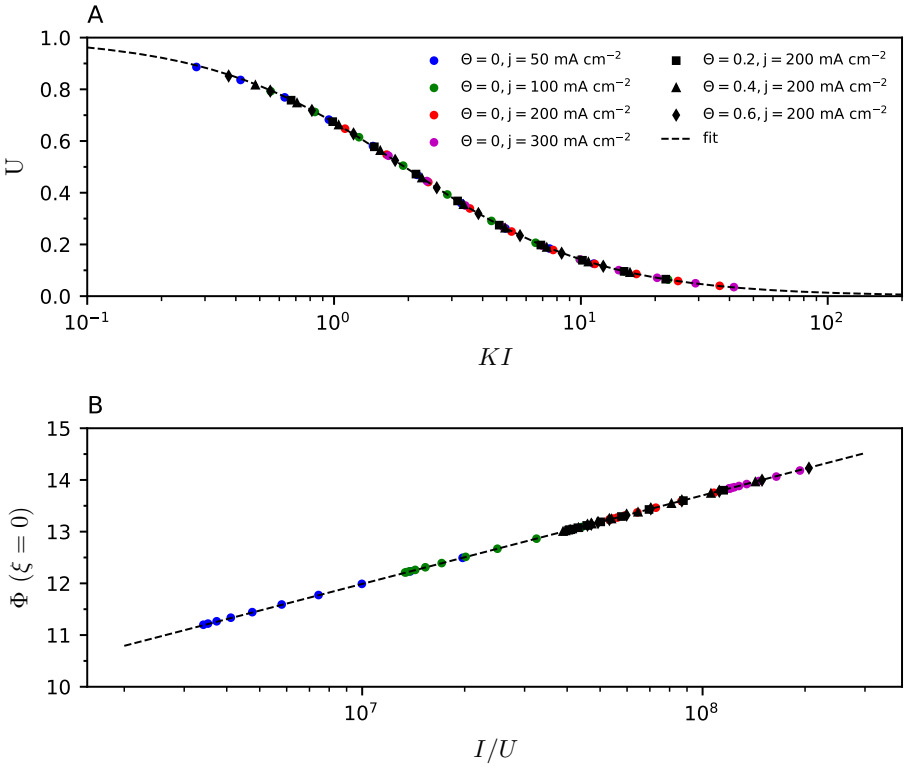

Figure 2.6: Dimensionless relationships between utilisation U, resistance parameter K, reduced current I and reduced overpotential at the front of the electrode $\Phi(\xi = 0)$. For each set of void fraction and current density, the polarisation and current distribution were modelled for electrode thicknesses in between 0.2 mm and 8 mm as shown in Figure 2.2 B. The data points were fitted using Equations 2.35 (A) and 2.34 (B); $m = 1.926$ and $k = 1.091$. KI can also be understood as a dimensionless voltage drop.

Increased 3D void fraction vs. reduction of electrode thickness

The structural electrode properties of the electrode thickness and 3D void fraction have a significant impact on utilisation and polarization in that they affect the effectively available reactive surface area. Understanding how electrode thickness and 3D void fraction relate to each other is essential to arrive at guidelines for the overall electrode design. To this end,

we conduct the following thought experiment: Consider two electrodes of thickness l_0 with an initial void fraction of zero and otherwise identical material properties. Both electrodes are operated at the same superficial current density j. For one electrode we decrease the thickness to l for an unchanged void fraction, for the other we increase the void fraction while maintaining the same electrode thickness. In the first step we determine when the utilisation is identical for both cases. As shown in Equation 2.35 and Figure 2.6, the utilisation is determined by the factor KI. An identical value for KI will therefore result in the same value for the utilisation, so that we can write:

$$(KI)_\Theta = (KI)_l \tag{2.36}$$

Here, $(KI)_\Theta$ and $(KI)_l$ refer to the cases for the increase in void fraction and the decrease in electrode thickness, respectively. Inserting the expressions for the resistance parameter K and the reduced current I and rearranging for the relative reduction in electrode thickness l/l_0 yields:

$$\begin{aligned} \frac{l_0 F j}{\kappa\left[(1-\Theta)\epsilon^\tau + \Theta\right] RT} &= \frac{l F j}{\kappa \epsilon^\tau RT} \\ \frac{\epsilon^\tau}{(1-\Theta)\epsilon^\tau + \Theta} &= \frac{l}{l_0} \end{aligned} \tag{2.37}$$

The void fraction Θ in Equation 2.37 represents the void fraction that results in the equivalent utilisation as a reduction of the electrode thickness by a factor of l/l_0 for a given porosity.

For two electrodes with the same utilisation, the polarization for a given superficial current density is determined by the reduced current I (Equation 2.34). Therefore, in order to identify the limit for the void fraction, we determine when the reduced current is equal for the case of decreasing the electrode thickness (I_l) and increasing the void fraction (I_Θ):

$$\begin{aligned} I_\Theta &= I_l \\ \frac{jA}{S_0(1-\Theta) l_0 j_{0,OER}} &= \frac{jA}{S_0 l j_{0,OER}} \\ 1-\Theta &= \frac{l}{l_0} \end{aligned} \tag{2.38}$$

which represents the equivalent reduction in electrode material volume, i.e. reactive surface area, for each case. Equations 2.36 and 2.38 are plotted in Figure 2.7 A. The intersection of both curves marks the upper limit for the void fraction, Θ_{max}, where the utilisation and the reduced current are identical for both the reduction of electrode thickness and the increase in void fraction. As a result, the electrode polarization is equal at this point (Equation 2.34). For void fractions below Θ_{max}, a 3D results in a higher effective surface available for OER which reduces electrode polarization. For void fractions higher than Θ_{max}, too much reactive surface area is removed compared to a reduction of electrode thickness. 3D electrodes offer the most significant benefits over a reduction in thickness, when the electrode porosity is low. For low porosities, the void fraction of the open 3D structure compensates for the reduced effective conductivity of the electrode material. As a result, Θ_{max} decreases for higher porosities (Figure 2.5 B). For porosities above approximately 0.62, employing a 3D electrode structure is less effective than reducing the thickness of a conventional electrode. Therefore, 3D electrodes are especially suitable for applications where the electrode porosity is lower. For example, this is the case for the hybrid battery and electrolysis electrodes discussed in section 2.3.2, where the theoretical battery capacity is determined by the amount of $Ni(OH)_2$ loaded within the pores.

Optimal void fraction for the reduction of electrode polarization

The discussion above provides an upper limit for the void fraction that is determined by the electrode porosity. However, once it has been established that a 3D structure can improve electrode performance, we need to determine a void fraction that maximizes the effectively used surface area and therefore minimizes electrode polarization. To this end, we insert Equation 2.35 in Equation 2.32, which yields an expression for the 3D surface enhancement:

$$\Gamma = \frac{1 + \left(\frac{Plj}{m\epsilon^{\tau}}\right)^{k}}{1 + \left(\frac{Plj}{m[(1-\Theta)\epsilon^{\tau}+\Theta]}\right)^{k}}(1-\Theta) \tag{2.39}$$

where $P = F/\kappa RT$. The optimal void fraction, Θ_{opt}, results in a maxi-

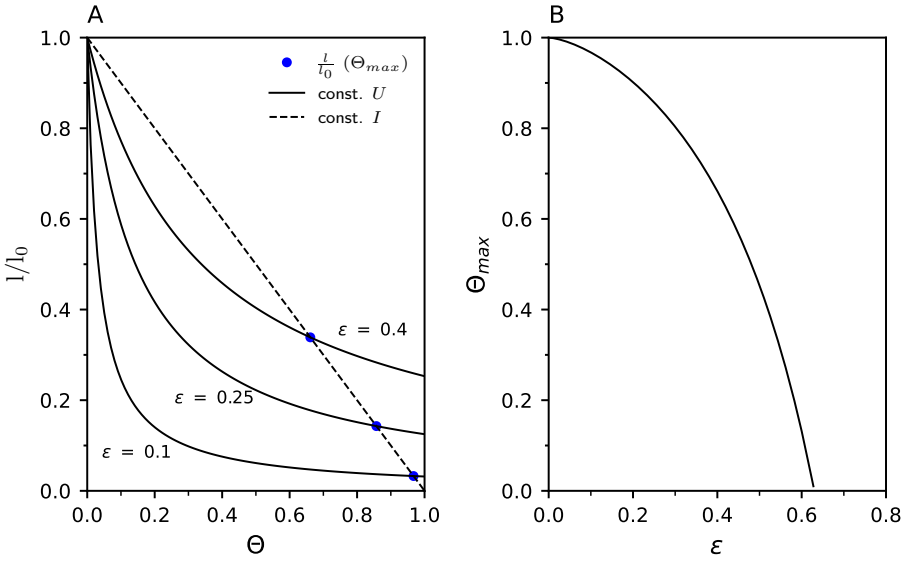

Figure 2.7: When is it more effective to increase the void fraction compared to decreasing the electrode thickness? (A) Equivalent decrease in electrode thickness by a factor of l/l_0 for a given void fraction Θ that results in the same utilisation U (——) and reduced current I (– – –). The maximum void fraction Θ_{max}, above which a decrease in electrode thickness is more beneficial, is defined by the intersection of the curves for constant U and I, and depends on the electrode porosity ϵ (B).

mum 3D surface enhancement for a given electrolyte conductivity, porosity, electrode thickness and superficial current density. We determine Θ_{opt} by setting the partial differential of Γ to zero and solving numerically for Θ:

$$\left.\frac{\partial \Gamma}{\partial \Theta}\right|_{\kappa,\epsilon,l,i} = 0, \quad 0 \leq \Theta < 1 \tag{2.40}$$

where

$$\left.\frac{\partial\Gamma}{\partial\Theta}\right|_{\kappa,\epsilon,l,j} = \frac{-k\left(\frac{Pjl}{m(\epsilon^\tau(1-\Theta)+\Theta)}\right)^k(1-\Theta)(\epsilon^\tau-1)}{(\epsilon^\tau(1-\Theta)+\Theta)\left(1+\left(\frac{Pjl}{m(\epsilon^\tau(1-\Theta)+\Theta)}\right)^k\right)^2} \times\left(1+\left(\frac{P\epsilon^{-\tau}jl}{m}\right)^k\right) - \frac{\left(1+\left(\frac{P\epsilon^{-\tau}jl}{m}\right)^k\right)}{\left(1+\frac{Pjl}{m(\epsilon^\tau(1-\Theta)+\Theta)}\right)^k} \tag{2.41}$$

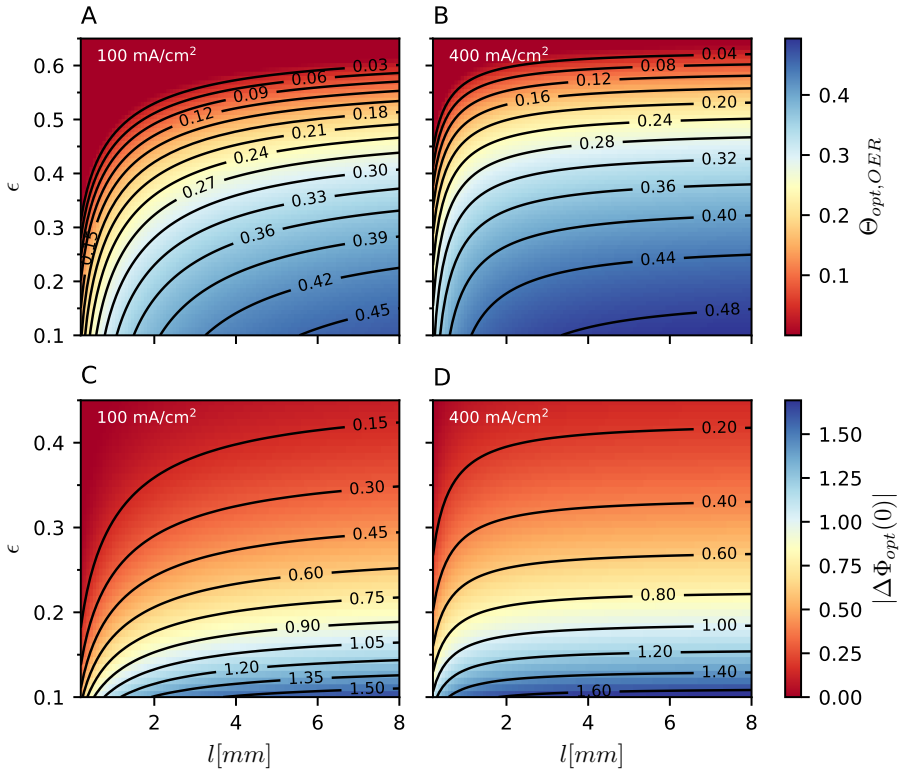

Figure 2.8: Optimal void fraction ($\Theta_{opt,OER}$) with respect to the oxygen evolution reaction and the resulting absolute difference in the reduced electrode polarisation ($|\Delta\Phi_{opt}|$) at varying electrode thicknesses (l) and porosities (ϵ) for a superficial current density of 100 mA/cm^2 (A, C) and 400 mA/cm^2 (B, D).

The optimal void fraction and the resulting absolute difference in the reduced polarization, $|\Delta\Phi_{opt}|$, are shown in Figure 2.8 for different porosities and electrode thicknesses at superficial current densities of 200 and 400 mA/cm^2. Generally, the optimal void fraction increases for thicker electrodes, lower porosities and higher current densities where the ionic voltage drop across the electrode is high. This higher ionic voltage drop is mitigated by the improved ionic conductivity of the more open 3D structures with a higher void fraction. Remarkably, regardless of current density, electrode thickness and porosity, the optimal void fraction is limited to values no higher than around 0.50. The threshold porosity above which 3D electrodes are not beneficial compared to conventional electrodes increases for higher current densities and thicker electrodes. It reaches a maximum at around 0.62 which is consistent with the porosity limit determined from the thought experiment above (Figure 2.7). For electrodes that exclusively perform OER, and without taking effects of bubble removal into account, a high porosity at or above this limit is preferable over a 3D structure as it simplifies the manufacturing process. On the other hand, hybrid battery electrodes, that are used as OER electrodes when fully charged, will generally exhibit lower porosities and more active mass per area as the battery capacity is determined by volume of $Ni(OH)_2$ filling the pores. As a result, the here discussed 3D electrodes are especially suitable for battery-electrolysis electrodes, where the channel structure allows for OER overpotentials comparable to those of a flat OER-only electrode with a higher porosity. In addition, the increased ionic conductivity of the channels is also expected to reduce overpotentials with respect to the battery charging reaction (CR).

2.3.2. Hybrid 3D battery and electrolysis electrodes

During charging, the battery charging reaction (CR), i.e. the electrooxidation of $Ni(OH)_2$ to NiOOH, is in competition with the oxygen evolution (OER). Since charge consumed by the OER instead of the CR reduces the charging efficiency, the OER has been considered a parasitic side reaction in conventional nickel battery electrodes. However, as the exchange current density for CR is orders of magnitude higher than for OER, significant OER typically first occurs at a higher state of charge as long as the ionic and electrical conductivity are not limiting. Moreover,

excessive gas evolution in battery cells with limited ventilation can result in pressure build up and poses an explosion hazard when combined with the hydrogen produced at the battery anode during charging. In a hybrid battery-electrolysis system like the battolyser™, on the other hand, the cells are pressure controlled and designed to mitigate the risks from gas cross-over. Furthermore, a low charging efficiency can be mostly compensated for by extended periods of overcharging, i.e. electrolysis, but at the cost of increased charging potentials.

Nonetheless, fast battery charging with little gas evolution and overpotential increase until the electrode is fully charged significantly increases the flexibility and efficiency in operation of the battolyser™. In periods of rapid changes in the energy price, the system can switch faster and store more energy between charging (low energy price) and discharging (high energy price). In addition, the nominal H_2/O_2 production rate is reached sooner after a period of discharging. For conventional nickel battery electrodes, the inhibition of the OER has been a central area of research over the past decades. This is typically achieved by increasing the OER potential compared to the charging potential by the addition of additives such as Co, Ca and Cd in the active material in combination with LiOH in the electrolyte [4] [40–42]. However, for the here discussed hybrid electrodes an increase in OER potential would reduce the overall energy efficiency for hydrogen production of the battolyser™. In the following, we demonstrate how a more open 3D-structured electrode, in addition to reducing OER overpotential, can also increase the battery charging efficiency.

In order to determine the charging characteristics of a 3D electrode, we first determine the ideal void fraction for a specific operating current density as outlined in the previous section (Figure 2.8). For this example, we set the operating current density to 200 mA/cm^2 for both charging and subsequent electrolysis, which is within the range of conventional alkaline electrolyzers [43]. For a 5 mm thick electrode, and a porosity of 0.25, this results in a void fraction of 0.42. Figure 2.9 compares the overall state of charge, SOC, and the Faradaic efficiency for the charging reaction (i_{CR}/i_{ch}) of the 3D electrode and a conventional electrode throughout charging and overcharging. For batteries, it is common to express the in-

[4] An increase in OER potential, i.e. the potential during overcharging, can be achieved using additives that either increase the equilibrium potential, $E_{0,OER}$, or decrease the exchange current density, $j_{0,OER}$, and the transfer coefficient, α_{OER}.

serted charge as a fraction of the nominal capacity. A charge insertion of 0.5 C, for example, is equivalent to inserting half of the nominal capacity during charging. Since the nominal capacity of a battery is specific to a set of operating conditions (charge insertion, charge and discharge rates), we normalize the inserted charge, C_{ch}, with respect to the theoretical maximum capacity, C_{th}, which is proportional to the mass of active material loaded within the pores of the nickel substrate. At the beginning of charging, the Faradaic charging efficiency is 100 %, so that the entire applied current contributes to increasing the state of charge of the electrode with no oxygen evolution. As a result, the state of charge initially increases linearly with charge insertion. However, with an increase of state of charge, oxygen evolution becomes more and more prevalent until it consumes all charge when the SOC approaches 1. The rate of change of the SOC and the Faradaic charging efficiency are related by:

$$\frac{dSOC}{d(C_{ch}/C_{th})} = \frac{i_{CR}}{i_{ch}} = 1 - \frac{i_{OER}}{i_{ch}} \tag{2.42}$$

A too early onset of oxygen evolution during charging results in slower charging of the battery. Consequently, electrodes should be designed to minimize oxygen evolution until the active material is fully charged (ideal charging, Figure 2.9). We define the onset of oxygen evolution as the relative charge insertion where the Faradaic charging efficiency decreases to below 98 %. As shown in Figure 2.9 B, this threshold is crossed after a charge insertion of 0.18 C and 0.52 C for the conventional and the 3D electrode, respectively. The delay in the onset of oxygen evolution of the 3D electrode results in a faster increase of the state of charge and a sharper transition to oxygen evolution compared to the conventional electrode. As a result of increased oxygen evolution, the conventional electrode requires a charge insertion of 2.8 C to reach a state of charge of 85 %, which constitutes a 180 % increase compared to the 3D electrode.

How the electrode structure can have such a significant impact on the Faradaic charging efficiency becomes clear when considering the current distribution within the electrode throughout charging (Figure 2.10). Due to the low state of charge throughout the electrode, $soc(\xi)$, and the orders of magnitude higher exchange current density, CR is greatly favored over OER at the beginning of the charging process. Since the overpoten-

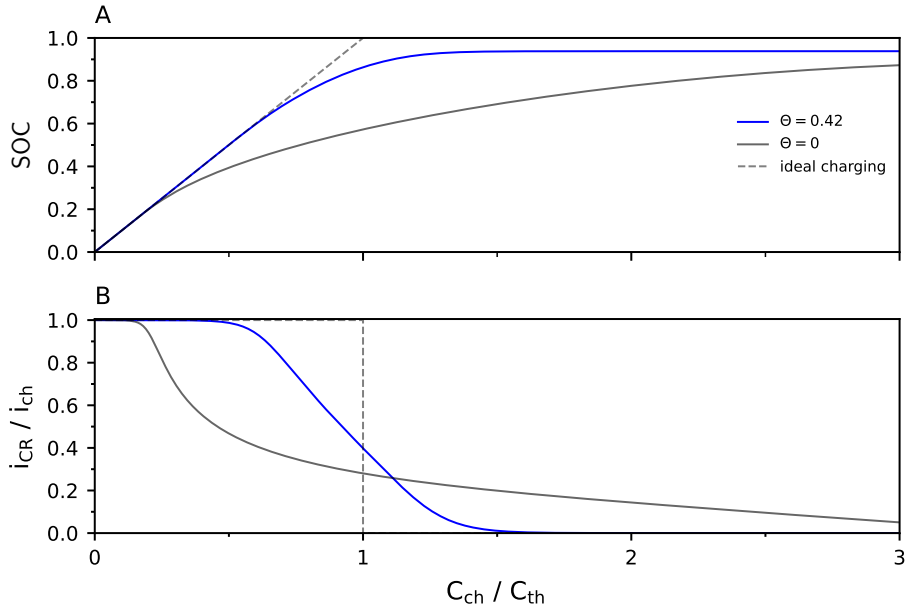

Figure 2.9: Overall state of charge (SOC) (A) and ratio of charging current (i_{CR}) to the total applied charging current (i_{ch}) (B) over the course of charging for a Non-3D electrode ($\Theta = 0$) and a 3D electrode with optimal void fraction at 200 mA/cm^2 ($\Theta = 0.42$). C_{ch} and C_{th} denote the inserted charge and the loaded capacity, respectively. Electrode thickness and porosity are 5 mm and 0.25, respectively, resulting in a loaded capacity of 172 mAh/cm^2 for the 3D electrode and 296 mAh/cm^2 for the Non-3D electrode for an initial electrode porosity of 0.75 (see Equation 2.45). Ideal charging represents the case where no oxygen evolution occurs and the entire inserted charge goes towards charging.

tials for both CR and OER decrease over the thickness of the electrode, the magnitude of the charging current is initially highest at the front of the electrode. Therefore, the active material close to the front is charged first and gradually transitions to oxygen evolution. Because of its high exchange current density, the CR can continue at the lower overpotentials deeper within the electrode while OER predominantly occurs in the areas with a higher state of charge and close to the electrode front where overpotentials are higher. As a result, a peak in the charging current moves from the front throughout the electrode as charging continues. As can be seen in Figure 2.10, the lower ionic resistance of the 3D electrode leads to

a more homogeneous distribution of the charging current which delays the onset of OER to a higher overall SOC (Figure 2.9). For the conventional non-3D structured electrode, on the other hand, the charging current is shifted towards the front of the electrode resulting in a faster increase of the local state of charge and thus an earlier onset of OER. Due to the higher ionic resistance, current densities for OER are high at the front of the electrode while the rest of the active material is trickle charged at low charging current densities.

While the model employed above can be used as a tool in the initial assessment of the charging performance, screening of different electrode parameters such as thickness, porosity an void fraction as well as operating current densities is still computationally expensive. Here, we demonstrate a technique that can serve as a rapid initial assessment of an electrode design for a given current density. As shown above, the homogeneity of the local charging current density affects the Faradaic charging efficiency and the onset of OER. In section 2.3.1 we introduced a concise relationship between the electrode utilisation for OER, the dimensionless resistance parameter and the reduced current (Equation 2.35). However, when considering both OER and CR in parallel, the kinetic parameters are a function of the local state of charge and thus vary spatially and temporally. Therefore, we consider the distribution of the local charging current density at the very beginning of charge, where the SOC is zero. Equation 2.18 then simplifies to:

$$j_{CR}(x) = 2\ j_{0,CR,ref}\ \frac{c_{OH}}{c_{OH,ref}}\ \exp\left(\frac{\alpha_{a,CR}F}{RT}\eta_{CR}(x)\right) \tag{2.43}$$

This is formally equivalent with the Tafel form used in the discussion of the current distribution for OER (Equation 2.3), so that the relationship between utilisation, resistance parameter K and reduced current I can be derived according to Equation 2.35.

As shown in Figure 2.11, the utilisation is shifted towards higher values of KI for the charging reaction at an SOC of 0, compared to oxygen evolution when fully charged. For Tafel kinetics differences in the exchange current density only affect the magnitude of the overpotentials, but not the current distribution and utilisation [36]. We find that the observed

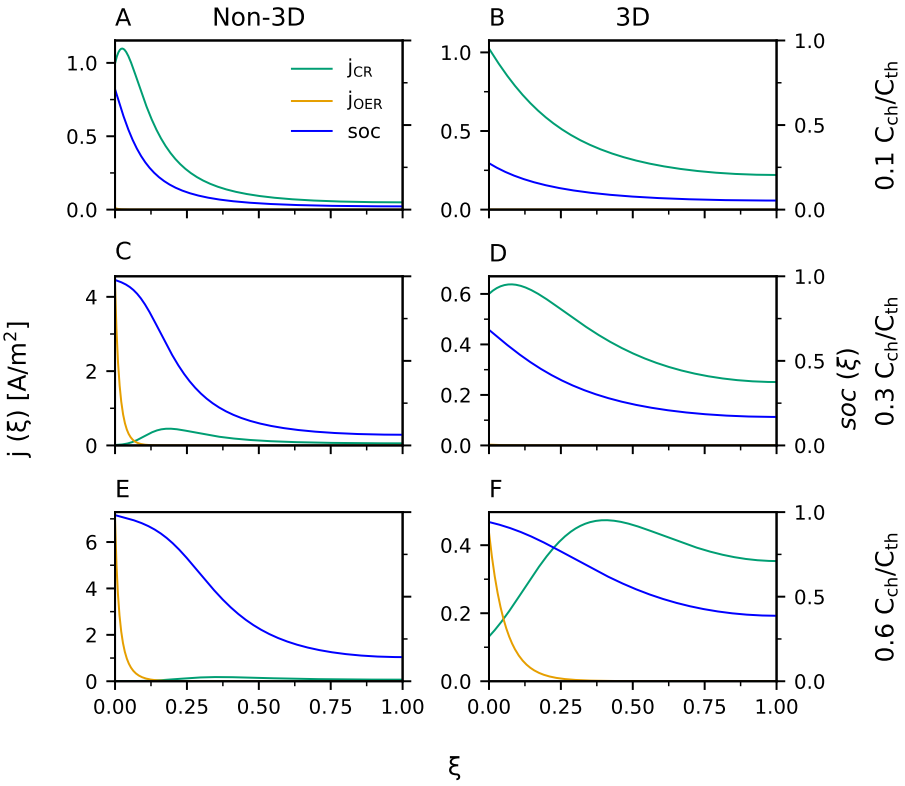

Figure 2.10: Local state of charge (soc) and current densities for oxygen evolution (j_{OER}) and battery charging reaction (j_{CR}) across the reduced electrode coordinate ($\xi = x/l$) for a Non-3D ($\Theta = 0$) and a 3D electrode with optimal void fraction at a charge rate of 200 mA/cm^2 ($\Theta_{opt,OER} = 0.42$). These are shown for increasing charge insertion (C_{ch}) relative to the loaded capacity (C_{th}). Electrode thickness and porosity are 5 mm and 0.25, respectively, resulting in a loaded capacity of 172 mAh/cm^2 for the 3D electrode and 296 mAh/cm^2 for the Non-3D electrode for an initial electrode porosity of 0.75 (see Equation 2.45).

shift of the utilisation is determined by the anodic transfer coefficients of the respective reactions which affect the parameter m in Equation 2.35, whereas the slope k remains mostly unchanged:

$$m_{CR} = \frac{\alpha_{a,OER}}{\alpha_{a,CR}} \, m_{OER} \tag{2.44}$$

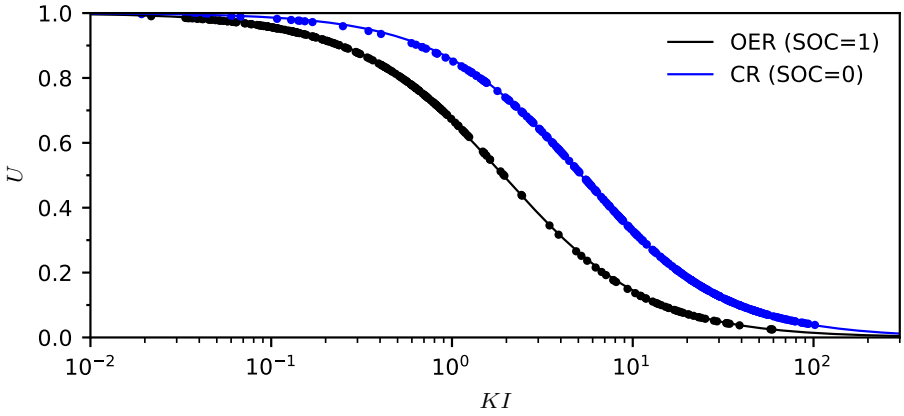

Figure 2.11: Dimensionless relationship between utilisation (U), resistance parameter (K) and reduced current (I) before charging ($SOC = 0$) and when fully charged ($SOC = 1$). Data points were generated by solving Equation 2.9 for various combinations of electrode thickness, porosity, void fraction and current density. The data were fit using Equation 2.35 resulting in the parameters $k_{OER} = 1.074$, $m_{OER} = 1.919$, $m_{CR} = 5.185$ and $k_{CR} = 1.089$.

Battery capacity in 3D electrodes

While 3D electrodes can reduce OER overpotentials and increase charging efficiency, the open channel volume reduces the porous substrate volume in which $Ni(OH)_2$ can be loaded into. As a result, the theoretical maximum capacity is reduced. In the electrode design process, this caveat must be weighed against the discussed benefits of 3D structured electrodes under consideration of the operating conditions. A high areal battery capacity per unit area of membrane reduces the total amount of cells, and therefore capital expenditures, required for a target system energy storage capacity. Assuming that the nickel substrate remains inert during battery cycling, the theoretical maximum areal battery capacity at 100 % utilisation is determined by the mass of active material filled into the pores of the sintered nickel scaffold with the initial porosity ϵ_0:

$$C_{A,th,3D} = \rho_{Ni(OH)_2}\, c_{Ni(OH)_2}\, l\, (1-\Theta)(\epsilon_0 - \epsilon) \tag{2.45}$$

where $\rho_{Ni(OH)_2}$ and $c_{Ni(OH)_2}$ are the density and the weight specific ca-

pacity (mAh/g) of the active material $Ni(OH)_2$, respectively. Figure 2.12 shows the optimal void fraction for OER and the resulting theoretical maximum areal capacities for varying electrode thicknesses and porosities at a superficial current density of 200 mA/cm^2. Thicker electrodes with a low final porosity and void fraction result in more active material per unit area. However, this comes at the cost of a decrease in utilisation and thus charging efficiency (higher values for KI, Figure 2.11).

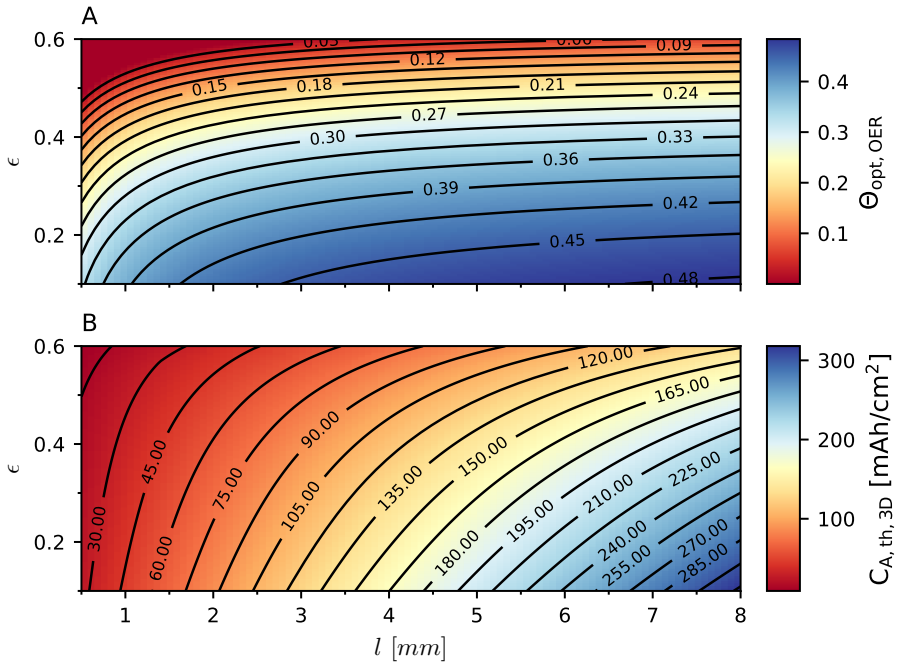

Figure 2.12: (A) Optimal void fraction ($\Theta_{opt,OER}$) with respect to the charging reaction at the beginning of charging ($SOC = 0$) for varying electrode thicknesses l and porosities ϵ after active material loading. (B) Resulting theoretical areal capacities ($C_{A,th,3D}$) that can be loaded onto a 3D electrode with an initial porosity of $\epsilon_0 = 0.75$ before active material loading and a void fraction of $\Theta_{opt,OER}$. The charge rate is 200 mA/cm^2.

With 172mAh/cm^2, the theoretical maximum areal capacity of the 3D electrode discussed above ($\Theta = 0.42$) is significantly lower than that of a conventional Non-3D structured electrode with 296mAh/cm^2. Nonetheless, for the first 1.3 hours of charging at 200 mA/cm^2 the charged areal

capacity is higher for the 3D electrode due to the significantly improved charging efficiency (Figure 2.13 A). For longer periods of charging and overcharging, the charged areal capacity of the conventional electrode exceeds that of the 3D electrode as more active material is trickle charged in parallel to OER. However, we note that in practice the extractable capacity will also depend on the discharge rate capability. This is expected to be higher in 3D electrodes due to the improved ionic conductivity resulting in a more homogenous distribution of the discharge current (Chapter 3). Faster charging of the 3D electrode also results in a stable oxygen production rate, $\dot{m}_{O_2}$, being reached sooner (Figure 2.13 B). This is beneficial for the balance of plant and downstream processing. Faster (re)charging and stabilisation of the oxygen output improve the ability of the hybrid battery-electrolyser to respond to fluctuations in the energy price and hydrogen demand. Moreover, in the modelled time period of 4.4 hours, the 3D electrode produces 15 % more oxygen.

The example above highlights the necessity to choose the void fraction under consideration of the required OER efficiency and production rate, areal capacity and current density. Generally, a 3D electrode with a high void fraction is beneficial at higher current densities for CR and OER and when the battery-electrolyser switches more frequently between charging/electrolysis and discharging. In addition, the 3D structure can be designed to facilitate bubble removal which reduces bubble-induced overpotentials [14, 15]. On the other hand, at low current densities and long uninterrupted periods of overcharging, the improved ionic conductivity of 3D electrodes with a high void fraction may not justify the loss in areal battery capacity. For increasingly thick electrodes with a high areal capacity, however, charging at such a low current density increases the charging duration. Overall, the 3D geometry and its void fraction present a novel degree of freedom that allows for tuning of battery-electrolyser electrodes across a spectrum between conventional battery electrodes with a high energy density and combined battery-electrolysis electrodes with a high power density (Figure 2.14).

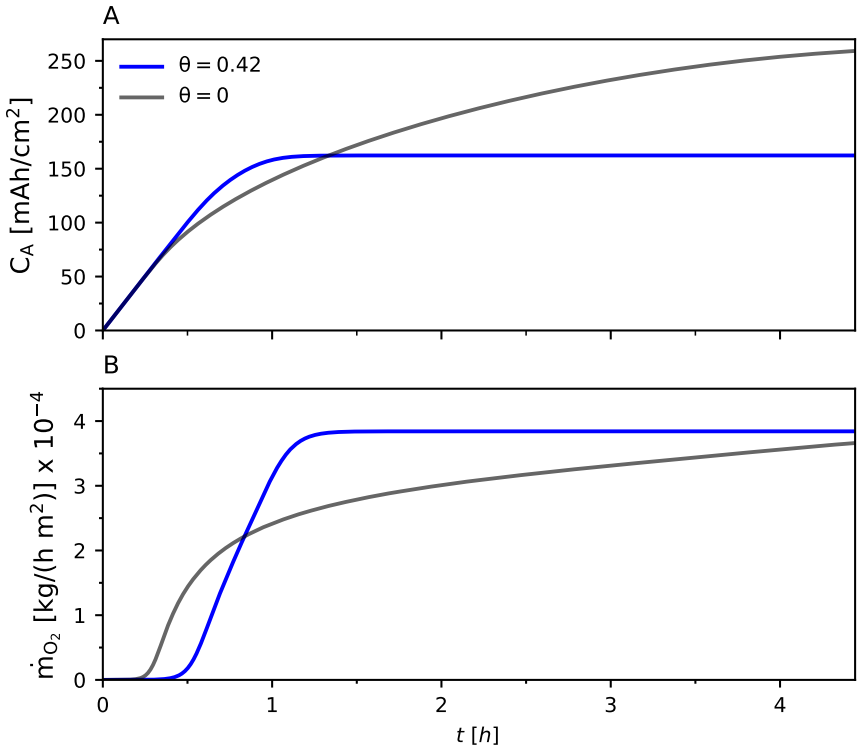

Figure 2.13: (A) Charged areal capacity (C_A) and (B) oxygen evolution rate ($\dot{m}_{O_2}$) for a Non-3D electrode ($\Theta = 0$) and a 3D electrode with optimal void fraction for OER at 200 mA/cm^2 ($\Theta_{opt,OER} = 0.42$). Electrode thickness and porosity are 5 mm and 0.25, respectively, resulting in a loaded capacity of 172 mAh/cm^2 for the 3D electrode and 296 mAh/cm^2 for the Non-3D electrode for an initial electrode porosity of 0.75 (see Equation 2.45).

2.4. Conclusions

In this work, we develop a 1D mathematical model in dimensionless notation that describes the current and potential distribution in 3D battery-electrolyser electrodes during charging and oxygen evolution. To this end, we expand the Bruggeman relation to define an effective ionic conductivity, $\kappa_{eff,3D}$, that includes the void fraction constituted by the electrode channels. While the reduced ionic resistance of a more open 3D geometry

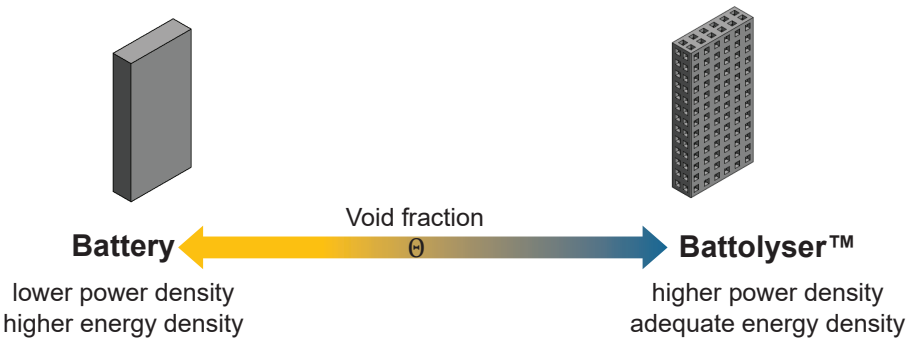

Figure 2.14: The void fraction (Θ) in 3D battery-electrolyser electrodes allows for tuning across a spectrum from battery to combined battery-electrolysis functionality.

results in a more homogeneous current distribution and increases electrode utilisation, the lower reactive surface area can increase activation overpotentials. Therefore, in order to minimize overpotentials, the void fraction must be chosen to maximize the effectively utilised reactive surface over which the applied current is distributed. Using the 1D model, we determine the electrode utilisation and polarisation for oxygen evolution for different electrode thicknesses, porosities and void fractions. We find simple relationships between the dimensionless parameters of utilisation U, reduced polarisation Φ, reduced total current I and resistance parameter K that allow for the fast assessment of an electrode's performance at a given current density.

Based on these dimensionless relationships, we develop a method to calculate the optimal electrode void fraction for a given electrode thickness, porosity and current density that minimizes the electrode polarisation for oxygen evolution. Void fractions of up to around 0.50 are especially beneficial for oxygen evolution in thick electrodes with porosities below around 0.62 and at high current densities. A 3D geometry can not only reduce electrode polarisation during oxygen evolution, but also significantly improve the charging efficiency as a result of the more homogeneous current distribution. However, these benefits must be weighed against the lower theoretical areal capacity of 3D electrodes under consideration of the operating conditions and requirements for energy storage and oxygen evolution.

The void fraction of 3D electrodes constitutes a novel degree of freedom in the development of battery-electrolyser electrodes. As such, it allows for the rational design of electrodes across a spectrum ranging from an emphasis on battery to electrolysis functionality. Even though our analysis neglects effects of bubbles as well as electrical and mass transfer resistances, the methods developed in this work allow for a first assessment of how electrode porosity, thickness, void fraction affect performance metrics such as utilisation, polarisation and charging efficiency.

References

[1] T. Wheeler and J. Von Braun, *Climate change impacts on global food security,* Science **341**, 508 (2013).

[2] C. H. Trisos, C. Merow, and A. L. Pigot, *The projected timing of abrupt ecological disruption from climate change,* Nature **580**, 496 (2020).

[3] N. S. Diffenbaugh and M. Burke, *Global warming has increased global economic inequality,* Proceedings of the National Academy of Sciences **116**, 9808 (2019).

[4] J. D. A. Young, *Climate change-increased storms & extreme weather,* The International Journal of Business & Management **10** (2022).

[5] F. M. Mulder, *Implications of diurnal and seasonal variations in renewable energy generation for large scale energy storage,* Journal of Renewable and Sustainable Energy **6** (2014).

[6] P. Denholm, D. J. Arent, S. F. Baldwin, D. E. Bilello, G. L. Brinkman, J. M. Cochran, W. J. Cole, B. Frew, V. Gevorgian, J. Heeter, *et al.*, *The challenges of achieving a 100% renewable electricity system in the united states,* Joule **5**, 1331 (2021).

[7] F. M. Mulder, B. M. H. Weninger, J. Middelkoop, F. G. B. Ooms, and H. Schreuders, *Efficient electricity storage with a battolyser, an integrated Ni–Fe battery and electrolyser,* Energy & Environmental Science **10**, 756 (2017).

[8] C. Li, J. Du, Y. Gao, F. Bu, Y. H. Tan, Y. Wang, G. Fu, C. Guan, X. Xu, and W. Huang, *Stereolithography of 3d sustainable metal electrodes towards high-performance nickel iron battery,* Advanced Functional Materials **32**, 2205317 (2022).

[9] X. Xu, Y. H. Tan, J. Ding, and C. Guan, *3D printing of next-generation electrochemical energy storage devices: from multiscale to multimaterial,* Energy & Environmental Materials **5**, 427 (2022).

[10] M. S. Saleh, J. Li, J. Park, and R. Panat, *3D printed hierarchically-porous microlattice electrode materials for exceptionally high specific*

capacity and areal capacity lithium ion batteries, Additive Manufacturing **23**, 70 (2018).

[11] D. Kong, Y. Wang, S. Huang, B. Zhang, Y. V. Lim, G. J. Sim, P. Valdivia y Alvarado, Q. Ge, and H. Y. Yang, *3d printed compressible quasi-solid-state nickel–iron battery,* ACS Nano **14**, 9675 (2020).

[12] J. C. Bui, J. T. Davis, and D. V. Esposito, *3d-printed electrodes for membraneless water electrolysis,* Sustainable Energy & Fuels **4**, 213 (2020).

[13] R. A. Márquez, K. Kawashima, Y. J. Son, R. Rose, L. A. Smith, N. Miller, O. A. Carrasco Jaim, H. Celio, and C. B. Mullins, *Tailoring 3d-printed electrodes for enhanced water splitting,* ACS Applied Materials & Interfaces **14**, 42153 (2022).

[14] T. Kou, S. Wang, R. Shi, T. Zhang, S. Chiovoloni, J. Q. Lu, W. Chen, M. A. Worsley, B. C. Wood, S. E. Baker, *et al.*, *Periodic porous 3D electrodes mitigate gas bubble traffic during alkaline water electrolysis at high current densities,* Advanced Energy Materials **10**, 2002955 (2020).

[15] I. Sullivan, H. Zhang, C. Zhu, M. Wood, A. J. Nelson, S. E. Baker, C. M. Spadaccini, T. Van Buuren, M. Lin, E. B. Duoss, *et al.*, *3D printed nickel–molybdenum-based electrocatalysts for hydrogen evolution at low overpotentials in a flow-through configuration,* ACS Applied Materials & Interfaces **13**, 20260 (2021).

[16] H. Vogt, *The actual current density of gas-evolving electrodes—notes on the bubble coverage,* Electrochimica Acta **78**, 183 (2012).

[17] B. E. Bongenaar-Schlenter, L. J. J. Janssen, S. J. D. Van Stralen, and E. Barendrecht, *The effect of the gas void distribution on the ohmic resistance during water electrolytes,* Journal of Applied Electrochemistry **15**, 537 (1985).

[18] G. F. Swiegers, R. N. Terrett, G. Tsekouras, T. Tsuzuki, R. J. Pace, and R. Stranger, *The prospects of developing a highly energy-efficient water electrolyser by eliminating or mitigating bubble effects,* Sustainable Energy & Fuels **5**, 1280 (2021).

[19] P. De Vidts and R. E. White, *Mathematical modeling of a nickel-cadmium cell: Proton diffusion in the nickel electrode,* Journal of the Electrochemical Society **142**, 1509 (1995).

[20] D. Fan and R. E. White, *Mathematical modeling of a nickel-cadmium battery: Effects of intercalation and oxygen reactions,* Journal of the Electrochemical Society **138**, 2952 (1991).

[21] W. B. Gu, C. Y. Wang, S. M. Li, M. M. Geng, and B. Y. Liaw, *Modeling discharge and charge characteristics of nickel–metal hydride batteries,* Electrochimica Acta **44**, 4525 (1999).

[22] Z. Mao, P. De Vidts, R. E. White, and J. Newman, *Theoretical analysis of the discharge performance of a NiOOH/H_2 cell,* Journal of the Electrochemical Society **141**, 54 (1994).

[23] B. Paxton and J. Newman, *Modeling of nickel/metal hydride batteries,* Journal of the Electrochemical Society **144**, 3818 (1997).

[24] T. Kadyk, D. Bruce, and M. Eikerling, *How to enhance gas removal from porous electrodes?* Scientific reports **6**, 1 (2016).

[25] V. S. Daniel'-Bek, *Polarization of porous electrodes I. distribution of current and potential within the electrode,* Zhurnal Fizicheskoi Khimii **22**, 697 (1948).

[26] F. Posey, *Methods for the calculation of polarization in porous electrodes,* Journal of the Electrochemical Society **111**, 1173 (1964).

[27] W. B. Gu, C. Y. Wang, S. M. Li, M. M. Geng, and B. Y. Liaw, *Modeling discharge and charge characteristics of nickel–metal hydride batteries,* Electrochimica Acta **44**, 4525 (1999).

[28] A. M. Raventos, G. Kluivers, J. W. Haverkort, W. De Jong, F. M. Mulder, and R. Kortlever, *Modeling the performance of an integrated battery and electrolyzer system,* Industrial & Engineering Chemistry Research **60**, 10988 (2021).

[29] S. Motupally, C. C. Streinz, and J. W. Weidner, *Proton diffusion in nickel hydroxide: prediction of active material utilization,* Journal of The Electrochemical Society **145**, 29 (1998).

[30] K. P. Ta and J. Newman, *Mass transfer and kinetic phenomena at the nickel hydroxide electrode,* Journal of the Electrochemical Society **145**, 3860 (1998).

[31] B. E. Conway and E. Gileadi, *Electrochemistry of the nickel oxide electrode: part iv. electrochemical kinetic studies of reversible potentials as a function of degree of oxidation,* Canadian Journal of Chemistry **40**, 1933 (1962).

[32] P. M. Gomadam, J. W. Weidner, R. A. Dougal, and R. E. White, *Mathematical modeling of lithium-ion and nickel battery systems,* Journal of Power Sources **110**, 267 (2002).

[33] D. M. Santos, C. A. Sequeira, and J. L. Figueiredo, *Hydrogen production by alkaline water electrolysis,* Química Nova **36**, 1176 (2013).

[34] A. K. Shukla, M. K. Ravikumar, and T. S. Balasubramanian, *Nickel/iron batteries,* Journal of Power Sources **51**, 29 (1994).

[35] S. Rausch and H. Wendt, *Morphology and utilization of smooth hydrogen-evolving raney nickel cathode coatings and porous sintered-nickel cathodes,* Journal of the Electrochemical Society **143**, 2852 (1996).

[36] J. Newman and W. Tiedemann, *Porous-electrode theory with battery applications,* AIChE Journal **21**, 25 (1975).

[37] M.-B. Liu, G. M. Cook, and N. P. Yao, *Transient current distributions in porous zinc electrodes in KOH electrolyte,* Journal of The Electrochemical Society **129**, 239 (1982).

[38] I. M. Lengyel, D. Soroldoni, A. C. Oates, and L. G. Morelli, *Nonlinearity arising from noncooperative transcription factor binding enhances negative feedback and promotes genetic oscillations,* Papers in Physics **6**, 0 (2014).

[39] N. N. Yazvinskaya, N. E. Galushkin, D. N. Galushkin, and B. Y. Kalmykov, *Analysis and comparison of generalized Peukert's equations parameters for nickel-cadmium batteries with pocket and sintered electrodes,* International Journal of Electrochemical Science **15**, 412 (2020).

[40] A. H. Zimmerman, *Technological implications in studies of nickel electrode performance and degradation,* Journal of Power Sources **12**, 233 (1984).

[41] M. Oshitani, Y. Sasaki, and K. Takashima, *Development of a nickel electrode having stable performance at various charge and discharge rates over a wide temperature range,* Journal of Power Sources **12**, 219 (1984).

[42] A. Yuan, S. Cheng, J. Zhang, and C. Cao, *The influence of calcium compounds on the behaviour of the nickel electrode,* Journal of Power Sources **76**, 36 (1998).

[43] K. Zeng and D. Zhang, *Recent progress in alkaline water electrolysis for hydrogen production and applications,* Progress in Energy and Combustion Science **36**, 307 (2010).

3

3D nickel electrodes for hybrid battery and electrolysis devices

A renewable power based energy system will require both short- and long-term electricity storage and conversion to hydrogen based fuels. This study investigates novel electrode dimensioning for an integrated alkaline Ni-Fe battery and electrolyser to come to current densities similar to those in alkaline electrolysers, while simultaneously reaching efficient hour duration battery storage capacities. We demonstrate that the combination of microporosity and a conductive three dimensional electrode design with macroscopic channels enables obtaining the required current densities during charge, electrolysis and discharge. The low ionic resistance within the electrolyte inside the designed 3D channels leads to significantly higher utilisation of electrochemically active surface area and effective reaction penetration depth into the electrodes. The 3D electrode then reaches higher utilisation of the active electrode mass and lower overpotentials during both the (dis)charge reaction and electrolysis. The double function of these electrodes is also understood from a general statistical model and a more detailed porous electrode model perspective. The production of comparable 3D structured electrodes as described here can be scaled with industrially established techniques.

The results in this chapter have been accepted for publication in Cell Reports Physical Science (2024).

3.1. Introduction

Climate change has been identified as one of the key dangers to our society [1–3]. Primarily driven by anthropogenic CO_2 emissions as a result of energy production from fossil fuels, the move to renewable, carbon-neutral energy sources is imperative in order to reach net zero CO_2 emissions by 2050 and limit global warming to 1.5 °C [3]. Such energy sources include wind and solar generated power with intrinsic seasonal and daily variations in output. To allow for a continuous energy supply and to stabilize the electrical grid, large scale energy storage solutions are necessary on short daily and long seasonal timescales [4, 5]. These include battery storage technologies as well as energy storage in the form of synthetic renewable fuels such as H_2 or NH_3. With round trip energy efficiencies as high as 90 %, batteries are an attractive solution for diurnal, short-term energy storage.

However, batteries are only of limited use for seasonal, long-term energy storage (i.e. months, years). This is due to the high cost of large-scale battery storage facilities that requires as many charge and discharge cycles over a year as possible to obtain a reduced cost per storage cycle; one cycle per year as seasonal storage makes batteries economically unattractive for this application. An energy carrier such as H_2, on the other hand, can be stored externally after being produced which makes it a good option for long-term energy storage. However, the overall electrical efficiency of energy storage in the form of hydrogen is low as it includes both the production via electrolysis and the recuperation into electricity, for example via a fuel cell or a gas turbine. As a result, both batteries as well as H_2 and H_2–derived fuels are expected to complement each other in the future energy storage infrastructure [6]. In addition H_2 is an important feedstock for the chemical industry, but its production from renewable power preferably only occurs when there is more green power than required for all other applications, and one is not firing up a gas fired powered power plant – on H_2– to generate electricity at the same time. Such H_2 feedstock generation occurs then necessarily at a lower utilisation or capacity factor than done currently with fossil H_2 generation.

A recent approach developed in our group is the development of a hybrid battery and alkaline electrolyser (battolyser™) [7]. In this concept, a nickel-iron battery functions as an alkaline electrolyser to produce H_2

and O_2 when overcharged, and can be discharged after electrolysis operation. The negative electrode is based on $Fe(OH)_2$ as active material that is reduced to Fe upon charge (-0.88 V vs. SHE):

$$Fe(OH)_2 + 2\,e^- \underset{\text{discharge}}{\overset{\text{charge}}{\rightleftharpoons}} Fe + 2\,OH^- \tag{3.1}$$

The positive electrode is based on $Ni(OH)_2$ as active material that releases a proton and electron during the charge reaction (+0.49 V vs. SHE):

$$Ni(OH)_2 + OH^- \underset{\text{discharge}}{\overset{\text{charge}}{\rightleftharpoons}} NiOOH + H_2O + e^- \tag{3.2}$$

The OH^- ions are conducted by an aqueous alkaline KOH electrolyte. During charging, Fe and NiOOH become increasingly present and function as efficient hydrogen (HER) and oxygen evolution reaction (OER) catalysts, respectively. As a result, the electrochemical reaction shifts from the battery charging reaction to electrolysis. Hydrogen evolution takes place at the negative iron electrode (-0.861 V vs. SHE at pH 14.6):

$$2\,H_2O + 2\,e^- \xrightarrow{\text{overcharging}} H_2(g) + 2\,OH^- \tag{3.3}$$

while oxygen is generated at the positive nickel electrode (+0.369 V vs. SHE at pH 14.6):

$$4\,OH^- \xrightarrow{\text{overcharging}} O_2(g) + 2\,H_2O + 4\,e^- \tag{3.4}$$

Thus, both energy efficient short-term battery storage, as well as long-term energy storage are integrated in a single device, which reduces cost and increases the overall utilisation factor compared to separated battery and electrolysis systems. Moreover, the main materials required for nickel-iron batteries (Ni, Fe) count among the most abundant elements in the earth crust. The first prototype developed by Mulder et al. [7] employed commercial nickel and iron pocket electrodes. It showed the double functionality enhanced the utilisation of the full battery capacity, mainly due to continuing charging while gas evolution also starts. Also high efficiencies were observed at 82 - 90 % combined battery round trip efficiency

and H_2 generation (w.r.t. HHV). Long-term cycling results indicate the feasibility of the approach.

In conventional Ni-Fe batteries, gas evolution due to electrolysis has been considered a parasitic side reaction that increases self-discharge and reduces the charging efficiency [8, 9]. The latter is adversely impacted by, and thus limits, high charge rates [10]. For this reason, suppressing OER and HER by means of additives in the active material and electrolyte has been a major focus in past battery electrode development [11–14]. However, when the water splitting adds useful product, these additives are no longer necessary, opening the possibility to optimize both battery and electrolysis activity. An example is replacing Co dopants in $Ni(OH)_2$ meant to suppress OER by Fe to promote OER, while remarkably also increasing the battery storage capacity [15]. Also, the current densities applied in alkaline electrolysis reach about 200-240 mA/cm^2 for non-noble catalyst Ni based systems at around 80 % efficiency (w.r.t. HHV) [16, 17]. Higher current densities require electrodes with noble metal catalysts and zero gap designs to reduce ohmic resistances. However, the latter come at the cost of enhanced gas crossover and therefore minimal power requirements, i.e. reduced operational flexibility [18, 19].

As indicated by Mulder [5] and the TenneT TSO Adequacy Outlook report [20], the typical total installed capacity of battery storage and electrolysis (power to gas) capacity is roughly similar on a future large GW scale system level (1:1 ratio) for the EU and North Africa. This is the result of the time pattern of PV and wind power compared to the demand pattern. For instance, assuming a battery and electrolysis capacity of 1 GW each, the combined capacity then becomes 1 GW + 1 GW = 2 GW. The battery storage needs to be able to store at this power for about four hours, resulting in an energy storage capacity of 1 GW × 4 h = 4 GWh. Therefore the ratio of electrolysis to battery capacity is expected to be 1:2[1]. Taking this as a possible reference target, one would therefore be interested in C/2 charge rates and C/4 discharge rates of an integrated battery- electrolyser system to support the fully renewables-based electricity system by 2050. Such can then be applied for daily approximately 4 to 6 hours of overproduction; during such periods of low electricity prices, the combined battery-electrolyser is first charged and subsequently produces

[1] 2xGW:4xGWh, for the example of xGW each for battery and electrolysis capacity.

H_2 at low cost, which can be used as chemical feedstock or for long-term energy storage. In the following 4 to 10 hours of renewable underproduction, the battery can be discharged at anticipated higher electricity price (C/4 to C/10 discharge rate). An illustration of such a charge/discharge scheme is given in the (Figure B.16), synchronized with the Dutch Day Ahead Market of April 19th, September 19th and 20th 2023. In addition to such diurnal battery and long-term H_2 energy storage, short-term energy arbitrage and grid stabilization services such as frequency regulation and voltage support may require higher charge and discharge rates to respond effectively to rapid changes in grid conditions, and capitalize on fluctuations in energy prices. To allow for more flexible power use, one can therefore also target a 1C charge rate and C/4 discharge rates, while the charge rate is also reaching similar current densities as state of the art, non-noble metal catalysed, alkaline electrolysers. The target could then become ~ 200mA/cm^2 and ~ 200 mAh/cm^2 at 1C charge and C/4 discharge.

The electrodes in commercial Ni-Fe batteries are not designed to facilitate these high current densities and typically only have rated capacities below 50-80 mAh/cm^2 at C/4 or C/10 discharge rates [7, 21]. In pocket type electrodes the active material and conductive additives are pressed and enclosed in perforated steel pockets. While these can be produced at low cost, material utilisation at higher charge and discharge rates is limited by the poor electronic conductivity provided by the contact between dispersed particles of active material and conductive additives (e.g. carbon, nickel powder). Sintered electrodes, on the other hand, are made by fusing (sintering) metal particles at high temperatures resulting in highly porous, conductive metal substrates with high surface area. The high porosity improves the ionic conductivity while the high surface area and electronic conductivity decrease overpotentials. As a result, sintered electrodes can operate at significantly higher charge and discharge rates and with improved active material utilisation compared to pocket type electrodes. Lim and Verzwyvelt [10] demonstrated sintered nickel electrodes with rated capacities as high as 130 mAh/cm^2 that were charged with current densities of up to 260 mA/cm^2 but returned a limited 44 % material utilisation (1.3 C charge insertion, 73 mAh/cm^2 charged capacity). Even though sintered electrodes offer significant improvements in rate capability, their thickness, and therefore their capacity, is still limited by the

effective ionic conductivity within the electrode. As a result, active material farthest from the front of the electrode is utilized the least, so that increasing the electrode thickness only yields diminishing returns in capacity increase [10, 22]. The effective thickness or areal capacity, however, is essential for increasing the energy density of the system by increasing the ratio of active material over inactive separator, current collector and electrolyte materials in the cell, while maintaining good transport properties [23]. Due to the comparatively high cost, sintered electrodes are therefore kept thin (< 1 mm) and applied in applications where power density is prioritized over energy density. Furthermore, electrolysis, i.e. overcharging, at the targeted current densities requires the effective removal of H_2 and O_2 bubbles from the electrode and cell. These reduce the effective electrolyte conductivity and shield electrochemically active sites resulting in an increase in cell potential [24, 25].

Overall, it is clear that the development of future integrated battery-electrolyser systems requires novel electrodes and cell concepts specifically designed for this hybrid application. In recent years, 3D electrodes have been demonstrated successfully for the use in electrochemical applications, where the electrode geometry presents an additional degree of freedom in electrode development [26–28]. 3D flow-through electrodes have been shown to improve mass transfer in electrochemical reactors[29–32] and facilitate bubble removal in alkaline electrolysis [33–35]. Saleh et al. [36] reported how 3D hierarchically porous micro lattice electrodes for Li-ion batteries increase electrolyte accessibility and available electrochemically active surface area, resulting in a 100 % increase in areal capacity. 3D electrodes have also been demonstrated for lightweight Ni-Fe batteries for the use in smart devices and wearable electronics [37, 38]. However, with areal capacities of around 10 mAh/cm^2 these are an order of magnitude below the application targeted in this work. Furthermore, Kou et al. [34] highlighted the benefits of an ordered channel structure of a 3D electrode for the removal of O_2 bubbles during electrolysis as compared to stochastically structured nickel foam electrodes.

Due to the benefits of 3D electrodes shown for both battery and electrolysis application, we hypothesized that such open and ordered structures should also improve the performance of hybrid battery-electrolysis electrodes. Herein, we report the development of a 3D hierarchically porous sintered nickel electrode with a high areal capacity of 140 mAh/cm^2

that facilitates rapid bubble release and increases the ionic conductivity within the electrode. Compared to a Non-3D structured conventional electrode geometry, this results in decreased overpotentials, high materials utilisation, as well as significantly improved rate capability approaching current densities of industrial alkaline electrolysers. Using a porous electrode model, we show how this boost in performance is the result of a more homogeneous current distribution throughout the 3D electrode. The designed 3D structure effectively channels the ionic current deeper into the electrode than without the 3D structure, a result in line with a porous electrode optimization approach of Roy et al. [39]. From this proof of concept the electrode geometry can be adjusted to allow for large-scale manufacturing using powder metallurgy processes such as press-and-sinter and metal injection moulding (MIM) [40–42].

Here, specific 3D structuring is shown, but also injection molded templates can be used to come to scalable manufacturing procedures [40–42].

3.2. Results and discussion

3.2.1. A general statistical model for a dual function battery-electrolyser electrode

To understand the interplay of battery charging and electrolysis, a simple statistical approach for describing the state of charge $SOC(q)$ as a function of inserted charge q is insightful. Assume the nickel electrode is limiting (oversized iron electrode) and the fraction of uncharged $Ni(OH)_2$ material is equal to $(1 - SOC(q))$ and that conductivities are ideal, so there are no effects of potential distribution. Upon charge insertion, the material will be charged according to Equation 3.2 and increase its $SOC_{uncharged}(q)$ as:

$$dSOC_{uncharged}(q) = (1 - SOC(q))dq \tag{3.5}$$

However, the fraction $SOC(q)$ that is already charged can perform two electrochemical activities: It can oxidize water to form O_2 as in Equation 3.4, or it can charge further with a probability $(1 - SOC(q))$. Then the increase of $SOC_{charged}(q)$ when inserting a charge dq becomes:

$$dSOC_{charged}(q) = SOC(q)(1 - SOC(q))dq \tag{3.6}$$

The total change in $dSOC$ then becomes:

$$\begin{aligned} dSOC(q) &= dSOC_{uncharged}(q) + dSOC_{charged}(q) \\ &= (1 - SOC(q))dq + SOC(q)(1 - SOC(q))dq \\ &= (1 - SOC^2(q))dq \end{aligned} \tag{3.7}$$

The solution of which is:

$$S(q) = tanh(q), \quad 0 \leq q \leq \infty \tag{3.8}$$

Note that Equation 3.7 can be rewritten as:

$$\begin{aligned} dSOC(q)/dq &= 1 - SOC^2(q) \\ &= 1 - tanh^2(q) \\ &= \frac{i_{CR}}{i_{ch}}(q) \end{aligned} \tag{3.9}$$

This indicates how much of the inserted charge i_{ch} is spent on the CR (i_{CR}), while the OER consumes $SOC^2(q)$.

Remarkably, this charge retention Equation 3.9 for $SOC(q)$ is the same as the 'logistic equation' observed in our previous work [7]. The description immediately indicates how the electrode can accommodate the two competing reactions of OER and CR (Equations 3.4 and 3.2). However, when applying higher current densities or thick electrodes, the resistances, transport phenomena, and activation potentials do become a factor of importance, and the electrochemistry occurs progressively more at the electrode side closest to the counter electrode. Then the random statistical aspect is an oversimplification, and a more detailed porous electrode model is required in which the current distribution across the electrode thickness as well as reaction kinetics are considered. Such a model is described in detail in Chapter 2.

3.2.2. Indirect 3D printing of nickel electrodes

The electrodes serving here as prototype were prepared using the technique of indirect 3D printing introduced by Hereijgers et al. [31] (Figures 3.1, B.1). In essence, this technique involves 3D printing a polymer mould of the electrode which is then filled with a slurry containing the metal powder, a liquefaction agent and a binder. Following the hardening of the binder, the mould is removed by dissolution in a suitable solvent which yields the green part of the electrode. The green part is then debinded and sintered to yield a mechanically stable, porous and electronically conductive 3D electrode substrate. Building on the methodology of Hereijgers et al. [31], we find that PLA, a commonly used and cost-efficient FDM printing material, can be used as mould material which can be removed with a concentrated potassium hydroxide solution (30 wt% KOH (aq.)). 3D electrode substrates manufactured with this technique exhibit porosities ranging from 70 % to 80 %. Such high porosities are required for the loading of $Ni(OH)_2$, which constitutes the active battery material and, when charged to NiOOH, catalyzes OER.

In order to assess the effectiveness of a 3D electrode for the hybrid application as battery and oxygen evolution electrode, we prepared a 3D electrode with a void fraction of around 39 % and a conventional Non-3D structured electrode as a control. As described in Chapter 2, the void fraction represents the ratio of the open channel volume to the total electrode volume. Each electrode was loaded with $Ni(OH)_2$ to an area specific capacity of approximately 140 mAh/cm^2 according to the procedure shown in Figure B.3. All steps of the electrode manufacturing procedure are outlined in detail in Appendix B.2.

3.2.3. Electrode activation and battery charging efficiency

The loaded active mass requires electrochemical activation before reaching its maximum discharge capacity [43]. Nickel electrode activation typically consists of charging and discharging cycles during which the electrode capacity gradually increases. Ideally, the time required for the activation procedure should be as short possible, so that the electrode operates sooner to specification. This is especially relevant for the nickel electrode, as it limits the battery capacity in a full cell. For batteries, (dis)charge

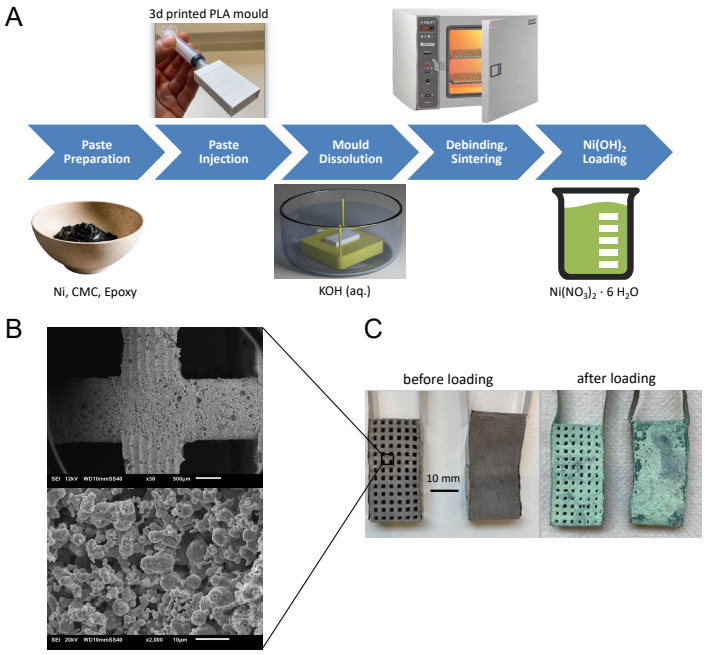

Figure 3.1: (A) Schematic of the indirect 3D printing procedure followed by active material loading via the thermal decomposition of nickel nitrate hexahydrate. (B) SEM images of a sintered 3D nickel electrode before active material loading at x30 and x2000 magnification. (C) 3D and Non-3D electrode with spot-welded contacts before and after active material loading.

rates and the inserted charge are typically expressed relative to a reference capacity. Here, we use the theoretical capacity of the loaded active material as reference (140 mAh/cm^2). For example, a charge rate of C/n (140/n mA/cm^2) indicates that inserting the charge of 1C (140 mAh/cm^2) takes n hours. We define the utilisation of the active material as the ratio of the discharge capacity C_{dc} to the theoretical capacity of the loaded active material C_{loaded}.

The as prepared electrodes were activated via the protocol described in Figure 3.2. A 1C charge rate was utilized since this is already faster than the C/2 rate indicated above as target for a full scale system. As shown in Figure 3.2 B, the 3D mesh electrode is activated far more effectively

and reaches a utilisation of over 90 % after only 8 activation cycles compared to 54 % for the Non-3D electrode. For further activation cycles, the discharge capacity of the 3D electrode increases steadily and eventually results in almost full utilisation of the active material at the 1C charge and C/2 discharge rate (cycle 41). The Non-3D electrode, on the other hand, exhibits no further increase in discharge capacity until the discharge rate is decreased by a factor of 10 to C/20 (20 h discharge rate, cycle 21). It appears that a slow discharge rate allows for increased material accessibility which facilitates activation. Following this slow discharge, the utilisation of the Non-3D electrode is increased to 60 % at the initial 1 C charge and C/2 discharge rate, yet does not increase further. This suggests that, in contrast to the 3D electrode, the active material of the Non-3D electrode is only partially accessible at the C/2 discharge rate, resulting in incomplete cycling and activation. A further factor affecting material utilisation is the battery charging efficiency, which describes the ratio of the inserted charge going towards the battery charging reaction CR as opposed to the competing OER. Whether CR or OER is dominant depends on kinetic parameters such as the anodic transfer coefficient and exchange current density, the state of charge as well as the overpotentials for the respective reactions (Equations 2.17-2.20). At the beginning of charging, CR is favored due to the many orders of magnitude higher exchange current compared to that of OER. With an increase in state of charge, however, the anodic term in Equation 2.18 decreases and approaches zero when fully charged. In addition, the equilibrium potential $E_{0,CR}$ increases which results in a reduced overpotential for CR (Figure B.12). As a result, the dominant electrode reaction shifts from CR to OER in the course of charging. However, even at a lower state of charge the significantly lower equilibrium potential $E_{0,OER}$, and at elevated electrode polarization, overpotentials for OER can become sufficiently high to cause a substantial OER current and reduction in charging efficiency. For this reason, a low charging potential is indicative of a high charging efficiency.

A common approach to increase the charging efficiency of nickel battery electrodes is to increase the OER potential by the addition of Cd or Ca in the $Ni(OH)_2$ in combination with LiOH in the electrolyte [12, 44, 45]. For a hybrid electrode, however, this suppression of OER is not required anymore, as water splitting is an intended product. In addition, as can be seen in Figure 3.2 A, the average charging potential of the 3D electrode

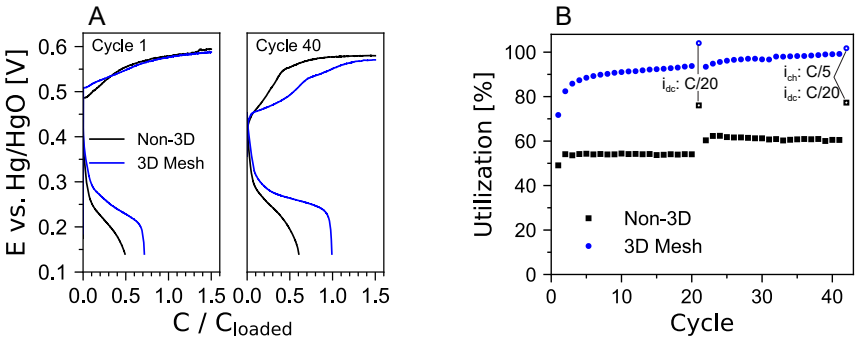

Figure 3.2: Activation cycles for the 3D mesh and the Non-3D electrode. (A) Comparison of the iR-corrected electrode potentials for activation cycles 1 and 40. The electrodes were overcharged by 50 % at a charge rate of 1C and discharge rate of C/2. (B) Active material capacity utilisation over the 42 activation cycles with respect to the theoretical capacity of 289 mAh/g for the $Ni(OH)_2$ / NiOOH redox couple. The discharge rate (i_{dc}) was reduced to C/20 in cycles 21 and 42. In cycle 42 the charge rate (i_{ch}) was reduced to C/5.

decreases noticeably during activation, and is about 30 mV lower compared to that of the Non-3D electrode in the final activation cycle at the 1C charge rate. Therefore, the high utilization and more effective activation of the 3D electrode is now also the result of decreased overpotential and increase in charging efficiency, without the use of OER suppressing additives.

The charging efficiency, i.e. the ratio of the charge going towards CR, i_{CR}, in relation to the total applied current, i_{ch}, can be estimated experimentally by inserting an increasing amount of charge and then measuring the discharge capacity C_{dc} after each charge insertion C_{ch} (Figure 3.3 A). The discharge rate is kept sufficiently low at C/4 to allow for the full discharge of the charged material, while the charge rate is varied in order to assess its impact on the charging efficiency. The charging efficiency can then be estimated as the rate of the increase of the discharge capacity when increasing the inserted charge (Figure 3.3 C,D):

$$\frac{i_{CR}}{i_{ch}} = \frac{dC_{dc}}{dC_{ch}} \approx \frac{dSOC}{dq} \tag{3.10}$$

Ideal charging describes the hypothetical case where OER only occurs after all of the active material is fully charged. However, as mentioned above, OER will already occur earlier. In this case, all the inserted current is initially spent on the CR but above 2C charge insertion the charging efficiency reduces to close to zero (Figure 3.3 B). A high charging efficiency is not only beneficial for nickel battery electrodes, but also for the operation of the hybrid electrodes presented here. Fast charging early on in the charging and electrolysis cycle allows for more flexible operation such as intermittent charge and discharge in response to electricity prices. As shown in Figure 3.3 C,D, OER already occurs at the beginning of charging for both the 3D and Non-3D electrode and is exacerbated by an increase in charge rate. For the tested charge rates of C/2 and 1.5C, the 3D electrode exhibits higher charging efficiencies, so that OER is shifted towards the end of charging. As a result, a charge insertion of 1C at the C/2 rate is sufficient to charge 80 % of the loaded active material of the 3D electrode vs. 74 % for the Non-3D electrode. Remarkably, for a threefold increase in charging current (1.5C), this value only decreases to 77 % for the 3D electrode as opposed to 60 % for the Non-3D electrode, that exhibits a low initial charging efficiency of 60 % (Figure 2.9 A, C, D). As shown for electrode activation (Figure 3.2 A), the differences in charging efficiency are again reflected in the charging potentials (Figure 3.3 C, D). These increase for higher charge rates and are considerably lower for the 3D electrode that shows about 50 mV reduction in the average charging potential for the 1.5C charge rate. Since both electrodes have been loaded with the same active material and loading procedure, the observed increase in charging efficiency must be the result of the more open electrode structure.

How the electrode structure can have such a significant impact on the Faradaic charging efficiency becomes clear when considering the current distribution within the electrode throughout charging as determined using the porous electrode model described in Chapter 2. These are shown in Figure 3.4 A for different levels of charge insertion, where $\xi = x/l$ is the lateral position x divided by the electrode thickness l. Whether OER or CR occurs at a depth x in the electrode, depends on the local state of charge and the local overpotentials for the respective reactions. Since the exchange current density for CR is orders of magnitude higher than for OER, CR is dominant if the local state of charge is low and the

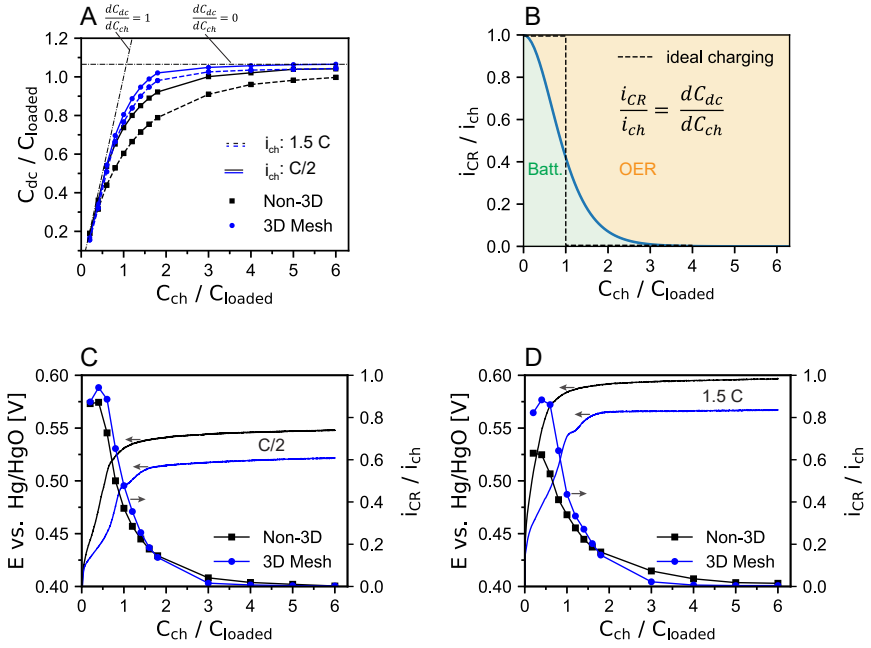

Figure 3.3: Charge retention and impact of oxygen evolution on battery capacity during charging. (A) Discharge capacity over charge insertion for charge rates of 0.5C and 1.5C and a constant discharge rate of C/4. (B) Schematic of the shift in partial current for battery charging, i_{CR}, in the course of charging and overcharging. This behavior is described by Equation 3.9. Ideal charging would be step function. (C,D) Experimentally determined partial current for battery charging at C/2 and 1.5C overlaid with the iR-corrected voltage progression during charging and overcharging to 6C.

overpotential for OER is sufficiently small compared to that of CR. The solution potential of the electrolyte, and therefore the overpotentials of the respective reactions η_{CR} and η_{OER}, decrease exponentially over the electrode thickness as a consequence of the effective ionic resistance of the electrolyte within the electrode. Therefore, at the beginning of charging, the magnitude of the CR current density is highest at the front of the electrode with only negligible OER (Figure 3.4 A). Here, the state of charge increases the fastest, resulting in the gradual transition from CR to OER. Charging continues within the electrode across a reaction front moving from the front to the back of the electrode. Comparing the current distri-

butions of the 3D with the Non-3D electrode, two observations stand out: First, at the beginning of charging, the battery charging current density j_{CR} is distributed more homogeneously over the 3D electrode, resulting in a more homogenous increase in state of charge (Figure 3.4 A, B). As a result, the onset of OER at the front of the electrode is delayed. Second, even when OER increases at the front of the 3D electrode, CR continues with a current density of a comparable order of magnitude across its thickness. Overall, this increased homogeneity of the current distribution significantly improves (re)chargeability and is the direct result of the higher effective electrolyte conductivity, i.e. lower ionic resistance, provided by the electrode channels.

Comparison with the experimental data shows that the simple porous electrode model can qualitatively describe the charging behavior for the here discussed electrodes of varying void fraction at the 1.5C charge rate (Figure 3.5). We find that the model overestimates the charging efficiency up to approximately 3C charge insertion. This is possibly due to the simplifying assumptions made that neglect effects such as proton and charge transfer resistances within the active material as well as the reduction of surface area and electrolyte conductivity due to O_2 bubbles. Notably, the full capacity is not reached in the model, neither for the 3D nor the Non-3D electrode, but the 3D comes closer. This is due to Equation 2.18 approaching zero when the anodic term reduces and the cathodic term increases when the state of charge approaches 1. In the model, this effectively stops charging even before the state of charge reaches 1.

3.2.4. High rate battery performance

Hybrid battery-electrolyser electrodes should provide a high charging efficiency and discharge capacity as well as sufficiently low overpotentials at increased charge and discharge rates. Figure 3.6 shows the impact of charge and discharge rates on discharge capacities and overpotentials for the 3D and Non-3D electrode. Increasing the charge rate from C/10 to C/2 results in no significant decrease in discharge capacity for the Non-3D electrode. Remarkably, the discharge capacity of the 3D mesh electrode increases up to a charge rate of 1C. Higher charge rates are known to increase the attainable oxidation state of the active material [44]. If the charge rate is still sufficiently low to limit OER, this increased oxidation

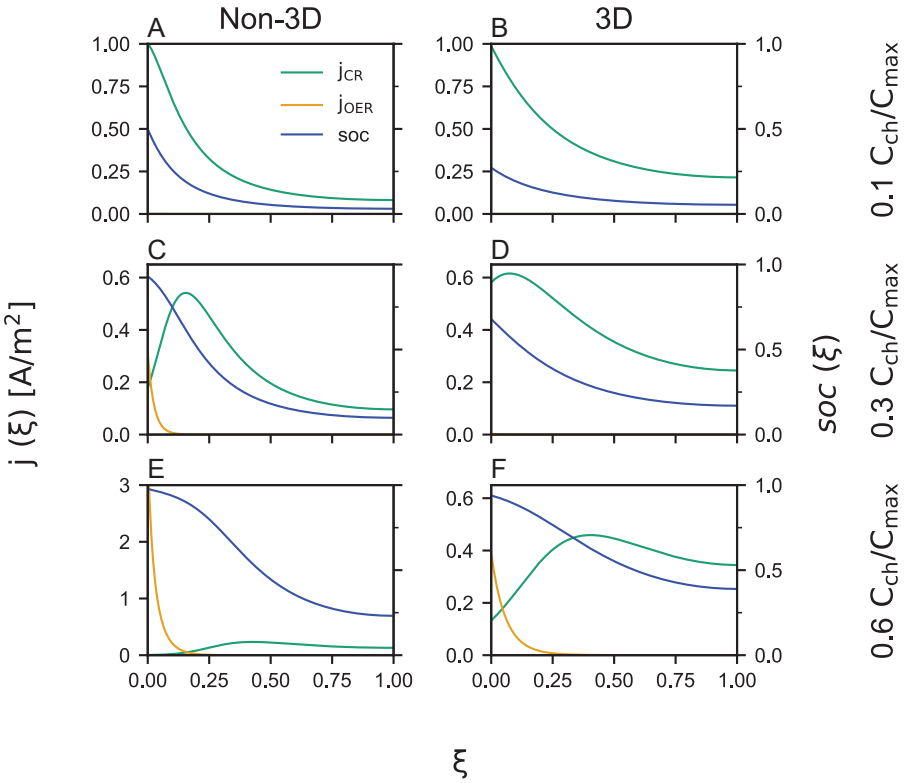

Figure 3.4: Modelled local state of charge (soc) and current distribution for the oxygen evolution (j_{OER}) and battery charging reaction (j_{CR}) for the 3D and Non-3D electrode at a charge rate of 1.5C. The local soc and current distribution are shown for a charge insertion of 0.1C (A,B), 0.3C (C,D) and 0.6 C (E,F) with reference to the maximum measured discharge capacity C_{max} (Figure 3.3 A). ξ refers to the lateral position x relative to the electrode thickness l: $\xi = x/l$. Here, we used the porous electrode model developed in Chapter 2.

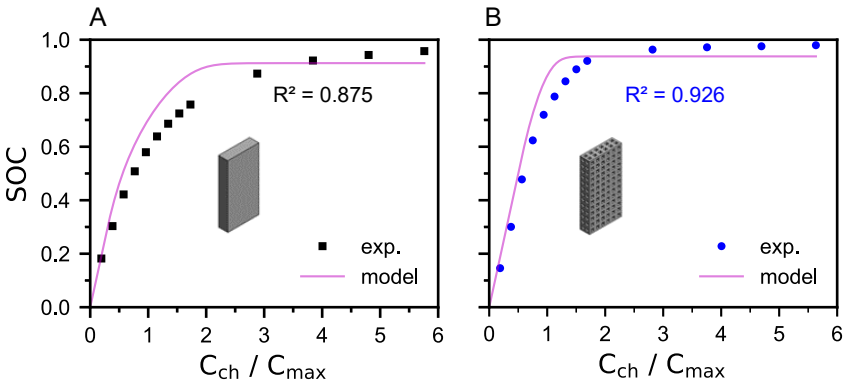

Figure 3.5: Overall state of charge (SOC) in the course of battery charging with a charge rate of 1.5 C for the Non-3D electrode (A) and the 3D electrode (B). Here we compare the SOC determined from the porous electrode model (Chapter 2) with experimental data. The experimentally determined SOC is estimated from the discharge capacities shown in Figure 3.3 A divided by the maximum measured discharge capacity C_{max}.

state results in higher discharge capacities. For charge rates exceeding 1C for the Non-3D electrode, and 2C for the 3D electrode, the discharge capacities appear to decrease logarithmically with increased charge rates (Figure 3.6 A). At a total charging time of only 18 minutes, i.e. a charge rate of 5C (700 mA/cm^2) and 50 % overcharge, the 3D mesh electrode can still provide a specific capacity of 114 mAh/cm^2 which is equivalent to a material utilisation of 81.5 %. This is 46 % higher compared to the Non-3D electrode with a material utilisation of 54 % (78 mAh/cm^2).

Higher current densities result in a shift of CR and OER towards the front of the electrode. This affects the charging efficiency in two ways. Firstly, as discussed above, the more inhomogeneous charging results in an earlier transition to OER at the front of the electrode while the state of charge in the rest of the electrode is still low. Secondly, the reduced utilisation of the electrode's electrochemically active surface area in combination with higher applied current densities results in increased electrode polarization, i.e. overpotentials for both CR and OER. Not only does this result in increased OER, it is also detrimental to the energy efficiency of charging and subsequent electrolysis. The lower ionic resistance of the 3D electrode can compensate for a higher charging current density, hereby fa-

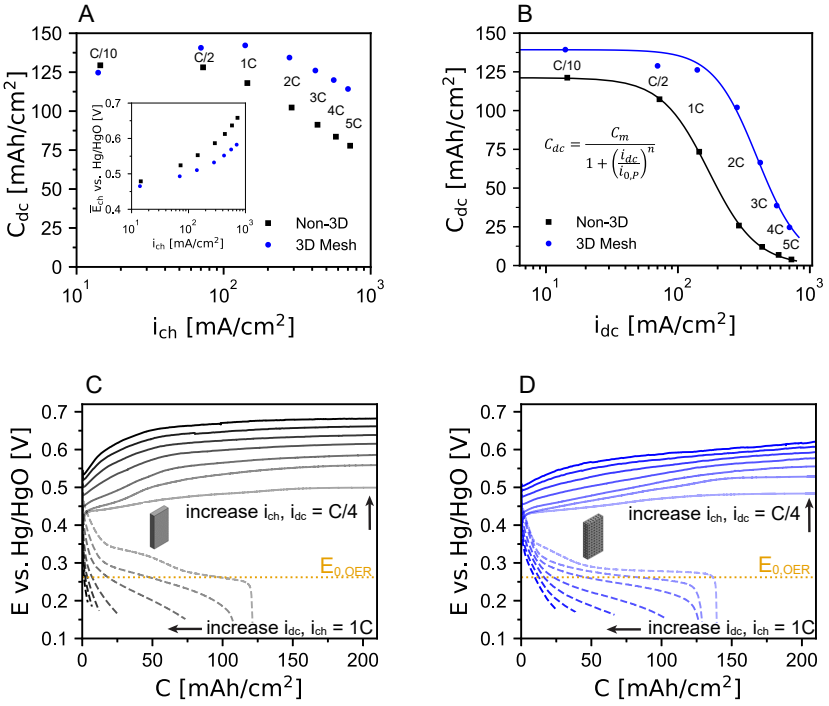

Figure 3.6: Impact of charge and discharge rate on battery capacity and electrode potential. (A) Experimental discharge capacity, C_{dc}, for varying charge rates, i_{ch}, at 1.5C charge insertion and a C/4 discharge rate. Inset: Average iR-corrected potential $\bar{E}_{ch}$ for each tested charge rate. (B) Experimental discharge capacity for varying discharge rates, i_{dc}, at a 1.5C charge insertion and a charge rate of 1C. The shown fit is based on the generalized Peukert equation (Equation 3.11)[22]. (C,D) iR-corrected electrode potentials of the Non-3D electrode (C) and the 3D mesh electrode (D) for varying charge rates (see A) and discharge rates (see B). The yellow line marks the equilibrium potential for oxygen evolution $E_{0,OER}$.

cilitating fast charging at a reduced loss in charging efficiency in addition to a reduction in overpotentials (Figures 3.6, B.9, B.10). This difference in charging potentials increases for higher charge rates and is as high as 100 mV at the 5C (700 mA/cm^2) charge rate.

As typical for nickel battery electrodes, recharging allows for significantly higher material utilisation at elevated current densities than discharging (Figure 3.6 A,B). This is because both proton diffusivity and

electronic conductivity within the active material film decrease for a lower state of charge [46]. In addition, the discharge starts from the active particles surface, resulting in a shell with decreased conductivity around the still charged core. Also during discharge, the polarization of the electrolyte results in an inhomogeneously distributed discharging current which reduces material utilisation farther from the electrode surface [10, 22]. In addition to electrode kinetics, these effects of inhomogeneous discharging on the scale of the active material thickness (~10 µm) and the scale of the electrode thickness (~5 mm) determine the relationship between discharge capacity and discharge rate [10, 22]. Yazvinskaya et al. [22] introduced a generalized form of the Peukert Equation that has been shown to describe this dependence of the discharge capacity on the discharge rate in batteries with nickel positive electrodes:

$$C_{dc} = \frac{C_m}{1 + \left(\frac{i_{dc}}{i_{0,P}}\right)^n} \tag{3.11}$$

Here, C_m is the maximum discharge capacity the battery can deliver at a low discharge rate and a given charge rate and charge insertion, i_{dc} is the discharge current density, $i_{0,P}$ is the discharge current density at which half of C_m can be extracted and the exponent n describes the slope of the curve. As shown in Figure 3.6 B, the experimental data can be fit with good agreement to this generalized Peukert equation. The 3D electrode can be discharged around 2.4 times faster than the Non-3D electrode and still deliver 50 % of the maximum discharge capacity (2.3 x higher $i_{0,P}$, Table 3.1) at a current density of 415 mA/cm^2. This is equivalent to an areal capacity of 70 mAh/cm^2 discharged in just 20 minutes. In contrast, at this current density, only 13 mAh/cm^2 can be discharged from the Non-3D electrode. To put these current densities into perspective, the pocket electrodes employed in the previous work reached an areal capacity of approximately 63 mAh/cm^2 at a significantly lower discharge rate of 20 mA/cm^2 [7]. However, it is important to note that the discharge current density in a Ni-Fe battery is limited by the iron electrode. Therefore, operating at such high current densities as reached for the herein discussed 3D nickel electrode will require further advancements in the rate capability of iron electrodes [47] (see also Chapter 4).

Table 3.1: Fit for the generalized Peukert equation (Equation 3.11, Figure 3.6 B).

	$i_{0,P}$ [mA/cm^2]	C_m [mAh/cm^2]	n [-]
Non-3D	171	121	2.40
3D Mesh	415	134	2.86
CI (Non-3D)	[167, 176]	[119, 123]	[2.28, 2.52]
CI (3D Mesh)	[381, 450]	[127, 141]	[2.20, 3.52]

C_m: Maximum discharge capacity.
$i_{0,P}$: Discharge current at which half of C_m is reached.
n: Exponent of the generalized Peukert equation.
CI: Confidence intervals for the fitted parameters $i_{0,P}$, C_m and n.

The significant increase in material utilisation of the 3D electrode implies that at high discharge current densities the ionic conductivity of the electrode limits the effectively utilized electrode thickness. This is further supported by the results of Lim and Verzwyfelt [10], who demonstrated that for current densities above 300 mA/cm^2 there is a limiting electrode thickness above which the discharge capacity increases no further. For a discharge current density of 300 mA/cm^2, they report a limiting thickness of 1 mm which is in agreement with our results for the Non-3D electrode. For this reason, sintered electrodes with high rate capability are typically thin, sacrificing energy for power density. Due to the increase in the effective ionic conductivity of the 3D electrode, this limiting value increases by 60 % to 1.6 mm.

The discussion above illustrates the drastically improved rate capability of the 3D electrode for both charging and discharging. In addition to the benefits for the here discussed hybrid battery-electrolyser system, the presented 3D electrode can contribute to the development of battery energy storage systems with higher power and energy density (e.g. Ni-Fe, Ni-Cd, Ni-MH, Ni-H_2). Furthermore, the use of thicker electrodes with high areal storage capacity reduces the number of cells required and the associated costs of components such as separators/membranes, connections and seals.

3.2.5. Electrolysis

After the nickel hybrid electrodes are fully charged, they function as electrolysis electrodes for OER. Sintered nickel electrodes impregnated with nickel hydroxide have been shown in the past to be highly active for oxygen evolution and even outperform noble metal catalysts such as IrO_2 in this respect [48, 49]. In order to evaluate the impact of the electrode geometry on electrolysis potentials, the Non-3D and 3D hybrid electrodes were first fully charged at the 1C rate for 3h before undergoing a series of increasing currents for oxygen evolution (Figure 3.7 A). The highest geometric current densities tested were 788 mA/cm^2 and 826 mA/cm^2 for the Non-3D and the 3D mesh electrode, respectively. For sufficiently high overpotentials, the relationship between current density and electrode overpotential can be described by the Tafel relationship $\eta_{OER} = b\ log_{10}(i/i_0)$. The Tafel slope b and electrode exchange current density i_0 are determined by fitting the experimental data to the Tafel equation. Generally, a higher electrode exchange current density and lower Tafel slope are characteristic for electrodes with a high activity towards oxygen evolution [50]. The fitted Tafel slopes are almost identical for the Non-3D and the 3D electrode with 87 and 90 mV/dec, respectively, but are shifted by the difference in the electrode exchange current density. With respect to the geometric surface area, the exchange current density $i_{0,geo}$ is 4.3 x 10^{-2} mA/cm^2 for the 3D mesh electrode vs. 2.7 x 10^{-2} mA/cm^2 for the Non-3D geometry, which constitutes an increase in activity by a factor of 1.6. At an overpotential of 350 mV, the 3D mesh electrode achieves a current density of 333 mA/cm^2 vs. 285 mA/cm^2 for the Non-3D electrode. This is significantly higher than the values reported by Kou et al. [34] (150 mA/cm^2 at 350 mV) who used a similarly structured 3D printed nickel electrode loaded with carbon doped NiO. However, the authors of this study employed a much lower electrolyte concentration compared to our work (1 M vs. ~7.1 M / 30 wt% KOH (aq.)). The 3D mesh electrode can provide a higher current even though the channel geometry reduces the electrochemically active surface area by 35 % (Appendix B.5). As a result, the presented 3D mesh electrode could reduce the material costs of the sintered nickel substrate by 44 % and still outperform a conventional Non-3D electrode. This is especially relevant for upscaling of the technology as the cost for Ni dominates the electrode material costs and is expected to be in rising demand in the course of the energy transition [51].

Evaluating the overpotentials with the current normalized to the electrochemically active surface area (ECSA) (Figure 3.7 B,C), suggests an apparently higher intrinsic activity of the active material in the 3D electrode (higher i_{ECSA} for a given η_{OER}). However, since both electrodes have been loaded with the same active material, a difference in catalytic activity is excluded. Thus, the differences in electrode polarization must be of structural origin relating to the accessibility, i.e. utilisation of active material. In order to estimate the increase in utilisation of the 3D electrode, the Tafel relation can be rewritten as [52]:

$$i_{geo} = a_{geo}\, i_{0,OER}\, U\, exp\, \left(2.303\, \frac{\eta_{OER}}{b}\right) \tag{3.12}$$

Where a_{geo} is the ECSA per geometric electrode area and U is the utilisation. Comparing two electrodes with the same Tafel slope b at a given overpotential, we can write [52]:

$$\begin{aligned} \frac{U_1}{U_2} &= \left(\frac{i_{geo,1}}{i_{geo,2}}\right)_{\eta_1=\eta_2} \frac{a_{geo,2}}{a_{geo,1}} \\ &= \frac{i_{0,ECSA,1}}{i_{0,ECSA,2}} \end{aligned} \tag{3.13}$$

Here, $i_{0,ECSA}$ is the exchange current density with respect to the ECSA (Figure 3.7 C). As the ratio $i_{geo,1}/i_{geo,2}$ at a given overpotential is independent of current density and polarization, the enhancement in utilisation is defined by the ratio of the electrodes' respective exchange current density $i_{0,ECSA}$. Applying Equation 3.13 to our experimental data, results in an estimated 2.5 fold increase in utilisation of the 3D electrode.

As discussed for the 3D electrode's improved charging efficiency and (dis)charge rate capabilities, the observed increase in utilisation can be explained with the lower effective ionic electrode resistance of the more open 3D structure. This results in a reduced gradient in overpotential across the electrode thickness and thus a more homogenous current distribution as determined with the porous electrode model from Chapter 2 (Figure 3.7 D and Figure B.11 C,D). Using said current distribution, the utilisation can be determined as:

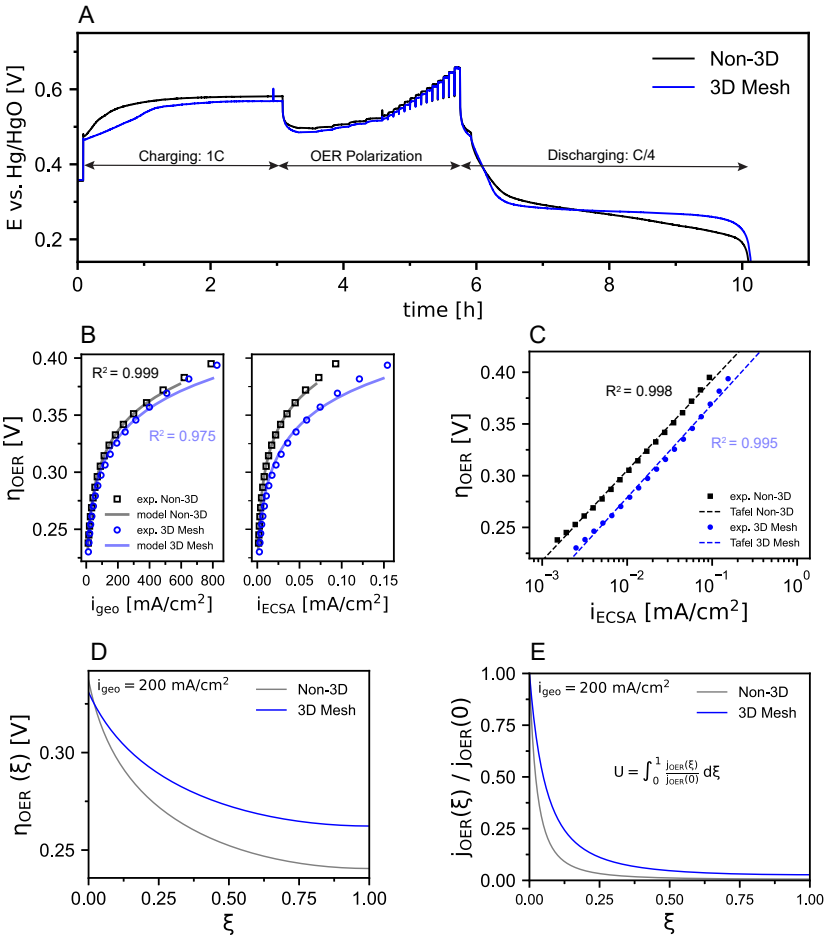

Figure 3.7: Overview of the electrolysis performance of a 3D mesh and Non-3D nickel battery-electrolyser electrode. (A) iR-corrected electrode potential over time during charging (1C $\approx$ 140 mA/cm^2), OER polarization experiments and subsequent discharge (C/4). (B) iR-corrected electrode potential vs. geometric current density i_{geo} (left) and vs. current density with respect to the electrochemically active surface area i_{ECSA} (right). The experimental data is compared to the results obtained from the porous electrode model. (C) Tafel fit of the iR-corrected oxygen evolution overpotential η_{OER} vs. i_{ECSA}. (D,E) OER overpotential and current distribution over the reduced position $\xi = x/l$ at a geometric current density of 200 mA/cm^2 determined from the porous electrode model.

$$U = \int_0^1 \frac{j_{OER}(\xi)}{j_{OER}(0)} d\xi \tag{3.14}$$

where $j_{OER}(\xi)$ is the local OER current density at the reduced position $\xi = x/l$ and $j_{OER}(0)$ is the current density at the electrode front facing the counter electrode. For an applied current density of 200 mA/cm^2, the utilisation is calculated as 5.3 % vs. 12.1 % for the Non-3D and 3D electrode, respectively. Remarkably, the utilisation enhancement calculated with the simple model is only marginally lower than that determined experimentally (2.2 vs. 2.5). Such low utilisation as the consequence of the high ionic voltage drop is the reason why the thickness of porous electrodes or active coatings is typically well below 1 mm for electrolysis [48, 49, 52].

While increasing the electrode thickness increases the ECSA, there is a limit above which any additional ECSA is not utilized due to the increasingly high ionic resistance. This limit is also known as the reaction penetration depth [53, 54]. Electrodes thicker than the reaction penetration depth do not increase the effectively utilized ECSA, so that electrode polarization does not decrease either. With regard to the 3D electrode discussed in this work, this poses an interesting optimization question. While a more open geometry with a high void fraction Θ increases the effective ionic electrode conductivity and electrode utilisation, the total ECSA is reduced by a factor $(1 - \Theta)$. This implies that there must be an optimal electrode void fraction for each current density that maximizes the ionically accessible ECSA and thus minimizes electrode polarization for a given thickness and porosity. This is discussed in detail in Chapter 2.

We note, that even if OER utilisation is low for the here discussed hybrid electrodes, most of the electrode is utilized for the battery (dis)charging reaction (Figures 3.4 and 3.6). As stated above, this is because at low $SOC(q)$ the exchange current density for charging is many orders of magnitude larger than for OER. Therefore, 3D hybrid battery-electrolysis electrodes will generally be thicker than dedicated electrolysis electrodes and will still be able to charge the full thickness.

In the discussion above we have not yet considered the possible effect of bubbles on electrode utilisation. Bubbles flooding the pores and adhering to the electrode surface are known to cover electrochemically active sites [25, 55] and reduce the effective electrolyte conductivity [56, 57], re-

sulting in a decrease in electrode utilisation [48, 49, 52]. Appleby et al. [49] demonstrated that only around 40 % of the ECSA is utilized for OER (extrapolated by Hall [48]) for a 0.15 mm thick sintered nickel electrode. For such thin electrodes, where the ionic resistance is not limiting, a reduction in utilisation can be attributed clearly to the adverse effects of bubbles within the pores. However, our results suggest that any adverse effects of bubbles on the utilisation are small compared to the impact of the effective ionic conductivity. Firstly, the simple electrode model appears to describe the overpotentials and utilisation enhancement for the tested electrodes reasonably well (Figure 3.7 B), even without taking bubbles into account. Secondly, if we assume that only 40 % [48, 49] of the OER generating ECSA is available due to bubble coverage (for example at 200 mA/cm2), that would decrease the utilisation of the Non-3D electrode further from 5.3 % to 2.12 % - an effectively negligible difference compared to the impact of the ionic resistance. Therefore, it is clear that in this work the main mechanism by which the 3D electrode increases electrode utilisation is by increasing the effective ionic conductivity of the electrode. The experimental data can be fitted using a simple Tafel relation with a current-independent Tafel slope b (Figure 3.7 C). This implies that the bubble coverage is not yet leading to additional transport resistances at these current densities, as has also been shown in earlier studies on sintered nickel electrodes for both OER [48, 49] and HER [52].

While the measured performance gain of the 3D electrode can be mostly attributed to an improved ionic conductivity into the porous electrode, one may expect additional advantages on current densities in a full electrolyser cell, where such an electrode can be configured in a zero-gap flow-through configuration. The electrolyte flowing through, rather than past, the electrode improves not only bubble removal but could also facilitate mass and heat transfer [35, 58–61]. The latter is especially relevant at high current densities, where over-heating can result in decreased battery cycling stability and charging efficiency [12, 13, 62]. A concept for such a cell is presented in Chapter 6.

3.2.6. Energy Efficiency

To put the reduction in overpotentials and the increased areal capacity into perspective for the practical application as an integrated battery-

electrolyser, we can estimate the overall energy efficiency for a full cell [7]:

$$\eta_{tot} = \frac{C_{dc}\left(\bar{E}_{Ni,dc} - \bar{E}_{Fe,dc} - \eta_{\Omega,dc}\right) + 1.48V\,(C_{ch} - C_{dc})}{C_{ch}\left(\bar{E}_{Ni,ch} - \bar{E}_{Fe,ch} + \eta_{\Omega,ch}\right)} \tag{3.15}$$

Here, $\bar{E}_{Ni}$ and $\bar{E}_{Fe}$ represent the average observed potentials during charge (ch) and discharge (dc) of the nickel and iron electrode, respectively. Ionic overpotentials induced by the electrolyte resistivity in the inter-electrode gap are denoted as η_Ω. Specifically for charging and electrolysis, this resistivity may be increased by some screening effect of bubbles as discussed above. The energy that can be stored and extracted from the cell consists of the energy retrieved during discharging of the battery determined by the average discharging potentials of anode and cathode. In addition, the energy stored in the form of hydrogen is determined from the thermoneutral voltage for alkaline water electrolysis (1.48V) while the charge insertion for electrolysis is estimated from the difference between inserted charge and discharge capacity. Here we assume that the battery is cycled from fully discharged, to charged and fully discharged, and the missing charge is converted to H_2 and O_2 either during discharge (or eventually due to self-discharge when idling after charge). In this work, the discussed nickel electrodes were only cycled individually and not in a full cell paired with an iron electrode. Therefore, we estimate the total energy efficiency with data from a Non-3D sintered iron electrode that had been operated at similar charging/discharging current densities and charge insertion (see Figure B.18). The ohmic potential drop between the electrodes is dependent on the exact cell configuration. Here only the electrolyte resistance in an assumed electrode gap of 1.5 mm is used. Effects of bubbles on the electrolyte resistance and a membrane resistance are not taken into account, which is justified for low current densities. The total energy efficiency was calculated for a charge rate of 1C and a discharge rate of C/4 which is equivalent to a charging/discharging current density of 145 mA/cm^2 / 36 mA/cm^2 for the Non-3D electrode, and 140 mA/cm^2 / 35 mA/cm^2 for the 3D-Mesh electrode. The electrodes were overcharged to 6C. This results in an estimated total energy efficiency of 76.4 % and 78.9 % for the Non-3D and 3D-Mesh electrode at

room temperature, respectively.

It is worth noting that similar benefits in overpotential and capacity utilisation are to be expected from a sintered iron electrode with comparable 3D structure. In addition, the efficiency can be increased further by operating the cell at higher temperatures. This reduces activation overpotentials and increases the conductivity of the electrolyte.

In total, the electrode tests including charge, discharge and electrolysis at different rates lasted for up to 345 hours, and 627 hours of discharging during more than 150 cycles (Figure B.17). The electrodes maintain capacity and rate performance although one can observe some $Ni(OH)_2$ directly on the surface has detached, as is observed in X-ray diffraction of the electrode surface (Figure B.15).

3.3. Conclusions

In summary, we have introduced an indirectly 3D printed hybrid nickel electrode that exhibits state of the art, high areal battery capacity at charge and discharge rates relevant for stationary renewable electricity storage. When overcharged, the electrode continues operation at industrially relevant current densities for alkaline electrolysis. Overall, competitive efficiencies and energy densities are reached for both applications at room temperature, with double use of the materials and system involved. The channel geometry facilitates electrolyte access, hereby increasing the effective ionic conductivity within the electrode. Especially at high current densities, this results in reduced overpotentials and a significant increase in material utilisation, not only for battery (dis)charging, but also for electrolysis. Using a porous electrode model which includes a channel volume fraction, we demonstrate how this improved performance can be explained by the more homogeneous current distribution over the thickness of 3D electrodes. In addition to parameters such as porosity, pore size and thickness, the 3D geometry presents a novel degree of freedom in electrode development. The step from this 3D prototyping to industrial powder metallurgical production techniques as applied in e.g. automotive, medical or electronic sectors will enable the production of 3D structured electrodes in a scalable manner [40–42].

References

[1] H. O. Portner, D. C. Roberts, H. Adams, C. Adler, P. Aldunce, E. Ali, R. A. Begum, R. Betts, R. B. Kerr, R. Biesbroek, *et al.*, *Climate change 2022: Impacts, adaptation and vulnerability*, Tech. Rep. (IPCC, 2022).

[2] L. Kemp, C. Xu, J. Depledge, K. L. Ebi, G. Gibbins, T. A. Kohler, J. Rockström, M. Scheffer, H. J. Schellnhuber, W. Steffen, *et al.*, *Climate endgame: Exploring catastrophic climate change scenarios,* Proceedings of the National Academy of Sciences **119**, e2108146119 (2022).

[3] O. Hoegh-Guldberg, D. Jacob, M. Taylor, T. Guillén Bolaños, M. Bindi, S. Brown, I. A. Camilloni, A. Diedhiou, R. Djalante, K. Ebi, *et al.*, *The human imperative of stabilizing global climate change at 1.5 °C,* Science **365**, eaaw6974 (2019).

[4] N. Blair, C. Augustine, W. Cole, P. Denholm, W. Frazier, M. Geocaris, J. Jorgenson, K. McCabe, K. Podkaminer, A. Prasanna, *et al.*, *Storage futures study: Key learnings for the coming decades*, Tech. Rep. (National Renewable Energy Lab.(NREL), Golden, CO (United States), 2022).

[5] F. M. Mulder, *Implications of diurnal and seasonal variations in renewable energy generation for large scale energy storage,* Journal of Renewable and Sustainable Energy **6** (2014).

[6] M. J. Palys and P. Daoutidis, *Using hydrogen and ammonia for renewable energy storage: A geographically comprehensive techno-economic study,* Computers & Chemical Engineering **136**, 106785 (2020).

[7] F. M. Mulder, B. M. H. Weninger, J. Middelkoop, F. G. B. Ooms, and H. Schreuders, *Efficient electricity storage with a battolyser, an integrated Ni–Fe battery and electrolyser,* Energy & Environmental Science **10**, 756 (2017).

[8] A. K. Shukla, M. K. Ravikumar, and T. S. Balasubramanian, *Nickel/iron batteries,* Journal of Power Sources **51**, 29 (1994).

[9] J. M. E. Abarro, J. N. L. Gavan, D. E. D. Loresca, M. A. A. Ortega, E. A. Esparcia Jr, and J. A. D. Paraggua, *A Tale of Nickel-Iron Batteries: Its Resurgence in the Age of Modern Batteries,* Batteries **9**, 383 (2023).

[10] H. S. Lim and S. A. Verzwyvelt, *Effects of electrode thickness on power capability of a sintered-type nickel electrode,* Journal of Power Sources **62**, 41 (1996).

[11] A. K. Manohar, C. Yang, S. Malkhandi, G. K. S. Prakash, and S. R. Narayanan, *Enhancing the performance of the rechargeable iron electrode in alkaline batteries with bismuth oxide and iron sulfide additives,* Journal of the Electrochemical Society **160**, A2078 (2013).

[12] M. Oshitani, Y. Sasaki, and K. Takashima, *Development of a nickel electrode having stable performance at various charge and discharge rates over a wide temperature range,* Journal of Power Sources **12**, 219 (1984).

[13] J. Li, E. Shangguan, D. Guo, Q. Li, Z. Chang, X.-Z. Yuan, and H. Wang, *Calcium metaborate as a cathode additive to improve the high-temperature properties of nickel hydroxide electrodes for nickel–metal hydride batteries,* Journal of Power Sources **263**, 110 (2014).

[14] Y. Sui and X. Ji, *Anticatalytic strategies to suppress water electrolysis in aqueous batteries,* Chemical Reviews **121**, 6654 (2021).

[15] A. Iranzo and F. M. Mulder, *Nickel-iron layered double hydroxides for an improved Ni/Fe hybrid battery-electrolyser,* Materials Advances **2**, 5076 (2021).

[16] M. Holst, S. Aschbrenner, T. Smolinka, C. Voglstätter, and G. Grimm, *Cost forecast for low-temperature electrolysis-technology driven bottom-up prognosis for PEM and alkaline water electrolysis systems,* Fraunhofer Institute for Solar Energy Systems ISE: Freiburg, Germany (2021).

[17] H. van't Noordende and P. Ripson, *A one-gigawatt green-hydrogen plant-advanced design and total installed-capital costs,* Institute for Sustainable Proces s Technology, Amersfoort (2022).

[18] J. W. Haverkort and H. Rajaei, *Voltage losses in zero-gap alkaline water electrolysis,* Journal of Power Sources **497**, 229864 (2021).

[19] R. L. G. Barros, J. T. Kraakman, C. Sebregts, J. van der Schaaf, and M. T. de Groot, *Impact of an electrode-diaphragm gap on diffusive hydrogen crossover in alkaline water electrolysis,* International Journal of Hydrogen Energy **49**, 886 (2024).

[20] TenneT, *TenneT Adequacy Outlook 2023*, Technical Report (TenneT, 2023).

[21] S. U. Falk and A. J. Salkind, *Alkaline storage batteries* (1969).

[22] N. N. Yazvinskaya, N. E. Galushkin, D. N. Galushkin, and B. Y. Kalmykov, *Analysis and comparison of generalized Peukert's equations parameters for nickel-cadmium batteries with pocket and sintered electrodes,* International Journal of Electrochemical Science **15**, 412 (2020).

[23] S. Chandrasekaran, D. Lin, Y. Li, and M. A. Worsley, *Aerogels, additive manufacturing, and energy storage,* Joule **7**, 866 (2023).

[24] G. Wosiak, J. da Silva, S. S. Sena, E. B. Carneiro-Neto, M. C. Lopes, and E. Pereira, *Investigation of the influence of the void fraction on the energy consumption of a vertical electrolyser under natural convection,* Journal of Environmental Chemical Engineering **10**, 107577 (2022).

[25] H. Vogt, *The actual current density of gas-evolving electrodes—notes on the bubble coverage,* Electrochimica Acta **78**, 183 (2012).

[26] S. Mooraj, Z. Qi, C. Zhu, J. Ren, S. Peng, L. Liu, S. Zhang, S. Feng, F. Kong, Y. Liu, *et al.*, *3D printing of metal-based materials for renewable energy applications,* Nano Research **14**, 2105 (2021).

[27] X. Xu, Y. H. Tan, J. Ding, and C. Guan, *3D printing of next-generation electrochemical energy storage devices: from multiscale to multimaterial,* Energy & Environmental Materials **5**, 427 (2022).

[28] L. Zeng, P. Li, Y. Yao, B. Niu, S. Niu, and B. Xu, *Recent progresses of 3D printing technologies for structural energy storage devices,* Materials Today Nano **12**, 100094 (2020).

[29] J. Lölsberg, O. Starck, S. Stiefel, J. Hereijgers, T. Breugelmans, and M. Wessling, *3d-printed electrodes with improved mass transport properties,* ChemElectroChem **4**, 3309 (2017).

[30] L. F. Arenas, C. P. de León, and F. C. Walsh, *3d-printed porous electrodes for advanced electrochemical flow reactors: A Ni/stainless steel electrode and its mass transport characteristics,* Electrochemistry Communications **77**, 133 (2017).

[31] J. Hereijgers, J. Schalck, J. Lölsberg, M. Wessling, and T. Breugelmans, *Indirect 3D printed electrode mixers,* ChemElectroChem **6**, 378 (2019).

[32] J. Hereijgers, J. Schalck, and T. Breugelmans, *Mass transfer and hydrodynamic characterization of structured 3D electrodes for electrochemistry,* Chemical Engineering Journal **384**, 123283 (2020).

[33] J. C. Bui, J. T. Davis, and D. V. Esposito, *3d-printed electrodes for membraneless water electrolysis,* Sustainable Energy & Fuels **4**, 213 (2020).

[34] T. Kou, S. Wang, R. Shi, T. Zhang, S. Chiovoloni, J. Q. Lu, W. Chen, M. A. Worsley, B. C. Wood, S. E. Baker, *et al.*, *Periodic porous 3D electrodes mitigate gas bubble traffic during alkaline water electrolysis at high current densities,* Advanced Energy Materials **10**, 2002955 (2020).

[35] I. Sullivan, H. Zhang, C. Zhu, M. Wood, A. J. Nelson, S. E. Baker, C. M. Spadaccini, T. Van Buuren, M. Lin, E. B. Duoss, *et al.*, *3D printed nickel–molybdenum-based electrocatalysts for hydrogen evolution at low overpotentials in a flow-through configuration,* ACS Applied Materials & Interfaces **13**, 20260 (2021).

[36] M. S. Saleh, J. Li, J. Park, and R. Panat, *3D printed hierarchically-porous microlattice electrode materials for exceptionally high specific capacity and areal capacity lithium ion batteries,* Additive Manufacturing **23**, 70 (2018).

[37] D. Kong, Y. Wang, S. Huang, B. Zhang, Y. V. Lim, G. J. Sim, P. Valdivia y Alvarado, Q. Ge, and H. Y. Yang, *3d printed compressible quasi-solid-state nickel–iron battery,* ACS Nano **14**, 9675 (2020).

[38] C. Li, J. Du, Y. Gao, F. Bu, Y. H. Tan, Y. Wang, G. Fu, C. Guan, X. Xu, and W. Huang, *Stereolithography of 3d sustainable metal electrodes towards high-performance nickel iron battery,* Advanced Functional Materials **32**, 2205317 (2022).

[39] T. Roy, M. A. Salazar de Troya, M. A. Worsley, and V. A. Beck, *Topology optimization for the design of porous electrodes,* Structural and Multidisciplinary Optimization **65**, 171 (2022).

[40] H. Danninger, R. D. O. Calderon, and C. Gierl-Mayer, *Powder metallurgy and sintered materials,* Addit. Manuf **19** (2017).

[41] S.-H. Chung, Y.-S. Kwon, C.-M. Hyun, K. Kim, M.-J. Kim, and R. M. German, *Analysis and design of a press and sinter process for fabrication of precise tungsten carbide cutting tools,* Advances in Powder Metallurgy and Particulate Materials, Part **8**, 8 (2004).

[42] A. Dehghan-Manshadi, P. Yu, M. Dargusch, D. StJohn, and M. Qian, *Metal injection moulding of surgical tools, biomaterials and medical devices: A review,* Powder Technology **364**, 189 (2020).

[43] D. Tuomi, *The forming process in nickel positive electrodes,* Journal of The Electrochemical Society **112**, 1 (1965).

[44] A. H. Zimmerman, *Technological implications in studies of nickel electrode performance and degradation,* Journal of Power Sources **12**, 233 (1984).

[45] A. Yuan, S. Cheng, J. Zhang, and C. Cao, *The influence of calcium compounds on the behaviour of the nickel electrode,* Journal of Power Sources **76**, 36 (1998).

[46] S. Motupally, C. C. Streinz, and J. W. Weidner, *Proton diffusion in nickel hydroxide: prediction of active material utilization,* Journal of The Electrochemical Society **145**, 29 (1998).

[47] A. K. Manohar, S. Malkhandi, B. Yang, C. Yang, G. K. S. Prakash, and S. R. Narayanan, *A high-performance rechargeable iron electrode for large-scale battery-based energy storage,* Journal of the Electrochemical Society **159**, A1209 (2012).

[48] D. E. Hall, *$Ni(OH)_2$ - Impregnated Anodes for Alkaline Water Electrolysis,* Journal of The Electrochemical Society **130**, 317 (1983).

[49] A. J. Appleby, G. Crepy, and J. Jacquelin, *High efficiency water electrolysis in alkaline solution,* International Journal of Hydrogen Energy **3**, 21 (1978).

[50] K. Zeng and D. Zhang, *Recent progress in alkaline water electrolysis for hydrogen production and applications,* Progress in Energy and Combustion Science **36**, 307 (2010).

[51] L. Boer, M. A. Pescatori, and M. Stuermer, *Energy transition metals* (International Monetary Fund, 2021).

[52] S. Rausch and H. Wendt, *Morphology and utilization of smooth hydrogen-evolving raney nickel cathode coatings and porous sintered-nickel cathodes,* Journal of the Electrochemical Society **143**, 2852 (1996).

[53] T. Kadyk, D. Bruce, and M. Eikerling, *How to enhance gas removal from porous electrodes?* Scientific reports **6**, 1 (2016).

[54] M.-B. Liu, G. M. Cook, and N. P. Yao, *Transient current distributions in porous zinc electrodes in KOH electrolyte,* Journal of The Electrochemical Society **129**, 239 (1982).

[55] J. R. Lake, A. M. Soto, and K. K. Varanasi, *Impact of bubbles on electrochemically active surface area of microtextured gas-evolving electrodes,* Langmuir **38**, 3276 (2022).

[56] S. Abdelghani-Idrissi, N. Dubouis, A. Grimaud, P. Stevens, G. Toussaint, and A. Colin, *Effect of electrolyte flow on a gas evolution electrode,* Scientific Reports **11**, 4677 (2021).

[57] B. G. Ateya and B. E. El-Anadouli, *Effects of gas bubbles on the polarization behavior of porous flow through electrodes,* Journal of the Electrochemical Society **138**, 1331 (1991).

[58] J. Eigeldinger and H. Vogt, *The bubble coverage of gas-evolving electrodes in a flowing electrolyte,* Electrochimica Acta **45**, 4449 (2000).

[59] R. J. Balzer and H. Vogt, *Effect of electrolyte flow on the bubble coverage of vertical gas-evolving electrodes,* Journal of the Electrochemical Society **150**, E11 (2002).

[60] F. Rocha, R. Delmelle, C. Georgiadis, and J. Proost, *Effect of pore size and electrolyte flow rate on the bubble removal efficiency of 3d pure ni foam electrodes during alkaline water electrolysis,* Journal of Environmental Chemical Engineering **10**, 107648 (2022).

[61] Q. De Radigues, G. Thunis, and J. Proost, *On the use of 3-D electrodes and pulsed voltage for the process intensification of alkaline water electrolysis,* International Journal of Hydrogen Energy **44**, 29432 (2019).

[62] C. Fierro, A. Zallen, J. Koch, and M. A. Fetcenko, *The influence of nickel-hydroxide composition and microstructure on the high-temperature performance of nickel metal hydride batteries,* Journal of the Electrochemical Society **153**, A492 (2006).

4

3D iron electrodes for hybrid battery and electrolysis application

In order to mitigate daily and seasonal fluctuations in the energy supply of renewable sources such as wind and solar, short-and long-term energy storage solutions are required. Batteries are well-suited for energy storage on short timescales, while hydrogen and hydrogen derived fuels are a promising option for long-term energy storage needs. An integrated alkaline Ni-Fe battery and electrolyser can efficiently store electricity as a battery and produce hydrogen in a single device. In this work, we present 3D-structured sintered iron electrodes specifically designed for this hybrid operation. These are manufactured using the technique of indirect 3D printing with an agar-based binder system. We demonstrate that these electrodes can provide high battery capacity while also allowing for efficient hydrogen production at industrially relevant current densities. While the high ionic conductivity of the channels in the 3D structure results in an increase in material utilisation, we also discuss limits to this approach. Next to the 3D structure, we show that the addition of conductivity enhancing additives such as carbon black can significantly increase material utilisation and rate capability resulting in discharge capacities as high as 651 mAh/cm^2 at 30 $°C$. The manufacturing procedure developed in this work can be scaled using techniques such as metal injection moulding (MIM) and material extrusion additive manufacturing (MEX).

4.1. Introduction

Mitigating climate change is going to require the large scale transition to renewable energy sources as well as the decarbonization of sectors such as transportation, steel production and the chemical industry [1, 2]. Due to the intermittency of renewable energy sources such as wind and solar, solutions for both long- and short-term energy storage are required [3]. For the latter, batteries are a promising option given their high energy efficiency, flexibility in location and rapid response time to changes in energy demand [4]. However, high self-discharge rates and a low energy density make batteries less suitable for seasonal, long-term energy storage compared to storing renewable energy in the form of hydrogen or hydrogen derived synthetic fuels such as methane or ammonia (power-to-gas) [5, 6]. Since hydrogen, methane and ammonia are also utilized as feedstock in the chemical industry, generating these via renewable energy would support the decarbonization of these sectors [7]. Therefore, both battery energy storage and power-to-gas will play key roles in a renewable energy future.

In 2017, Mulder et al. [8] introduced the concept of an integrated battery-electrolyser (battolyser™) which is based on a nickel-iron battery. Here, the nickel and iron battery electrodes also perform electrolysis once fully charged to produce oxygen and hydrogen, respectively. As a result, the battery-electrolyser integrates both short-term (battery) and long-term energy storage (hydrogen) in a single device. In periods of overproduction, renewable energy in excess of the battery storage capacity can still be stored in the form of hydrogen. In addition, in periods of high energy cost, i.e. underproduction of renewables, the battery electrodes discharge the stored energy into the grid. This dual-functionality results in a high utilization factor and lower footprint compared to two separate systems for battery storage and electrolysis.

Conventional nickel and iron electrodes employed in nickel-iron batteries are not designed for electrolysis. On the contrary, electrolysis has been considered an unwanted side reaction that reduces the charging efficiency [9–11]. Therefore, the development of new types of electrodes tailored towards the dual functionality of battery operation and electrolysis is required. In Chapters 2 and 3 we introduced the concept of 3D-structured

The results in this chapter have been submitted for publication.

sintered nickel electrodes. The open channel geometry results in a decrease in ionic resistance which leads to improved material utilization, higher rate capability and decreased oxygen evolution overpotentials. In addition, the channel geometry is expected to facilitate gas removal and reduce overpotentials associated with the reduction in electrolyte conductivity and bubble surface coverage [12, 13]. However, the manufacturing procedures used for the nickel electrodes in Chapter 3 and Chapter 5 cannot be adapted for iron electrodes. This is due to the high temperatures required in atmosphere in order to remove the epoxy resin that serves as the binder of the green parts. The oxidation of iron and the successive reduction leads to significant changes in volume and results in brittle electrodes. The goal of this chapter is to develop 3D-structured sintered iron electrodes that can operate at competitive charging and electrolysis current densities while also providing a high area-specific storage capacity.

Sintered iron electrodes are made by compacting iron powder and heating it below the melting point, so that particles are bonded, i.e. sintered, together. This results in a mechanically stable, self-supporting and highly porous iron structure. The high porosity and inter-particle bonds improve the ionic and electrical conductivity, respectively. As a result, high charge and discharge currents can be achieved. Furthermore, neither an additional current collector nor conductive additives are necessary as is the case in pocket-type or polymer-bonded iron electrodes. The lack of such inactive components results in a higher loading of iron and thus higher volume-specific capacities.

During discharge of the iron electrode, iron is first converted to iron (II) hydroxide:

$$Fe + 2OH^- \leftrightarrow Fe(OH)_2 + 2e^- \quad (E^0 = -0.88\ V) \tag{4.1}$$

All equilibrium potentials are with reference to the Standard Hydrogen Electrode (SHE). Upon recharging, the reverse reaction takes place. At a pH of 14.6, the equilibrium potential for hydrogen evolution is 20 mV more positive than that of the iron reaction (Reaction 4.1). As a result, some hydrogen evolution occurs as a side reaction, even at open-circuit poten-

tial. Once fully charged, the iron electrode functions fully as a hydrogen-evolving electrode:

$$2H_2O + 2e^- \rightarrow H_2(g) + 2OH^- \quad (E^0 = -0.86\ V) \tag{4.2}$$

In a second discharge step, iron (II) hydroxide can be converted further to iron (II,III) oxide (Reaction 4.3) or iron (III) oxyhydroxide (Reaction 4.4):

$$3Fe(OH)_2 + 2OH^- \leftrightarrow Fe_3O_4 + 4H_2O + 2e^- \quad (E^0 = -0.662\ V) \tag{4.3}$$

$$Fe(OH)_2 + OH^- \leftrightarrow FeOOH + H_2O + e^- \quad (E^0 = -0.552\ V) \tag{4.4}$$

However, due to the lower cell voltage, discharging the iron electrode beyond the first step is typically avoided in nickel-iron batteries.

The discharge product iron (II) hydroxide from the first discharge step is electronically insulating and has a 3.72 times higher molar volume compared to iron, which can result in pore blockage [14]. Thus, both the electronic and ionic conductivity decrease in the course of discharging. This limits the utilisation, rate capability and rechargeability of iron electrodes and must be addressed in order to get to high area-specific capacities. In the present study, we develop a novel, scalable technique of manufacturing 3D-structured iron electrodes. These electrodes maintain their dual functionality and can still be fully discharged and cycled after being exposed to electrolysis current densities exceeding 1000 mA/cm^2. Moreover, we show how the inclusion of channels and the addition of carbon black address the above-mentioned issues of low ionic and electrical conductivity, respectively.

4.2. A method for indirect 3D printing of sintered iron electrodes

3D sintered iron electrodes were prepared using the technique of indirect 3D printing as shown in Figure 4.1. This technique allows for the manufacturing of porous electrodes with complex geometries at low cost using

standard polymer 3D printers. First introduced by Hereijgers et al. [15], indirect 3D printing involves 3D printing a polymer mold which is then filled with a metal paste consisting of the metal powder, a binder and a liquefaction agent. Following the curing of the binder, the 3D printed mold is dissolved in a solvent, yielding a part of sufficient mechanical strength for further handling. This part is then debinded and finally sintered resulting in a mechanically stable and porous electrode. The combination of 3D printed mold material, mold removing solvent and binder for a given metal powder is essential for indirectly 3D printing electrodes. In order to increase accessibility of the method, the mold should be printable with low-cost materials on consumer grade 3D printers. In addition, the solvent must dissolve the mold material in a reasonable time frame with little residue while being inert to the binder, so as not to reduce the mechanical stability of the green part. Finally, the debinding process must be compatible with the metal in order to allow for successful sintering of the metal particles.

In Chapter 3 we introduced a procedure to manufacture indirectly 3D printed nickel electrodes. We found that polylactic acid (PLA), a commonly used low-cost material used in fused deposition modelling (FDM) 3D printing, is a suitable mold material that can be dissolved in highly concentrated aqueous potassium hydroxide solution (25 wt%) at 40 °C within 15 hours. We used epoxy resin as a binder in combination with an aqueous solution of carboxymethyl cellulose as a liquefaction agent. However, Hereijgers et al. [15] found that epoxy resin requires oxygen and temperatures of 600 °C to decompose fully without carbon residues. Such carbon residues were found to prevent sintering of the individual nickel particles resulting in parts with low mechanical strength [15]. As a result, nickel was oxidized in the debinding step which required a second sintering and reduction step in a 5 % H_2 in argon atmosphere to yield an electrically conductivity nickel electrode. When adapting this indirect 3D printing technique for iron, we found that iron oxidation during the debinding step and the subsequent reduction resulted in fragile and brittle electrodes. This is due to the substantial change in specific volume of around 50 % when iron (Fe) oxidizes to either hematite (Fe_2O_3) or magnetite (Fe_3O_4). Therefore, a binder was required that decomposes without harmful residue and in the absence of oxygen, i.e. without oxidizing the iron.

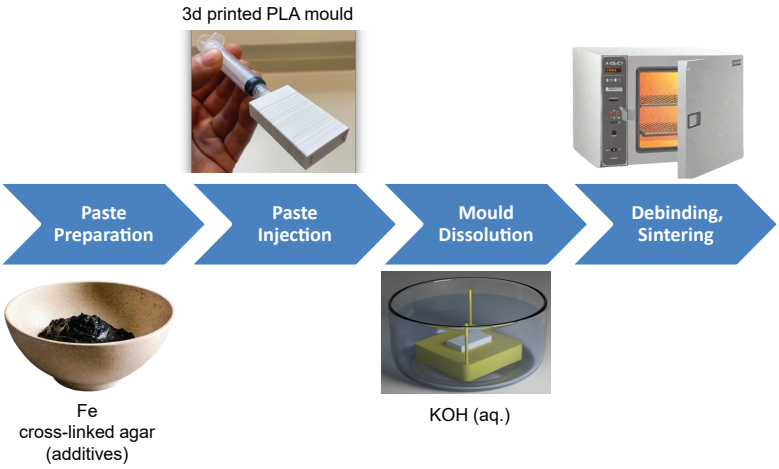

Figure 4.1: Manufacturing procedure for indirectly 3D-printed iron electrodes using a sodium tetraborate cross-linked agar binder. For a detailed description of the manufacturing procedure we refer to the Appendix C.

Water-based agar binder systems employed in metal injection molding (MIM) provide sufficient mechanical strength of the green part and can be burnt out in a reductive atmosphere such as H_2/Ar mixtures under exclusion of oxygen [16, 17]. As a result, the debinding step can be integrated with sintering, so that manufacturing time is significantly reduced. Agar based binder systems consist of agar, a water-soluble polysaccharide derived from algae, and a gel strength enhancing additive such as sodium borate dissolved in water [18, 19]. To prepare the agar binder, agar (5 wt% of final binder) was first dissolved in demineralized water at 90°C under constant stirring. Sodium borate (0.5 wt% of final binder) dissolved in water was then added to the fully mixed agar-water solution. At temperatures above the gel point, preferably in the range of 80 to 95°C [18], the binder forms a gel of decreased viscosity that allows for the mixing with iron powder to a paste that can be injected into the mold. We chose carbonyl iron powder specifically for its high purity that has been shown to increase charging efficiency in sintered iron electrodes [20–22]. Typically, the metal loading in MIM with similar binder systems is as high as 92 wt%

in order to yield dense parts of high mechanical stability [17]. We adjusted the iron loading in the paste to 60 wt% which allows for manual injection with a syringe and yields sintered electrodes with porosities ranging from 53 % to 58 % (see Appendix C.3). Also, electrodes were prepared with the addition of Super P conductive Carbon Black (1.81 wt% w.r.t. paste mass) into the paste. In order to maintain good flowability, the iron content of those pastes was reduced to 55 wt%, the balance consisting of the sodium borate enhanced binder. For the latter, the contents of agar and sodium borate were reduced to 3 wt% and 0.3 wt%, respectively. Following injection, the filled mold is cooled to room temperature at which the binder solidifies. We find that in the following step of dissolving the mold material in 30 wt% KOH (aq.) at 40°C over 15 hours, the agar binder softens but does not cause the disintegration of the green part. After mold dissolution, the green part is rinsed in demineralized water at room temperature to remove KOH (aq.) after which it is structurally stable enough to be handled. Before debinding and sintering, the electrode green parts must be dried to prevent damage caused by water vapor escaping from the structure. To this end, the green parts were first immersed in acetone for 5 minutes and then dried in air. This solvent-exchange drying procedure was repeated 3 times to ensure sufficient moisture removal. Debinding and sintering were conducted in a tube oven with a flow of 150 ml/min of a 5 % / 95 % H_2/Ar mixture. For debinding, the green part was first heated to 300 °C at a heating rate of 5 °C/min followed by a holding time of 1 h. In the following sintering step, the temperature was increased to 800 °C at a heating rate of 1 °C/min and a subsequent holding time of 2 h. The iron electrode containing the carbon additive was sintered at a reduced temperature of 750 °C in order to mitigate carbon reduction. Finally, the tube oven was cooled down back to room temperature at a cooling rate of 5 °C/min.

The porosity was measured by immersing the electrodes for 5 minutes in isopropanol as described by Yang et al. [20]. Following immersion, excess isopropanol on the electrode surface was blown off and the electrode was weighed. The pore volume was then calculated from the mass uptake and density of isopropanol. In order to account for the electrode channels, the porosity was not calculated via the ratio of pore volume to geometric electrode volume but rather via the volume of iron determined from the

electrode mass and density of iron[1]. The procedure described above results in mechanically stable iron electrodes with porosities ranging from 53 % to 58 %.

4.3. Results and discussion

4.3.1. Impact of electrode void fraction and channel size

In Chapters 2 and 3 we demonstrated the benefits of open 3D electrode structures for battery and oxygen evolution performance in nickel electrodes. However, we found that these benefits must be weighed against the reduction in electrochemically active surface area and battery capacity under consideration of the target current density and energy storage capacity. We defined the void fraction Θ as the ratio of the channel volume to the total electrode volume as a measure of how open an electrode geometry is. In order to understand how this void fraction affects electrolysis and battery performance of 3D iron electrodes, we prepared four electrodes with increasing channel dimensions while maintaining the same number of channels in x, y and z-dimension. We refer to these in order of ascending void fraction as "3D-M1", "3D-M2" and "3D-M3". An electrode of conventional geometry with no channels ($\Theta = 0$), referred to as "Non-3D", served as a control (Figure 4.2).

Electrode formation and overcharging

Iron electrodes initially require numerous charge-discharge cycles during which the discharge capacity increases gradually and eventually stabilizes. This process is commonly referred to as "formation", where the repeated conversion of iron to iron (II) hydroxide and vice versa results in changes in surface morphology, an increase in electrochemically active surface area and electrical conductivity while also removing impurities from the iron [23–25]. Typically, iron electrodes are formed by the manufacturer prior to shipment. Therefore, reducing the number and the duration of formation cycles has the potential to reduce battery costs by increasing production output and/or reducing capital investment for the required equipment.

[1] Analogous to the technique described in Appendix B.3.

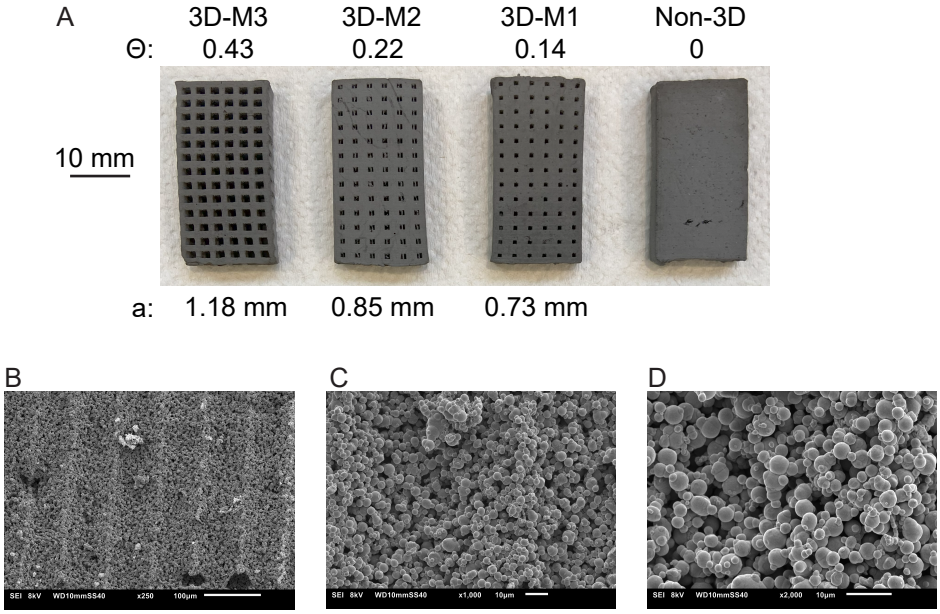

Figure 4.2: (A) SEM images of tested electrode geometries with varying void fraction Θ and channel width a. (B) SEM images of the Non-3D electrode at x250, x1000 and x2000 magnification.

Unlike conventional iron electrodes employed in batteries, where overcharging and the hydrogen evolution reaction (HER) are avoided, the HER is an integral part of the operation of the here discussed hybrid battery and electrolysis electrodes. However, it was not known if the as prepared electrodes would allow for industrially relevant HER current densities up to 200 mA/cm^2 or above, as reached in noble metal free alkaline electrolysers, and still maintain their mechanical integrity and battery functionality. In particular, at these high current densities, the formation of bubbles in small pores on the scale of micrometers and below can result in significant capillary pressures contributing to mechanical deterioration of the surrounding electrode structure [26–28]. For this reason, prior to formation, we subjected the electrodes to HER current densities as high as 1090 mA/cm^2 via linear sweep voltammetry (Figure C.2). Even though these HER current densities are significantly higher than intended for the

battolyser™, this approach allows for the fast assessment of electrode composition and sintering conditions with regard to mechanical stability and capacity utilization following high current density HER. Given that formation cycling alone takes around 14 days, this method significantly accelerates electrode screening.

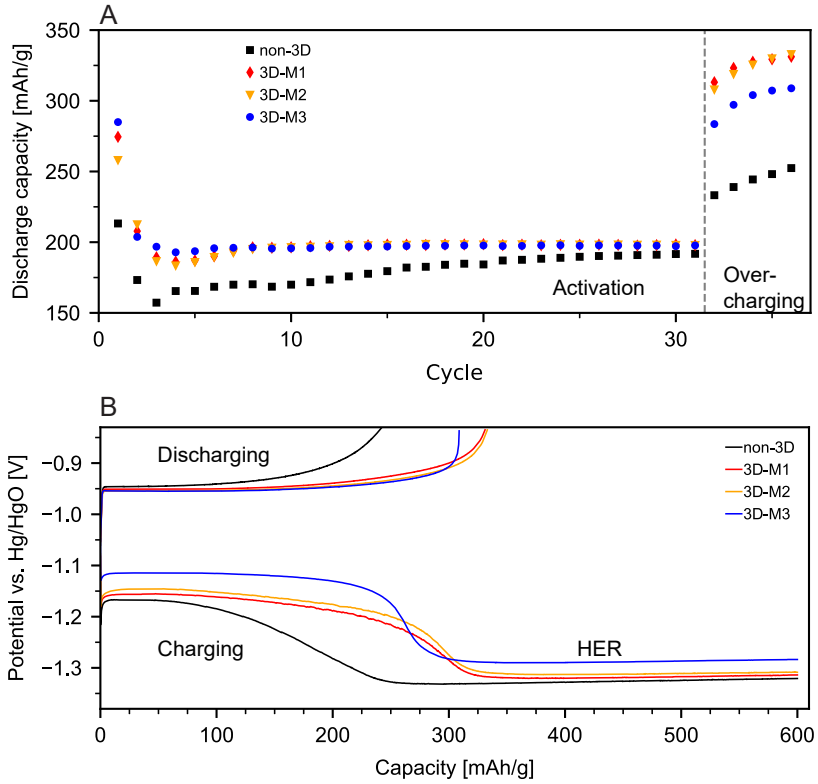

Figure 4.3: Electrode activation followed by overcharging of iron electrodes with different void fraction and channel width. The charge and discharge rates for activation and overcharging were 100 mA/g and 20 mA/g, respectively. For overcharging, the charge insertion was increased to 600 mAh/g from 200 mAh/g during activation.

The changes in discharge capacity over the course of formation cycling are shown in Figure 4.3 A. Compared to the Non-3D electrode, we observe

a significantly higher discharge capacity for all 3D electrodes in the first discharge cycle following linear sweep voltammetry. The electrode with the largest channel volume (3D-M3) exhibits a discharge capacity of 285 mAh/g which constitutes a 34 % increase in material utilization over the Non-3D electrode (213 mAh/g). For all electrodes, the discharge capacity decreases in the subsequent 3 cycles before increasing again. This was expected since the as prepared electrodes consisted of fully reduced iron that can discharge initially to capacities above the recharged capacity of 200 mAh/g of the following cycles. Interestingly, the discharge capacity in the second cycle of the 3D electrodes was still higher than the recharged 200 mAh/g. If iron in excess of the recharged capacity becomes accessible, both the recharged and the newly accessible iron are discharged. In principle, this could continue until the inserted charge is not sufficient to access more iron.

Remarkably, the discharge capacities were significantly higher for the 3D electrodes and stabilized after only 7 formation cycles. The charging efficiency describes how much of the inserted charge goes towards the charging reaction rather than HER and is defined here as the ratio of discharge capacity to inserted capacity. Here, we report charging efficiencies of around 99 % for the 3D electrodes after stable capacities are achieved. The Non-3D electrode, on the other hand, requires approximately 28 formation cycles to stabilize at charging efficiencies of around 96 %. For reference, Yang et al. [20] reported charging efficiencies of 96 % for sintered carbonyl iron electrodes. However, the reported electrodes were 2 mm thick and discharged at about half the discharge rate ($\sim$ 10 mA/g) compared to the 4.7 mm (Non-3D) thick electrodes described in this work. In addition, a direct comparison is difficult as the authors added sodium sulfide to the electrolyte, which resulted in significantly improved discharge rate capability. In this work, no additives were added to the electrolyte. A minor difference is that we charged and discharged the electrodes from two sides, while Yang et al. only employed one counter electrode. While material utilization in thicker electrodes with low porosity is typically lower, this can be mitigated to a limited extent by (dis)charging from both sides. Such an electrode configuration is also more typical in batteries consisting of multiple cells connected in parallel. However, for highly porous electrodes at thicknesses and current densities typical for iron electrodes, the effective ionic conductivity within the electrode is that high that the use

of one or two counter electrodes does not alter the capacity significantly.

Following formation cycling, the electrodes were overcharged with a charge insertion of 600 mAh/g as shown in Figure 4.3. Not only did this result in an increase in discharge capacity compared to the previous activation cycles, formation also appeared to continue as evidenced by the increase in discharge capacity with each cycle. Such a dependence of the discharge capacity on the charge insertion during formation cycling has also been reported by Weinrich et al. [29]. While overcharging results in gas evolution mostly at the front of the electrode (Chapters 2 and 3), it also allows for concurrent charging, and thus formation, of deeper-lying active material. In conventional iron-based batteries, HER constitutes a safety hazard as hydrogen can mix with oxygen generated at the anode to form an explosive mixture. In a battery-electrolyser as discussed in this work, however, the gases generated at each electrode are separated by a diaphragm or membrane to prevent mixing, and extracted continuously. As a result, the charged electrodes can be safely overcharged during electrolysis for as long as electricity prices are low (e.g. during oversupply of renewables) while the active material is (trickle) charged further. This ability to safely overcharge therefore has the added benefit of increasing material utilization, i.e. discharge capacity. Notably, the electrodes 3D-M1 and 3D-M2 exhibit a maximum discharge capacity of around 333 mAh/g compared to 252 mAh/g for the Non-3D electrode. This constitutes an increase in material utilization of 32 %. Electrode 3D-M3, the electrode with the highest void fraction, yields a lower improvement in material utilization of around 23 % (303 mAh/g). Interestingly, while a higher void fraction does not appear to correlate with an increase in material utilization, it is associated with a reduction in charging and HER overpotentials (Figure 4.3 B). Thus, compared to the Non-3D electrode, electrode 3D-M3 exhibits the largest reduction in average charging and HER overpotentials with 79 mV and 40 mV, respectively, followed by 3D-M2 and 3D-M1.

As discussed in Chapters 2 and 3, the observed decrease in overpotential can be explained with the improved effective ionic conductivity provided by the channels within a 3D electrode. This results in a more homogeneous distribution of current across the active material which in turn reduces polarization overpotential and improves charging efficiency. Since a larger void fraction, i.e. larger total channel volume, increases

the effective ionic conductivity, we had expected electrode 3D-M3 to yield the highest value for material utilization (Figure 2.11). The observation that the electrodes 3D-M1 and 3D-M2 with lower void fraction exhibited higher material utilization led us to the hypothesis that the void fraction of the 3D-structure could also affect the electrical conductivity during discharging. This could result in the lower than expected discharge capacities measured for the highest void fraction (3D-M3).

Discharge rate capability

One of the biggest challenges in the development of iron electrodes is the loss in discharge capacity and rechargeability as the result of too high discharge rates. There are two main reasons thought to be responsible for this deactivation behavior. Firstly, the discharge product, $Fe(OH)_2$, is electrically insulating and forms a non-conductive passivating layer which inhibits to which degree the iron particles can be discharged and recharged [20, 22, 30, 31]. Secondly, the molar volume of $Fe(OH)_2$ is approximately 3.72 times higher than that of Fe [14]. Consequently, $Fe(OH)_2$ expands into the pore volume and reduces the porosity (Figure 4.5 B). This reduces or even cuts off electrolyte access to interior parts of the electrode resulting in a decrease in ionic conductivity [20]. Especially for thick electrodes as discussed in this work ($\sim$ 4.5mm), this can result in little to no utilization of active material located deeper within the electrode. Therefore, iron electrodes require a sufficiently high initial porosity to compensate for the high molar volume of $Fe(OH)_2$. Yang et al. [20] calculated that an initial porosity of 73 % would be required to reach the theoretical limit of 962 mAh/g for the full conversion of Fe to $Fe(OH)_2$. However, the authors note that due to the low electrical conductivity of $Fe(OH)_2$, some Fe is required for rechargeability. Assuming that 20 vol% of iron is not discharged, they determine an initial porosity of 61 % resulting in a maximum discharge capacity of around 550 mAh/g. The porosities of the electrodes discussed in this work ranged from 53 % to 58 %.

In order to mitigate the described effects of passivation and porosity reduction and maximize material utilization, the discharge current should be distributed as homogeneously as possible across the electrode thickness. As described in Chapter 2, this is the case for a high effective ionic conductivity within the electrode, e.g. low electrode thickness and high porosity,

and/or a sufficiently low current density. If the discharge current is chosen too high for a given effective ionic conductivity, the current distribution shifts farther to the front of the electrode with the effect of locally higher current densities. Not only does this increase activation overpotentials, it can also result in local overdischarging beyond the limits for electrical conductivity and volume expansion that would still allow for effective recharging. In addition, the formation of a non-conductive layer with little porosity at the front of the electrode would prevent further discharging of the rest of the electrode (Figure 4.5 A, B). While this deactivation limits the capacity that can be extracted for a given discharge rate, it also impedes rechargeability at higher charge rates leading to an effectively inert fraction of active material. This in turn inhibits the following discharge cycle leading to further deactivation. Thus, deactivation can progress over numerous cycles at a rate depending mostly on the discharge current.

Figure 4.4 A shows the impact of the weight-specific discharge rate on the weight-specific discharge capacity, i.e. material utilization. As a result of the deactivation described above, as well as increased ionic and activation overpotentials, the discharge capacity that can be extracted before the cut-off voltage is reached decreases significantly with an increase in discharge rate. For sufficiently high discharge rates, only a fraction close to the electrode surface can be discharged resulting in close to zero discharge capacity. In order to prevent deactivation from high discharge rates affecting the subsequent cycles, the electrodes were discharged at a low discharge rate of 10 mA/g after initially reaching the discharge voltage limit at the high rates tested. This proved to be an effective way to mitigate deactivation as shown in Figure C.3. All 3D electrodes exhibited improved discharge rate capability compared to the Non-3D electrode. At a discharge rate of 50 mA/g, the Non-3D electrode provided effectively no capacity, while electrode 3D-M2 could discharge 263 mAh/g followed by 3D-M1 and 3D-M3 with 172 mAh/g and 121 mAh/g, respectively. Furthermore, electrode 3D-M2 could be discharged at discharge rates as high as 80 mA/g, which constitutes an increase of 60 % compared to the Non-3D electrode.

An open 3D geometry benefits the discharge rate capability in two ways: Firstly, as shown in Chapters 2 and 3, the increased effective ionic conductivity provided by the channels results in a more homogeneous current distribution during discharging and recharging. As discussed above,

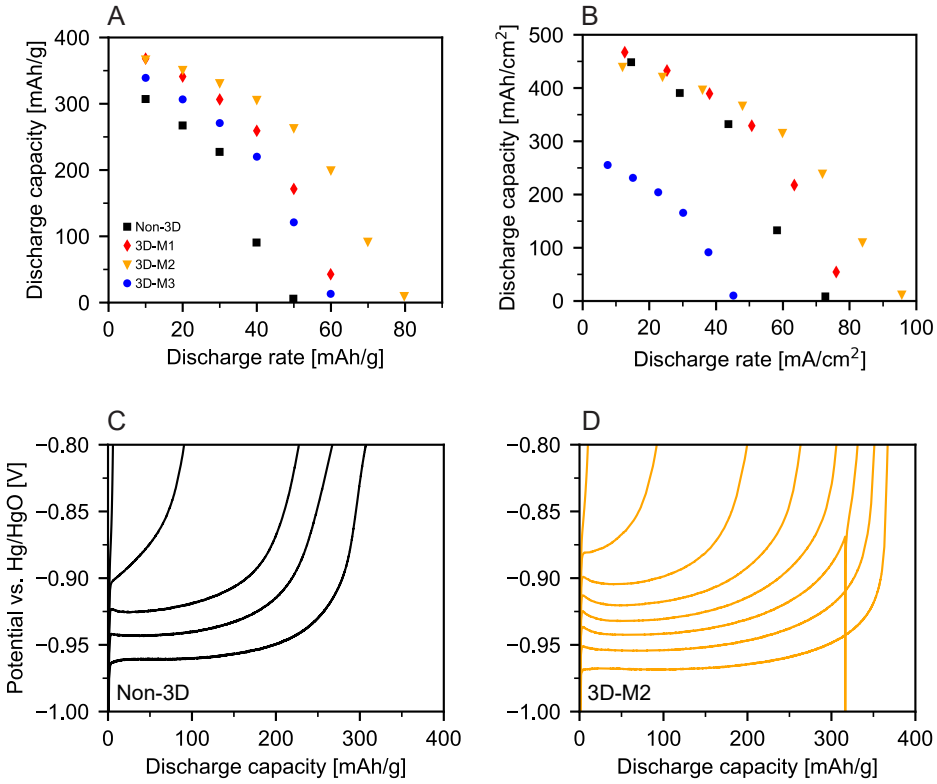

Figure 4.4: Impact of discharge rate on discharge capacity for iron electrodes with different void fraction and channel width. The electrodes were charged to 600 mAh/g at a rate of 100 mA/g. Discharge rates were increased in each cycle followed by a slow discharge at 10 mA/g to prevent passivation. The discharge capacities are shown with respect to the mass of iron (A) and the superficial surface area (B). The discharge potentials are shown for the Non-3D electrode (C) and 3D-M2 electrode (D).

this is expected to mitigate electrode deactivation. Secondly, once the active material close to the front is fully discharged and decreases in porosity, the electrode channels function as a bypass for electrolyte to access material farther to the back (Figure 4.5 C). Thus, the channel volume can compensate for the decrease in porosity during discharging. Based on this explanation, one could have expected the rate capability to improve with

higher void fractions. However, while electrode 3D-M2 ($\Theta = 0.22$) outperforms electrode 3D-M1 ($\Theta = 0.14$), electrode 3D-M3 with the highest void fraction ($\Theta = 0.43$) exhibits the lowest discharge rate capability of the tested 3D electrodes. Consequently, the optimal void fraction with respect to material utilization appears to be in the range $0.14 < \Theta < 0.43$.

To explain these observations, consider the basic 3D electrode geometry shown in Figure 4.5 C, D. The 3D electrode consists of periodically repeating beams in x- and y-direction and columns in z-direction. Increasing the void fraction, i.e. the channel dimensions, reduces the cross-sectional area of said beams and columns. This has two effects on the discharging and recharging behavior: Firstly, the combination of increased electrolyte availability and thinner electrode structures results in more extensive conversion to $Fe(OH)_2$ in the first discharge cycles during formation. However, as discussed above, too extensive discharging negatively affects rechargeability due to the low electrical conductivity of $Fe(OH)_2$. Secondly, the reduced cross-sectional area of the beams and columns increases the electrical resistance of the already discharged material further. Since the current collector is welded to the side of the electrode, all electrical current must pass through the reduced cross-section of the y-beams which constitutes an electron bottleneck (Figure 4.5 C, D). In contrast, the path of electrical current to the current collector in a Non-3D electrode is omnidirectional, i.e. not limited to the cross-section of beams and columns in a 3D electrode. Thus, areas of low electrical conductivity can be circumvented. The combination of excessive discharge and increased electrical resistance could result in a fraction of active material being insulated permanently during the process of formation. Viewing the channels as a macroscopic porosity, we can draw an analogy to the microscopic porosity of iron electrodes. As described by Yang et al. [20], a high porosity, i.e. ionic conductivity, in combination with narrow sintering necks between iron particles could result in extensive discharging and prohibit recharging of these particles. Indeed, electrode 3D-M3 exhibited the highest material utilization of all tested electrodes in the first discharge cycles of formation. Following formation, however, material utilization was lower compared to the other 3D electrodes when overcharged with a high charge insertion of 600 mAh/g (Figure 4.3 A).

In literature on the development of iron electrodes, discharge capacities are typically reported relative to the weight of iron in the electrode

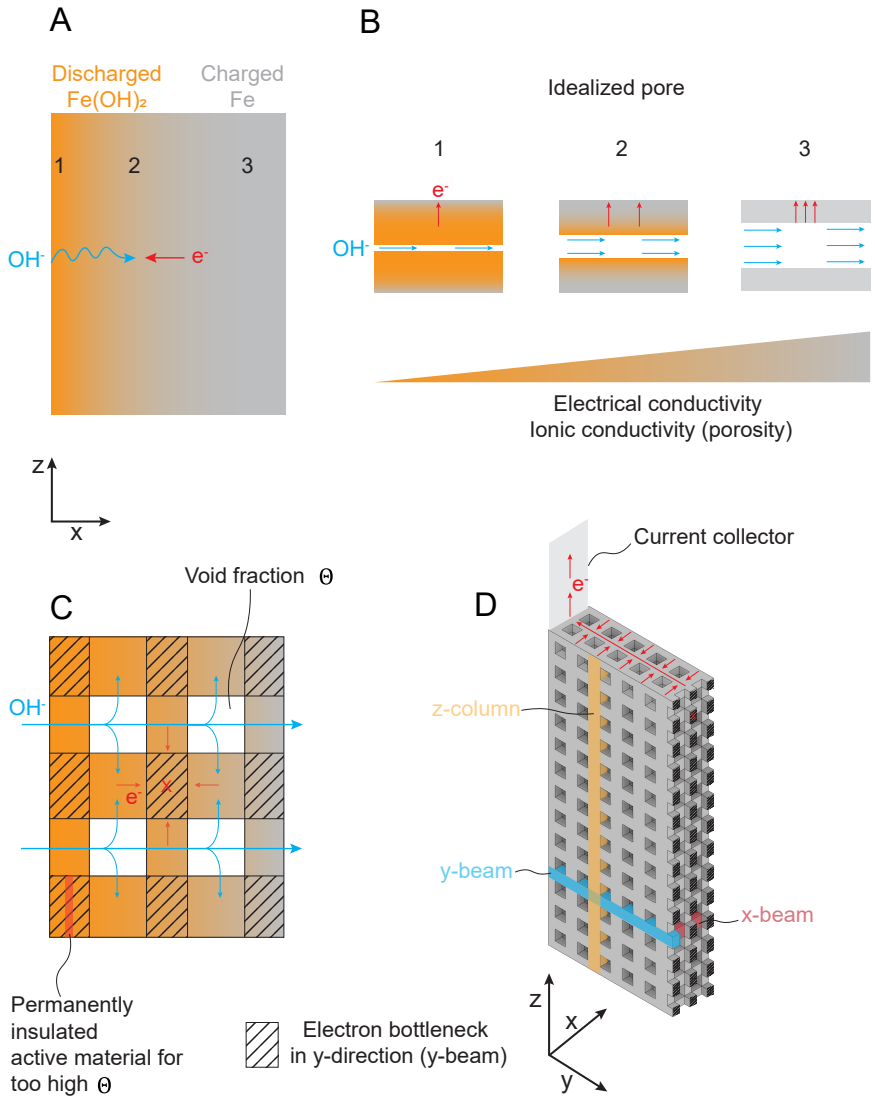

Figure 4.5: Illustration of the impact of state of charge and electrode geometry on the ionic and electronic conductivity during discharge in a 3D electrode. (A) The front of the electrode discharges first resulting in a gradient in Fe and $Fe(OH)_2$ composition. (B) Towards the front of the electrode, where the state of charge is lower (more $Fe(OH)_2$), both the porosity and electronic conductivity are reduced. (C) The open channel geometry increases electrolyte accessibility but also reduces the cross-section and number of pathways through which electrons are conducted (electron bottlenecks). Areas close to the electrode surface can overdischarge with reduced reversibility. (D) Illustration of possible electron conduction pathways along the x-, y- and z-beams of a 3D electrode.

(mAh/g) [20, 21, 24, 29, 32–34]. While this constitutes a necessary metric to assess material utilization, the capacity per geometric electrode area (width x height, mAh/cm^2) is essential for cell and stack development. Batteries utilizing electrodes with a large area-specific capacity require fewer electrochemically inactive components such as current collectors and separators to reach a target system capacity which results in a decrease in material and assembly costs. Specifically in the case of the integrated battery-electrolyser or battolyser™, where the half-cells are separated by a membrane to separate oxygen and hydrogen, this leads to a reduction in the required number of cells, membrane area and associated material and maintenance costs. Furthermore, the capacity of the iron electrode is limiting in iron-air batteries, as there is principally no limit as to how much oxygen can be reduced at the air electrode. Iron electrodes with higher area-specific capacities would decrease the number of air electrodes and separator membranes, which typically require expensive catalysts based on precious metals such as Pd/C [35]. In order to achieve high area-specific capacities, both a high material utilization and a large amount of iron per geometric surface area are required. However, as shown in Chapter 2, design strategies to increase the amount of iron, e.g. by increasing electrode thickness and reducing porosity/void fraction, decrease the effective ionic conductivity of the electrode and thus reduce material utilization. Iron that cannot be utilized not only increases material costs, but also costs for the cell and stack as these are overdimensioned to accommodate thicker electrodes. Therefore, the design of electrodes requires the balance of material utilization and the amount of iron per cm^2 with respect to the target charge and discharge current densities. For the integrated battery-electrolyser, the target also depends on what capacity the nickel electrode can provide. As described previously in Chapters 2 and 3, a capacity of 200 mAh/cm^2 appears to be a feasible target for the 3D nickel electrodes at discharge rates relevant for stationary battery storage in a renewable energy future (C/4, i.e. 50 mA/cm^2).

Figure 4.4 B shows the discharge rate capability of the tested 3D electrodes and Non-3D electrode with respect to the geometric surface area. Even though electrode 3D-M3 exhibited a higher material utilization than the Non-3D electrode, the large channels reduce the mass of iron to an extent that resulted in significantly lower area-specific capacities. For discharge current densities up to around 50 mA/cm^2, the 3D electrodes

3D-M1 and 3D-M2 performed similarly to the Non-3D electrode. For higher current densities, however, electrode 3D-M2 exhibited the highest discharge rate capability, followed by 3D-M1 and the Non-3D electrode. While no capacity could be extracted from the Non-3D electrode at current densities of approximately 72 mA/cm^2, 3D-M1 and 3D-M2 could discharge 54 mAh/cm^2 and 239 mAh/cm^2, respectively. Therefore, 3D-M2 is a good example for an electrode with a sufficiently high void fraction to allow for high material utilization without compromising area-specific capacity significantly. However, we note that for the use as integrated battery-electrolyser electrodes, the void fraction and channel dimensions must also be chosen under consideration of effective bubble removal [12].

Charge rate capability and electrolysis

During charging, the battery charging reaction (Reaction 4.1) and hydrogen evolution (Reaction 4.2) occur in parallel. Especially at elevated overpotentials, this reduces the charging efficiency and increases the time to fully charge the electrode. For a battery-electrolyser, concurrent hydrogen evolution is less of a disadvantage as hydrogen is a product. In addition, as charging is followed by electrolysis/overcharging, charge insertion is significantly higher compared to conventional nickel-iron batteries. As a result, a high state of charge can still be achieved [29, 36]. However, a high charging efficiency is still advantageous for a battery-electrolyser if the battery function is used to compensate for short-term fluctuations in the energy supply and demand (e.g. peak shaving). In this case, the battery-electrolyser should be able to store as much energy as possible on a short timescale, i.e. at high charge rates, in order to discharge it back into the grid shortly after.

As discussed in Chapters 2 and 3, the charging efficiency at high charge rates is not only reduced due to the proximity of the respective equilibrium potentials of the charging reaction and hydrogen evolution, but also due to inhomogeneous charging across the electrode thickness. As a consequence of the ionic resistance of the electrolyte, higher current densities shift the charging and hydrogen evolution reaction closer to the front of the electrode. Thus, active material at the front is charged first and transitions to hydrogen evolution before the rest of the electrode is charged. Especially in electrodes with a low effective ionic conductivity, this can result in a

significant fraction of the applied current going towards hydrogen evolution at the front of the electrode, while the remaining active material is only trickle charged and utilized poorly.

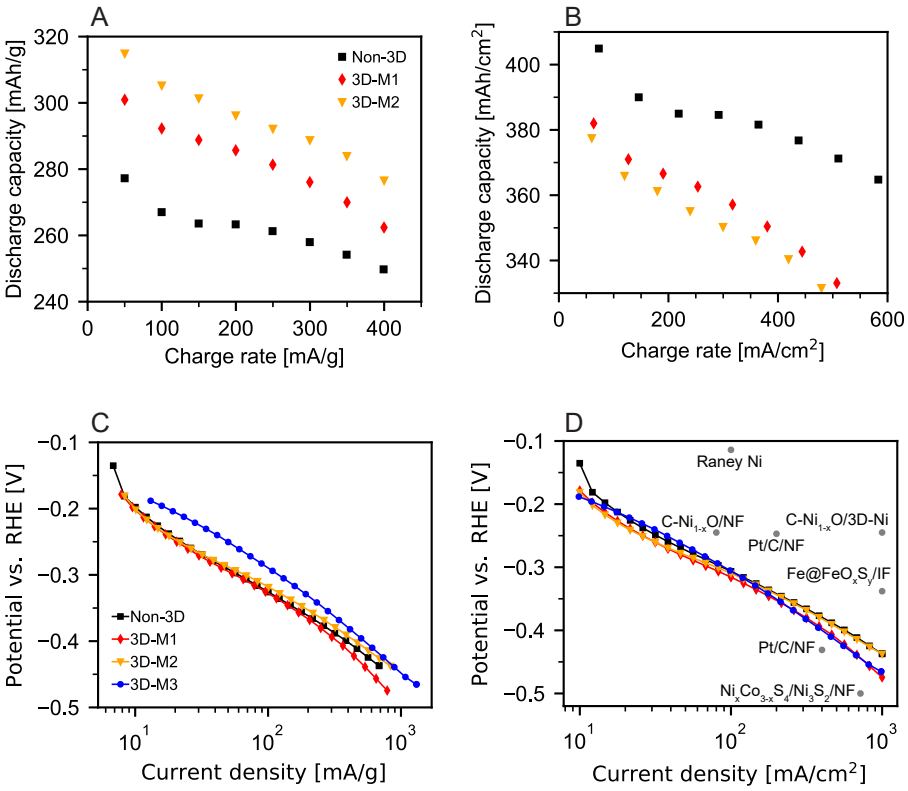

Figure 4.6: (A, B) Impact of charge rate on discharge capacity. The electrodes were charged to 600 mAh/g at varying charge rates followed by a discharge at 20 mA/g. Electrode 3D-M3 is not shown as it deactivated fully following the previous discharge rate experiments.(C, D) Potential of fully charged electrodes at varying electrolysis current densities. Prior to electrolysis, the electrodes were charged to 600 mAh/g at 200 mA/g. Results are shown with respect to the electrode weight (A, C) and superficial surface area (B, D). (D) Examples of overpotentials at room temperature for HER catalysts such as Raney nickel (Ni50%Al) in 1 M NaOH [37], Fe@FeO_xS_y core-shell-type nanoparticles on Fe-foam (IF) in 1 M KOH [38], C – $Ni_{1-x}O$ loaded on a 3D printed nickel electrode and nickel foam (NF) in 1 M KOH [12], $Ni_xCo_{3-x}S_4/Ni_3S_2$ and 20 wt% Pt/C + Nafion® on nickel foam (NF) in 1 M KOH [39].

Figures 4.6 A and B show the impact of the charge rate on the discharge capacity for a charge insertion of 600 mAh/g. Here, a reduction in discharge capacity is equivalent with an increase in hydrogen evolution, i.e. a reduction in battery charging efficiency, during charging. Electrode 3D-M3 is not shown as it deactivated in the cycles following the discharge rate capability experiments (Figure 4.4). It is not known if this was caused by the high discharge rates, or if it was an accumulative effect from the previous cycles (Figure C.6 B). In terms of the iron mass, the discharge capacity increases with the electrode void fraction for all tested charge current densities (Figure 4.6 A). As discussed for the nickel electrode in Chapters 2 and 3, this increased material utilisation is likely the result of the higher effective ionic conductivity provided by the electrode channels. However, as the addition of channels reduces the amount of active material per superficial electrode area, the Non-3D electrode still exhibits the highest area-specific discharge capacities (Figure 4.6 B). Remarkably, all tested electrodes exhibit only a low decrease in discharge capacity with higher charge rates. Increasing the charge rate by a factor of 8 from 50 mA/g to 400 mA/g, results only in a 10 %, 13 % and 12 % decrease in discharge capacity for the Non-3D, 3D-M1 and 3D-M2 electrode, respectively.

After charging, the iron electrode is used fully for hydrogen evolution. A key factor in the energy efficiency of this reaction is the electrochemically active surface area over which the applied electrolysis current is distributed. There are two reasons why 3D electrodes with a larger void fraction and channel size could reduce the HER overpotential. Firstly, the shift in the current distribution to the front of the electrode, caused by a low ionic conductivity within the electrode and/or high electrolysis currents, results in a lower utilisation of the electrochemically available surface area (ECSA). Thus, the local electrolysis current density increases, resulting in higher activation overpotential (Chapter 2). Secondly, bubbles covering the electrode surface can reduce the ECSA further and increase electrolyte resistance which causes an additional increase in overpotential [40]. Larger and ordered channels in 3D electrodes have been shown to enhance bubble removal and thus reduce bubble-induced overpotentials compared to a stochastically structured nickel foam [12]. As the electrodes discussed here were all manufactured the same way and cycled comparably, we can assume that the ECSA per g of iron is similar for the electrodes discussed above. The overpotential at a weight-specific current

can therefore indicate the utilisation of the electrode's ECSA (Figure 4.6 C, D).

As the electrode channels increase the ionic conductivity within the electrode resulting in an increased utilisation of the electrode's ECSA, i.e. a more homogeneous current distribution, one would expect the overpotential to decrease with the electrode void fraction when the electrolysis current is normalized with respect to the weight of iron. As shown in Figure 4.6, electrode 3D-M3 with the highest void fraction does indeed exhibit the lowest overpotentials up to around 800 mA/g above which the overpotential is on par with that of 3D-M2 and close to that of the Non-3D electrode. Interestingly, the Non-3D, 3D-M1 and 3D-M2 electrodes perform similarly up to current densities of approximately 60 mA/g. For higher current densities, 3D-M2 exhibits a lower overpotential. Unexpectedly, overpotentials for electrode 3D-M1 are higher compared to those of the Non-3D electrode at current densities exceeding around 200 mA/g. Thus, there is no apparent correlation between higher void fractions, i.e. larger channel dimensions, and a reduction in HER overpotential for these higher current densities. This could be explained by the comparably high porosities of the electrodes discussed here (53 % - 58%). As shown in Chapter 2, 3D electrodes with a high void fraction are most beneficial when the porosity is low as is the case in nickel electrodes where the pores are filled with the active material.

The size of an electrolyser, and thus the capital cost of the stack, are largely determined by the maximum operating current density with respect to the superficial electrode area. As discussed above in the context of the battery capacity, the inclusion of channels results in the removal of active material, i.e. ECSA per cm^2 of superficial electrode area. This reduction in ECSA must be weighed against the higher utilisation that electrode channels can provide by increasing the effective ionic conductivity. In Chapter 2, we develop a method to calculate the optimal void fraction that minimizes the electrode overpotential for a given area-specific current density. Generally, for a given porosity and electrode thickness, the integration of channels is only beneficial at high area-specific current densities (Figure 2.5).

However, our data show that for current densities over 100 mA/cm^2, the Non-3D electrode performs similarly to 3D-M2 but clearly outperforms

electrodes 3D-M1 and 3D-M3 (Figure 4.6 D). Consequently, for the case of hybrid iron battery-electrolyser electrodes, the integration of channels appears to offer no benefit for reducing overpotentials when the current density is viewed with respect to the superficial electrode area. However, we note that the channel dimensions are likely to have a higher impact in cell configurations with a more confined electrolyte volume such as in a flow-through electrolyser (Chapter 6). In such a cell, efficient bubble removal provided by the ordered channels is essential in order to prevent an increase in cell resistance [41, 42]. Here, a larger void fraction, i.e. larger channels, could improve electrolyte flow, facilitate bubble removal and thus reduce the volume fraction of bubbles. That said, electrode 3D-M3 deactivated shortly after the discharge rate capability experiments and exhibited no discharge capacity. As discussed in more detail in Section 4.3.3, this could be the result of structural damage affecting the electrical conductivity. While electrolysis is still possible with a deactivated electrode, such structural damage is likely to also increase overpotentials. Linear sweep voltammetry prior to cycling, showed that electrode 3D-M3 outperformed the Non-3D electrode at current densities over around 375 mA/cm^2 (Figure C.2 A).

Due to its high activity, Pt/C is often used as a benchmark for newly developed HER electrocatalysts. Remarkably, at a current density of around 400 mA/cm^2, our electrodes Non-3D and 3D-M2 operate at an approximately 50 mV lower overpotential (380 mV vs. 430 mV) compared to an electrode with 20 wt% Pt/C loaded on nickel foam as shown by Wu et al. [39][2]. In recent years, significant progress has been made in the development of novel and efficient HER catalysts for alkaline electrolysis [43]. While numerous electrodes have been shown to operate at lower HER overpotential compared to the electrodes discussed in this work [12, 37, 38](Figure 4.6 D), we point out that these have been developed specifically for electrolysis and have no battery functionality.

Iron and nickel have similar exchange current densities for HER, which indicates that their activity for HER is comparable [44, 45]. However, the use of nickel as HER catalyst is influenced by the formation of a nickel hydride phase during prolonged electrolysis at sufficient overpotential [45]. This hydride formation results in increasing overpotentials and reduced

[2] 1 M KOH (aq.) and 0.56 mg/cm^2 catalyst loading.

HER activity. One way to counteract this effect, has been to use Fe surface coating of the Ni, which showed the suppression of the NiH formation and sustained HER efficiency [46]. This may illustrate that having an Fe surface as the active catalyst is beneficial compared to a pure Ni electrocatalyst.

In principle, iron electrodes could be coated with efficient HER catalysts such as the one developed by Zou et al. [38]. However, an increase in HER activity should not come at a significant cost to the charging efficiency. Furthermore, such a catalyst would have to be able to withstand repeated cycling between the more positive potentials during discharge and negative potentials during recharge and HER. For instance, highly active catalysts for HER such as Raney nickel [37] are known to degrade at such intermittent operation resulting in a decrease in activity [47]. Especially in a renewable energy future, intermittent operation will be unavoidable, which poses a challenge for conventional alkaline electrolysers. Here we develop electrodes that are specifically meant to work intermittently, and in addition have a battery functionality.

4.3.2. Addition of carbon black

As discussed above, the low conductivity of $Fe(OH)_2$ in the discharged state is a limiting factor in electrode utilisation. To mitigate this low conductivity, we added carbon black to a Non-3D electrode ($\sim$ 3.18 wt% w.r.t. the electrode weight). Carbon nanomaterials such as carbon black and acetylene black can form a conductive network that maintains the electrical conductivity between discharged particles and thus allows for increased material utilization as well as faster charge and discharge rates [20, 48–52].

Electrode formation and overcharging

Figure 4.8 A shows the discharge capacities for a Non-3D electrode with and without carbon black addition during formation and subsequent overcharging. The addition of carbon results in two initial discharge cycles with capacities of around 290 mAh/g, an increase of 36 % compared to the pure iron electrode. While the capacity of the pure iron electrode first decreases to below 165 mAh/g before slowly increasing again, the capacity

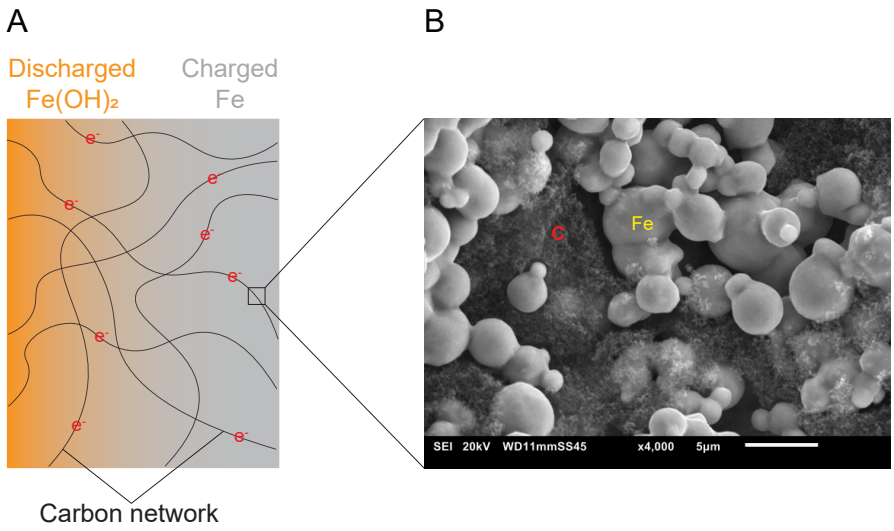

Figure 4.7: (A) Illustration of carbon black forming a conductive network embedded within the sintered iron structure. (B) SEM image at x4000 magnification of a sintered iron electrode containing carbon black.

of the electrode with added carbon stays above 200 mAh/g for the next 13 cycles after which it stabilizes at 198 mAh/g. Since the charge insertion is 200 mAh/g, this is equivalent to a charging efficiency of 99 % compared to 96 % observed for the pure iron electrode when stabilized after 28 formation cycles. We also see a discharge capacity above the recharged 200 mAh/g in the second cycle for the 3D electrodes (Figure 4.3 A). The fact that the Non-3D electrode with carbon maintains such high charging efficiencies above 100 % for 13 cycles indicates a more effective formation and more iron being activated compared to the pure iron electrodes discussed in this work. This is confirmed by overcharging with a charge insertion of 600 mAh/g which results in a discharge capacity of close to 500 mAh/g compared to 250 mAh/g for the pure iron Non-3D electrode (Figure 4.8). This is also substantially higher than values obtained for the best performing 3D electrode 3D-M2 (330 mAh/g) as shown in Figure 4.3.

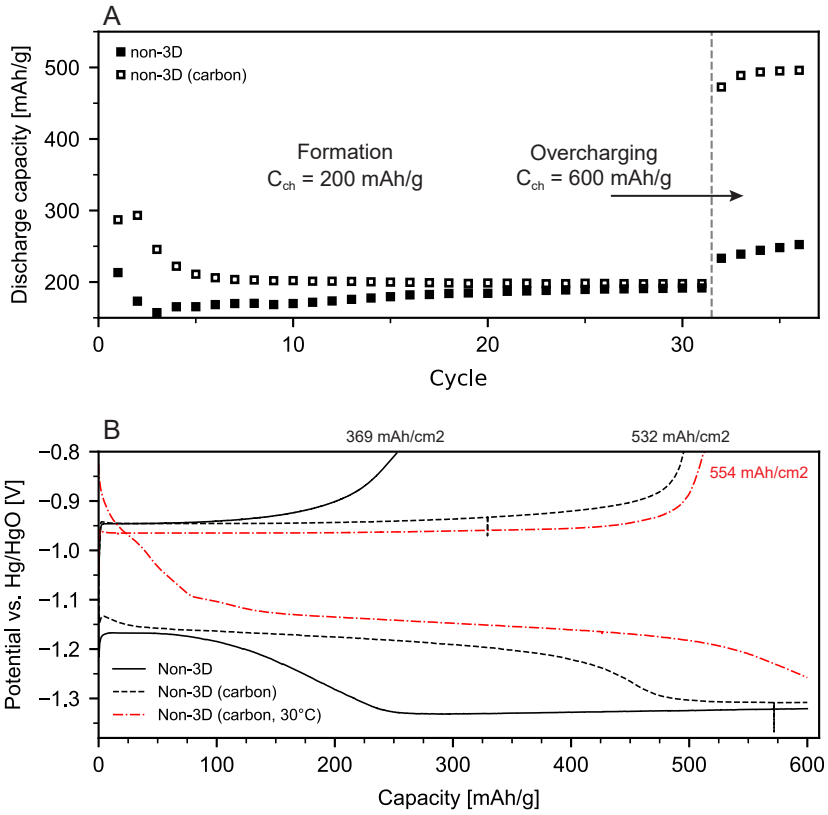

Figure 4.8: Impact of the addition of carbon black on electrode activation and overcharging. Electrodes were charged at 100 mA/g and discharged at 20 mA/g. Charge insertion (C_{ch}) was 200 mAh/g for formation and 600 mAh/g for overcharging. (A) Discharge capacity with respect to iron mass. (B) Electrode potential for the final cycle of overcharging at room temperature (~22 °C) and a cycle at 30 °C during rate capability testing of the electrode with carbon black addition (Figure 4.9).

Discharge rate capability

The addition of carbon black results in a significantly improved discharge rate capability. As shown in Figure 4.9 A, the pure iron electrode cannot be discharged effectively at discharge rates of 50 mA/g or higher. At the same discharge rate, the addition of carbon black results in a discharge

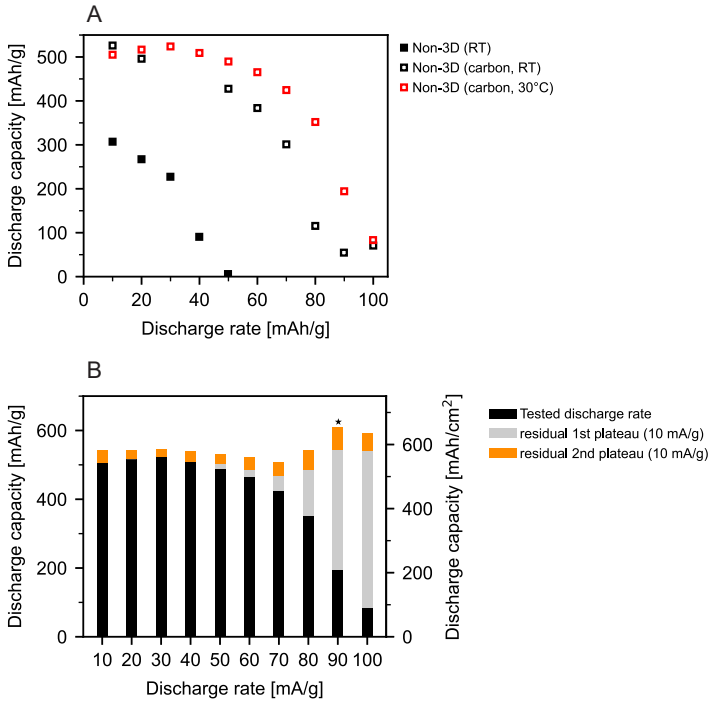

Figure 4.9: Impact of carbon addition and temperature on discharge rate capability. (A) Discharge capacity at varying discharge rates with respect to iron mass. (B) Discharge capacity at tested discharge rate and residual capacity obtained from a subsequent slow discharge at 10 mA/g at 30°C. ⋆ marks the cycle at which the maximum accumulative capacity of 607 mAh/g (651 mAh/cm^2, 1330 mAh/cm^3) was reached.

capacity of 428 mAh/g, which is equivalent to an area-specific capacity of 460 mAh/cm^2 at a corresponding current density of 54 mA/cm^2. In order to see if the rate capability can be improved even further, we repeated the experiment at 30 °C. An increase in temperature increases the electrolyte conductivity and facilitates the iron (dis)charge kinetics resulting in enhanced material utilization and decreased overpotentials [36, 53–55]. Here we report discharge capacities above 500 mAh/g (536 mAh/cm^2) up to discharge rates of 40 mA/g (43 mAh/cm^2) at 30 °C (Figure 4.9). Especially at higher discharge rates above 20 mA/g and up to 80 mA/g, we observe

an increasing benefit of the elevated temperature with respect to discharge capacity. For a discharge rate of 80 mA/g (86 mA/cm^2), the discharge capacity is increased by a factor of 3 to 352 mAh/g (377 mAh/cm^2).

In order to prevent deactivation, after each tested discharge rate, the electrode was discharged at a slow rate of 10 mA/g ($\sim$ 10.7 mA/cm^2) before recharging. Interestingly, at 30 °C and this low discharge rate, the discharge overpotential is decreased to such an extent that the electrode is partially discharged at the second plateau before the cut-off voltage of -0.8 V vs. Hg/HgO is reached (Figure C.4). Due to the more negative equilibrium potential of Reaction 4.3, we suspect that the observed plateau corresponds to the oxidation of $Fe(OH)_2$ to Fe_3O_4.

Figure 4.9 B depicts the accumulative capacity consisting of the discharge capacity at 30 °C for each tested discharge rate and the residual capacity of the following slow discharge at 10 mA/g. Here, we differentiate between the capacities obtained for the first and second discharge plateau. At a tested discharge rate of 90 mA/g (97 mA/cm^2), we measure the highest accumulative capacities of 540 mAh/g (590 mAh/cm^2) for the first discharge plateau and 607 mAh/g (652 mAh/cm^2) including the partial discharge at the second plateau. While discharging the second plateau results in higher discharge capacities, Lee et al. [56] have shown that the formation of a non-reactive layer of maghemite ($\gamma - Fe_2O_3$) results in capacity fading. For the use in a battery-electrolyser in combination with the nickel electrodes discussed in Chapter 3 ($\sim$ 140 mAh/cm^2), the presented electrodes provide a sufficiently high capacity without the second discharge step beyond $Fe(OH)_2$. Besides an expected improved electrode lifetime, limiting operation to the first discharge plateau also results in higher cell discharge voltages. Temperatures above 30 °C are likely to increase rate capability even further. For reference, iron-air batteries developed by the Swedish National Development Company (SNDC) were designed for operation at 40 °C and are stable up to 60 °C [54]. Our work shows that increasing the electrical conductivity by addition of carbon black in combination with elevated operating temperatures results in significantly improved rate capability and material utilization. Also, adding channels with optimized dimensions could improve rate capability even further (Figure 4.4).

4.3.3. Electrode stability

The cycling history and times of failure for all tested electrodes are shown in Figures C.5 to C.7. After around 50 cycles, and shortly after the discharge rate capability experiment, electrode 3D-M3 started deactivating and rapidly lost its entire discharge capacity. The Non-3D electrode and electrodes 3D-M1 and 3D-M2 first started deactivating following the charge rate capability and electrolysis experiments at around cycle 60. Moreover, the spot welded contacts detached from the Non-3D electrode with carbon black addition after 54 cycles. In addition, we observe pitting on the surface of all tested electrodes. This suggests that the electrodes sustain structural damage throughout cycling and electrolysis.

Such damage to the electrode structure could be caused by changes in electrode morphology [56] and/or hydrogen bubbles within the electrode pores. High capillary forces during the formation of the latter result in mechanical stress that can eventually lead to structural damage [26, 27]. According to the Young-Laplace equation, the pressure difference between the gas within a bubble, p_b, and the surrounding electrolyte, p_s, is given by:

$$p_b - p_s = \frac{2\gamma}{r} cos(\alpha) \tag{4.5}$$

where γ is the surface tension, r describes the radius of the bubble and α denotes the contact angle with the pore wall. The maximum size of a bubble is given by the pore radius. Prior to formation, the pore radius is in the order of 1 μm as shown in Figure 4.2. Further, we assume complete wetting, so that $\alpha = 0$. At ambient pressure ($p_s = 1$ bar) and a surface tension of 95.4 $\times 10^{-3}$ N/m [57] for 30 wt% KOH (aq.) at 25 °C Equation 4.5 yields a bubble pressure of 2.9 bar. Lee et al. [56] showed that iron particles fragment into nano-sized granules in the course of formation cycling. While this increases the electrochemically active surface and improves material utilization, the formation of nano-sized pores would also result in higher capillary pressures which could exacerbate structural damage to the electrode during bubble formation. For instance, a bubble with a 10 nm radius would have a gas pressure of around 192 bar.

We hypothesize that damages to the sintered electrode structure induced by bubble formation could reduce the connectivity between iron particles and thus reduce the electrical conductivity. This would be exacerbated by high electrolysis current densities resulting in a decrease in material utilization and rate capability. Indeed, the Non-3D electrode and electrodes 3D-M1 and 3D-M2 started deactivating following high charge rates and electrolysis. A mechanically more stable sintered structure can be achieved by increasing the sintering temperature and duration and is expected to be more resilient to such bubble induced deterioration.

To test this hypothesis, we prepared a 3D electrode of the same geometry and composition as 3D-M3 that had been sintered at a lower temperature of 750 °C and for only 1 h. While formation was successful, we observed a drastic decrease in rate capability following linear sweep voltammetry to current densities of up to 1090 mA/cm^2 (Figure C.8). In order to determine if this decrease in rate capability following high current density electrolysis is affected by the geometry, we repeated the experiment with a Non-3D electrode. No decrease in capacity and rate capability was observed. This is consistent with our hypothesis that a too open geometry like that of 3D-M3 can negatively affect the electrical conductivity as discussed in Section 4.3.1. This would be exacerbated by structural damage incurred from bubbles. Further research is required to understand the impact of sintering conditions, geometry, electrolysis duration and current density on structural stability and battery functionality of hybrid battery-electrolyser iron electrodes.

As shown by Lee et al. [56], changes in morphology and phase throughout cycling can affect the stability of iron electrodes resulting in a loss of capacity. Fully discharging the electrode could therefore affect the structural integrity of the iron framework, particularly in the thinner structures present in the discussed 3D electrodes. In order to determine the maximum capacity and study the limits of stability, the electrodes discussed in this work were fully discharged. In practice, the discharge capacity of our iron electrodes exceeds the depth of discharge required in a full battery-electrolyser cell. As shown in Figure 4.10, this is estimated to be no higher than 250 mAh/cm^2, which is between approximately 40-60 % of what can be reached by fully discharging the electrodes discussed here. Consequently, 40-60 % of the iron present in the electrode could remain unoxidised and not be affected structurally by morphology and

phase changes. Future research will determine which minimum capacity is to remain undischarged to obtain long term cycling stability. Other approaches are as in [58], where a stable current collector such as a steel mesh is integrated within the electrode for this purpose.

4.3.4. Comparison of discharge capacities with literature.

The results discussed above can be put into perspective when compared to previously reported values from literature. Differences in electrode preparation and thickness, electrolyte composition, test cell set-up and operating conditions make a direct comparison difficult. However, considering the area- and volume-specific capacities can provide insight into the viability of the presented electrodes for commercial application in batteries (e.g. Ni-Fe or Fe-Air) and the integrated battery-electrolyser discussed in this work. Which of these metrics to prioritize depends on the design specifications of the system and cost-driving components. For instance, for battery applications where space is limited and a high volumetric energy density is required, a high volume-specific capacity is beneficial. For a battery-electrolyser, on the other hand, the cost of the diaphragm separating the half-cells contributes significantly to the cost per cell. Electrodes with a high area-specific capacity reduce the number of cells required in a stack to reach a target system energy storage capacity. Thus, the required area, i.e. cost, of the diaphragms is reduced.

In order to prevent overdischarge of the iron electrode, the cell capacity in Ni-Fe batteries is typically limited by the capacity of the nickel electrode [59, 60]. In Chapter 3 we demonstrated a 3D-structured nickel electrode with an area-specific capacity of around 140 mAh/cm^2 at a discharge duration between 4 h and 10 h (C/4 - C/10). This is equivalent to discharge current densities between 14 mA/cm^2 and 35 mA/cm^2. As shown in Chapter 2, we expect area-specific capacities of up to 200 mAh/cm^2 to be feasible for 3D hybrid nickel electrodes, if porosity, void fraction and thickness are adjusted under consideration of reducing oxygen evolution overpotentials (Figure 2.12). Adding a safety margin of 25 % to prevent overdischarge and assuming electrode thicknesses between 3 mm and 4.5 mm, we arrive at a target range of 175-250 mAh/cm^2 and 388-833 mAh/cm^3 for the area- and volume-specific capacity of the iron electrodes, respectively.

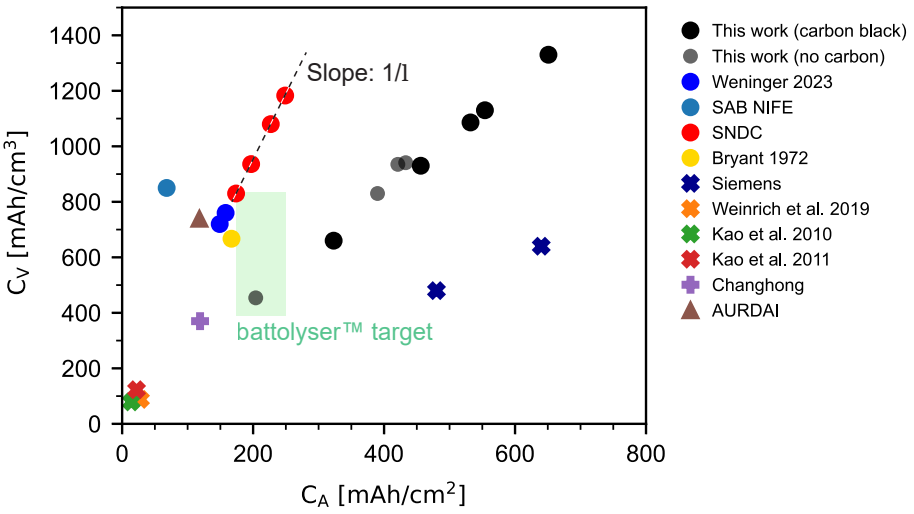

Figure 4.10: Comparison of results presented in this work with volumetric (C_V) and areal (C_A) capacities reported in literature [32, 36, 49, 52, 54, 58, 61, 62]. See also Table 4.1. The green area shows the target range in area- and volume-specific capacities for the integrated battery-electrolyser when based on the limiting capacity of the nickel electrode (see Chapters 2 and 3). l represents the electrode thickness.

Figure 4.10 and Table 4.1 provide an overview of capacities obtained in this work compared to values found in literature. For a comprehensive overview of recent developments in iron anode materials, we recommend the review by Abarro et al. [63]. Kao et al. [62] reported nanosized iron/copper composite particles with a weight-specific capacity of around 560 mAh/g_{Fe} for the first discharge plateau at a discharge current density of 3200 mA/g_{Fe}. Relative to the mass of iron in the electrode, this discharge current density is two orders of magnitude higher while still delivering an 8 % increased weight-specific capacity compared to the highest value for the first discharge plateau reported in this work (516 mAh/g at 20 mA/g and 30 °C). However, while material utilization and rate-capability are extremely high, the authors load the active material on 1.8 mm thick nickel foam and use PTFE as a binder. The binder immobilizes the particles on the nickel foam which functions both as a substrate

and a current collector electrically connecting the iron particles. While required for electrochemical testing in such polymer-bonded electrodes, the binder and current collector are inactive with respect to the discharge reaction. As a result, the loading of iron is low with only 0.04 g_{Fe}/cm^2. Therefore, even though capacity and discharge rate are high with respect to the mass of iron, the low amount of iron per electrode area translates to an area-specific capacity and discharge rate of only 22 mAh/cm^2 and around 8 mA/cm^2, respectively. In comparison, the iron loading per area of the here presented Non-3D electrode containing carbon black is a factor 26.8 higher (1.07 g_{Fe}/cm^2) resulting in a high area-specific capacity of 554 mAh/cm^2 at a discharge current density of 21.5 mA/cm^2. However, we note that studies focusing on the development of novel iron anode materials typically work with a lower iron loading and focus on the electrochemical characterization of the material itself [52, 64]. Effects of ionic resistance, which become relevant in thicker electrodes with lower porosity, i.e. electrodes with high iron loading per area, are typically not considered in such studies.

Cnobloch (Siemens) [49] presented a 10 mm thick iron electrode for the use in iron-air batteries. It contained alternating layers of high and low porosity stacked perpendicular to the electrode-electrolyte interface. The layers with high porosity consisted of iron fibers that facilitated transport processes and increased the ionic electrode conductivity. In this sense, the function of these porous layers is comparable to that of the channels in x-direction of the 3D electrodes shown in this work (Figure 4.5). The layers with low porosity consisted of iron powder, acetylene black and an organic hydrophilic binder loaded onto iron fibers. Cnobloch reported an area-specific capacity of 640 mAh/cm^2 at a discharge current density of 80 mA/cm^2. To the best of our knowledge, this constitutes the highest reported area-specific capacity for iron electrodes. From the cell potential of the demonstrated iron-air battery, it appears that this partially included the second discharge plateau. Approximately 75 % of the reported discharge capacity, i.e. 480 mAh/cm^2, can be attributed to the first discharge plateau. At a comparable discharge current density of 75 mA/cm^2 (70 mA/g), the around 50 % thinner sintered Non-3D electrode containing carbon black delivers lower discharge capacities of 323 mAh/cm^2 and 456 mAh/cm^2 at room temperature and 30 °C, respectively. Even though we report area-specific discharge capacities as high as 651 mAh/cm^2 in-

Table 4.1: Comparison of presented indirectly 3D printed iron electrodes with those previously reported in literature.

Electrode type	Material	L [mm]	T [°C]	Discharge rate [mA/g_{Fe}]	Discharge rate [mA/cm^2]	Discharge capacity [mAh/g_{Fe}]	Discharge capacity [mAh/cm^2]	Discharge capacity [mAh/cm^3]	DC Plateau	Ref.
Sintered (Non-3D)	Carbonyl Fe, carbon black	4.9	30	90 \10[a]	96.5 \10.7[a]	607	651	1330	1+2[b]	this work
		4.9	30	20	21.5	516	554	1130	1	this work
		4.9	30	70	75	424	456	930	1	this work
		4.9	RT	20	21.5	496	532	1086	1	this work
		4.9	RT	70	75	301	323	660	1	this work
Sintered (Non-3D)	Carbonyl Fe	4.7	RT	20	29	267	390	830	1	this work
Sintered (3D-M1)	Carbonyl Fe	4.6	RT	20	25	341	433	941	1	this work
Sintered (3D-M2)	Carbonyl Fe	4.5	RT	20	24	351	421	935	1	this work
Sintered (3D-M3)	Carbonyl Fe	4.5	RT	30	23	271	204	454	1	this work
Sintered	Fe, Zr	2.07	RT	45	25	269	149	720	1	[36]
		2.07	40	36	20	285	158	760	1	[36]
Sintered (SAB NIFE)	Fe	0.8	RT	-	6.67	-	68	850	1	[58, 65]
Sintered (SNDC[c])	Fe	2.1	40	-	25	-	249	1183	1	[54]
		2.1	25	-	25	-	227	1080	1	[54]
		2.1	40	-	80	-	197	936	1	[54]
		2.1	25	-	80	-	174	830	1	[54]
Sintered	Fe	2.5	44	-	50	$\sim$ 400	167	667	1	[61]
Polymer-bonded (Siemens)	Fe, acetylene black	10	RT	-	80	-	640	640	1+2[b]	[49]
		10	RT	-	80	-	480	480	1	[49]
Polymer-bonded	Carbonyl Fe, Bi_2S_3	3.25	RT	6.2	8.8	20	28	88	1	[32]
Polymer-bonded	Fe, carbon black, Na_2S	1.8	RT	200	8.5	327	14	79	1	[52]
Polymer-bonded	Fe, Cu, Na_2S	1.8	RT	3200	7.9	562	22	123	1	[62]
Pocket (Changhong)	Commercial	3.2	RT	-	25	-	119	370	1	[36]
Rolled (AURDAI[d])	Fe	1.6	RT	-	6.67	-	118	739	1	[58]

[a] Initial discharge at 90 mA/g followed by discharge at 10 mA/g.
[b] Partial discharge at the second plateau.
[c] Swedish National Development Corporation.
[d] All-Union Research Designing Accumulator Institute.

cluding a partial discharge at the second plateau, a direct comparison with the results provided by Cnobloch is not possible as he only reports values for a discharge current density of 80 mA/cm^2. Considering the thickness of the electrode, a lower discharge rate would have likely resulted in even higher discharge capacities.

To the best of our knowledge, the Swedish National Development Corporation (SNDC) developed sintered electrodes with the highest reported volume-specific capacity [54, 65]. These electrodes exhibited a structure consisting of microporous iron grains sintered together to form macropores. The microporous iron grains provide a high internal surface area while the macropores facilitate electrolyte access. At 25 °C and a discharge current density of 25 mA/cm^2, these electrodes provided a volume-specific capacity of 1080 mAh/cm^3. This can be compared to 1086 mAh/cm^3 obtained for the Non-3D electrode containing carbon black at room temperature and 21.5 mA/cm^2. While the volume-specific capacity is similar, our electrode is 4.9 mm thick compared to 2.1 mm for the SNDC electrode. As a result, the area-specific capacity for the Non-3D carbon black electrode is 134 % higher than that of the SNDC electrode (532 mAh/cm^2 vs. 227 mAh/cm^2). Remarkably, even without the addition of carbon, our indirectly 3D printed electrodes 3D-M1 and 3D-M2 reach capacities exceeding 400 mAh/cm^2 and 900 mAh/cm^3.

Overall, both the area-specific and the volume-specific capacities of the iron electrodes presented in this work are among the highest reported in literature and exceed the initial goal set for battolyser™ electrodes shown in Figure 4.10. In order to reach the upper range of the targeted area-specific capacity, 250 mAh/cm^2, the thickness of the Non-3D electrode with carbon addition could be reduced from 4.9 mm to 2.3 mm. This would reduce material cost and cell/stack length. Alternatively, the excess iron could serve as a conductive backbone that is never discharged to mitigate electrode passivation. In an Fe-air battery or iron-air-battery-electrolyser, where the capacity is limited by the iron electrode, the electrodes presented in this work could significantly increase the energy density. We expect that increasing the thickness further will result in area-specific capacities exceeding 650 mAh/cm^2. The voltage drop over such thick electrodes could be mitigated by including channels with an appropriate void fraction.

4.4. Scaling for industrial manufacturing

The application of the herein discussed electrodes in battery-electrolysers for large-scale energy storage and hydrogen production will require scaling of the presented electrode manufacturing procedure. The indirect 3D printing technique used in this work, while useful for research purposes and prototyping, is not suitable for the production of electrodes on large scale. This is due to the long durations of 3D printing the PLA moulds, mould dissolution as well as rinsing and drying of the parts. Also, KOH (aq.) containing dissolved PLA and water used for rinsing the parts would constitute significant waste streams.

Iron electrodes could be manufactured on large scale using industrially established powder metallurgy processes such as press-and-sintering and metal injection moulding (MIM) [66]. Press-and-sintering involves compacting metal powder in a die yielding a mechanically stable part that can then be sintered. In MIM, a metal paste containing a binder is injected at elevated temperatures into a mould. Here, the binder provides stability to the part after cooling down so that it can be transferred to the debinding and sintering station [66]. In fact, the agar binder system used in this work was adapted from MIM and adjusted to yield parts with a high porosity [17, 18]. Thus, electrode manufacturing with the feedstock formulated in this work can be integrated with existing MIM systems. In addition, due to the significantly lower metal loading, our feedstock formulation does not require high injection pressures which could reduce the cost of the machinery and the mould.

However, the two-piece design of the die and mould used in press-and-sintering and MIM, respectively, must allow for the release of the part after pressing/injection without damage. Therefore, complex features such as multi-directional channels and cavities are impossible to realize with press-and-sintering or MIM. Using these techniques, the direction of the electrode channels must align with the direction of the die/mould release. For instance, instead of channels in x-, y- and z-direction as shown in this work (Figure 4.5 D), a MIM/sinter-and-press manufactured electrode could have only channels in y-direction. In the future, advanced techniques of additive manufacturing such as material extrusion additive manufacturing (MEX) with an agar-binder system could be used to scale the production of electrodes with a complex channel geometry similar to

the one presented in this work [67]. MIM and MEX in combination with the agar binder system could also be used to scale the production of the sintered 3D nickel electrodes discussed in Chapter 3.

4.5. Conclusions

In this work, we present indirectly 3D printed hybrid iron electrodes that integrate battery and electrolysis functionality. These exhibit high area- and volume-specific battery capacities and can be overcharged efficiently at industrially relevant current densities to produce hydrogen. While electrode channels increase the electrolyte accessibility resulting in higher material utilisation and discharge rate capability, we find that a too high channel volume, i.e. void fraction, is detrimental. The addition of carbon black as a conductivity enhancing additive and increasing the temperature to 30 °C, lead to specific discharge capacities as high as 651 mAh/cm^2 and 1330 mAh/cm^3. By transferring the iron-agar feedstock formulation to industrial powder metallurgy techniques such as metal injection moulding (MIM) and material extrusion additive manufacturing (MEX), the production of 3D structured iron electrodes can be scaled. Overall, the 3D electrode structure adds a new dimension to electrode development, complementing advances in material development.

References

[1] S. J. Davis, N. S. Lewis, M. Shaner, S. Aggarwal, D. Arent, I. L. Azevedo, S. M. Benson, T. Bradley, J. Brouwer, Y.-M. Chiang, *et al.*, *Net-zero emissions energy systems,* Science **360**, eaas9793 (2018).

[2] P. Danieli, M. Masi, A. Lazzaretto, G. Carraro, E. Dal Cin, and G. Volpato, *Is banning fossil-fueled internal combustion engines the first step in a realistic transition to a 100% RES share?* Energies **16**, 5690 (2023).

[3] F. M. Mulder, *Implications of diurnal and seasonal variations in renewable energy generation for large scale energy storage,* Journal of Renewable and Sustainable Energy **6** (2014).

[4] K. Prakash, M. Ali, M. N. I. Siddique, A. A. Chand, N. M. Kumar, D. Dong, and H. R. Pota, *A review of battery energy storage systems for ancillary services in distribution grids: Current status, challenges and future directions,* Frontiers in Energy Research **10**, 971704 (2022).

[5] J. J. Brey, *Use of hydrogen as a seasonal energy storage system to manage renewable power deployment in Spain by 2030,* International Journal of Hydrogen Energy **46**, 17447 (2021).

[6] G. Glenk and S. Reichelstein, *Reversible power-to-gas systems for energy conversion and storage,* Nature Communications **13**, 2010 (2022).

[7] N. Rambhujun, M. S. Salman, T. Wang, C. Pratthana, P. Sapkota, M. Costalin, Q. Lai, and K.-F. Aguey-Zinsou, *Renewable hydrogen for the chemical industry,* MRS Energy & Sustainability **7**, E33 (2020).

[8] F. M. Mulder, B. M. H. Weninger, J. Middelkoop, F. G. B. Ooms, and H. Schreuders, *Efficient electricity storage with a battolyser, an integrated Ni–Fe battery and electrolyser,* Energy & Environmental Science **10**, 756 (2017).

[9] K. Shinyama, Y. Magari, A. Funahashi, T. Nohma, and I. Yonezu, *Improvement of high-temperature characteristics of the sintered nickel positive electrode for an alkaline storage battery,* Electrochemistry **71**, 686 (2003).

[10] J. O. G. Posada and P. J. Hall, *Controlling hydrogen evolution on iron electrodes,* International Journal of Hydrogen Energy **41**, 20807 (2016).

[11] Y. Sui and X. Ji, *Anticatalytic strategies to suppress water electrolysis in aqueous batteries,* Chemical Reviews **121**, 6654 (2021).

[12] T. Kou, S. Wang, R. Shi, T. Zhang, S. Chiovoloni, J. Q. Lu, W. Chen, M. A. Worsley, B. C. Wood, S. E. Baker, *et al.*, *Periodic porous 3D electrodes mitigate gas bubble traffic during alkaline water electrolysis at high current densities,* Advanced Energy Materials **10**, 2002955 (2020).

[13] I. Sullivan, H. Zhang, C. Zhu, M. Wood, A. J. Nelson, S. E. Baker, C. M. Spadaccini, T. Van Buuren, M. Lin, E. B. Duoss, *et al.*, *3D printed nickel–molybdenum-based electrocatalysts for hydrogen evolution at low overpotentials in a flow-through configuration,* ACS Applied Materials & Interfaces **13**, 20260 (2021).

[14] D. R. Lide, *CRC handbook of chemistry and physics*, Vol. 85 (CRC press, 2004).

[15] J. Hereijgers, J. Schalck, J. Lölsberg, M. Wessling, and T. Breugelmans, *Indirect 3D printed electrode mixers,* ChemElectroChem **6**, 378 (2019).

[16] X. Li, *Thermal Debinding of Metal Injection Molded Parts with an Agar-Gel Binder System*, Master's thesis (2007).

[17] B. A. Mathew and R. Mastromatteo, *Metal injection moulding for automotive applications,* Metal Powder Report **57**, 20 (2002).

[18] A. Fanelli, M. Behi, C. P. Ballard Jr, and J. V. Burlew, *Gel strength enhancing additives for agaroid-based injection molding compositions,* (1998), U.S. Patent Nr. 5,746,957.

[19] M. Sekido, H. Nakayama, M. Nukaya, and Y. Noro, *Injection-molding of metal or ceramic powders,* (1993), U.S. Patent 5,258,155.

[20] C. Yang, A. K. Manohar, and S. R. Narayanan, *A high-performance sintered iron electrode for rechargeable alkaline batteries to enable*

large-scale energy storage, Journal of The Electrochemical Society **164**, A418 (2017).

[21] A. K. Manohar, S. Malkhandi, B. Yang, C. Yang, G. K. S. Prakash, and S. R. Narayanan, *A high-performance rechargeable iron electrode for large-scale battery-based energy storage,* Journal of the Electrochemical Society **159**, A1209 (2012).

[22] A. K. Manohar, C. Yang, S. Malkhandi, G. K. S. Prakash, and S. R. Narayanan, *Enhancing the performance of the rechargeable iron electrode in alkaline batteries with bismuth oxide and iron sulfide additives,* Journal of the Electrochemical Society **160**, A2078 (2013).

[23] K. Vijayamohanan, A. K. Shukla, and S. Sathyanarayana, *Formation mechanism of porous alkaline iron electrodes,* Journal of Power Sources **32**, 329 (1990).

[24] A. K. Manohar, C. Yang, S. Malkhandi, B. Yang, G. S. Prakash, and S. Narayanan, *Understanding the factors affecting the formation of carbonyl iron electrodes in rechargeable alkaline iron batteries,* Journal of the Electrochemical Society **159**, A2148 (2012).

[25] S. U. Falk and A. J. Salkind, *Alkaline storage batteries* (1969).

[26] P. R. Vassie and A. C. C. Tseung, *A study of gas evolution in teflon bonded porous electrodes—i: The mechanical and chemical stability of teflon bonded graphite electrodes,* Electrochimica Acta **20**, 759 (1975).

[27] P. R. Vassie and A. C. C. Tseung, *A study of gas evolution in teflon bonded porous electrodes—ii: Factors affecting the mechanical strength,* Electrochimica Acta **20**, 763 (1975).

[28] X. Zhao, H. Ren, and L. Luo, *Gas bubbles in electrochemical gas evolution reactions,* Langmuir **35**, 5392 (2019).

[29] H. Weinrich, M. Gehring, H. Tempel, H. Kungl, and R.-A. Eichel, *Impact of the charging conditions on the discharge performance of rechargeable iron-anodes for alkaline iron–air batteries,* Journal of Applied Electrochemistry **48**, 451 (2018).

[30] N. I. Villanueva-Martínez, C. Alegre, J. Rubín, R. Mckerracher, C. P. de León, H. A. F. Rodríguez, and M. J. Lázaro, *Investigation of the properties influencing the deactivation of iron electrodes in iron-air batteries,* Electrochimica Acta **465**, 142964 (2023).

[31] A. K. Manohar, C. Yang, and S. R. Narayanan, *The role of sulfide additives in achieving long cycle life rechargeable iron electrodes in alkaline batteries,* Journal of The Electrochemical Society **162**, A1864 (2015).

[32] H. Weinrich, M. Gehring, H. Tempel, H. Kungl, and R.-A. Eichel, *Electrode thickness-dependent formation of porous iron electrodes for secondary alkaline iron-air batteries,* Electrochimica Acta **314**, 61 (2019).

[33] W. A. Bryant, *The importance of physical structure to the capacity of porous iron electrodes,* Journal of The Electrochemical Society **126**, 1899 (1979).

[34] A. Ito, L. Zhao, S. Okada, and J.-i. Yamaki, *Synthesis of nano-fe3o4-loaded tubular carbon nanofibers and their application as negative electrodes for fe/air batteries,* Journal of Power Sources **196**, 8154 (2011).

[35] H. Figueredo-Rodríguez, R. McKerracher, M. Insausti, A. G. Luis, C. P. de León, C. Alegre, V. Baglio, A. Aricò, and F. Walsh, *A rechargeable, aqueous iron air battery with nanostructured electrodes capable of high energy density operation,* Journal of The Electrochemical Society **164**, A1148 (2017).

[36] B. Weninger, *Bridging intermittency with iron electrodes*, Ph.D. thesis, Delft University of Technology (2023).

[37] P. Los, A. Rami, and A. Lasia, *Hydrogen evolution reaction on Ni-Al electrodes,* Journal of Applied Electrochemistry **23**, 135 (1993).

[38] X. Zou, Y. Wu, Y. Liu, D. Liu, W. Li, L. Gu, H. Liu, P. Wang, L. Sun, and Y. Zhang, *In situ generation of bifunctional, efficient Fe-based catalysts from mackinawite iron sulfide for water splitting,* Chem **4**, 1139 (2018).

[39] Y. Wu, Y. Liu, G.-D. Li, X. Zou, X. Lian, D. Wang, L. Sun, T. Asefa, and X. Zou, *Efficient electrocatalysis of overall water splitting by ultrasmall $Ni_xCo_{3-x}S_4$ coupled ni_3s_2 nanosheet arrays,* Nano Energy **35**, 161 (2017).

[40] H. Vogt and R. J. Balzer, *The bubble coverage of gas-evolving electrodes in stagnant electrolytes,* Electrochimica Acta **50**, 2073 (2005).

[41] J. Eigeldinger and H. Vogt, *The bubble coverage of gas-evolving electrodes in a flowing electrolyte,* Electrochimica Acta **45**, 4449 (2000).

[42] H. Vogt, *The actual current density of gas-evolving electrodes—notes on the bubble coverage,* Electrochimica Acta **78**, 183 (2012).

[43] H. G. Xu, X. Y. Zhang, Y. Ding, H. Q. Fu, R. Wang, F. Mao, P. F. Liu, and H. G. Yang, *Rational design of hydrogen evolution reaction electrocatalysts for commercial alkaline water electrolysis,* Small Structures **4**, 2200404 (2023).

[44] J. M. Bockris and E. C. Potter, *The mechanism of the cathodic hydrogen evolution reaction,* Journal of The Electrochemical Society **99**, 169 (1952).

[45] H. E. G. Rommal and P. J. Moran, *Time-dependent energy efficiency losses at nickel cathodes in alkaline water electrolysis systems,* Journal of The Electrochemical Society **132**, 325 (1985).

[46] A. E. Mauer, D. W. Kirk, and S. J. Thorpe, *The role of iron in the prevention of nickel electrode deactivation in alkaline electrolysis,* Electrochimica Acta **52**, 3505 (2007).

[47] F. M. Sapountzi, J. M. Gracia, H. O. Fredriksson, J. H. Niemantsverdriet, *et al.*, *Electrocatalysts for the generation of hydrogen, oxygen and synthesis gas,* Progress in Energy and Combustion Science **58**, 1 (2017).

[48] Q. Zhang, Z. Yu, P. Du, and C. Su, *Carbon nanomaterials used as conductive additives in lithium ion batteries,* Recent Patents on Nanotechnology **4**, 100 (2010).

[49] H. Cnobloch, *Fuel cells and metal-air batteries as electrochemical energy storage systems,* in *Energy Storage* (Elsevier, 1980) pp. 172–184.

[50] P. S. Arunkumar, T. Maiyalagan, S. Kheawhom, S. Mao, and Z. Jiang, *Effect of carbon material additives on hydrogen evolution at rechargeable alkaline iron battery electrodes,* Materials Science for Energy Technologies **4**, 236 (2021).

[51] H. A. F. Rodriguez, R. D. Mckerracher, C. P. de León, and F. C. Walsh, *Improvement of negative electrodes for iron-air batteries: comparison of different iron compounds as active materials,* Journal of The Electrochemical Society **166**, A107 (2019).

[52] C.-Y. Kao and K.-S. Chou, *Iron/carbon-black composite nanoparticles as an iron electrode material in a paste type rechargeable alkaline battery,* Journal of Power Sources **195**, 2399 (2010).

[53] R. J. Gilliam, J. W. Graydon, D. W. Kirk, and S. J. Thorpe, *A review of specific conductivities of potassium hydroxide solutions for various concentrations and temperatures,* International Journal of Hydrogen Energy **32**, 359 (2007).

[54] L. Öjefors and L. Carlsson, *An iron—air vehicle battery,* Journal of Power Sources **2**, 287 (1978).

[55] L. Öjefors, *Temperature dependence of iron and cadmium alkaline electrodes,* Journal of The Electrochemical Society **123**, 1139 (1976).

[56] D.-C. Lee, D. Lei, and G. Yushin, *Morphology and phase changes in iron anodes affecting their capacity and stability in rechargeable alkaline batteries,* ACS Energy Letters **3**, 794 (2018).

[57] P. M. Dunlap and S. R. Faris, *Surface tension of aqueous solutions of potassium hydroxide,* Nature **196**, 1312 (1962).

[58] J. Černỳ, J. Jindra, and K. Micka, *Comparative study of porous iron electrodes,* Journal of Power Sources **45**, 267 (1993).

[59] D. Linden, *Handbook of Batteries and Fuel Cells* (McGraw-Hill, New York, 1983).

[60] A. K. Shukla, M. K. Ravikumar, and T. S. Balasubramanian, *Nickel/iron batteries,* Journal of Power Sources **51**, 29 (1994).

[61] W. A. Bryant, *The structure and performance of sintered iron electrodes,* Electrochimica Acta **24**, 1057 (1979).

[62] C.-Y. Kao, Y.-R. Tsai, and K.-S. Chou, *Synthesis and characterization of the iron/copper composite as an electrode material for the rechargeable alkaline battery,* Journal of Power Sources **196**, 5746 (2011).

[63] J. M. E. Abarro, J. N. L. Gavan, D. E. D. Loresca, M. A. A. Ortega, E. A. Esparcia Jr, and J. A. D. Paraggua, *A Tale of Nickel-Iron Batteries: Its Resurgence in the Age of Modern Batteries,* Batteries **9**, 383 (2023).

[64] H. Tang, C. Zhang, K. Chang, E. Shangguan, B. Li, and Z. Chang, *Synthesis of nis coated fe3o4 nanoparticles as high-performance positive materials for alkaline nickel-iron rechargeable batteries,* International Journal of Hydrogen Energy **42**, 24939 (2017).

[65] B. E. C. Andersson, L. I. Carlsson, and R. C. R. Johnsson, *Porous electrode for a chemo-electric cell and a method of preparing the same,* (1978), U.S. Patent 4,109,060.

[66] H. Danninger, R. D. O. Calderon, and C. Gierl-Mayer, *Powder metallurgy and sintered materials,* Addit. Manuf **19** (2017).

[67] C. Suwanpreecha and A. Manonukul, *A review on material extrusion additive manufacturing of metal and how it compares with metal injection moulding,* Metals **12**, 429 (2022).

5

Eliminating redox-mediated electron transfer mechanisms on a supported molecular catalyst enables CO_2 conversion to ethanol

Maryam Abdinejad*, Amirhossein Farzi*, Robin Möller-Gulland*, Fokko Mulder, Chengyu Liu, Junming Shao, Jasper Biemolt, Marc Robert, Ali Seifitokaldani, Thomas Burdyny

Molecular catalysts play a significant role in chemical transformations, utilizing changes in redox states to facilitate reactions. In the broadening field of carbon dioxide (CO_2) electrolysis to value added products, catalyst choice strongly impacts product formation. To date molecular electrocatalysts have efficiently produced single-carbon products from CO_2 but have struggled to achieve the carbon-carbon coupling step needed to reach highly valued multi-carbon products. Conversely, copper acts as the only reliable bulk metal that enables carbon-carbon coupling, but leads to broad

*These authors contributed equally to this work.

*C_{2+} product spectrums. Here we designed a molecular electrocatalyst system that subverts the traditional redox-mediated reaction mechanisms of organometallic compounds, facilitating electrochemical C-C coupling to produce ethanol. By pairing iron tetraphenylporphyrin (Fe-TPP) with a nickel electrode, we fixed the iron oxidation state during electrocatalytic CO_2 reduction to enable further reductions and coupling of *CO intermediates. This represents a marked behavioural shift compared to the same metalloporphyrin deposited onto carbon-based electrodes. Extending the approach to a 3D porous nickel support with adsorbed Fe-TPP, we attain ethanol Faradaic efficiencies of 68 % +/- 3.2 % at -0.3 V vs a reversible hydrogen electrode (pH = 7.7) with partial ethanol current densities of -21 mA cm^{-2}. Separately we demonstrate maintained ethanol production over 60 hours of operation. Further consideration of the wide parameter space of molecular catalyst and metal electrodes shows promise for additional novel chemistries and achievable metrics.*

This chapter has been published in Nature Catalysis 7, 1109-1119 (2024), https://doi.org/10.1038/s41929-024-01225-1 [1].

5.1. Introduction

Many organometallic molecular compounds can function as excellent catalysts for carbon dioxide (CO_2) reduction due to their ability for their reduced forms to spontaneously form an adduct [2]. Through oxidation of the molecular catalyst and electron donation, CO_2 can then be reduced to value-added products. However, the redox-mediated mechanisms of molecular catalysts mean that electrons cannot be donated ad infinitum, and the oxidation state of the molecular catalyst must be regenerated through an electrode or electron donors prior to further reductions (Figure 5.1 A). While efficient, the mechanism of CO_2 reduction on molecular catalysts has traditionally been limited to 2-electron products such as carbon monoxide (CO) and formate ($HCOO^-$) due at least partly to the limited oxidation states of organometallic compounds before requiring regeneration. Modifications to the molecular structure, the addition of proton-electron donors, and tandem catalysis scenarios can allow for conversion to higher-electron products, but demonstrations have been scarce [3, 4]. To improve electron regeneration and the turnover number of molecular catalysts, they have been immobilized primarily onto inert carbon-based electrodes such as graphene and nanotubes. While this has allowed for current densities >100 mA cm^{-2}, demonstrations of higher electron products have not increased, indicating that additional limitations still exist.

One such limitation lies in the changes in the metal oxidation states during the redox-mediated reduction of CO_2. During reduction of the CO_2-adduct, the oxidation state of the metal centre (which is typically characterized as binding to CO_2 and its intermediates) also varies. Changes in the oxidation state upon successive electron or proton transfers then greatly modify the binding energy of the metal site to the CO_2 reduction intermediates. For example, in the classical case of iron porphyrins [5] the reduction of Fe(II) to Fe(I) facilitates the release of *CO. If the Fe(II) state were instead maintained, CO would be strongly bound to iron similar to what happens during CO poisoning of haemoglobin. While the oxidation state changes to Fe(I) allows for the release of CO as a product, it inhibits the reduction and coupling of CO intermediates into higher-electron products such as methane (CH_4), methanol (CH_3OH), ethylene (C_2H_4) and ethanol (C_2H_5OH). Conversely, in bulk metals delocalized

electrons allow for continuous electrons to be supplied for CO_2 reduction under an applied potential. Only copper and copper-based catalysts, however, can obtain higher-electron products at meaningful current densities due to their moderate binding energy towards CO that allows for further reductions. Thus copper catalysts have enabled ethylene and ethanol selectivity independently >50 %, and collectively >85 % [6–18]. Problematically though, the branching pathway between ethylene and oxygenates on copper is downhill from the rate determining steps, leaving few means of experimentally shifting ethylene:oxygenate ratios. Selective production of a specific multi-carbon product is then highly challenging.

Despite their limitations to date, molecular catalysts have long been hypothesized to reach higher electron products if a strong enough interaction exists between the catalyst and substrate. Under these conditions, the molecular catalyst could be positioned inside the electric double layer, which would allow for electrons to be shuttled through the catalyst at faster rates than they are consumed in the CO_2 reduction reaction. The local oxidation state of the metal site could then remain fixed (schematic in Figure 5.1 B) [4, 19]. Under such conditions, the molecular catalyst would then function as a hybrid electrocatalyst whose potential is modulated by the electrode, thus breaking redox-mediated limitations. A recent example which uses a molecular catalyst directly conjugated to graphene has shown such behavior. Here the oxidation state remains fixed due to the molecular catalyst residing inside the electric double layer [20], creating 'metal-like molecules' [21]. Such behavior was in part attributed to the lack of solvation in aqueous media of the hydrophobic cobalt tetraphenylporphyrin.

5.2. Results and discussion

To circumvent traditional limitations of molecular catalysts, we sought to create strong electronic coupling between a catalyst and an electrode support. While carbon-based materials have traditionally been used as a catalyst support due to their relatively-inert electrochemical behaviour, several characterization and electrochemical works report that strong chemisorption-type interactions [22–28] are possible using metal supports. Further, X-ray photoelectron spectroscopy examining cobalt(II) phthalocyanine ad-

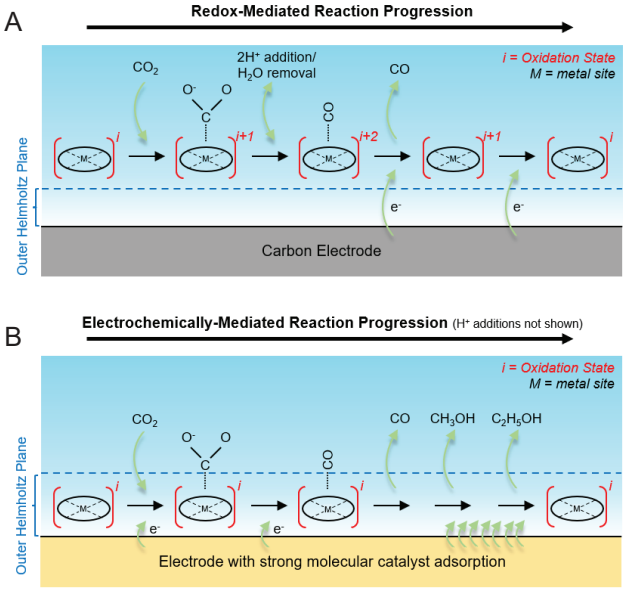

Figure 5.1: (A) Schematic representation of a general redox-mediated reaction mechanism using organometallic molecular catalysts for CO_2 reduction. Here the molecular catalyst reduces CO_2 to CO and is then regenerated via electron transfers from an inert electrode. (B) Schematic representation of an electrochemical reaction mechanism where a molecular catalyst resides inside the electric double layer. Here electron transfers from the electrode occur during the CO_2 reduction reaction, preventing substantial oxidation of the hybrid organometallic catalyst or its metal centre.

sorbed onto Ag(111), and Ni(111) has also seen direct electronic interactions between the metal centre and electrode, resulting in electron density transfer from cobalt to the more electronegative Ag and Ni metals [24, 27, 28]. We then hypothesized that during electrochemical applications, such interactions could then stabilize oxidation states while facilitating continuous electron transfers. Further, the binding energies of *CO to an organometallic metal centre could be modulated by the choice of metal electrode.

With these principles in mind, we aimed to combine a metal electrode with a molecular catalyst. Iron-tetraphenylporphyrin (Fe-TPP) is a logical molecular catalyst to test due to its efficient production of CO, and

well-understood oxidation states during CO2 reduction [29]. Meanwhile, nickel was chosen as a metal support due to its relative inertness for CO_2 reduction [30, 31] and its previously reported interactions with molecular catalysts. We then performed density functional theory (DFT) computations to compare the adsorption of Fe-TPP on graphene vs. Ni(111) (see Appendix D for computational details). Here DFT computations showed the Fe site within 2.00 Å of the nickel surface, with a shift in electron density from the Fe site to the nickel atoms (Figure 5.2 A). Such interactions between Ni and Fe have previously been shown to decrease the orbital energy levels, which increased the oxidation state of iron but with reduced binding energies for *CO [32]. The comparable graphene case, however, is more reminiscent of weak physisorption with 3.92 Å between the carbon and Fe site and an intact electronic structure of the carbon atoms (Figure 5.2 B).

Following these results, we then drop casted Fe-TPP onto a nickel mesh and applied cathodic potentials under both CO_2 and CO saturated electrolytes in a flow-cell (Figure 5.2 C and Figure D.1) and H-cell, respectively. For the CO_2-saturated electrolyte, ethanol was observed as the dominant reaction product at a Faradaic efficiency (FE) of 58.2 % after 4 hours of operation with an applied potential of -0.3 V vs RHE, with ethanol steadily increasing in the initial hours of operation (Figure 5.2 D). The ethanol partial current density at the end of the experiment was 0.37 mA cm^{-2}. The remaining products were CO and H_2. The lower ethanol FE initially may indicate that *CO or *CHO must accumulate sufficiently before coupling can occur. Such a result is notably distinct from decades of literature where Fe-TPP only produced CO and H_2.

Additionally, a 47 % Faradaic efficiency towards ethanol, with $j_{ethanol}$ = -0.23 mA cm^{-2}, was observed when CO was directly used as a reactant (Figure 5.2 E), with an additional 57 % FE for H_2 (Figure D.2). The CO reduction experiment indicates that the Fe oxidation state in the complex can bind directly to CO, and thus may not be the Fe(I) traditionally hypothesized. The analysis of the liquid phase upon 1H-NMR revealed the formation of ethanol as only liquid products, as shown by the presence of a triplet peak at 1.17 ppm and a quartet peak at 3.64 ppm (Figure 5.2 F).

For the twelve electron transfers needed to form ethanol, and for *CO to not desorb from Fe-TPP, it is anticipated that the oxidation state of

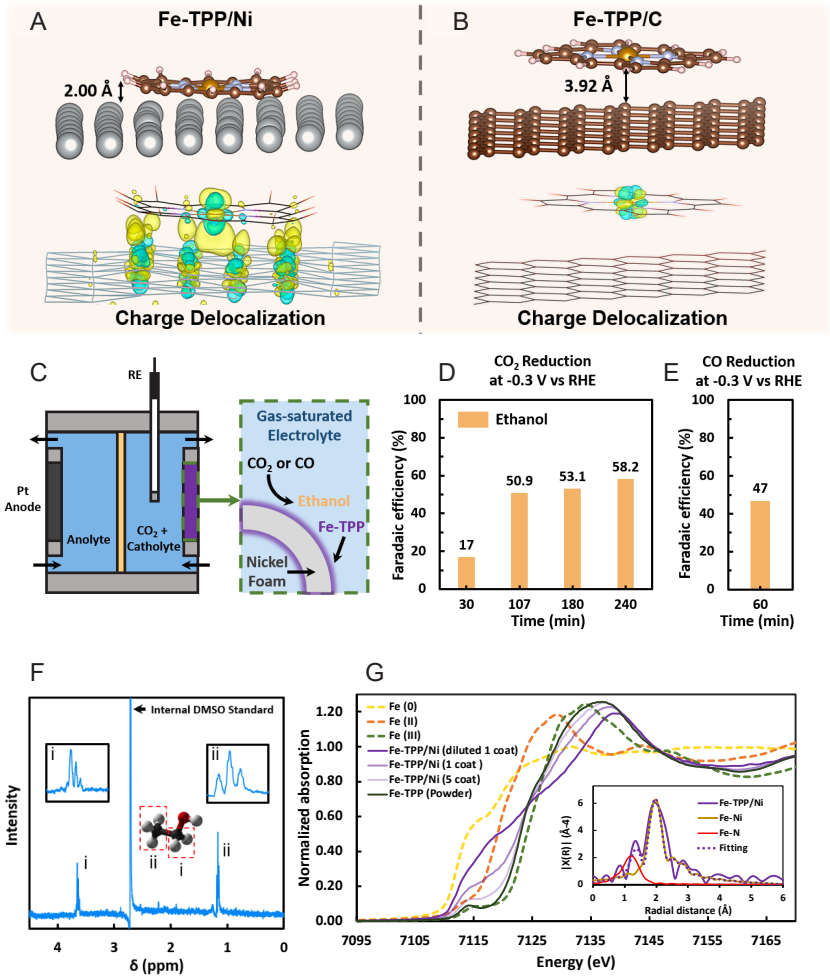

Figure 5.2: Atomic positions of Fe-TPP on (A) nickel and (B) graphene with the minimum distance between the substrate and Fe center. Charge delocalization graphs of immobilized Fe-TPP on (A) nickel and (B) graphene, both at an isosurface level of 0.008 e bohr^{-3} calculated with density functional theory (DFT). Yellow shows the electron accepted, and blue shows the charge donated. (C) Schematic of the CO_2 flow cell used in experiments, and the combined Fe-TPP/Ni catalyst. (D) Ethanol production after 4 h electrolysis of Fe-TPP/Ni foam under CO_2 at -0.30 V vs. RHE in a flow cell. (E) Ethanol production after 4 h of electrolysis of Fe-TPP/Ni in an H-cell under CO at -0.30 V vs. RHE. (F) 1H NMR spectrum of the electrolyte after electrolysis (E = -0.30 V vs. RHE, t = 4 h) in CO_2-saturated solution. (G) In-situ X-ray absorption near-edge spectroscopy (XANES) on Fe-TPP/Ni catalyst with various deposition coating catalysts.

the Fe site centre remains fixed during all CO_2 reduction steps and is more oxidized than Fe(I). To examine the Fe oxidation state during operation, we performed *in-situ* and *ex-situ* X-ray absorption near-edge spectroscopy (XANES) on the drop casted Fe-TPP into sputtered Ni (Fe-TPP/Ni) (Figure D.3). Applied potentials from -0.1 V to -3.0 V vs. RHE were examined (Figure D.4, Table D.1). A systematic comparison of normalized XAS spectra of various Fe-TPP loadings onto Ni was carried out (Figure 5.2 G). The Fe(II), Fe(III) and Fe foil as Fe(0) were used as a reference. In the case of Fe-TPP powder, iron appears in the Fe(II) and Fe(III) oxidation states, but when depositing it onto nickel catalysts, Fe(0) and Fe(III) become the main oxidation states of iron.

Figure 5.2 G and Table D.2 show the impact of varying Fe-TPP loading onto Ni on the oxidation state of the Fe centre. As the sample loading increases, a greater presence of the Fe(III) oxidation state was detected. The similar lowest energy transitions belong to weak 1s $\rightarrow$ 3d pre-edge peaks at approximately 7.111-7.113 eV indicating a similar electronic structure at the iron centre in all cases [33, 34]. The Fe center of Fe-TPP clearly shows the highest-energy pre-edge feature, similar to ferric iron (Fe(III)), whereas depositing Fe-TPP on nickel shows lower-energy pre-edges at ~7.111 eV. These observations suggest that the oxidation state of Fe-TPP is similar to the ferric iron (Fe(III)). However the line shape changes for the higher loading which can be due to a change of oxidation state for Fe from (III) to (0) [35]. The correlation of this second peak with Ni is further substantiated by the observed trend illustrated in Figure D.5. In this context, the emergence and intensification of the metal-metal interaction are evident as the system progresses toward the formation of the Fe-TPP monolayer on Ni.

To obtain higher selectivity and current density, we sought to increase the surface loading of Fe-TPP on nickel to increase CO_2 reduction and reduce by-product hydrogen production likely coming from the nickel substrate. For this reason, we designed and fabricated a 3D, highly porous Ni electrode (Figures 5.3 A, 5.3 B and Figures D.7-D.11). After deposition of Fe-TPP via drop casting with dichloromethane, an Fe-TPP/Ni electrode was formed (Figures 5.3 C, 5.3 D and Figures D.12-D.13). The corresponding elemental mapping using energy-dispersive X-ray spectroscopy (EDX) shows a uniform distribution of Fe, Ni, N and C on the collected sample from the electrode surface after deposition, which confirms dis-

tributed Fe-TPP on the Ni surface (Figures D.14 and D.15). Next, X-ray photoelectron spectroscopy (XPS), shown in Figures D.16-D.18, was employed to investigate the bonding and surface electronic states for both bare nickel and the Fe-TPP/Ni catalysts. The fabricated electrodes were positioned in a custom-designed flow-cell for electrochemical testing where CO_2 flows through the pores of the electrode (Figure 5.3 E, Figures D.19-D.23). Here the hydrophobic Fe-TPP catalyst was deposited without a binding agent and remains fixed in the micropores of the sintered nickel electrode even during electrolyte immersion and during electrochemical operation.

The electrocatalytic activity of the designed system for CO_2RR was examined by cyclic voltammetry (CV) (Figure D.24) and chronoamperometry with and without electrolyte flow in aqueous solutions of 0.5 M $KHCO_3$ (Figures D.28 and D.29). No strong correlation was found between $KHCO_3$ concentration and ethanol production (Figure D.25). We chose 0.5 M concentrations for the remainder of the tests, with CO_2 purging through the bottom of the reactor (pH = 7.7). The results presented here focus on the flow system shown in Figure 5.3 E. Three additional control catalysts were also created and tested to elucidate the effect of coupling Fe-TPP to the nickel electrode. These include a bare 3D nickel structure, TPP deposited onto Ni without a Fe metal site, and a comparable 3D carbon structure covered in Fe-TPP (named Fe-TPP/C – see Figure D.26). Comparing the CVs of these catalysts in Figure 5.3 F shows a large deviation in current vs. voltage, with the Fe-TPP/Ni showing substantially higher current densities in the range of -0.3 V to -0.6 V vs. a reversible hydrogen electrode (RHE).

The Faradaic efficiencies of the four different catalysts were then examined via chronoamperometry over a range of potentials. Different CO_2 gas flow rates between 10 and 50 standard cubic centimetres per minute (SCCM) were examined (Figure D.27), where the 40 SCCM was selected as an optimal flow rate. The 40 SCCM chronoamperometry experiments are shown in Figures 5.3 G, 5.3 H and Figures D.28-D.29 for Fe-TPP/Ni. Here Fe-TPP/C and the bare Ni samples showed only CO and H_2 as products as expected from literature, with Ni showing < 20 % FE for CO. Conversely, the Fe-TPP/Ni catalyst produced ethanol as a product with a 68 % +/- 3.2 % Faradaic efficiency at -0.3 V vs. RHE and a current density of -31 mA cm^{-2}. Traces of methanol, propanol and a 3 % selec-

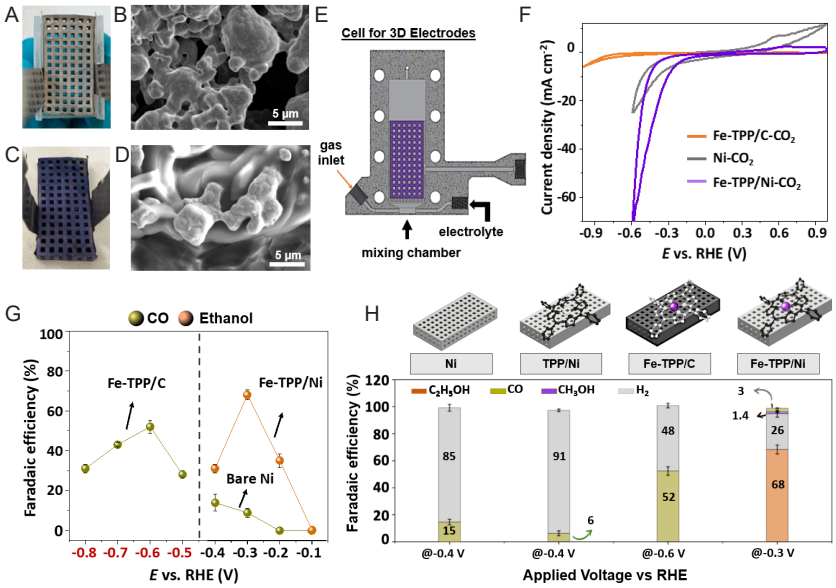

Figure 5.3: (A) A macroscopic and (B) scanning electron microscopy (SEM) image of a 3D porous nickel electrode. (C) A macroscopic and (D) SEM mage of a 3D porous nickel electrode with iron tetraphenylporphyrin drop casted on top using dichloromethane (Fe-TPP/Ni). (E) Schematic of cell design for electrochemical testing of the 3D electrodes. (F) Cyclic voltammetry (CV) comparison of bare nickel, Fe-TPP/Ni and Fe-TPP/C under CO_2-saturated 0.5 M $KHCO_3$ aqueous electrolyte. (G) Faradaic efficiency comparison of the major products of Fe-TPP/C, Fe-TPP/Ni and bare Ni at different potentials in 0.5 M $KHCO_3$. (H) Faradaic efficiency of TPP and Fe-TPP/Ni at their optimal potential of -0.3 V; bare nickel at the optimal potential of -0.4 V; and Fe-TPP/C at the optimal potential of -0.6 V vs. RHE. The error bars in (G) and (H) represent the standard deviation of the products from three separate experiments.

tivity for CO were also observed (Figures D.30-D.35 and Table D.4). The only C_2 product detected is then ethanol, in contrast to copper electrodes which produce substantial hydrocarbon and oxygenate side products such as ethylene and acetate. Notably, the formation of three-carbon species in the form of propanol is observed, indicating higher alcohol formation can also occur. Only hydrogen evolution was observed when replacing CO_2 bubbling with N_2.

The results in Figure 5.3 show that the hybrid metal electrode and molecular catalyst system can greatly modify the traditional behaviour of Fe-TPP. The absence of substantial CO as a product can be explained by the Fe oxidation state remaining between Fe(II) and Fe(III) as observed in the XANES spectra in Figure 5.2 F, preventing the CO release typically observed upon Fe reduction to Fe(I). Further, the dominant formation of ethanol (12 electrons) as a product indicates further CO reduction and coupling of CO intermediates is occurring in the hybrid system at substantial rates. While inorganic nickel oxygenate-derived electrocatalysts have demonstrated the ability to reduce CO_2 to C_{2+} products [31], nickel itself is incapable of CO_2 or CO reduction to multicarbon products at substantial reaction rates, a pure tandem catalytic reaction between Fe-TPP and the Ni electrode cannot explain ethanol formation. A short discussion on the function of nickel itself is also warranted given recent demonstrations of short and long-chain alkane and alkene production during CO_2 reduction [36, 37]. While in our Fe-TPP/Ni case we observe alcohol production at lower potentials and different rates than the alkene/alkane production of pure nickel, the various roles of nickel in electrocatalysis requires further investigation. For example, nickel binds CO strongly, meaning that the exposed nickel sites could provide a C-C coupling species. Alternatively, the poisoning or coking of nickel sites via *CO could serve the role of preventing excess H_2 formation in our case, thus allowing for higher ethanol FE to be reached. These possibilities point to the complex role that the choice of substrate could play in modifying adsorbed molecular species, shuttling intermediates, or providing competing reactions. We then hypothesize that the iron site of the molecular catalyst is able to perform further reductions of bound CO intermediates due to the strong interactions with the Ni electrode as illustrated in Figure 5.1 B. In essence, the hybrid catalyst appears to prevent CO release by inhibiting Fe(I) formation (Figure 5.2 F), while the Ni-Fe interactions could weaken the binding of *CO when iron is in Fe(II)/Fe(III) states [32].

Although the above results indicate how a molecular catalyst can break redox-limitations to reach higher-electron products, they do not explain how carbon-carbon coupling occurs, which typically requires two metal atoms and CO intermediates. Notably, we have shown experimentally that ethanol can be observed as a product when using both CO_2 and CO as a reactant (Figures 5.2 D and E). Additionally, the absence of substantial

by-product CO formation on the Fe-TPP/Ni samples during CO_2 reduction indicates that tandem reactions are not dominant. Carbon-carbon coupling then appears to occur through bound intermediates. While we cannot discern how the coupling step occurs, here we provide speculation based upon the observed experimental data and DFT. Such speculations also allow us to assess reaction mechanisms that allow alcohol to be formed on Fe-TPP/Ni without by-product ethylene (C_2H_4). The mechanism here then likely differs from that of copper electrodes where ethylene:ethanol production rates are close to 2 [38].

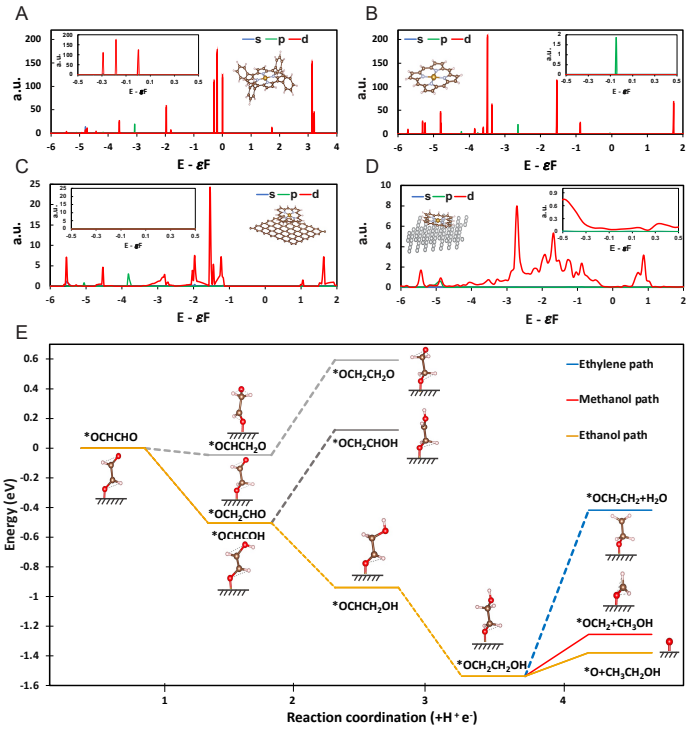

Figure 5.4: Projected density of states of Fe atom in (A) molecular Fe-TPP (B) modified Fe-TPP (C) modified Fe-TPP on graphene, and (D) modified Fe-TPP on nickel. (E) Energy diagram of possible reaction intermediates.

Fe-TPP has been extensively studied—both experimentally and computationally—as a homogeneous catalyst for the CO2RR to 2-electron products such as carbon monoxide and formate. Thus, almost all com-

putational studies on these types of homogeneous catalysts are limited to two proton-coupled-electron transfer (PCET) steps in accordance with experimental observations. Using DFT, we have extended the computational studies on Fe-TPP to further investigate the reaction energetics and mechanism beyond two PCET steps, hypothesizing that there will be a continuous source of electrons to the Fe site to activate it as soon as it is oxidized. We then aim to (i) offer insights into the electronic structure of Fe-TPP, especially when immobilized on a nickel surface, (ii) tackle the most probable pathways for the further protonation of mono-carbonic intermediates, and (iii) analyze the most likely post C-C coupling reaction pathway to understand why ethanol is observed, but not alkanes/alkenes. Without experimental details supporting the coupling step, we do not provide an explicit model for C-C coupling itself.

We then first provide a more in-depth DFT examination of the electronic impact of anchoring Fe-TPP on various substrates. We generated the densities of states for the iron core in Fe-TPP (Figure 5.4 A), modified Fe-TPP (Figure 5.4 B), where the phenyl moiety was substituted with a hydrogen atom, modified Fe-TPP/Gr (Figure 5.4 C), and modified Fe-TPP/Ni (Figure 5.4 D). Analysis of the projected densities of states, specifically considering molecular systems, revealed intermittent electron presence at various energy levels. The deposition of this structure onto a carbon substrate exhibited a broadened density of states, though non-continuous, consistent with previous findings in the literature. Conversely, when the same molecule was adsorbed onto a nickel substrate, the influence of the substrate effect was evident. In this case, a continuous and non-zero density of states was observed, extending even to the Fermi level. This outcome signifies a facilitated electron transfer from the valence band to the conduction band.

Building upon the aforementioned observations, we used the modified Fe-TPP adsorbed on Ni in our reaction energy calculations of reaction energy. This comprehensive system encompassed all considerable mono-carbon reaction intermediates. Notably, we identified the highest reaction energy at the stage where CO undergoes protonation. Contrary to the energetics associated with *COH formation or CO desorption (1.22 eV), we found that the thermodynamics favor the formation of *CHO (0.543 eV), as depicted in Figure D.36. For reaction pathways where the carbon atom is bound to Fe, these simulations then indicate why CO is not observed

as a major reduction product. Contrary to Fe-TPP molecule, we found that mono-carbonic species cannot adsorb onto the modified Fe-TPP/Ni through oxygen; instead, the adsorption occurs solely through the carbon atom. Remarkably, with the inclusion of bi-carbonic intermediates, the scenario is entirely reversed, with adsorption observed solely through oxygen to the surface in both systems. While we have not yet directly observed the mechanism of C-C coupling, given this interaction and reaction energetics of mono-carbon species, we can speculate that a C-C coupling mechanism could lead to the formation of an oxygen-bound *OCHCHO intermediate.

In our final DFT analysis, we then examine further reduction pathways towards methanol, ethanol and ethylene, beginning from *OCHCHO. In particular, we observed a thermodynamic preference toward the formation of the pivotal intermediate *OCH2CH2OH (Figure 5.4 E). This intermediate holds significance as it gives rise to three distinct products, depending on three different protonation scenarios. Notably, the most energy-demanding reaction occurs when protonating the OH functional group, resulting in the formation of a water molecule and *OCH2CH2. This intermediate is recognized for its contribution to ethylene formation. In alternative scenarios, protonation of the two carbon atoms in the key intermediate produces ethanol and methanol, with ethanol displaying higher thermodynamic favorability, as evidenced in Figure 5.4 E. The reduced reaction energies observed in the production of both ethanol and methanol, compared to the previously provided CO protonation energy, indicate the availability of the necessary energy within the reaction environment. Notably, the lower reaction energy for ethanol formation, as compared to methanol (0.157 eV vs. 0.282 eV), underscores a higher Faradaic efficiency in favor of ethanol production. Furthermore, our analysis, illustrated in Figure D.37, indicates that the site regeneration process is characterized by consistently negative reaction energies, mitigating the risk of reaction site poisoning.

Finally, to test the stability of the designed system over longer operation, we operated the Fe-TPP/Ni for an initial 62 h at the constant potential of -0.3 V vs. RHE and a CO_2 flow rate of 10 SCCM (Figure 5.5, Figure D.38, and Figure D.39). During the long-term reaction, a 7 % decrease in ethanol selectivity was observed during the test. Further, by comparing the initial and final catalyst loading, we observed a 5 % decrease

in the amount of immobilized Fe-TPP on the Ni. Nevertheless, no structural damage was detected following electrolysis using scanning electron microscopy and X-ray photoelectron spectroscopy (Figures D.44-D.46).

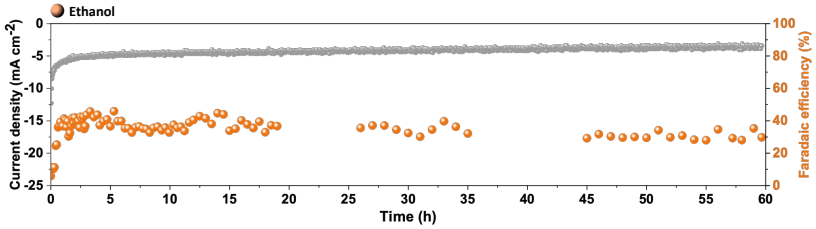

Figure 5.5: Long-term stability test of Fe-TPP/Ni at a constant potential of -0.3 V vs. RHE in 0.5 M $KHCO_3$ with a CO_2 flow rate of 10 SCCM.

5

5.3. Summary and conclusion

Here we have shown that the traditional behaviour of a molecular catalyst can be significantly altered by positioning it onto a metal electrode, demonstrating both CO_2 to ethanol and CO to ethanol conversion with close to unity carbon yields. Critically we have examined only a singular commonly-utilized metalloporphyrin and metal electrode combination. The future variations possible to further alter electrochemical reactions and selectivity are then broad, particularly in view of the substantial existing set of molecular catalysts widely available.

Acknowledgements

R.M.-G. and F.M. acknowledge NWO project 15169 for infrastructure support. A.S. would like to acknowledge the support received from the NSERC Discovery Grant (RGPIN-2020-04960) and the Canada Research Chair (950-23288). M.R. acknowledges the Institut Universitaire de France (IUF) for partial financial support. The DFT computations carried out in this study was supported by Calcul Quebec, Compute Canada. The XAS measurements were performed at the Canadian Light Source (CLS) under the project 36G12729. T.B. would also like to thank Prof. Evgeny Pidko and Prof. Megan Jackson for mechanistic discussions during the project

as well as D. Ripepi for the SEM study.

Author contributions

M.A. conceived the initial project. M.A. synthesized the molecular catalysts. R.M.-G. designed and built the flow cell and 3D structured nickel and carbon electrodes. M.A. and R.M.-G. setup, performed and optimized cell design for the initial sets of flow experiments leading to ethanol formation. M.A. performed the parameterization and stability tests of the 3D porous electrode flow cell experiments, and the 3D electrode material characterizations. A.F. and A.S. performed the DFT computations, analyzed and discussed the results. A.F. also performed the XAS experiments. A.S. supervised the computations and the in-situ XAS experiments. C.L. and J.S. performed the CO_2 and CO experiments of Fe-TPP drop casted onto nickel foam, which were supervised and checked by M.R. T.B. supervised the project. The work was written and edited by all co-authors.

Competing interests

M.A. and T.B. of the Delft University of Technology have filed provisional patent application no. 2034424 regarding the electronic-coupling of a molecular catalyst and metal electrode for electrochemical CO_2 conversion to ethanol.

5.4. Methods

Reagents and chemicals

All reagents and solvents were of commercial reagent grade and were used without further purification, except where noted. Deuterium oxide (D_2O), (> 99.8 %D), iron (II) chloride ($FeCl_2$), N,N-Diisopropylethylamine (> 99 %), and 3-Nitrobenzoic acid (99 %), and potassium bicarbonate (99.7 %) were purchased from Sigma-Aldrich. Nickel powder (-325 mesh, < 53 μm, 99.8 %) and carboxymethylcellulose sodium salt were purchased from Alfa Aesar. Ni foam (99.5%) was purchased form Goodfellow. Araldite two-component epoxy adhesive was purchased from RS Components. The H_2 /Ar mixture (5 %/95 %) was acquired from Linde. The resins used with the Formlabs Form-2 stereolithographic 3D-printer (clear and castable wax resin) were purchased from MakerPoint. Column Chromatography was carried out using Caledon Silica Gel 60. Ultrapure water was generated with a Merck Milli-Q Plus 185. The CO gas used for the blank measurements was supplied by the Linde group and has the 2.0 classification, which corresponds to a purity of $\geq$ 99.0 vol %, with $\leq$ 4000 ppm N_2, $\leq$ 10 ppm H_2, $\leq$ 30 ppm O_2 + Ar, $\leq$ 10 ppm C_xH_y and $\leq$ 5 ppm H_2O. The Ar gas used for purging the cell before the experiments was also supplied by the Linde and has the 5.0 classification, which corresponds to a purity of $\geq$ 99.999 vol %, with < 5 ppm H_2O, < 5 ppm O_2 and < 0.2 ppm C_xH_x.

Material characterization

X-ray photoemission spectroscopy (XPS), X-ray diffraction (XRD) and Scanning Electron 370 Microscopy (SEM)

The XRD, XPS and SEM data were obtained using the Delft University of Technology research facilities. XPS measurements were performed with a Thermo Scientific K-alpha spectrometer using a monochromatic Al Kα excitation source. The spectrometer was calibrated using the C 1s adventitious carbon with a binding energy of 284.8 eV. The base pressure at the analysis chamber was about 2 x 10^{-9} mbar. The spectra were recorded using a spot size of 400 μm at a pass energy of 50 eV and a step size of 0.1 eV. Scanning electron microscopy (SEM) measurements were per-

formed on a Jeol JSM-6010LV. XRD was performed using a Bruker D8 Advanced diffractometer with Cu-Kα source (Cu radiation wavelength: Kα1(100) = 1.54060 Å, Kα2(50) = 1.54439 Å) and Lynxeye-XE-T position sensitive detector. The entire Fe-TPP/Ni electrode was fixed onto the sample stage. Because small inhomogeneities in the sample height exist for a large electrode, there were some shifts of the observed peak positions. This shift is corrected by comparing the measured nickel metal peaks with those from pure nickel as found in Bruker's database. With a fixed-sample-illumination of 3mm, a step size of 0.01, a measuring time of 0.02 s/step for the electrode of 2Θ = 5-90°, 0.6 s/step for electrode of 2Θ = 5-41°and 0.05 s/step for Fe-TPP powder of 2Θ = 5-90°were employed. The data were evaluated by Bruker software DiffracSuite [39, 40].

X-ray Absorption Near Edge Structure (XANES) and Extended X-ray Absorption Fine Structure (EXAFS)

The measurements were conducted at the Canadian Light Source (CLS) using a seven-element silicon drift detectors (SDD) array manufactured by Mirion Technologies. Energy steps with respect to the Fe K-edge were set at 2.0 eV intervals from -80 eV to -6 eV, and 0.35 eV intervals from -6 eV to 40 eV. Each sample underwent two scans, and the average absorptions at each energy level were reported. A dwell time of 1 second was used for each energy level within both mentioned ranges. During the in-situ tests, the gas diffusion layer was exposed to a CO_2-saturated chamber, and 0.5 M $KHCO_3$ was circulated in the anode and cathode chambers with two separate peristaltic pumps. In-situ scans were conducted once per applied potential.

In-situ Fe K-edge X-ray absorption spectra for Fe-TPP/Ni was obtained using the SXRMB beamline at the Canadian Light Source. To simulate reaction conditions, Fe-TPP was drop-casted on 200 nm of Ni sputtered on carbon paper with a gas diffusion layer on its back. Then, using a three compartment flow cell with CO_2 flowing on the gas chamber and 0.5 M $KHCO_3$ as the electrolyte, different constant voltages were applied to obtain XANES plots. Before any in-situ scan, we also used the vacuum chamber at 5 x 10^{-6} torr to obtain ex-situ EXAFS result of the same drop-casted Fe-TPP/Ni, presented in Table D.2.

The experimental procedure Involved the dissolution of Fe-TPP pow-

der in dichloromethane (DCM) at a ratio of 20 mg per 1 ml of DCM. Subsequently, samples comprising 1, 3, and 5 coats were prepared through the spray coating method on a 100 nm thick Ni/CP substrate, resulting in loadings of 0.5, 1.5, and 2.5 mg/cm^2, respectively. The process was repeated with the precursor diluted 10 and 20 times to achieve loadings of 0.05 and 0.025 mg/cm^2, respectively. Fe_2O_3 powder (99.995 % purity) served as the Fe(III) standard, while FeO powder (99.6 % purity) was used as the Fe(II) reference, both purchased from Sigma Aldrich. The measurements were conducted at the Canadian Light Source (CLS) using a seven-element silicon drift detectors (SDD) array manufactured by Mirion Technologies. Energy steps with respect to the Fe K-edge were set at 2.0 eV intervals from -80 eV to -6 eV, and 0.35 eV intervals from -6 eV to 40 eV. Each sample underwent two scans, and the average absorptions at each energy level were reported. A dwell time of 1 second was used for each energy level within both mentioned ranges. During the in-situ tests, the gas diffusion layer was exposed to a CO_2 saturated chamber, and 0.5 M $KHCO_3$ was circulated in the anode and cathode chambers with two separate peristaltic pumps. In-situ scans were conducted once per applied potential.

CO_2RR and CORR experiments in figures 5.2 D and E

The experiments performed in Figures 5.2 D and E were undertaken at Université Paris Cité. The CO_2 electrolysis work was performed in a flow-cell while the CO electrolysis was performed in an H-Cell as described below.

Preparation of deposited porphyrins onto nickel foam for flow and H-cells

The nickel foam was cleaned with acetone using ultrasound for 5 minutes to remove organic impurities from the surface, followed by immersion in a 1 M HCl solution to remove surface oxides. A solution of Fe-TPP (32.5 mg) was made in dichloromethane (1 mL) and was drop-casted onto the pre-prepared nickel foam (1 cm^2) electrode in order to completely cover the surface (catalyst areal loading of 6.5 mg /cm^2). The electrode was dried in a vacuum oven at 50 °C for 2 hours.

CO_2RR electrolysis in flow cell (Figure 5.2 D)

A solution of Fe-TPP (32.5 mg) was made in dichloromethane (1 mL) and was drop casted onto the pre-prepared nickel foam (1 cm^2) electrode to cover the surface completely. The electrode was dried in a vacuum oven for 2 hours. Fe-TPP/Ni foam was assembled onto the cathode in the flow cell device with Ag/AgCl as a reference electrode and Pt/Ti alloy as the anode. The cathode and anode chambers were separated by a Sustainion membrane (Dioxide Materials). CO_2 gas flow was delivered at a flow rate of 20 sccm on the cathode side, while a 0.5 M $NaHCO_3$ (Sigma-Aldrich, >99.7 %) electrolyte was circulated at a flow rate of 10 mL/min in both cathode and anode chambers. The applied potential conversion from SCE reference to RHE reference followed the equation: E (V vs. RHE) = E (V vs. Ag/AgCl) + 0.197 + 0.059 pH. The electrolysis experiment was conducted using a PARSTAT 4000A potentiostat (Princeton Applied Research).

CO2RR electrolysis in H-cell (Figure 5.2 E)

The working electrode was arranged in a three-electrode configuration, with a saturated calomel electrode (SCE) serving as the reference electrode (Hach), and a platinum foam (Goodfellow) serving as the counter electrode. The counter electrode was placed inside an anolyte compartment bridge, which contained the same electrolyte, and was separated from the catholyte by a glass frit. The applied potential conversion from SCE reference to RHE reference followed the equation: E (V vs. RHE) = E (V vs. SCE) + 0.244 + 0.059 pH.

Prior to the start of electrolysis, the gas of interest (Ar and CO both from Air Liquid) was flushed for 20 minutes. After 20 minutes, the gas flow was stopped, and the electrolysis experiment was then initiated. After electrolysis, 100 μL of gas headspace above the catholyte was sampled using a gas-tight syringe (Hamilton) inserted through the rubber septum and injected into a GC-TCD system (Agilent Technologies 7820A GC) for analysis. The liquid products were analyzed using a Bruker AC 400 MHz NMR apparatus. A total of 392 μL of the solution of interest, 48 μL of D_2O (Sigma Aldrich, 99 % atoms D), and 40 μL of a 4 mM DMSO (Sigma Aldrich, Anhydrous 99.8 %) solution were mixed in an NMR tube.

A minimum of 128 scans were accumulated using the water pre-saturation method with a relaxation time of 25 s. Quantification was performed relative to the DMSO peak.

CO_2RR experiments on 3D electrodes in Figure 5.3 and Figure 5.5

Preparation of the porous 3D-nickel electrodes

The nickel electrode in Figure 5.3 A was fabricated based on the technique of indirect 3D-printing first introduced by Hereijgers et al. [41, 42]. The electrode moulds were designed in the CAD software Autodesk Inventor 2019 and 3D printed in Formlabs Castable Wax resin on a Formlabs Form-2 stereolithographic 3D-printer. A paste consisting of nickel powder (61.7 wt %), epoxy resin (10 wt%) and an aqueous solution of 3 wt% carboxymethylcellulose sodium salt (CMC, 24.3 wt%) and sodium chloride (4 wt%) was mixed thoroughly in a ceramic bowl and then filled into a 10 ml syringe with Luer-Lock connector. CMC functions as a liquefaction agent in order to create a paste that can be injected into the electrode mould (Figure D.3) [43, 44]. Sodium chloride serves as a pore former which is washed out of the final sintered electrode structure. The epoxy resin provides the green part with the necessary mechanical strength following mould removal. In order to facilitate the injection of the nickel paste, the 3D printed electrode mould includes an integrated Luer-Lock connector. This allows for the application of the required pressure to pass the paste through the electrode mould. The filled electrode mould was then placed in an oven at 60 °C for 24 hours under atmospheric conditions in order to cure the epoxy resin. Following the curing procedure, the Luer-Lock connector of the mould was sawed off and excess material was filed off from the mould openings with a powered filing tool (Dremel). This is essential in order to prevent blockage of the channels in the final electrode.

The removal of the wax mould, debinding of the epoxy resin and initial sintering were combined in a furnace (Nabertherm L5/12/C450) under atmospheric conditions based on the recommendations of Formlabs: In an initial drying step, the temperature is increased to 150 °C (5 °C min^{-1}) followed by a dwell time of 1h at the same temperature. During this step, residual moisture in the green part and the electrode mould was removed

by evaporation. The temperature was then increased to 371 °C (2.2 °C min^{-1}) and held for 2 h. This causes the wax in the mould to melt out slowly, which increases airflow to the rest of the resin. Burnout of the wax-resin begins slowly with moderate expansion, preventing damage to the green part. The remaining resin burned out in the following step: The temperature is increased to 732 °C (2 °C min^{-1}), and the green part is held at this temperature for 4.7 h. In the final sintering step, the temperature was slowly increased to 1000 °C (1 °C min^{-1}) and held for 10 min, followed by a cooldown back to room temperature at approximately 5 °C min^{-1}.

The porosity of the electrode can be determined by the mass of water absorbed by the electrode pores:

$$\begin{aligned}\epsilon &= \frac{V_p}{V_p + V_s} \\ &= \frac{\frac{m_{H_2O}}{\rho_{H_2O}}}{\frac{m_{H_2O}}{\rho_{H_2O}} + \frac{m_{Ni}}{\rho_{Ni}}} \\ &= \frac{\frac{1.14\,\mathrm{g}}{0.997\,\frac{\mathrm{g}}{\mathrm{cm}^3}}}{\frac{1.14\,\mathrm{g}}{0.997\,\frac{\mathrm{g}}{\mathrm{cm}^3}} + \frac{3.451\,\mathrm{g}}{8.908\,\frac{\mathrm{g}}{\mathrm{cm}^3}}} = 0.7469\end{aligned} \tag{5.1}$$

where m_{H_2O} is the mass of absorbed water, m_{Ni} is the weight of the nickel electrode, ρ_{H_2O} is the density of water and ρ_{Ni} is the density of nickel. Finally, the electrode was dried under vacuum at 80 °C to constant weight. Nickel contacts (0.15 mm thick) were purchased from NKON and spot-welded onto the sides of the electrode with a SUNKKO 738 AL spot welding machine purchased from Banggood. The first contact was welded directly onto the electrode side, and a second contact is spot welded perpendicular on the first contact and leads out of the cell.

The initial sintering step described above needs to be conducted in the presence of oxygen, i.e. atmospheric conditions, in order to fully burn out the mould material and epoxy. Under an inert argon atmosphere, i.e. pyrolysis conditions, Hereijgers et al. [41] report carbon residues from the epoxy resin that prevents the sintering of the nickel particles. However, this results in the oxidation of the nickel structure, significantly reducing the electrical conductivity. Therefore, a second sintering step under a reducing atmosphere (H_2/Ar) is necessary. The brown parts ware transferred to a tube oven (Applied Test Systems, Inc., Series 3210) with a

quartz tube of 35 mm in diameter. Air was removed by evacuating and refilling the tube with a mixture of 5 % H2 in Argon three times. The flow rate of the H_2/Ar-mixture was then set to 150 ml/min and, following the reduction procedure outlined by Hereijgers et al. [41], the temperature was increased to 800 °C (1 °C min^{-1}) and held for 2 h. In addition to the reduction of nickel oxide formed during the initial sintering step under atmospheric conditions, the nickel sintered further, which yields a mechanically more stable electrode. In the next step, the sodium chloride pore former was removed by rinsing the electrode for 1h at 80 °C in demineralized water.

Preparation of deposited porphyrins onto 3D-nickel electrode (Fe-TPP/Ni)

As shown in Scheme 1, iron porphyrins were synthesized beginning with the condensation of pyrrole and benzaldehyde by an electrophilic substitution reaction to form tetraphenylporphyrin (TTP) as reported in our previous works [45, 46]. It was then metalated using $FeCl_2$ to form iron porphyrin compound (Fe-TPP).

A solution of Fe-TPP (130 mg) in dichloromethane (4 mL) was drop casted onto the pre-prepared 3D nickel electrode and let dry in a vacuum oven for 2 hours. Turning the electrode colour from gray to purple indicates the nickel electrode has been fully covered with purple Fe-TPP, making it easy to distinguish any uncovered surface area. The Fe-TPP catalyst concentration was calculated as 2.7 x 10^{-5} mol cm^{-2} relative to the geometrical electrode area (5.16 cm^2).

Fabrication of the carbon black control electrode (Fe-TPP/C)

To evaluate the Fe-TPP catalyst performance and product composition in the absence of nickel, a replica of the sintered nickel electrode was 3D-printed (SLA Formlabs Form 2, clear resin) and subsequently coated with carbon black to yield a conductive 525 surface. A solution of Fe-TPP (130 mg) in dichloromethane (4 mL) and 5 % Nafion was then drop casted onto the carbon black electrode (Figure D.26). Unlike the sintered nickel electrode, contacts could not be spot welded onto the electrode surface. Instead, nickel contacts were pressed onto the electrode surface and then

glued with epoxy resin.

Cell design for the 3D electrodes

The three-electrode setup was comprised of a RHE reference electrode (Mini-Hydroflex, Gaskatel), a nickel foam counter electrode, and one of the described 3D electrodes (Ni, TPP-Ni, Fe-TPP/C and Fe-TPP/Ni). Using a custom-designed cell reactor allows for CO_2 to be bubbled through the bottom of the reactor and through the porous electrode channels. The cell set-up is shown in Figures D.19-D.22. The anode and cathode chambers of the electrolyzer were separated by a Nafion-17 ion-exchange membrane, resulting in two separate flow circuits for the electrolyte. The electrolyte was pumped through both the anode and the cathode chamber using a 2-channel peristaltic pump.

In addition to the electrolyte, the exiting streams of the anode and cathode chamber contained gaseous O_2 and reaction products (liquid and gaseous). These were separated from the electrolyte in the catholyte and anolyte reservoirs before flowing to the gas chromatograph (GC) or being vented. The gas flow entering the cathode chamber was controlled by a flow controller (Bronkhorst EL-Flow Select). A flow meter (Bronkhorst Low deltaP-Flow) was used to measure the flow rate of the gas stream exiting the catholyte reservoir. This flow meter served two purposes: Firstly, by comparing the outlet flow with the set inlet flow (FC, Figure D.23), leaks could be detected during the set-up. Secondly, the outlet flow rate was required for the calculation of the gaseous Faradaic efficiency. The pressure of the catholyte circuit was controlled by a pressure controller (Bronkhorst EL-Press) and was set to atmospheric pressure. The temperature within the catholyte chamber was measured via a K-type thermocouple and recorded with a Picolog TC-08 data logger. The thermocouple was inserted into the cell and sealed via an Idex flangeless male nut and ferrule.

As a result of the 2-point measurement shown in Figure D.22, contact resistances were not present in the potential measurement. The volume of the cathode compartment was sufficiently high to also allow for measurements without flow, i.e. in H-cell configuration (~28 ml). The temperature in the cathode compartment was measured via a thermocouple positioned behind the working electrode at half the electrode height. Nickel foam

with a spot-welded nickel tab served as the counter electrode. Electrode contacts, ion-exchange membrane and the counter electrode are placed and sealed in between EPDM flat gaskets. The anode compartment consisted of the anode flow chamber, which allowed for electrolyte flow between the counter electrode and the Nafion membrane, as well as an electrolyte reservoir.

Electrochemical measurements for the 3D electrodes

For each electrochemical reaction, the solution was first saturated with either CO_2 or Ar. The gas flow rate was then set using a gas flow controller (FC, Figure D.23) and purged through the bottom of the custom cell. The electrochemical studies were carried out using a P4000 potentiostat (Princeton Applied Research) with a three-electrode setup. Deposited iron porphyrin onto nickel (Fe-TPP/Ni) served as a working electrode in the cathode chamber, nickel foam (auxiliary) and a reversible hydrogen electrode (RHE) (reference electrode). Chronoamperometry measurements were performed using determined RHE potentials.

CO_2 electrolysis gas product analysis for the 3D electrodes

To estimate the Faradaic efficiency of gaseous products produced 569 in the CO_2RR, the outlet flow of the cathode compartment was periodically analyzed using a gas chromatograph (InterScience PerkinElmer Clarus 680) coupled with two thermal conductivity detectors (TCD) and a flame ionization detector (FID). The concentration of gas products (CO and H_2) from CO2RR was calculated from an average of four GC injections. The volume fraction of gas products from GC is equal to the mole fraction for ideal gases. The mole fraction of water vapour exiting the reactor was measured using a humidity sensor and found to be 78 % ($x_{H_2O} = 0.023$). Since the sum of mole fractions is equal to 1, the mole fraction of CO_2 exiting was calculated as below.

$$x_{CO_2,out} = 1 - (x_{CO} + x_{H_2O} + x_{H_2}) \tag{5.2}$$

After calculating the mole fractions of all gaseous products, the volumetric flow rate at the outlet of the reactor was measured with the flow

meter and used to calculate the moles of each product:

$$\dot{n}_{CO} = \dot{V}_{outlet} \times x_{CO} \tag{5.3}$$

$$\dot{n}_{H_2O} = \dot{V}_{outlet} \times x_{H_2} \tag{5.4}$$

$$FE_{CO} = \frac{n_{CO} \times n^{e^-} \times F}{I} \times 100\% \tag{5.5}$$

Here: $\dot{n}_{CO}$ – moles/s of CO produced, n^{e^-} – number of electrons inovlved in CO_2RR (2 electrons for CO), F – 96485 C/mol and I – applied current (in Amperes).

CO_2 electrolysis liquid product analysis for the 3D electrodes

Following CO2RR, electrolyte samples were taken from the cathode compartment. 1H NMR was measured using Bruker 400 MHz and processed using MestreNova. 400 μl of electrolyte sample, 50 μl of a solution of dimethyl sulfoxide (DMSO) as internal standards, and 50 μl of D_2O were mixed for the 1H NMR analysis. 1H NMR chemical shifts (δ) are reported in ppm in deuterium oxide (D_2O).

The liquid products were also analyzed in a high-pressure liquid chromatograph (HPLC, 1290 Infinity II, Agilent) to determine the composition of the liquid products. An aminex HPX-87H organic acid analysis column is used for the HPLC analysis. The product peaks in the HPLC chromatogram of the experimental sample were compared with the calibration peaks of the reference components to determine the type of the component (by comparing the retention time) and its concentration (by comparing the area). The retention time of the observed peak is around 39-40 minutes, which corresponds to ethanol's retention time according to the HPLC calibration data. The concentration of ethanol is calculated using the formula:

$$C = m \times A \tag{5.6}$$

where, C is the concentration of the product in mM, A is the area of the product peak, and m is the slope of the calibration curve for the component. The calibration curve for a component was generated by analyzing various concentrations of the component in HPLC, such as 0.1 mM, 0.5 mM, 1 mM, 5 mM, 10 mM, 25 mM and 50 mM, and then plotting the peak areas of the component on the x-axis and concentrations on the y-axis to obtain the slope of the calibration curve, m. In the above example, the concentration of ethanol in the experimental sample can be calculated to be 55.52 mM, using an m value of 7.0807 x 10^{-4} units.

Protocol for the quantitative analysis of the pervaporate concentration with gas chromatography

To provide greater information regarding the evolution of C_{2+} products, the volatile effluents (methanol, ethanol, propanol) in the CO_2-off-gas were detected by the flame ion detector (FID). This allowed us to see increases and decreases of products over time separately from the NMR and HPLC characterizations. Here the calibration protocol for a quantitative use of this technique is outlined.

To perform the qualitative calibration of volatile compounds, a set of controlled experiments was designed according to the volatility principle of their liquid mixtures (Figure D.30). A partially filled beaker was filled with x % vol. of ethanol in Milli-Q Water (where x varied from 0 to 50 %). Once enough energy is supplied to break apart the bonds between molecules, the molecules are free to expand and escape the liquid surface in the form of a gas, through the process of vaporization. This depends upon the chemical properties of the liquid (i.e. hydrogen bonding specifically can be a determinant of the volatility of a molecule in water). Volatile liquids, including ethanol, vaporize with relative ease. With sufficient kinetic energy, the liquid particles of ethanol would liberate from the surface, vaporize and transition into the gas phase inside the beaker. As gas concentration accumulates in the head-space of the beaker, the distance separating individual molecules (such as ethanol vs. H_2O vapour/humidity) decreases until Van der Waals and hydrogen bonds can drive clusters of molecules back into liquid form (condensation) [47].

Eventually, vaporization and condensation reach a state of equilibrium, where no particles are lost but instead, the gas phase is constantly being

recycled into the liquid phase. Hence, purging an inert gas such as Ar into the mixture provides sufficient kinetic energy to obtain a semi-quantitative calibration of that mixture. An example is given in Figures D.25 A and B, where we have used four different volumetric concentrations of Ethanol (1, 10, 20 and 50 % vol. Ethanol in MQ-Water). The beaker was exposed to air for a few seconds while changing the ethanol mixture to measure the peak area for different concentration levels. This resulted in an increase in the nitrogen (N_2) and oxygen (O_2) amount at the headspace, observed by the TCD peak area. We have noticed that the concentration of O_2 decreased by 3-fold, alongside a stable N_2 concentration. The following injections after that point gave a stable ethanol peak area, which suggests that the liquid-alcohol equilibrium is established once all the air (in the form of O_2:N_2) is purged by the GC sampling loop. To compensate for any error at this point, a minimum of 20 injections (each of 4 min) were collected to ensure an equilibrium at the headspace. Hence, a stable FID peak area of ethanol was obtained, resulting in a linear calibration curve. The same protocol was successfully applied for other hydrocarbons, such as methanol, acetone and propanol, leading to a linear calibration.

Density functional theory computational details

DFT computations were performed using the Vienna Ab initio simulation package (VASP) [48], on Compute Canada clusters. In all computations, we used the projected augmented wave (PAW) pseudopotentials and the generalized gradient approximation (GGA) of Perdew-Burke-Ernzerhof (PBE) to describe the exchange-correlation functionals [49]. A cut-off energy of 450 eV for the planewave basis sets and a 2x2x1 Γ-centered Monkhorst-Pack mesh for the k-point sampling in the first Brillouin zone, with a first order Methfessel-Paxton smearing parameter σ of 0.05 eV, ensured that the energy convergence criteria are better than 1 meV for a vacuum of 20 Å or greater. The self-consistent field (SCF) convergence criterion is set to 10^{-4} eV for electronic iteration, and the ionic relaxation continued till the maximum force was less than 0.02 eV/Å that was updated by the conjugate gradient approach. Dipole corrections and spin polarization are implemented. The DFT-D3 method with the Becke-Jonson damping is performed for the Van der Waals correction. The electrostatic charge density around each ion is calculated by the Bader charge analysis

method [50]. VESTA software is used for the visualization [51]. Structure optimization, electron density and delocalization calculations follow the standard procedures described in literature [52].

References

[1] M. Abdinejad, A. Farzi, R. Möller-Gulland, F. M. Mulder, C. Liu, J. Shao, J. Biemolt, M. Robert, A. Seifitokaldani, and T. Burdyny, *Eliminating redox-mediated electron transfer mechanisms on a supported molecular catalyst enables CO_2 conversion to ethanol,* Nature Catalysis **7**, 1109 (2024).

[2] C. Costentin, M. Robert, and J.-M. Savéant, *Molecular catalysis of electrochemical reactions,* Current Opinion in Electrochemistry **2**, 26 (2017).

[3] H. Rao, L. C. Schmidt, J. Bonin, and M. Robert, *Visible-light-driven methane formation from CO_2 with a molecular iron catalyst,* Nature **548**, 74 (2017).

[4] J. Shen, R. Kortlever, R. Kas, Y. Y. Birdja, O. Diaz-Morales, Y. Kwon, I. Ledezma-Yanez, K. J. P. Schouten, G. Mul, and M. T. Koper, *Electrocatalytic reduction of carbon dioxide to carbon monoxide and methane at an immobilized cobalt protoporphyrin,* Nature Communications **6**, 8177 (2015).

[5] I. Bhugun, D. Lexa, and J.-M. Savéant, *Catalysis of the electrochemical reduction of carbon dioxide by iron (0) porphyrins: Synergystic effect of weak Brönsted acids,* Journal of the American Chemical Society **118**, 1769 (1996).

[6] E. Boutin, M. Wang, J. C. Lin, M. Mesnage, D. Mendoza, B. Lassalle-Kaiser, C. Hahn, T. F. Jaramillo, and M. Robert, *Aqueous electrochemical reduction of carbon dioxide and carbon monoxide into methanol with cobalt phthalocyanine,* Angewandte Chemie International Edition **58**, 16172 (2019).

[7] J. Wu, S. Ma, J. Sun, J. I. Gold, C. Tiwary, B. Kim, L. Zhu, N. Chopra, I. N. Odeh, R. Vajtai, *et al.*, *A metal-free electrocatalyst for carbon dioxide reduction to multi-carbon hydrocarbons and oxygenates,* Nature Communications **7**, 13869 (2016).

[8] Y. Song, R. Peng, D. K. Hensley, P. V. Bonnesen, L. Liang, Z. Wu, H. M. Meyer III, M. Chi, C. Ma, B. G. Sumpter, *et al.*, *High-*

selectivity electrochemical conversion of CO_2 to ethanol using a copper nanoparticle/N-doped graphene electrode, ChemistrySelect **1**, 6055 (2016).

[9] W. Ma, S. Xie, T. Liu, Q. Fan, J. Ye, F. Sun, Z. Jiang, Q. Zhang, J. Cheng, and Y. Wang, *Electrocatalytic reduction of CO_2 to ethylene and ethanol through hydrogen-assisted C–C coupling over fluorine-modified copper,* Nature Catalysis **3**, 478 (2020).

[10] T. T. H. Hoang, S. Ma, J. I. Gold, P. J. A. Kenis, and A. A. Gewirth, *Nanoporous copper films by additive-controlled electrodeposition: CO_2 reduction catalysis,* ACS catalysis **7**, 3313 (2017).

[11] F. Li, Y. C. Li, Z. Wang, J. Li, D.-H. Nam, Y. Lum, M. Luo, X. Wang, A. Ozden, S.-F. Hung, B. Chen, Y. Wang, J. Wicks, Y. Xu, Y. Li, C. M. Gabardo, C.-T. Dinh, Y. Wang, T.-T. Zhuang, D. Sinton, and E. H. Sargent, *Cooperative CO_2-to-ethanol conversion via enriched intermediates at molecule–metal catalyst interfaces,* Nature Catalysis **3**, 75 (2020).

[12] M. Jouny, W. Luc, and F. Jiao, *General techno-economic analysis of co_2 electrolysis systems,* Industrial & Engineering Chemistry Research **57**, 2165 (2018).

[13] K. Jiang, R. B. Sandberg, A. J. Akey, X. Liu, D. C. Bell, J. K. Nørskov, K. Chan, and H. Wang, *Metal ion cycling of Cu foil for selective C–C coupling in electrochemical CO_2 reduction,* Nature Catalysis **1**, 111 (2018).

[14] Z.-Q. Liang, T.-T. Zhuang, A. Seifitokaldani, J. Li, C.-W. Huang, C.-S. Tan, Y. Li, P. De Luna, C. T. Dinh, Y. Hu, *et al.*, *Copper-on-nitride enhances the stable electrosynthesis of multi-carbon products from CO_2,* Nature Communications **9**, 3828 (2018).

[15] D. Ren, B. S.-H. Ang, and B. S. Yeo, *Tuning the selectivity of carbon dioxide electroreduction toward ethanol on oxide-derived Cu_xZn catalysts,* ACS Catalysis **6**, 8239 (2016).

[16] M. Abdinejad, C. Dao, B. Deng, F. Dinic, O. Voznyy, X.-a. Zhang, and H.-B. Kraatz, *Electrocatalytic reduction of co_2 to ch_4 and co in*

aqueous solution using pyridine-porphyrins immobilized onto carbon nanotubes, ACS Sustainable Chemistry & Engineering **8**, 9549 (2020).

[17] M. Abdinejad, T. Yuan, K. Tang, S. Duangdangchote, A. Farzi, H.-P. Iglesias van Montfort, M. Li, J. Middelkoop, M. Wolff, A. Seifitokaldani, *et al.*, *Electroreduction of Carbon Dioxide to Acetate using Heterogenized Hydrophilic Manganese Porphyrins,* Chemistry–A European Journal **29** (2023).

[18] X. Wang, Z. Wang, F. P. García de Arquer, C.-T. Dinh, A. Ozden, Y. C. Li, D.-H. Nam, J. Li, Y.-S. Liu, J. Wicks, *et al.*, *Efficient electrically powered CO_2-to-ethanol via suppression of deoxygenation,* Nature Energy **5**, 478 (2020).

[19] J.-M. Savéant, *Molecular catalysis of electrochemical reactions. Mechanistic aspects,* Chemical Reviews **108**, 2348 (2008).

[20] M. N. Jackson, C. J. Kaminsky, S. Oh, J. F. Melville, and Y. Surendranath, *Graphite conjugation eliminates redox intermediates in molecular electrocatalysis,* Journal of the American Chemical Society **141**, 14160 (2019).

[21] S. D. Tilley, *Metal-like molecules,* Nature Catalysis **5**, 359 (2022).

[22] B. E. Murphy, S. A. Krasnikov, N. N. Sergeeva, A. A. Cafolla, A. B. Preobrajenski, A. N. Chaika, O. Lubben, and I. V. Shvets, *Homolytic cleavage of molecular oxygen by manganese porphyrins supported on Ag (111),* ACS nano **8**, 5190 (2014).

[23] D. A. Duncan, P. S. Deimel, A. Wiengarten, R. Han, R. G. Acres, W. Auwärter, P. Feulner, A. C. Papageorgiou, F. Allegretti, and J. V. Barth, *Immobilised molecular catalysts and the role of the supporting metal substrate,* Chemical communications **51**, 9483 (2015).

[24] F. Petraki, H. Peisert, F. Latteyer, U. Aygul, A. Vollmer, and T. Chassé, *Impact of the 3d electronic states of cobalt and manganese phthalocyanines on the electronic structure at the interface to Ag (111),* The Journal of Physical Chemistry C **115**, 21334 (2011).

[25] F. Petraki, H. Peisert, P. Hoffmann, J. Uihlein, M. Knupfer, and T. Chassé, *Modification of the 3d-electronic configuration of man-*

ganese phthalocyanine at the interface to gold, The Journal of Physical Chemistry C **116**, 5121 (2012).

[26] F. Petraki, H. Peisert, I. Biswas, U. Aygül, F. Latteyer, A. Vollmer, and T. Chassé, *Interaction between cobalt phthalocyanine and gold studied by X-ray absorption and resonant photoemission spectroscopy,* The Journal of Physical Chemistry Letters **1**, 3380 (2010).

[27] J. Uihlein, H. Peisert, M. Glaser, M. Polek, H. Adler, F. Petraki, R. Ovsyannikov, M. Bauer, and T. Chassé, *Communication: Influence of graphene interlayers on the interaction between cobalt phthalocyanine and Ni (111),* The Journal of Chemical Physics **138** (2013).

[28] M. Schmid, A. Kaftan, H.-P. Steinrück, and J. M. Gottfried, *The electronic structure of cobalt (II) phthalocyanine adsorbed on Ag (111),* Surface Science **606**, 945 (2012).

[29] C. Costentin, M. Robert, and J.-M. Saveant, *Current issues in molecular catalysis illustrated by iron porphyrins as catalysts of the co$_2$-to-co electrochemical conversion,* Accounts of Chemical Research **48**, 2996 (2015).

[30] Y. i. Hori, *Electrochemical co$_2$ reduction on metal electrodes,* Modern Aspects of Electrochemistry , 89 (2008).

[31] Y. Zhou, A. J. Martín, F. Dattila, S. Xi, N. López, J. Pérez-Ramírez, and B. S. Yeo, *Long-chain hydrocarbons by CO2 electroreduction using polarized nickel catalysts,* Nature Catalysis **5**, 545 (2022).

[32] Z. Zeng, L. Y. Gan, H. Bin Yang, X. Su, J. Gao, W. Liu, H. Matsumoto, J. Gong, J. Zhang, W. Cai, *et al.*, *Orbital coupling of heterodiatomic nickel-iron site for bifunctional electrocatalysis of CO_2 reduction and oxygen evolution,* Nature Communications **12**, 4088 (2021).

[33] T. E. Westre, P. Kennepohl, J. G. DeWitt, B. Hedman, K. O. Hodgson, and E. I. Solomon, *A multiplet analysis of Fe K-edge 1s→ 3d pre-edge features of iron complexes,* Journal of the American Chemical Society **119**, 6297 (1997).

[34] C. Römelt, J. Song, M. Tarrago, J. A. Rees, M. van Gastel, T. Weyhermuller, S. DeBeer, E. Bill, F. Neese, and S. Ye, *Electronic structure of a formal iron (0) porphyrin complex relevant to CO_2 reduction,* Inorganic Chemistry **56**, 4745 (2017).

[35] A. Kumar, *Interfacial electronic properties of FeTPP-Cl on HOPG,* Materials Today: Proceedings **57**, 898 (2022).

[36] Y. Zhou, A. J. Martín, F. Dattila, S. Xi, N. López, J. Pérez-Ramírez, and B. S. Yeo, *Long-chain hydrocarbons by CO_2 electroreduction using polarized nickel catalysts,* Nature Catalysis **5**, 545 (2022).

[37] R. E. Vos and M. T. M. Koper, *Nickel as Electrocatalyst for CO_2 Reduction: Effect of Temperature, Potential, Partial Pressure, and Electrolyte Composition,* ACS Catalysis **14**, 4432 (2024).

[38] M. Jouny, W. Luc, and F. Jiao, *High-rate electroreduction of carbon monoxide to multi-carbon products,* Nature Catalysis **1**, 748 (2018).

[39] N. Li, Z. Su, P. Coppens, and J. Landrum, *X-ray diffraction study of the electronic ground state of (meso-tetraphenylporphinato) iron (ii),* Journal of the American Chemical Society **112**, 7294 (1990).

[40] S. C. Hunter, B. A. Smith, C. M. Hoffmann, X. Wang, Y.-S. Chen, G. J. McIntyre, and Z.-L. Xue, *Intermolecular interactions in solid-state metalloporphyrins and their impacts on crystal and molecular structures,* Inorganic Chemistry **53**, 11552 (2014).

[41] J. Hereijgers, J. Schalck, J. Lölsberg, M. Wessling, and T. Breugelmans, *Indirect 3D printed electrode mixers,* ChemElectroChem **6**, 378 (2019).

[42] J. Hereijgers, J. Schalck, and T. Breugelmans, *Mass transfer and hydrodynamic characterization of structured 3D electrodes for electrochemistry,* Chemical Engineering Journal **384**, 123283 (2020).

[43] M. Oshitani, H. Yufu, K. Takashima, S. Tsuji, and Y. Matsumaru, *Development of a pasted nickel electrode with high active material utilization,* Journal of the Electrochemical Society **136**, 1590 (1989).

[44] W.-H. Zhu, D.-J. Zhang, and J.-J. Ke, *Electrochemical impregnation and performance of nickel hydroxide electrodes with porous plaques of hollow nickel fibres,* Journal of Power Sources **56**, 157 (1995).

[45] M. Abdinejad, A. Seifitokaldani, C. Dao, E. H. Sargent, X.-a. Zhang, and H. B. Kraatz, *Enhanced electrochemical reduction of CO_2 catalyzed by cobalt and iron amino porphyrin complexes,* ACS Applied Energy Materials **2**, 1330 (2019).

[46] M. Abdinejad, C. Dao, X.-A. Zhang, and H. B. Kraatz, *Enhanced electrocatalytic activity of iron amino porphyrins using a flow cell for reduction of CO_2 to CO,* Journal of Energy Chemistry **58**, 162 (2021).

[47] P. Atkins, *Chemical Principles* (W.H. Freeman and Company, New York, NY, 2013).

[48] G. Kresse and J. Hafner, *Ab initio molecular dynamics for liquid metals,* Physical Review B **47**, 558 (1993).

[49] J. P. Perdew, K. Burke, and M. Ernzerhof, *Generalized gradient approximation made simple,* Physical Review Letters **77**, 3865 (1996).

[50] G. Henkelman, A. Arnaldsson, and H. Jónsson, *A fast and robust algorithm for Bader decomposition of charge density,* Computational Materials Science **36**, 354 (2006).

[51] K. Momma and F. Izumi, *Vesta: a three-dimensional visualization system for electronic and structural analysis,* Journal of Applied Crystallography **41**, 653 (2008).

[52] H. Al-Mahayni, X. Wang, J.-P. Harvey, G. S. Patience, and A. Seifitokaldani, *Experimental methods in chemical engineering: Density functional theory,* The Canadian Journal of Chemical Engineering **99**, 1885 (2021).

6

Outlook: A flow-through battery-electrolyser

Increasing the efficiency for electrolysis of an integrated battery-electrolyser requires the reduction of ohmic resistances and bubble induced losses. Here, we present a 3D printed flow cell employing the 3D structured flow-through electrodes developed in this thesis. In preliminary experiments, we demonstrate efficient electrolysis at current densities as high as 1000 mA/cm^2. The flow cell set-up can serve as a platform for future studies on the impact of electrolyte flow rate, temperature and electrode geometry.

6.1. Introduction

While the development of electrodes as discussed in the previous chapters can significantly contribute to improving the performance of an integrated battery-electrolyser, the cell design must also be considered. Especially at higher current densities, bubbles generated during electrolysis contribute significantly to energetic losses by increasing the electrolyte resistance and covering the catalytically active electrode surface [1–4]. The reduction in electrolyte conductivity, κ, can be approximated using the Bruggeman equation [4, 5]:

$$\kappa = \kappa_0 \, (1 - f)^{3/2} \tag{6.1}$$

where κ_0 refers to the intrinsic electrolyte conductivity in the absence of bubbles and f describes the volume fraction of the electrolyte occupied by gas bubbles. In a conventional electrolyser with planar electrodes, the bulk of the bubbles occupies the volume between the anode and cathode, i.e. the inter-electrode gap. For a given current density, increasing the distance will increase the inter-electrode electrolyte volume and thus lower the volume fraction of gas bubbles. While this reduces ohmic losses incurred from bubbles, the cell resistance increases due to the larger electrode distance. This implies that there is an optimal electrode distance for electrolysis at a given current density [6]. However, specifically in the case of an integrated battery-electrolyser as discussed in this thesis, any increase in the electrode distance that mitigates bubble losses during electrolysis will also increase overpotentials during discharging when no bubbles are generated. Therefore, a solution is needed that allows for efficient electrolysis without negatively affecting subsequent discharging.

With the 3D structured nickel and iron electrodes described in this thesis, the inter-electrode gap can be reduced significantly while still allowing for effective gas removal via the electrode channels (Figure 6.1 B). This also reduces the required cell volume and can therefore reduce the costs per cell in a stack. Electrolyte flowing through, rather than past, the electrode further facilitates the removal of bubbles from the cell. While materials such as metal foams [7, 8] and microfibers [9] have been successfully demonstrated as flow-through electrodes in alkaline water electrolysis, bubbles can be easily trapped due to their disordered structure

[10, 11].

3D structured electrodes with an ordered geometry, on the other hand, can be designed and 3D printed specifically to facilitate bubble removal [11, 12]. In addition, the geometry of such electrodes can be adjusted to significantly reduce the pressure drop of electrolyte flowing through [13]. This enables higher electrolyte flow velocities which have been shown to effectively reduce screening effects of bubbles [3, 14]. Finally, higher electrolyte flow rates as well as more intimate contact with the electrode surface are expected to improve heat transfer which facilitates cooling at high current densities and reduces the time required to reach operating temperatures during start-up. Here, we present the design for a flow-through battery-electrolyser and show preliminary results for the combination of a sintered 3D nickel battery anode and a sintered 3D nickel cathode.

6.2. Cell design for 3D flow-through electrodes

Figures 6.1 and 6.2 show the cell design we developed for a battery-electrolyser employing 3D structured flow-through electrodes. All cell components were 3D printed using a Formlabs Form 2 stereolithographic 3D printer. The cell is divided into two identical halves containing the anode (nickel electrode) and the cathode (iron electrode). The two halves are separated by a membrane (Zirfon PERL UTP 500, Agfa) in order to prevent mixing of hydrogen and oxygen generated during electrolysis. Electrolyte (30 wt% KOH(aq.)) enters each cell half via the inlet at the bottom of the cell and is distributed over the cross-section of each electrode via a flow-distributor consisting of rectangular 15 x 4 array of channels with a diameter of 0.8 mm. After flowing through the electrode, the electrolyte exits the electrode compartment at the top of the cell. Each electrode is placed into a 3D printed frame close to the membrane. This reduces the ohmic resistance in the inter-electrode gap between anode and cathode and prevents electrolyte flowing past rather than through the electrode. The latter facilitates bubble removal.

Electrode contacts are spot-welded to each electrode as described in Chapter5. The cell includes a total of four EPDM flat gaskets (ERIKS) with an uncompressed thickness of 1 mm. These seal the membrane and the contact leads exiting the cell. In order to compress the flat gaskets

more effectively and improve the seal, the cell features compression plates machined from stainless steel (316) on each side. If the compression of the gaskets is taken into account, the electrode frame can be designed to define the distance between the electrode and the membrane. In the configuration discussed in this work, this distance is approximately 0.62 mm. Including the 0.5 mm thick membrane, this amounts to an inter-electrode gap of approximately 1.74 mm[1].

The electrode potential in each cell half is measured against a reversible hydrogen electrode (Mini-HydroFlex, Gaskatel) connected to the electrolyte inlet via a capillary. As a result, not only the cell potential is measured, but also the potentials of the individual electrodes. This enables simultaneous monitoring of the individual electrode potential as well as the overall cell potential. The temperature of each cell half is measured via a thermocouple (RS PRO Type T, 1.5 mm diameter, RS online). A cut-out in the electrode frame next to the tip of the thermocouple allows for a more direct measurement of the temperature close to the electrode. The reference electrodes and thermocouples are sealed via boss-type seal using EPDM o-rings (ERIKS). All voltage and temperature measurements are recorded by the Maccor 4000 battery cycling system used for running the electrochemical experiments.

A two-channel peristaltic pump (Masterflex L/S Digital Drive with Easy-Load-II pumphead, Metrohm) circulates the electrolyte between the cell halves and their respective anolyte and catholyte reservoirs. The only connection between the reservoirs is a hydraulic bridge to compensate for changes in filling levels that occur during long-term operation of the cell. Hydrogen and oxygen exit the catholyte and anolyte reservoir, respectively, through a tube submerged approximately 15 mm under water. This prevents air from entering the cell. The temperature of the electrolyte is regulated by placing the reservoir flasks onto a hot-plate. In order to compensate for heat losses across the tubing from the reservoirs to the cell, the setting of the heat plate is adjusted based on the measurement of the thermocouples installed in the cell.

[1] $2 \times 0.62\ \text{mm} + 0.5\ \text{mm} = 1.74\ \text{mm}$.

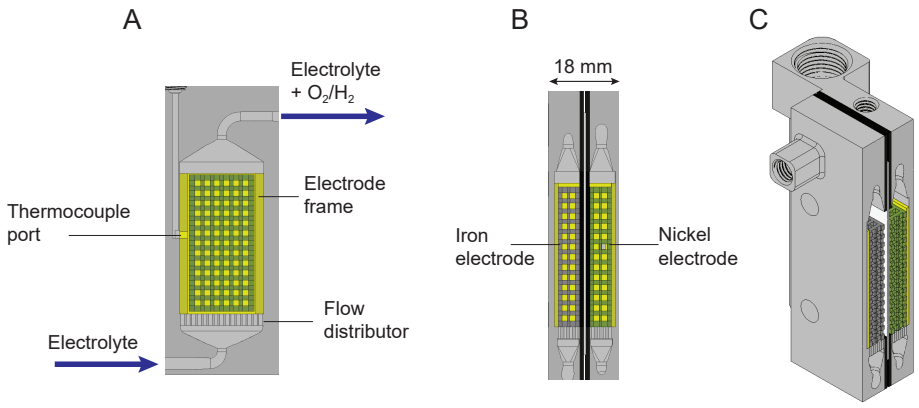

Figure 6.1: Front view (A), side view (B) and isometric view (C) of the internal flow cell design. The compression plates are not shown here. The inter-electrode gap including the 0.5 mm thick membrane is approximately 1.7 mm.

6.3. Preliminary results

At the time the flow cell was ready for initial testing, the iron electrodes discussed in Chapter 4 had not been developed yet. For this reason, we manufactured two indirectly 3D printed porous nickel electrodes as described in Chapter 5. To demonstrate the integrated battery and electrolyser functionality, one electrode was loaded with $Ni(OH)_2$ as shown in Appendix B. The loaded areal capacity was approximately 44 mAh/cm^2. This electrode served as the anode, while the 3D nickel electrode with no active material loading served as the cathode.

Following activation cycling, the anode was charged for 1 h at a charge rate of 200 mA/cm^2. This was followed by polarization experiments at increasing current densities up to 1000 mA/cm^2 and varying electrolyte flow velocities and temperatures. As shown in Figure 6.3, increasing the electrolyte flow rate from 50 ml/min to 200 ml/min at 22 °C results in a decrease in cell potential of 33 mV at 1000 mA/cm^2. This indicates improved bubble removal from the cell at higher flow velocities. Increasing the electrolyte temperature to 60 °C decreases the cell potential by an

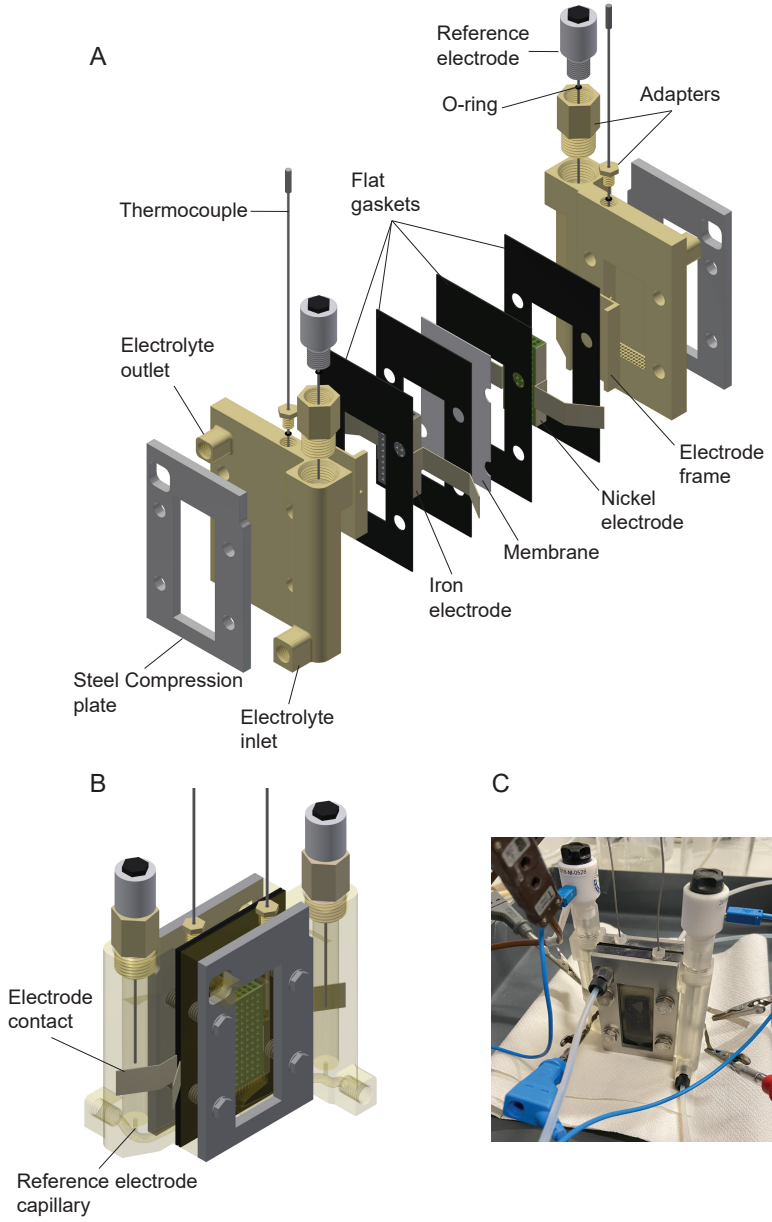

Figure 6.2: Flow-through battolyser™ cell design. Explosion view (A) and assembled view (B) of the CAD model. (C) Photo of the fully assembled 3D printed flow cell.

additional 765 mV to a cell voltage of 2.14 V. This is equivalent to a thermal energy efficiency of 69 %. At a current density of 200 mA/cm^2 and 400 mA/cm^2, the thermal efficiency increases to 91 % (1.62 V) and 83 % (1.78 V), respectively. We note, that while our results include the electrolyte and membrane resistance, the electronic contact resistances are not taken into account. This is because one of the two contacts on each electrode was used for current insertion, while the other served for the potential measurement.

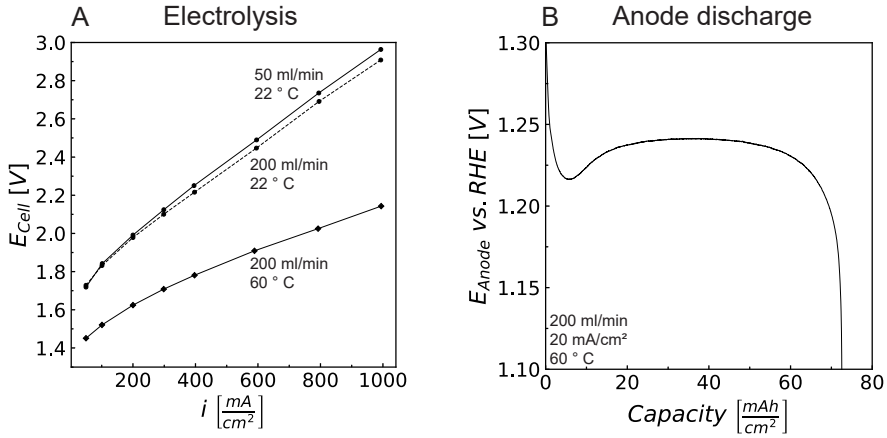

Figure 6.3: Preliminary results obtained from the flow cell with a 3D nickel cathode and a 3D nickel anode loaded with $Ni(OH)_2$. The dimensions of each electrode were approximately 16 mm x 5 mm x 31 mm (width x thickness x height) with channels of 1 mm x 1 mm. (A) Cell potentials for electrolysis at various current densities, temperatures and electrolyte (30 wt% KOH(aq.)) flow rates through the 3D electrodes. The battery anode was charged at a current density of 200 mA/cm^2 for one hour prior to electrolysis. (B) Following the polarization experiments in (A), the anode was discharged at a discharge current density of 20 mA/cm^2 at 60 °C and an electrolyte flow rate of 200 ml/min.

Following the electrolysis experiments, the anode was discharged at a discharge current density of 20 mA/cm^2. The electrolyte flow rate and electrolyte temperature were maintained at 200 ml/min and 60 °C, respectively. As shown in Figure 6.3 B, the anode maintains a consistent discharge voltage for most of the discharge cycle. Remarkably, the discharge capacity is 66 % higher than the originally loaded capacity (73 mAh/cm^2 vs. 44 mAh/cm^2). High charge rates as well as significant overcharging

are known to promote the formation of $\gamma-$NiOOH with a higher oxidation state compared to $\beta-$NiOOH [15, 16]. In addition, high overpotentials in combination with elevated temperatures can result in the oxidation of the sintered nickel scaffold to $Ni(OH)_2$ [17]. These combined effects could explain the high discharge capacity exceeding that of the initially loaded $Ni(OH)_2$ active mass.

6.4. Conclusions

In summary, we presented a 3D printed flow cell for a battery-electrolyser that employs the 3D structured flow-through electrodes developed in this thesis. The reduction of the inter-electrode gap as well as facilitated bubble removal via the electrode channels reduce the cell resistance and thus increase electrolysis efficiency. Using a nickel anode loaded with $Ni(OH)_2$ and a bare nickel cathode, we demonstrated efficient water electrolysis at low cell potentials. Despite electrolysis currents of up to 1000 mA/cm^2, the nickel anode could still be discharged. Our preliminary experiments demonstrate that the flow cell set-up can serve as a platform for future studies on the impact of electrolyte flow speed, temperature and electrode geometry.

References

[1] A. Angulo, P. van der Linde, H. Gardeniers, M. Modestino, and D. F. Rivas, *Influence of bubbles on the energy conversion efficiency of electrochemical reactors,* Joule **4**, 555 (2020).

[2] H. Vogt, *The actual current density of gas-evolving electrodes—notes on the bubble coverage,* Electrochimica Acta **78**, 183 (2012).

[3] B. E. Bongenaar-Schlenter, L. J. J. Janssen, S. J. D. Van Stralen, and E. Barendrecht, *The effect of the gas void distribution on the ohmic resistance during water electrolytes,* Journal of Applied Electrochemistry **15**, 537 (1985).

[4] G. F. Swiegers, R. N. Terrett, G. Tsekouras, T. Tsuzuki, R. J. Pace, and R. Stranger, *The prospects of developing a highly energy-efficient water electrolyser by eliminating or mitigating bubble effects,* Sustainable Energy & Fuels **5**, 1280 (2021).

[5] P. Mandin, J. Hamburger, S. Bessou, and G. Picard, *Modelling and calculation of the current density distribution evolution at vertical gas-evolving electrodes,* Electrochimica Acta **51**, 1140 (2005).

[6] Y. Nishiki, K. Aoki, K. Tokuda, and H. matsuda, *Effect of gas evolution on current distribution and ohmic resistance in a vertical cell under forced convection conditions,* Journal of Applied Electrochemistry **16**, 615 (1986).

[7] Q. De Radigues, G. Thunis, and J. Proost, *On the use of 3-D electrodes and pulsed voltage for the process intensification of alkaline water electrolysis,* International Journal of Hydrogen Energy **44**, 29432 (2019).

[8] F. Rocha, R. Delmelle, C. Georgiadis, and J. Proost, *Effect of pore size and electrolyte flow rate on the bubble removal efficiency of 3d pure ni foam electrodes during alkaline water electrolysis,* Journal of Environmental Chemical Engineering **10**, 107648 (2022).

[9] F. Yang, M. J. Kim, and B. J. Wiley, *Alkaline Water Electrolysis at 20 A cm-2 with a Microfibrous, flow-through Electrolyzer,* in *Elec-*

trochemical Society Meeting Abstracts 235, 29 (The Electrochemical Society, Inc., 2019) pp. 1379–1379.

[10] L. Wang, X. Huang, S. Jiang, M. Li, K. Zhang, Y. Yan, H. Zhang, and J. M. Xue, *Increasing gas bubble escape rate for water splitting with nonwoven stainless steel fabrics,* ACS Applied Materials & Interfaces **9**, 40281 (2017).

[11] T. Kou, S. Wang, R. Shi, T. Zhang, S. Chiovoloni, J. Q. Lu, W. Chen, M. A. Worsley, B. C. Wood, S. E. Baker, *et al.*, *Periodic porous 3D electrodes mitigate gas bubble traffic during alkaline water electrolysis at high current densities,* Advanced Energy Materials **10**, 2002955 (2020).

[12] F. Rocha, R. Delmelle, C. Georgiadis, and J. Proost, *Electrochemical performance enhancement of 3D printed electrodes tailored for enhanced gas evacuation during alkaline water electrolysis,* Advanced Energy Materials **13**, 2203087 (2023).

[13] J. Hereijgers, J. Schalck, and T. Breugelmans, *Mass transfer and hydrodynamic characterization of structured 3D electrodes for electrochemistry,* Chemical Engineering Journal **384**, 123283 (2020).

[14] R. J. Balzer and H. Vogt, *Effect of electrolyte flow on the bubble coverage of vertical gas-evolving electrodes,* Journal of the Electrochemical Society **150**, E11 (2002).

[15] D. Singh, *Characteristics and effects of γ-NiOOH on cell performance and a method to quantify it in nickel electrodes,* Journal of the Electrochemical Society **145**, 116 (1998).

[16] A. H. Zimmerman, *Technological implications in studies of nickel electrode performance and degradation,* Journal of Power Sources **12**, 233 (1984).

[17] U. Erdmann, H. Ewe, and E. W. Justi, *Positive Raney-Nickel-DSK-Elektroden für alkalische Akkumulatoren,* Energy Conversion **13**, 103 (1973).

A

3D hybrid battery-electrolyser nickel electrodes: A theoretical analysis

Supporting information to Chapter 2.

A

A.1. Derivation of $\kappa_{eff,3D}$

The differential equation describing the potential distribution (Equation 2.6) requires the average cross-sectional electrolyte area A_{el} over the electrode thickness. This includes the average cross-sectional electrolyte area of the channels with void fraction Θ and the pores with porosity ϵ:

$$A_{el} = A_{el,\Theta} + A_{el,\epsilon} \tag{A.1}$$

$A_{el,\epsilon}$ can be determined from the porosity, the volume of porous electrode material V_p and the electrode thickness l:

$$A_{el,\epsilon} = \frac{\epsilon V_p}{l} \tag{A.2}$$

The void fraction Θ is defined as $\Theta = V_{ch}/V_{tot}$. Here, V_{ch} and V_{tot} represent the channel volume and the total geometric electrode volume (width x height x thickness), respectively. With $V_p = V_{tot}(1-\Theta)$, we can write:

$$A_{el,\epsilon} = \frac{V_{tot}}{l}\epsilon(1-\Theta) \tag{A.3}$$

$A_{el,\Theta}$ can be defined as:

$$A_{el,\Theta} = \frac{\Theta V_{tot}}{l} \tag{A.4}$$

Inserting Equations A.3 and A.4 in Equation A.1 yields:

$$\begin{aligned} A_{el} &= \frac{V_{tot}}{l}\left[(1-\Theta)\epsilon + \Theta\right] \\ &= A\left[(1-\Theta)\epsilon + \Theta\right] \end{aligned} \tag{A.5}$$

where A is the superficial electrode area (width x height). For κA_{el} in Equation 2.6, we can then write:

$$\begin{aligned} \kappa A_{el} &= \kappa\left[(1-\Theta)\epsilon^{\tau} + \Theta\right] A \\ &= \kappa_{eff,3D}\ A \end{aligned} \tag{A.6}$$

Note that we included the tortuosity τ of the pores. For a conventional Non-3D electrode, i.e. $\Theta = 0$, $\kappa_{eff,3D}$ then reduces to the Bruggeman relation:

$$\kappa_{eff,3D}(\Theta = 0) = \kappa_{eff} = \kappa\epsilon^{\tau} \tag{A.7}$$

In principle, a tortuosity describing the channels could also be included. However, such a tortuosity would require a well-defined geometry and would also change with the void fraction. As the goal of this work was the modelling of the current and potential distribution independent of the specific electrode geometry, such a channel tortuosity was not taken into account here.

A.2. Calculation of $\Delta\Phi(0)$

For high overpotentials, the superficial current density j can be calculated as [1]:

$$j = \frac{USl}{A} j_0 \exp\left(\frac{\alpha F}{RT}\eta(0)\right) \tag{A.8}$$

Where $\eta(0)$ refers to the measured overpotential at the front of the electrode ($x = 0$). Solving for the overpotential:

$$\eta(0) = \frac{RT}{\alpha F} \ln\left(\frac{A}{USl}\frac{j}{j_0}\right) \tag{A.9}$$

The difference between the overpotentials for a 3D electrode and a conventional electrode can then be written as:

$$\begin{aligned}\Delta\eta(0) &= \frac{RT}{\alpha_a F} \ln\left(\frac{A}{U_{3D}S_0(1-\Theta)l}\frac{j}{j_0}\right) - \frac{RT}{\alpha_a F} \ln\left(\frac{A}{U_0 S_0 l}\frac{j}{j_0}\right) \\ &= \frac{RT}{\alpha_a F} \ln\left(\frac{U_0}{U_{3D}(1-\Theta)}\right)\end{aligned} \tag{A.10}$$

Inserting Equation 2.32 yields:

$$\Delta\eta(0) = \frac{RT}{\alpha_a F} \ln\left(\frac{1}{\Gamma}\right) \tag{A.11}$$

And with $\Phi = RT\eta/F$:

$$\Delta\Phi(0) = \frac{1}{\alpha_a} \ln\left(\frac{1}{\Gamma}\right) \tag{A.12}$$

A.3. Approximation of the reaction penetration depth

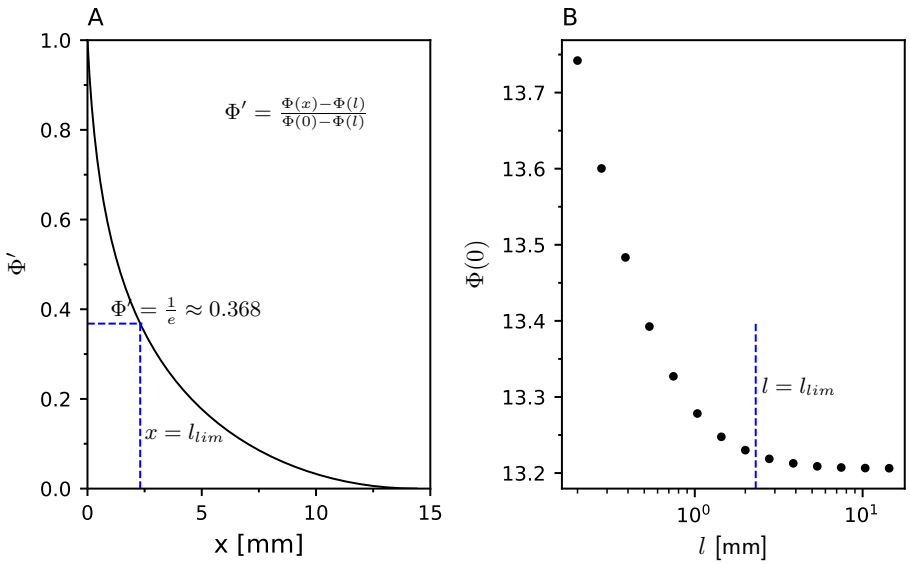

Figure A.1: Approximation of the reaction penetration depth at a superficial current density of 200 mA/cm^2 and an electrode porosity of 0.38. (A) Normalized electrode polarization Φ' as defined by Posey [2] at position x across the electrode thickness l. The reaction penetration depth l_{lim} is approximately where $\Phi' = 1/e$ [3]. (B) Increasing the electrode thickness beyond l_{lim} does not lead to a significant reduction in the reduced electrode polarisation at the front of the electrode ($\Phi(0)$).

A.4. Model implementation

The dimensionless differential Equations 2.9 and 2.24 were solved via the finite difference method implemented in Python version 3.8.5. To accelerate computation, we used the Cython programming language that optimizes Python code by compiling it into C [4]. All computations were performed on an Alienware Aurora R13 PC with an intel CORE i7 processor. The model implementation was validated for OER by comparison with the results of Posey et al. [2].

A.5. Modeling parameters

Table A.1: Modeling parameters.

Parameter	Value	Unit	References
κ	62.11	S/m	[5]
$j_{0,OER,ref}$	$1 \cdot 10^{-7}$	A/m^2	[6]
$j_{0,CR,ref}$	1.22	A/m^2	[6]
$\alpha_{a,OER}$	1.35[a]	-	[6, 7]
$\alpha_{a,OER}$	0.5	-	[6]
$\alpha_{a,CR}$	0.5	-	[6]
c_{OH}	6.89	mol/L	
$c_{OH,ref}$	7.1	mol/L	[6]
$E_{0,OER}$	0.271	V vs. Hg/HgO	
$E_{0,1/2}$	0.4	V vs. Hg/HgO	[8]
S_0	906[b]	m	
A	$6.34 \cdot 10^{-4}$	m^2	
τ	1.5	-	[9]
T	293	K	

[a] Determined to fit the experimentally measured Tafel slope of around 89 mV/dec (Chapter 3), it lies within the range used in the references [6, 7].

[b] Based on values measured for the electrochemically active surface area (ECSA) in Appendix B.5.

A

References

[1] S. Rausch and H. Wendt, *Morphology and utilization of smooth hydrogen-evolving raney nickel cathode coatings and porous sintered-nickel cathodes,* Journal of the Electrochemical Society **143**, 2852 (1996).

[2] F. Posey, *Methods for the calculation of polarization in porous electrodes,* Journal of the Electrochemical Society **111**, 1173 (1964).

[3] M.-B. Liu, G. M. Cook, and N. P. Yao, *Transient current distributions in porous zinc electrodes in KOH electrolyte,* Journal of The Electrochemical Society **129**, 239 (1982).

[4] S. Behnel, R. Bradshaw, C. Citro, L. Dalcin, D. S. Seljebotn, and K. Smith, *Cython: The best of both worlds,* Computing in Science & Engineering **13**, 31 (2010).

[5] R. J. Gilliam, J. W. Graydon, D. W. Kirk, and S. J. Thorpe, *A review of specific conductivities of potassium hydroxide solutions for various concentrations and temperatures,* International Journal of Hydrogen Energy **32**, 359 (2007).

[6] P. De Vidts and R. E. White, *Mathematical modeling of a nickel-cadmium cell: Proton diffusion in the nickel electrode,* Journal of the Electrochemical Society **142**, 1509 (1995).

[7] P. De Vidts, J. Delgado, and R. E. White, *A multiphase mathematical model of a nickel/hydrogen cell,* Journal of the Electrochemical Society **143**, 3223 (1996).

[8] A. Iranzo and F. M. Mulder, *Nickel-iron layered double hydroxides for an improved Ni/Fe hybrid battery-electrolyser,* Materials Advances **2**, 5076 (2021).

[9] A. M. Raventos, G. Kluivers, J. W. Haverkort, W. De Jong, F. M. Mulder, and R. Kortlever, *Modeling the performance of an integrated battery and electrolyzer system,* Industrial & Engineering Chemistry Research **60**, 10988 (2021).

B

3D nickel electrodes for hybrid battery and electrolysis devices

Parts of this appendix have been accepted for publication in Cell Reports Physical Science as supplementary information to "3D Nickel Electrodes for Hybrid Battery and Electrolysis Devices" (2024, Chapter 3).

B.1. Chemicals

Nickel powder (-325 mesh, < 53 μm, 99.8 %), potassium hydroxide (85 %), nickel (II) nitrate hexahydrate (98 %) and carboxymethylcellulose sodium salt (CMC) were purchased from Alfa Aesar. Araldite two-component epoxy resin was purchased from RS Components. Ultrapure water was prepared using a Merck Milli-Q Plus 185. The H_2 / Ar mixture (5 % / 95 %) was purchased from Linde. The resin used with the Formlabs Form-2 stereolithographic (SLA) 3D-printer ("Clear" resin) was purchased from MakerPoint. The 3D electrode moulds were 3D printed from the Poly-Lactic Acid (PLA) filament "EasyFil PLA" purchased from Form Futura.

B.2. Electrode preparation

Electrode moulds and filling tools were designed in the CAD software Autodesk Inventor 2019. The electrode moulds were then printed in PLA via fused deposition modelling (FDM) on a Prusa MK3 S 3D-printer. Filling tools used to inject the paste into the 3D electrode moulds were printed in clear resin on a Formlabs Form-2 SLA 3D-printer. Using the filling tools and a 5 ml syringe with Luer-Lock connection, the electrode moulds were filled with a nickel paste consisting of nickel powder (61.5 wt%), epoxy (14.3 wt%) and an aqueous solution of 3 wt% carboxymethylcellulose sodium salt (24.2 wt%). The ratios of the paste compounds are based on the findings of Hereijgers et al. [1]. Before the removal of the electrode mould, solidifying the electrode paste is required by curing the epoxy resin at 60 °C for 3 hours. Following the curing procedure, excess hardened paste is filed off from the mould openings with a powered filing tool (Dremel). This is essential to prevent blockage of the channels in the final electrode. After curing of the epoxy, the PLA mould material was removed by placing the moulds in well stirred 25 wt% aqueous potassium hydroxide solution at 80 °C for 15 hours. This results in the dissolution of most of the mould material. Any remaining PLA is softened sufficiently to be blown off with pressurized nitrogen. The epoxy, and thus the mechanical integrity of the green part, were not affected by the potassium hydroxide solution. Following the mould removal, the green parts are rinsed thoroughly in demineralised water in order to remove the potassium hydroxide. Finally, the green parts are dried at 80 °C under vacuum (100

mbar) to constant weight (Thermo Scientific VT 6025 Vacuum Drying Oven).

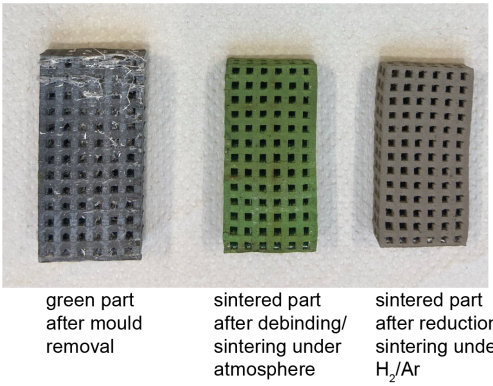

Figure B.1: 3D electrode scaffold at different stages of the manufacturing process.

In the next step, the rinsed green parts are sintered in a furnace under atmospheric conditions (Nabertherm L5/12/C450). We adapted the sintering procedure from Hereijgers et al. [1]: Under atmospheric conditions, the green part is first heated to 350 °C (5 °C min^{-1}), followed by a temperature increase to 600 °C (1 °C min^{-1}). The green part is kept at 600 °C for 1 h in order to burn away the epoxy before increasing the temperature to 1000 °C (1 °C min^{-1}). Sintering of the metal particles is achieved by maintaining the temperature at 1000 °C for 1 h followed by a cool down to room temperature at a rate of 5 °C min^{-1} . This initial sintering step must be conducted in the presence of oxygen, i.e. atmospheric conditions, in order to fully burn out the epoxy resin and any PLA residues. Under an inert argon atmosphere, i.e. pyrolysis conditions, Hereijgers et al. [1] report carbon residues from the epoxy resin that prevents the sintering of the nickel particles. However, this results in the oxidation of the nickel structure, significantly reducing the electrical conductivity. Therefore, a second sintering step under a reducing atmosphere (H_2/Ar) is necessary. The brown parts ware transferred to a tube oven (Applied Test Systems, Inc., Series 3210) with a quartz tube of 35 mm in diameter. Air is removed by evacuating and refilling the tube with a mixture of 5 % H_2 in Argon three times. The temperature is then increased to 800 °C (1 °C min^{-1}) and held for 2 h at a flow rate of 100 ml/min. This allows for the com-

plete reduction of nickel oxide formed in the brown part during the initial sintering step under atmosphere. The degree of reduction is assessed via the weight decrease of the electrode (21 % decrease in weight from NiO to Ni) as well as via XRD. During the sintering procedure the electrodes shrink as summarized in Table B.1. We observe further that temperature inhomogeneities induced by the gas flow in the tube oven can result in warpage of the electrodes. This warpage is more likely to occur for the Non-3D electrodes as the open structure of the 3D electrodes facilitates a more homogeneous temperature profile. Nickel contacts (0.15 mm thick) were purchased from NKON and spot-welded onto the sides of the electrode with a SUNKKO 738 AL spot welding machine purchased from Banggood. Prior to spot-welding, the electrodes were cleaned with acetone using ultrasound for 5 minutes, followed by drying at 80 °C under vacuum (100 mbar) to constant weight.

Table B.1: Shrinkage during sintering.

	3D [% shrinkage]	Non-3D [% shrinkage]
Width	14.5	11.5
Height	11.5	10.5
Thickness	13.3	13.3

Nickel Hydroxide ($Ni(OH)_2$) is loaded on the reduced electrodes by thermal decomposition of nickel (II) nitrate hexahydrate ($Ni(NO3)_2 \cdot 6$ H_2O) based on the procedure outlined by Falk and Salkind [2]. Nickel nitrate hexahydrate (~ 200 g) is filled in a SAN container (500 ml, Mepal) and placed in a preheated vacuum oven at 100 °C. As soon as the nitrate bath reaches a temperature of approximately 90 °C, the electrodes are placed in the molten nickel nitrate hexahydrate and vacuum (40 mbar) is applied for 4 min followed by 6 min under atmospheric condition. Note that no additional water is added. The electrodes are then removed from the nickel nitrate bath and excess material on the electrode surface is blown off with nitrogen. In the next step, the now loaded electrodes are roasted in a furnace at 220 °C for 1 h under atmosphere. The electrodes are then removed from the oven and excess material is once again brushed off from the electrode surface. Special care has to be taken to remove material that has accumulated within the open structures of the electrodes. In the next step, the electrodes are placed in 25 wt% aqueous potassium hydroxide

solution at 80 °C overnight. This is followed by a rigorous rinsing step in demineralised water at 80 °C in order to remove remaining nitrates. The loaded electrodes are then dried at 80 °C under vacuum (100 mbar) to constant weight. This loading procedure was repeated four times to reach the desired theoretical capacity of ~ 140 mAh/cm^2 (based on 289 mAh/g of $Ni(OH)_2$). We note that it is essential to spot-weld the contacts before the loading procedure.

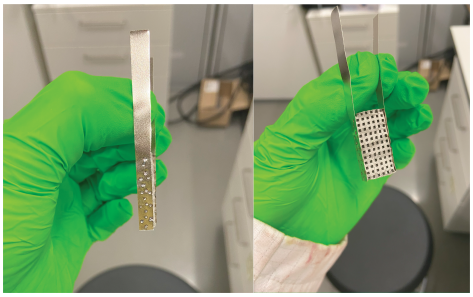

Figure B.2: Contacts spot-welded onto the sintered nickel scaffolds before active material loading.

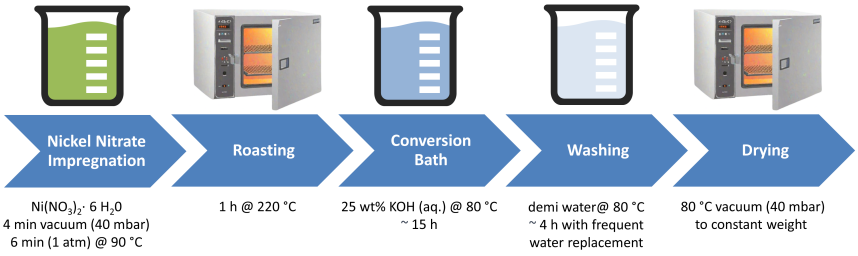

Figure B.3: Procedure for loading $Ni(OH)_2$ onto the nickel electrodes.

B.3. Measuring the electrode porosity and void fraction

The porous electrode model described in Chapter 2 requires both the void fraction Θ and porosity ϵ as inputs. To determine the porosity, the electrodes are soaked in water for at least 20 min. The porosity is then determined by the change in weight, i.e. the mass of water absorbed by the electrode pores:

$$\begin{aligned}\epsilon &= \frac{V_P}{V_{el,s}} \\ &= \frac{V_P}{V_P + V_{Ni} + V_{Ni(OH)_2}} \\ &\approx \frac{\frac{m_{H_2O}}{\rho_{H_2O}}}{\frac{m_{H_2O}}{\rho_{H_2O}} + \frac{m_{Ni}}{\rho_{Ni}} + \frac{m_{Ni(OH)_2}}{\rho_{Ni(OH)_2}}}\end{aligned} \tag{B.1}$$

Here $V_{el,s}$ is the volume of the porous electrode material excluding the volume of the electrode channels. It is comprised of the pore volume V_P, the volume of the sintered nickel scaffold V_{Ni} and the volume of loaded $Ni(OH)_2$ $V_{Ni(OH)_2}$. These are determined from the density ρ and the mass m of each compound. Using this technique, the porosity can be determined after each loading iteration following the water rinsing step. However, we find that at higher material loadings the electrode channels reduce in size due to active material depositing on the surface (Figure B.14). While most of this surface loading flakes off during electrode activation and the electrode channels regain their original size, it can hinder the removal of water during the porosity measurement resulting in an overestimate of the porosity. This is apparent from Figure B.4, where the decrease in porosity of the 3D electrode does not follow the same trend as observed for the Non-3D electrode. Alternatively, the porosity can be determined first before loading (ϵ_0) when water retention in the channels is low, and then be estimated from the mass of loaded $Ni(OH)_2$:

$$\epsilon \approx \epsilon_0 - \frac{m_{Ni(OH)_2}}{\rho_{Ni(OH)_2} V_{el,geo}(1-\Theta)} \tag{B.2}$$

where $V_{el,geo}$ refers to the geometric electrode volume (height x width x thickness). Note that Equation B.2 assumes all the loaded active material to be in the pores. Therefore, it constitutes a lower boundary for the porosity. After four loading cycles, the water uptake technique for the 3D electrode yields a porosity of 50 % compared to 40 % determined with Equation B.2. The void fraction represents the ratio of the channel volume $V_{el,ch}$ to the geometric electrode volume. It can be estimated experimentally from the measured values for the geometric electrode volume, initial porosity and weight of the sintered nickel scaffold:

$$\begin{aligned}\Theta &= \frac{V_{el,ch}}{V_{el,geo}} \\ &\approx 1 - \frac{m_{Ni}}{\rho_{Ni} V_{el,geo}} \left(1 + \frac{\epsilon_0}{1-\epsilon_0}\right)\end{aligned} \tag{B.3}$$

This yields an estimated void fraction of 39 % for the 3D electrode compared to 53 % determined from the CAD model. This discrepancy could be the result of inhomogeneous shrinkage during sintering. We note that Equation B.3 assumes the measured initial porosity ϵ_0 to include the entire porosity of the electrode. The presence of inaccessible pores would result in an increase in calculated void fraction.

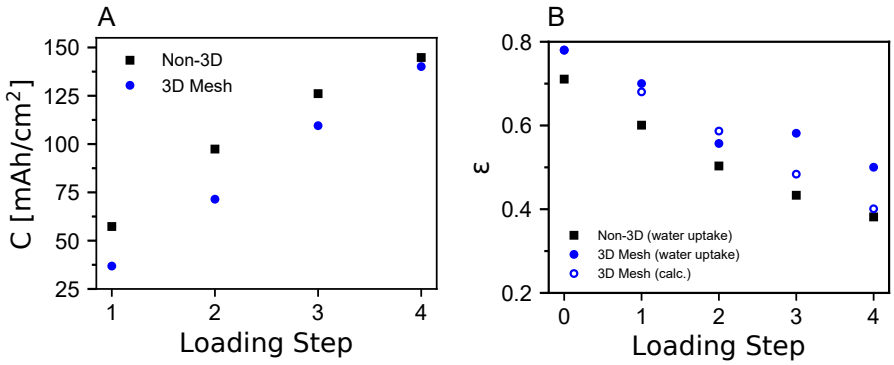

Figure B.4: (A) Areal capacity after each loading step based on a gravimetric capacity of 289 mAh/g for $Ni(OH)_2$. (B) Porosity after each loading step based on the water uptake and calculated via Equation B.2 for the 3D electrode.

B.4. Electrochemical testing

The electrodes were placed in a 3D printed frame as shown in Figure B.5. The frame was designed in Autodesk Inventor 2019 and printed with a Formlabs Form-2 stereolithographic 3D printer using Formlabs' proprietary "Clear" resin. It allows for the secure and reproducible positioning of the reference electrode (RE), counter electrode (CE, Ni foam) and the working electrode (WE). The Hg/HgO reference electrode (Origalys Origasens) was placed adjacent to the working electrode and connected ionically via a capillary. Due to the vicinity of the RE to the WE, the required voltage correction due to the solution resistance is reduced. A groove in the frame allows for bubbles to escape between the electrode contact and capillary so that noise in the potential measurement (WE vs. RE) is significantly reduced. One of the two welded electrode contacts was used to insert the current, the other was used to measure the electrode potential. This removes the electronic resistance of the nickel strip as well as the contact resistance from the measurement. Note that a CE was installed on either side of the WE, but for all data shown in this work only one CE was connected. Furthermore, a thermocouple (RS PRO Type T, 1.5 mm diameter, purchased from RS Online) was placed next to the WE. This was included to ensure that temperatures do not rise excessively, especially at high current densities. The frame including the WE, RE, CE and thermocouple was placed in a 500 ml SAN container (Mepal) filled with approximately 450 g of 30 wt% KOH(aq.). Contacts, RE and thermocouple were led through openings cut in the lid and secured with Parafilm (Figure B.6). All experiments involving battery cycling, i.e. charging and discharging, were conducted with a Maccor 4000 battery cycling system. EIS and ECSA measurements were conducted using a PARSTAT 4000A potentiostat (Princeton Applied Research). Water consumed during electrolysis was replaced regularly with ultrapure water to minimize changes in electrolyte concentration. Ultrapure water was prepared using a Merck Milli-Q Plus 185. The potential of the used Hg/HgO reference electrodes vs. the reversible hydrogen electrode (RHE) was determined using a HydroFlex RHE purchased from Gaskatel.

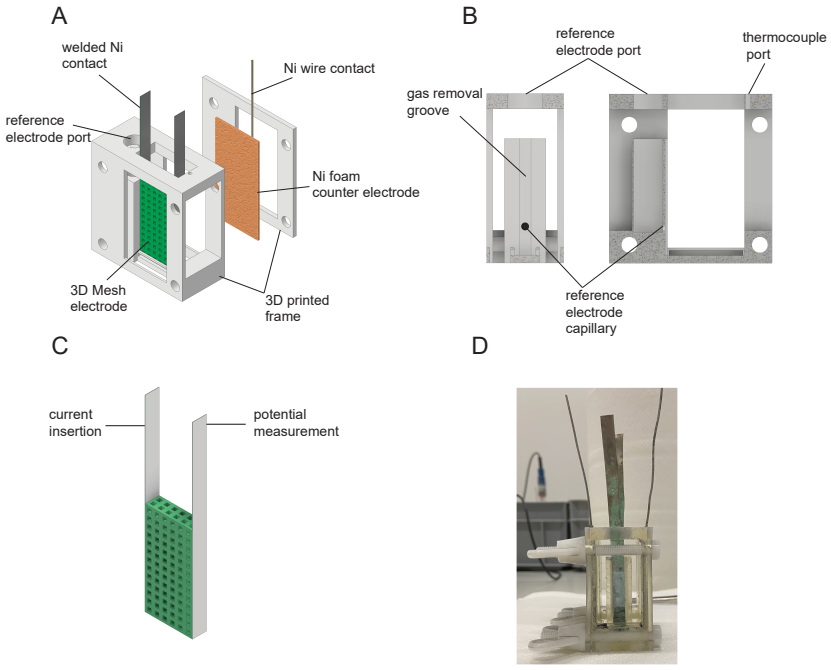

Figure B.5: 3D printed frame for electrochemical testing. (A) Illustration of the frame assembly. (B) Cut views of the 3D printed frame showing the gas removal groove as well as the reference electrode port and capillary. (C) Illustration of the 3D mesh electrode with welded nickel contacts. One contact is used for current insertion, the other for the measurement of the electrode potential vs. the reference electrode. (D) Photo of the 3D electrode inserted in the 3D printed frame before insertion in the cell.

B.5. Electrochemically active surface area (ECSA)

The ECSA was estimated from the double-layer capacitance measured as shown in Figure B.7. In a potential window where Faradaic currents such as battery charging/discharging or electrolysis can be excluded, cyclic voltammetry scans result in a scan rate-dependent current associated with the charging of the double layer. In the study of OER catalysts, this potential window is typically ± 0.1 V centered around the open circuit potential (OCP) [3]. For dedicated OER electrodes, such a potential window mostly excludes OER, so that the measured current can be attributed to double-

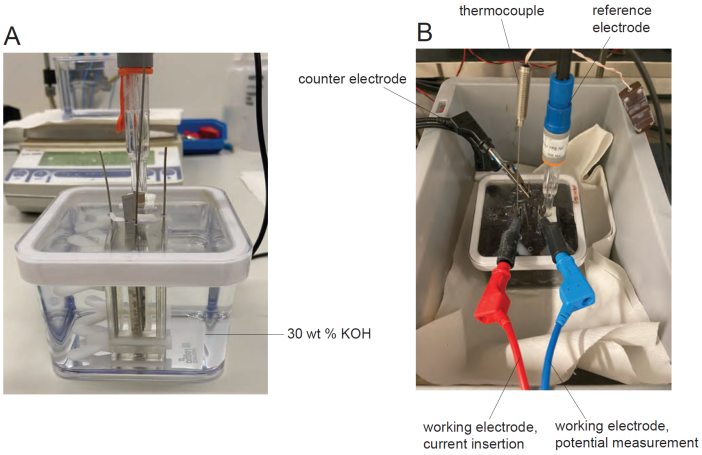

Figure B.6: Assembled test set-up before (A) and during (B) electrochemical testing.

layer charging. In the case of the here discussed hybrid battery-electrolysis electrodes, however, a CV scan towards lower or higher potentials around the OCP results in discharging or charging, respectively, which does not correspond to charging of the double layer capacity. Therefore, fully discharging the electrodes and conducting the CV in a potential window well below the OCP (0 - 0.2 V vs. Hg/HgO) should prevent recharging and thus eliminate faradaic currents. As shown in Figure B.7 A, the electrodes were discharged first at the C/10 rate to 0.14 V vs. Hg/HgO followed by a second discharge at C/100 to -0.2 V vs. Hg/HgO. The latter extremely slow discharge is required to fully discharge any residual capacity which is thought to result from an insulating layer of β-Ni(OH)$_2$ between the sintered nickel current collector and the charged active material layer [4]. Consistent with data shown by Barnard et al. [4], a second discharge plateau approximately 0.3 V more negative than the initial one is observed at sufficiently low discharge rates. We find that omitting the discharge of residual capacity still results in significant faradaic currents in the potential window of 0 V to 0.2 V vs. Hg/HgO. Following the deep discharge, cyclic voltammograms at increasing scan rates were measured within the potential window including a 10 s hold at each potential vertex (Figure B.7 B). The resulting charging currents for the positive and negative scan rate, I^+ and I^-, respectively, were evaluated at 0.1 V vs. Hg/HgO. These are

related to the scan rate ν and the double layer capacitance C_{DL} as follows [3, 5, 6]:

$$I^{\pm} = \nu C_{DL}^{\pm} \tag{B.4}$$

Thus, the slope of the capacitive current vs. the scan rate constitutes the double layer capacitance and can be determined from a linear fit of the experimental data (Figure B.7 C). It is common practice to report the average double layer capacitance $\bar{C}_{DL}$ determined from the average of the absolute values of both positive and negative potential sweeps [3, 7]:

$$\bar{C}_{DL} = \frac{C_{DL}^{+} + \left|C_{DL}^{-}\right|}{2} \tag{B.5}$$

The ECSA can then be estimated from the specific capacitance of the sample, C_s [3]:

$$ECSA = \frac{\bar{C}_{DL}}{C_s} \tag{B.6}$$

The specific capacitance C_s represents the capacitance per unit area of an ideally smooth surface of the studied material paired with an electrolyte. Technically, C_s has to be determined experimentally for each catalyst and electrolyte condition. While specific capacitances have been measured for nickel in various NaOH and KOH solutions, these values vary significantly depending on the electrolyte composition and concentration [3]. Here, we used the average value of 40 μF/cm^2 reported by McCrory et al. [3] for alkaline solutions. This results in an estimated ECSA of 32440 cm^2 and 53850 cm^2 for the 3D mesh and the Non-3D electrode, respectively. The lower ECSA of the 3D mesh electrode, $ECSA_{3D}$, is consistent with the reduction in electrode volume resulting from the channels, i.e. void fraction Θ of around 39 %:

$$ECSA_{3D} = ECSA_0(1 - \Theta) \tag{B.7}$$

where $ECSA_0$ refers to the ECSA of the Non-3D electrode.

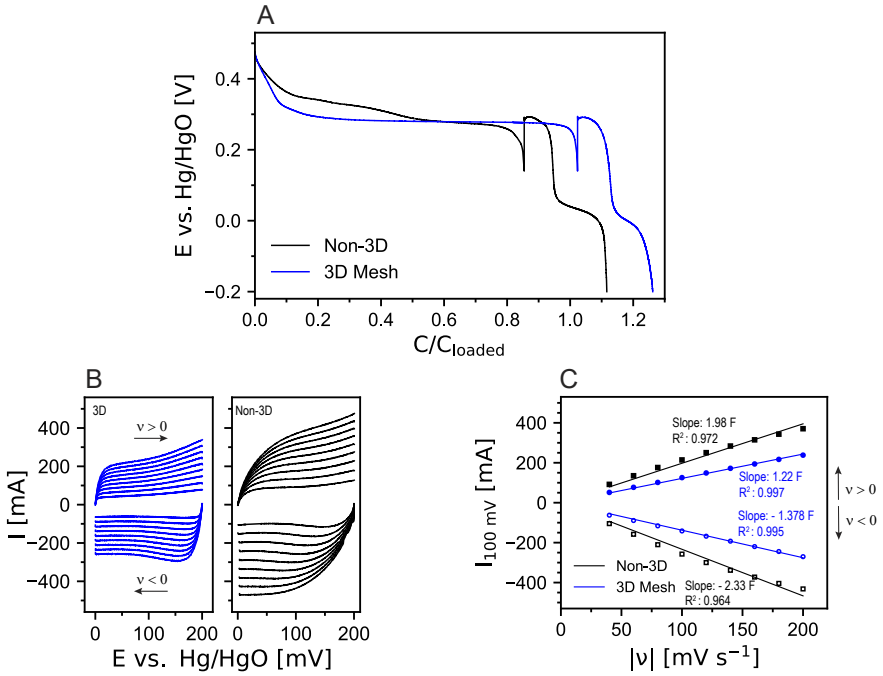

Figure B.7: Determination of the electrochemically active surface area (ECSA) for the 3D and the Non-3D electrodes. (A) Deep discharge prior to ECSA measurement. C/10 to 0.14 V vs Hg/Hg0 followed by C/100 to -0.2 V vs. Hg/HgO. (B) Potential scans at increasing scan rates (ν) between 0 V and 0.2 V vs. Hg/HgO (40, 60, 80, 100, 120, 140, 160, 180, 200 mV/s). (C) Double layer capacitance determined from the capacitive charging currents evaluated at 100 mV for the scan rates shown in (B).

B.6. Electrochemical impedance spectroscopy (EIS)

EIS measurements were conducted on fully charged electrodes in a frequency range from 10,000 Hz to 0.01 Hz with a voltage amplitude of 5 mV at open circuit potential. As shown in Figure B.8, the experimental data was fitted to an equivalent circuit using the software ZView2. Constant phase elements (CPE), rather than ideal capacitors, were used to take the inhomogeneous porous electrode surface into account [8–10]. The fitting parameters are listed in Tables B.2 and B.3 for Non-3D and 3D electrodes, respectively.

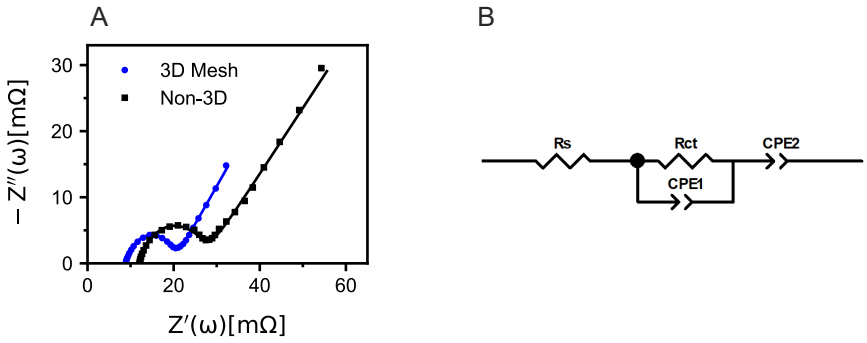

Figure B.8: Determination of the solution resistance via EIS. (A) Nyquist plots and fitted equivalent circuit for a fully charged 3D mesh and Non-3D electrode. (B) Equivalent circuit used for fitting data shown in (A) containing solution resistance (R_s), charge transfer resistance (R_{ct}) and two constant phase elements (CPE).

Table B.2: Parameter fit of the equivalent circuit for the Non-3D electrode determined in ZView2 (see Figure B.8).

Element	Freedom	Value	Error	Error %
Rs	Free(+)	0.011995	3.7893E-05	0.31591
Rct	Free(+)	0.01456	0.00017258	1.1853
CPE1-T	Free(+)	1.014	0.046348	4.5708
CPE1-P	Free(+)	0.78678	0.0080726	1.026
CPE2-T	Free(+)	97.14	1.4545	1.4973
CPE2-P	Free(±)	0.50012	0.005166	1.033

Table B.3: Parameter fit of the equivalent circuit for the 3D electrode determined in ZView2 (see Figure B.8).

Element	Freedom	Value	Error	Error %
Rs	Free(+)	0.0089009	2.0863E-17	2.3439E-13
Rct	Free(+)	0.011099	1.0731E-16	9.6684E-13
CPE1-T	Free(+)	2.452	7.9254E-14	3.2322E-12
CPE1-P	Free(+)	0.79849	6.5378E-15	8.1877E-13
CPE2-T	Free(+)	237.1	4.6148E-12	1.9464E-12
CPE2-P	Free(±)	0.54728	6.512E-15	1.1899E-12

B.7. Modelling Results

Table B.4: Electrode properties for the tested 3D, Non-3D electrodes used in the porous electrode model. See Table A.1 for model parameters.

Description	Unit	3D	Non-3D	Commercial
Loaded capacity	mAh	848	919	-
Loaded gravimetric capacity	mAh/g	127	93	75-120 [11, 12]
Loaded areal capacity	mAh/cm^2	140	145	30-40 [13]
Loaded volumetric capacity	mAh/cm^3	279	270	300-444 [11, 13]
Mass of $Ni(OH)_2$	g/cm^3	1.53	1.34	1.4-2 [11, 13]
Porosity before loading	-	0.78	0.71	-
Porosity after loading	-	0.4	0.39	-
Void fraction	-	0.39	0	-
Geometric surface area[a]	cm^2	6	6.3	-
Thickness	cm	0.52	0.52	-
ECSA[b]	m^2	3.2	5.4	-
ECSA/Volume[c]	m^{-1}	1.03×10^6	1.63×10^6	-

[a] Electrode width x height.
[b] Electrochemically active surface area.
[c] Geometric volume, i.e. electrode width x heigh x thickness.

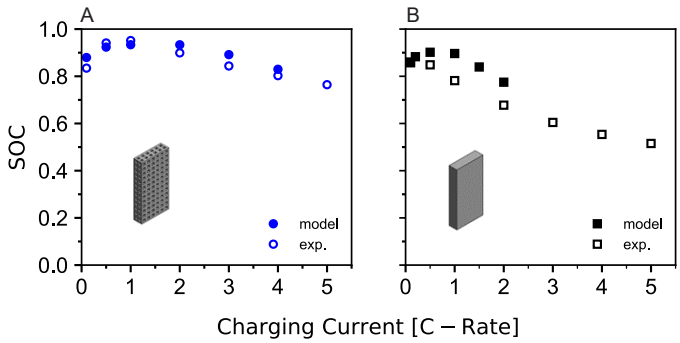

Figure B.9: Comparison between the modelled overall state of charge *SOC* and experimental values for the 3D and Non-3D electrode. The charge insertion is 1.5C. Here, we used the porous electrode model described in Chapter 2.

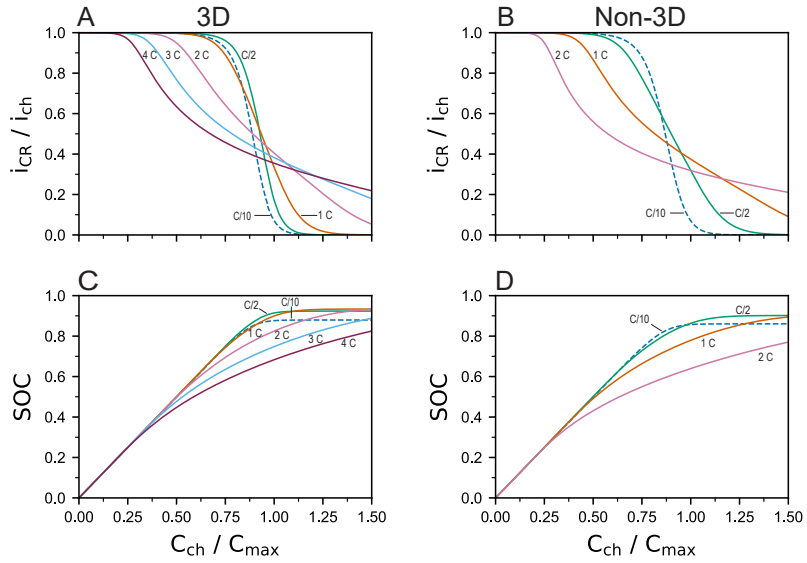

Figure B.10: Modelled Faradaic charging efficiency (i_{CR}/i_{ch}) (A,B) and overall state of charge SOC (C,D) for charge rates of C/10, C/2, 1C, 2C, 3C and 4C for the 3D and Non-3D electrode at various values for the charge insertion C_{ch}. C_{max} refers to the maximum discharge capacity. i_{CR} is the current going towards charging and i_{ch} is the total applied current during charging. Here, we used the porous electrode model described in Chapter 2.

B.8. Scanning Electron Microscopy (SEM) and X-ray diffraction (XRD)

SEM measurements were performed on a SEM-JEOL6060LA. Images before and after $Ni(OH)_2$ loading were obtained as shown in Figures B.13 and B.14. For XRD studies, a Bruker D8 Advance diffractometer with Cu-Kα source (Cu radiation wavelength: Kα1(100)=1.54060 Å, Kα2(50)=1.54439 Å) and Lynxeye-XE-T position sensitive detector was employed. The samples were placed on a sample stage with adjustable sample height and were scanned in a 2Θ range of 4-90°with a step size of 0.01°and 0.05 s/step. The Bruker software DiffracSuite was used to evaluate the XRD data in Figure B.15.

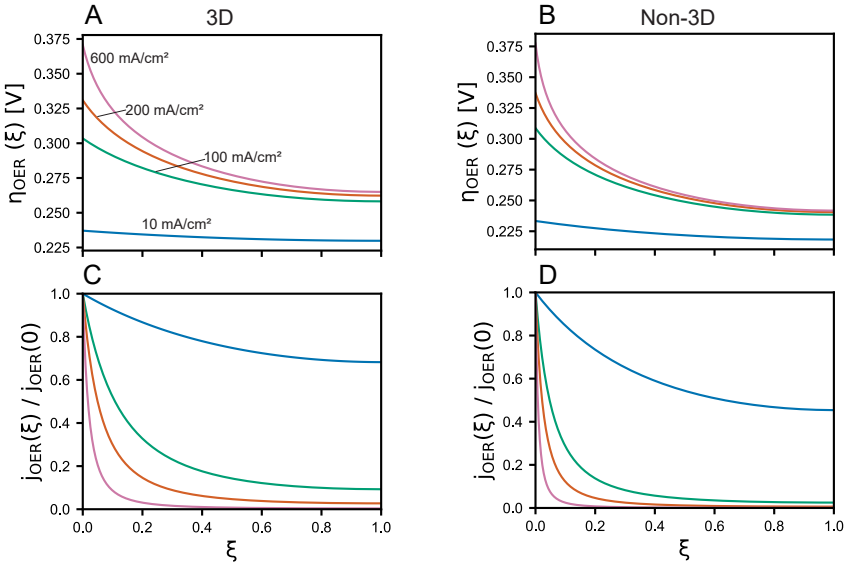

Figure B.11: (A,B) OER overpotential distribution over the reduced electrode coordinate $\xi = x/l$ for the fully charged 3D electrode (A) and Non-3D electrode (B). (C,D) Current distribution over the reduced electrode position $\xi = x/l$ for the 3D electrode (C) and the Non-3D electrode (D). $j_{OER}(\xi)$ refers to the local OER current density and $j_{OER}(0)$ refers to the OER current density at the front of the electrode ($\xi = 0$). Here, we used the porous electrode model described in Chapter 2.

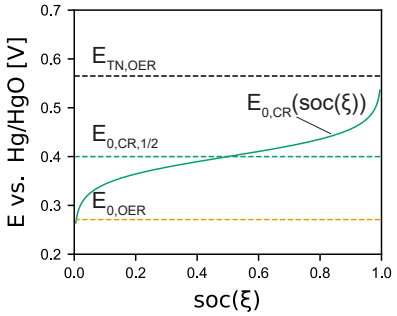

Figure B.12: OER equilibrium potential ($E_{0,OER}$), OER thermoneutral potential ($E_{TN,OER}$), CR equilibrium potential ($E_{0,CR}$) as a function of the local state of charge $soc(\xi)$ [14] and the CR equilibrium potential at 50 % state of charge ($E_{0,CR,1/2}$).

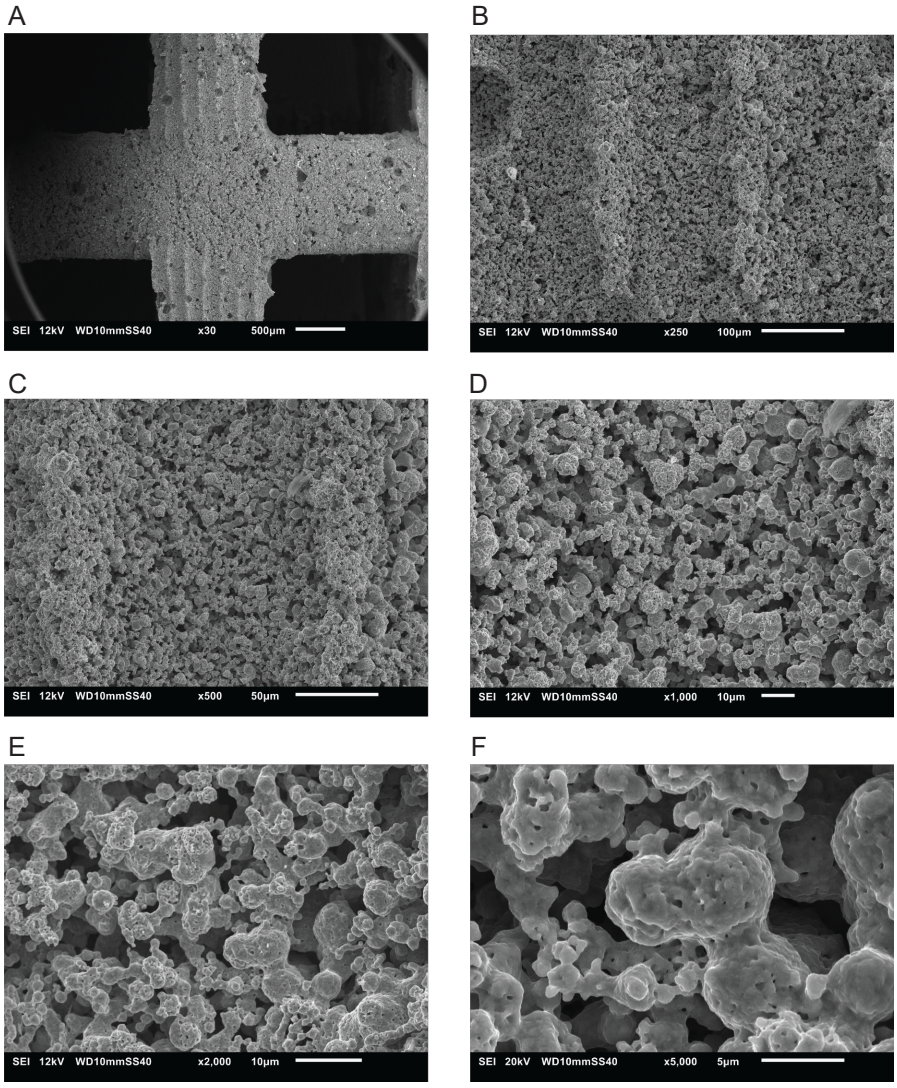

Figure B.13: SEM images of of a 3D electrode before active material loading.

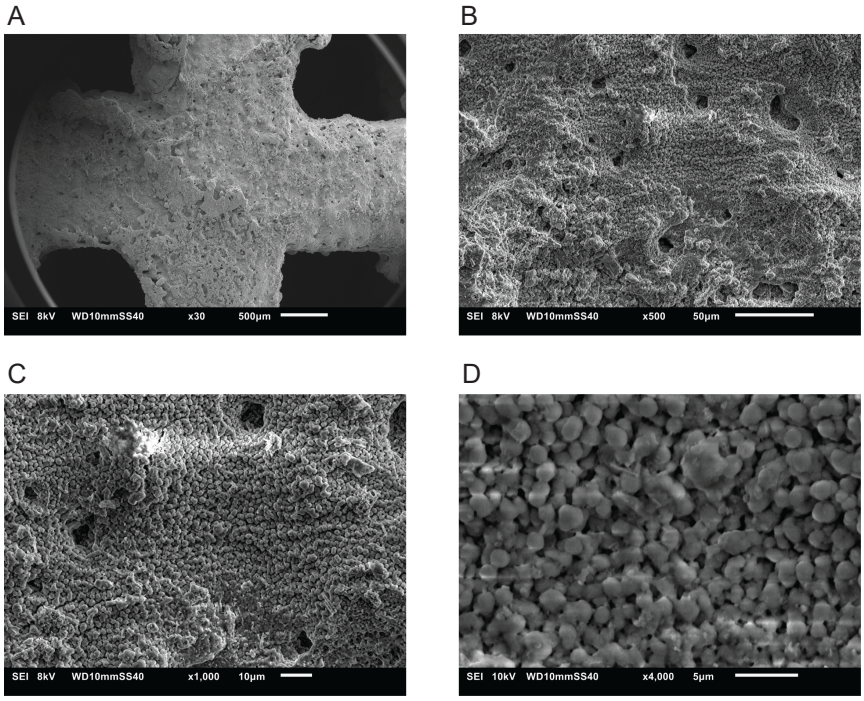

Figure B.14: SEM images of of a 3D electrode after four cycles of active material loading (see Figure B.3).

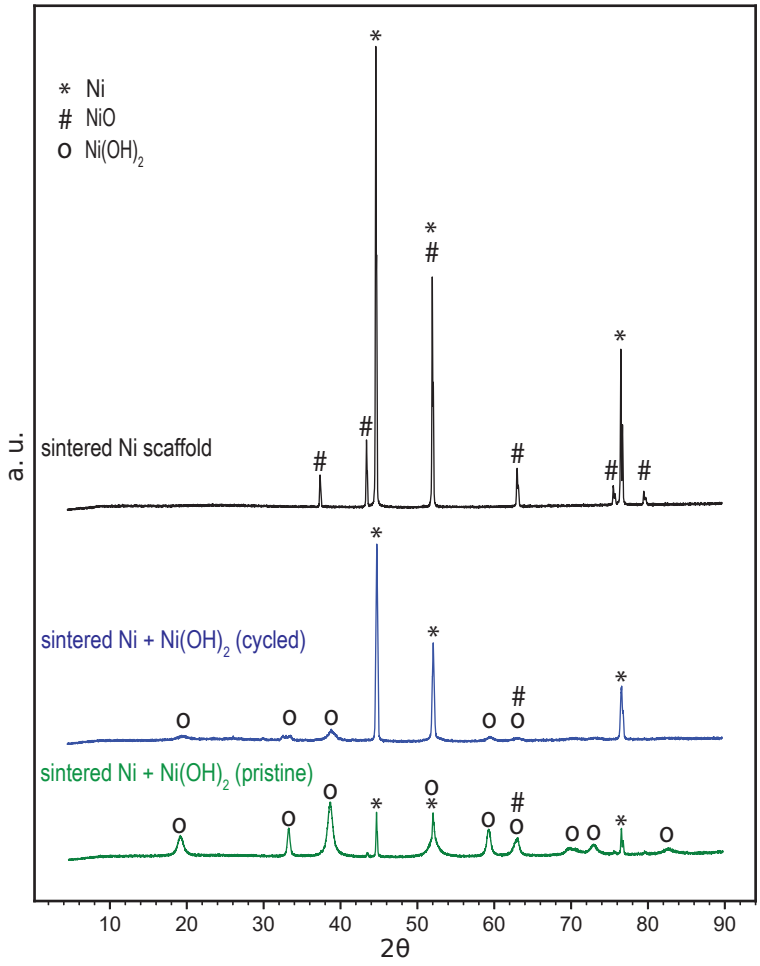

Figure B.15: XRD spectra of a sintered nickel scaffold and a sintered nickel scaffold loaded with $Ni(OH)_2$ before and after electrochemical cycling.

B.9. Supporting Figures

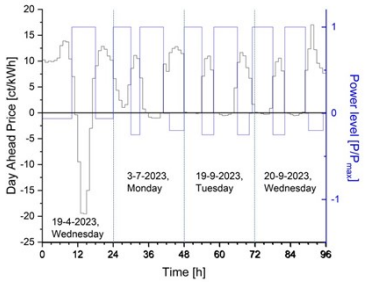

Figure B.16: Charge and discharge sequences in relation to electricity price levels. Day Ahead Market prices in the Netherlands on the indicated days in 2023. Also indicated a possible action of the battery-electrolyser (or battolyser™): Either charge insertion at full power or discharge at a rate where the battery can discharge fully in the available time. Such charge and discharge pattern can be optimised for optimum yield of battery and electrolysis revenues.

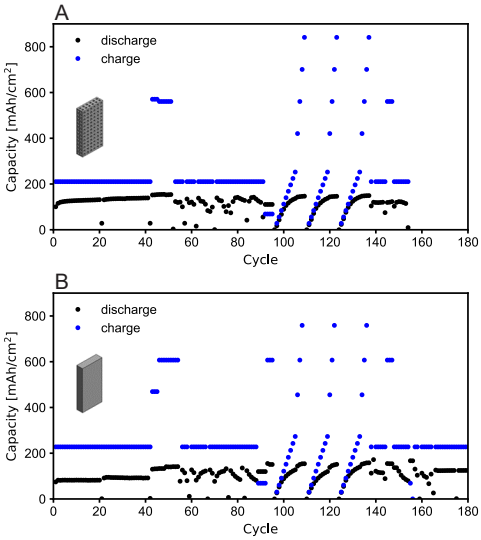

Figure B.17: Inserted charge and discharge capacity for the 3D Mesh electrode (A) and the Non-3D electrode (B) throughout the conducted experiments.

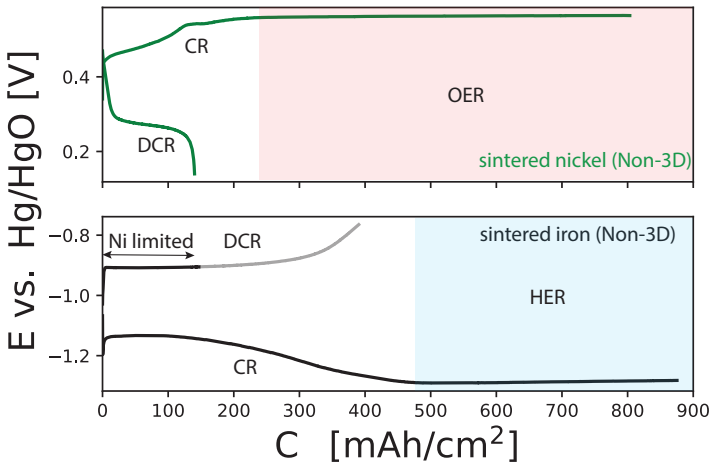

Figure B.18: Data used for the estimate of the total energy efficiency of a full cell including a sintered Non-3D nickel and Non-3D iron electrode (Chapter 4). Each electrode was measured at room temperature in a separate cell at a charge rate of 145 mA/cm^2 and discharge rate of 36 mA/cm^2. Note that in a full cell, the nickel electrode is typically limiting which would result in incomplete discharge and thus earlier HER of the iron electrode. CR: charging, and DCR: discharging, HER/OER: Hydrogen and oxygen evolution, respectively.

B

References

[1] J. Hereijgers, J. Schalck, J. Lölsberg, M. Wessling, and T. Breugelmans, *Indirect 3D printed electrode mixers,* ChemElectroChem **6**, 378 (2019).

[2] S. U. Falk and A. J. Salkind, *Alkaline storage batteries* (1969).

[3] C. C. L. McCrory, S. Jung, J. C. Peters, and T. F. Jaramillo, *Benchmarking heterogeneous electrocatalysts for the oxygen evolution reaction,* Journal of the American Chemical Society **135**, 16977 (2013).

[4] R. Barnard, G. T. Crickmore, J. A. Lee, and F. L. Tye, *The cause of residual capacity in nickel oxyhydroxide electrodes,* Journal of Applied Electrochemistry **10**, 61 (1980).

[5] P. Connor, J. Schuch, B. Kaiser, and W. Jaegermann, *The determination of electrochemical active surface area and specific capacity revisited for the system MnOx as an oxygen evolution catalyst,* Zeitschrift für Physikalische Chemie **234**, 979 (2020).

[6] S. P. Zankowski and P. M. Vereecken, *Electrochemical determination of porosity and surface area of thin films of interconnected nickel nanowires,* Journal of The Electrochemical Society **166**, D227 (2019).

[7] T. Kou, S. Wang, R. Shi, T. Zhang, S. Chiovoloni, J. Q. Lu, W. Chen, M. A. Worsley, B. C. Wood, S. E. Baker, *et al.*, *Periodic porous 3D electrodes mitigate gas bubble traffic during alkaline water electrolysis at high current densities,* Advanced Energy Materials **10**, 2002955 (2020).

[8] A. Alobaid, C. Wang, and R. A. Adomaitis, *Mechanism and Kinetics of HER and OER on NiFe LDH Films in an Alkaline Electrolyte,* Journal of The Electrochemical Society **165**, J3395 (2018).

[9] X. Yin, G. Sun, A. Song, L. Wang, Y. Wang, H. Dong, and G. Shao, *A novel structure of Ni-(MoS2/GO) composite coatings deposited on Ni foam under supergravity field as efficient hydrogen evolution reaction catalysts in alkaline solution,* Electrochimica Acta **249**, 52 (2017).

[10] B. Łosiewicz, A. Budniok, E. Rówiński, E. Łągiewka, and A. Lasia, *The structure, morphology and electrochemical impedance study of the hydrogen evolution reaction on the modified nickel electrodes,* International Journal of Hydrogen Energy **29**, 145 (2004).

[11] W. Ferrando, W. W. Lee, and R. A. Sutula, *A lightweight nickel composite electrode I: concept and feasibility,* Journal of Power Sources **12**, 249 (1984).

[12] H. S. Lim and G. R. Zelter, *Lightweight nickel electrodes for nickel/hydrogen cells,* Journal of Power Sources **45**, 195 (1993).

[13] W. R. Scott and D. W. Rusta, *Sealed-cell nickel-cadmium battery applications manual*, Tech. Rep. (1979).

[14] P. De Vidts and R. E. White, *Mathematical modeling of a nickel-cadmium cell: Proton diffusion in the nickel electrode,* Journal of the Electrochemical Society **142**, 1509 (1995).

C

3D iron electrodes for hybrid battery and electrolysis application

Supporting information to Chapter 4.

C.1. Materials and equipment

Carbonyl iron powder ($\geq$ 97 %) and sodium tetraborate (99 %) were purchased from Sigma Aldrich. Potassium hydroxide (85 %) and agar powder were obtained from Alfa Aesar. TIMCAL Super P Conductive Carbon Black was purchased from nanografi. Ultrapure water used for the electrolyte was prepared with a Merck Milli-Q® A1 water purification system. The electrodes were sintered in a tube oven (Applied Test Systems, Inc., Series 3210) using a quartz tube of 35 mm in diameter. The H_2/Ar mixture (5 %/ 95 %) was purchased from Linde. Electrode frames for testing were 3D printed with a Formlabs Form-2 SLA 3D printer in "Clear" resin obtained from MakerPoint. The 3D electrode moulds were designed with the CAD software Autodesk Inventor 2019 and 3D printed with an Ultimaker S3 FDM 3D printer from the Poly-Lactic Acid (PLA) filament "EasyFil PLA" purchased from Form Futura. Nickel strips used as electrode contacts (0.15 mm thick, 5 mm wide) were purchased from NKON and spot welded onto the electrodes using a SUNKKO 738 AL spot welding machine purchased from Banggood. The electrodes were dried using a vacuum oven (Thermo Scientific VT 6025). Scanning electron microscopy (SEM) measurements were performed on a SEM-JEOL6060LA.

C.2. Electrochemical testing

T test the electrodes, they were placed in the 3D printed frame shown in Figure C.1. This has the advantage that the working electrode (WE, iron), the reference electrode (RE, Hg/HgO, Origalys Origasens) and the two counter electrodes (CE, nickel foam) on either side of the WE can be positioned securely and reproducibly. A nickel contact was spot welded on either side of the WE. One was used to insert the current, the other was used to measure the electrode potential vs. the RE. This excludes contact resistances from the measured voltage. The two nickel foam counter electrodes were contacted via nickel wire. The RE was placed next to the contact of the WE which was used for the potential measurement. WE and RE were connected ionically via a capillary. Compared to placing the RE in between WE and CE, the short distance between RE and WE significantly reduces the necessity for an iR correction in the voltage measurement. This is typically necessary due to the gradient in the

electrode potential between WE and RE. Bubble induced noise of the voltage measurement (WE vs. RE) was significantly reduced by integrating a groove between the electrode contact and capillary which allowed for effective bubble escape. In addition, the temperature close to the WE was measured via a thermocouple (RS PRO Type T, 1.5 mm in diameter, purchased from RS Online). This was used primarily to monitor the cell temperature at high current densities and to set a certain oven temperature (e.g. 30 °C tested for the Non-3D electrode with carbon black addition). The assembly including the frame, WE, RE, CE and thermocouple was placed in a 500 ml SAN container (Mepal) filled with 450 g of KOH (a.q., 30 wt %). Openings were cut into the lid of the container in order to thread the contacts, thermocouple and RE through. These were then fixed in place with Parafilm.

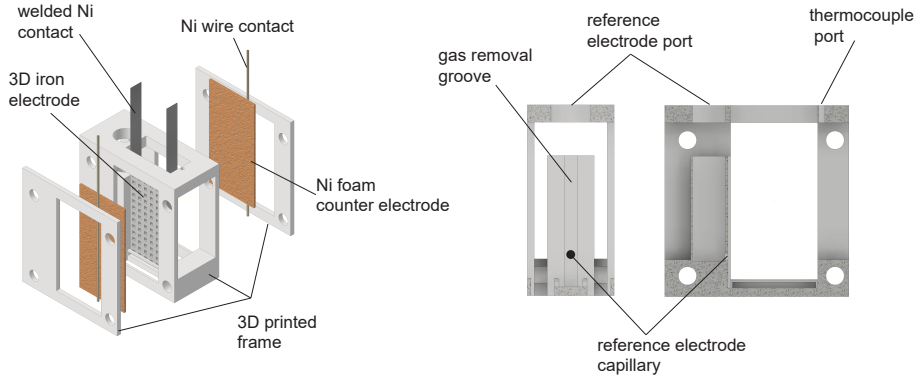

Figure C.1: 3D printed frame for electrochemical testing of iron electrodes.

Electrochemical experiments involving battery cycling and electrolysis were conducted with a Maccor 4000 battery cycling system. Prior to cycling, the solution resistance required for iR correction was determined via EIS using a PARSTAT 4000A potentiostat (Princeton Applied Research). This EIS measurement was conducted prior to activation in a frequency range from 10,000 Hz to 1 Hz at open circuit potential with a voltage amplitude of 5 mV. Due to the comparably low currents applied during battery cycling, the measured voltages were only iR-corrected for electrolysis experiments (LSV and Tafel). The Hg/HgO reference electrodes were calibrated vs. a reversible hydrogen electrode (HydroFlex RHE purchased

from Gaskatel) that was used only for this purpose.

C.3. Electrode properties

Table C.1: Electrode properties

Electrode	m_{Fe} [g]	A [cm^2]	l [mm]	ϵ [-]	Θ [-]	a [mm]
Non-3D	6.858	4.70	4.7	0.53	0	-
3D-M1	6.080	4.84	4.6	0.56	0.14	0.73
3D-M2	5.797	4.80	4.5	0.55	0.22	0.85
3D-M3	3.529	4.68	4.5	0.58	0.43	1.18
Non-3D (carbon)	5.58	5.2	4.9	0.58	0	-

m_{Fe}: Mass of iron.
A: Superficial electrode area (width x height).
l: Electrode thickness.
ϵ: Porosity as determined from isopropanol uptake.
Θ: Void fraction as determined from the CAD model.
a: Channel dimension (width=height=depth) as measured via SEM.

C.4. Supporting results

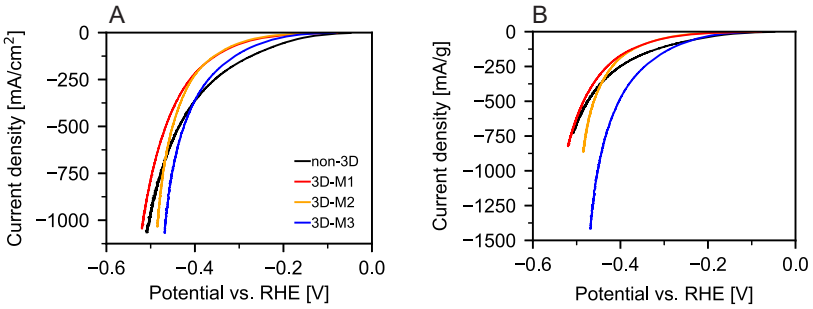

Figure C.2: Linear sweep voltammetry before activation in order to screen for electrodes that can withstand high HER current densities and still function as battery in a following discharge. The shown potential is iR corrected.

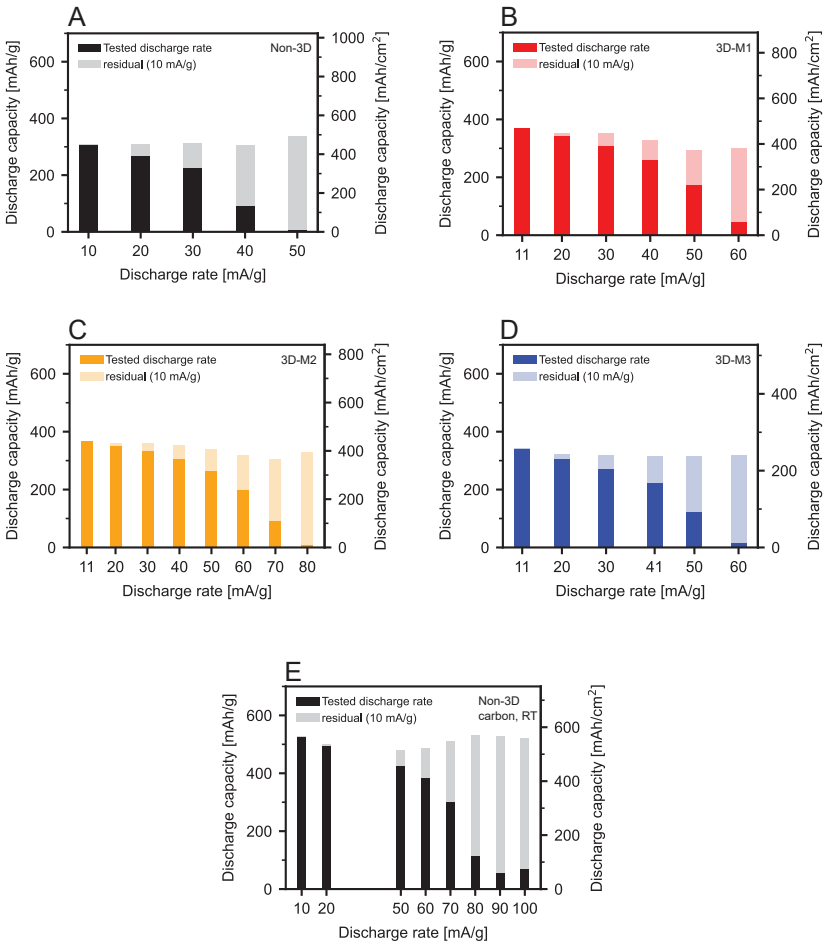

Figure C.3: Discharge capacities at tested discharge rates and residual capacity obtained in the following slow discharge at 10 mA/g for electrodes Non-3D (A), 3D-M1 (B), 3D-M2 (C), 3D-M3 (D) and Non-3D with carbon black addition at room temperature (E). See also Figures 4.4 and 4.9.

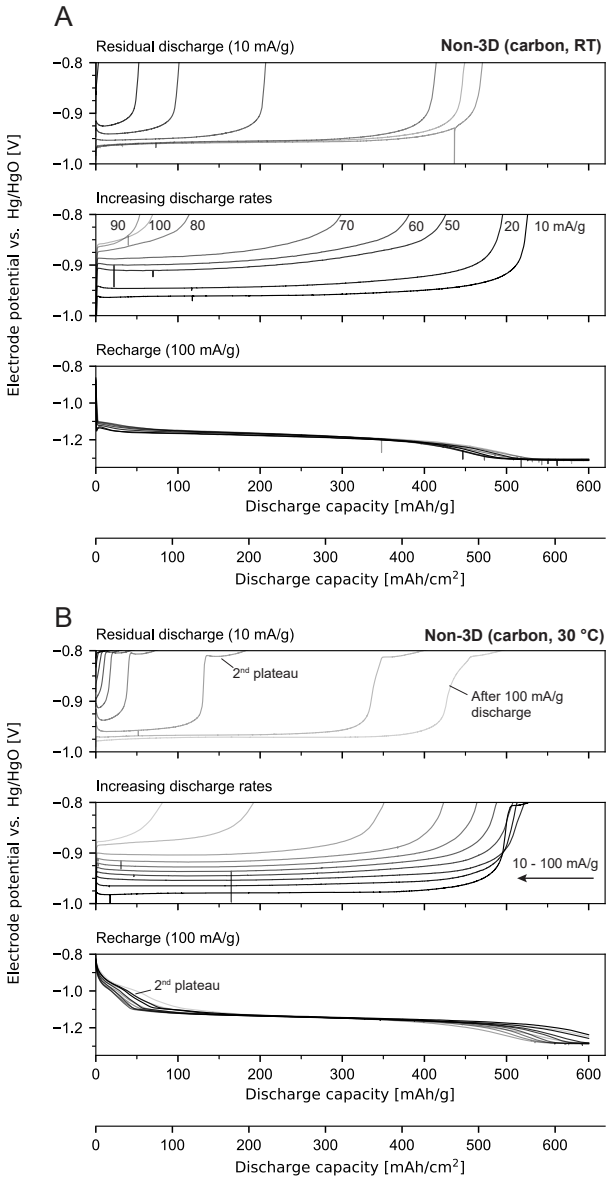

Figure C.4: Electrode potential for varying discharge rates, subsequent slow discharge at 10 mA/g and recharging at 100 mA/g for the Non-3D electrodes with carbon black addition at room temperature (A) and at 30°C (B). The cut-off voltage was set to -0.8 V vs. Hg/HgO. Progressively lighter lines mark higher discharge current densities. For the slow discharge rate of 10 mA/g at 30°C, overpotentials are sufficiently low to partially discharge at the 2nd discharge plateau. Related to Figure 4.9.

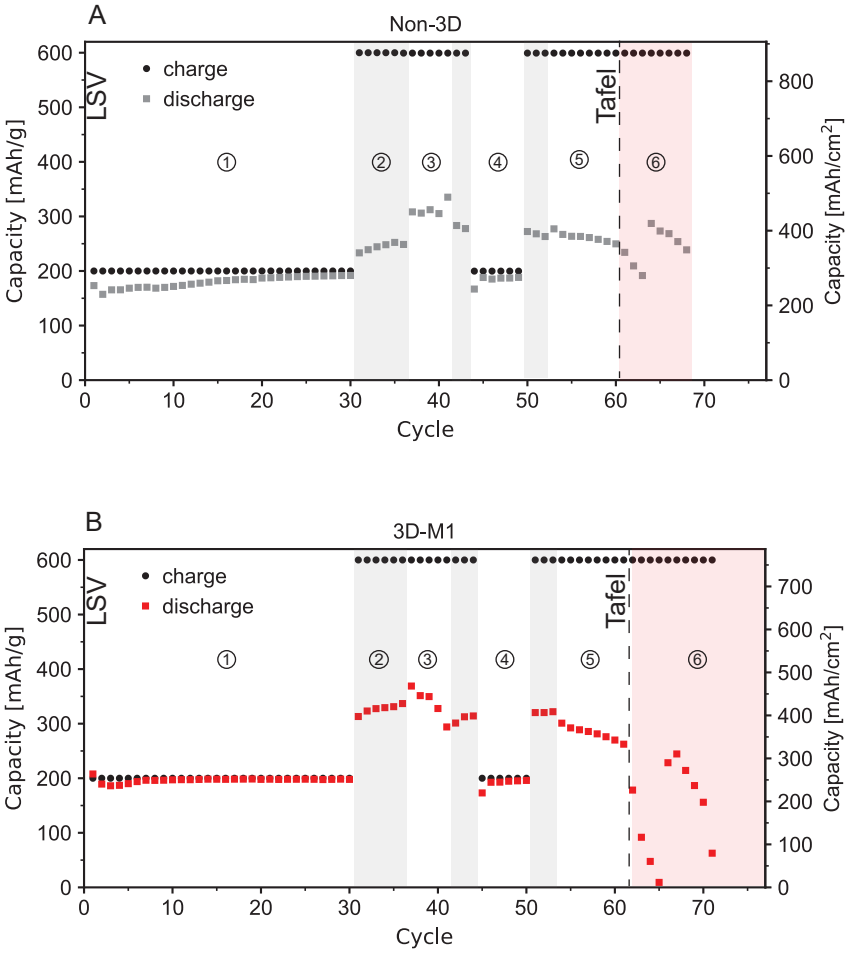

Figure C.5: Overview of the discharge capacities and charge insertion of the Non-3D electrode (A) and electrode 3D-M1 (B) in the course of experiments conducted for this work. LSV: Linear sweep voltammetry conducted prior to formation cycling (Figure C.2). ① Formation cycling and ② overcharging (Figure 4.3). ③ Discharge rate variation (Figure 4.4). ④ Repeated formation cycling. ⑤ Charge rate variation (Figure 4.6). Tafel experiment to measure electrolysis performance shown in Figure 4.6. ⑥ Attempts at repeated formation cycling following deactivation.

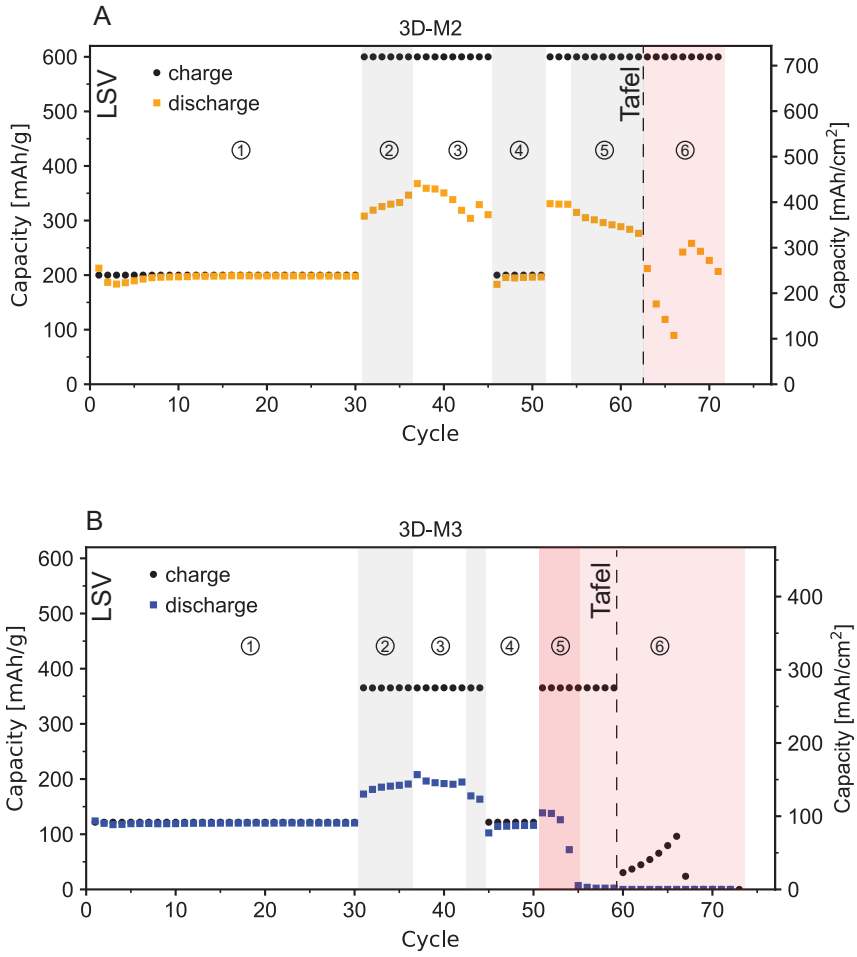

Figure C.6: Overview of the discharge capacities and charge insertion of electrodes 3D-M2 (A) and 3D-M3 (B) in the course of experiments conducted for this work. LSV: Linear sweep voltammetry conducted prior to formation cycling (Figure C.2). ① Formation cycling and ② overcharging (Figure 4.3). ③ Discharge rate variation (Figure 4.4). ④ Repeated formation cycling. ⑤ Charge rate variation (Figure 4.6). Tafel experiment to measure electrolysis performance shown in Figure 4.6. ⑥ Attempts at repeated formation cycling following deactivation.

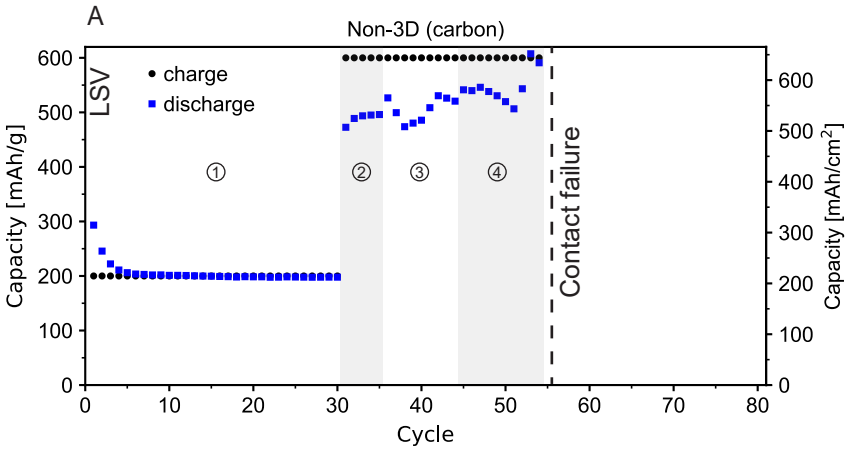

Figure C.7: Overview of the discharge capacities and charge insertion of the Non-3D electrode with carbon black addition in the course of experiments conducted for this work. LSV: Linear sweep voltammetry conducted prior to formation cycling (Figure C.2). ① Formation cycling and ② overcharging (Figure 4.8). ③ Discharge rate variation at room temperature and ④ 30 °C, see Figure 4.9. The spot-welded contacts detached after 55 cycles.

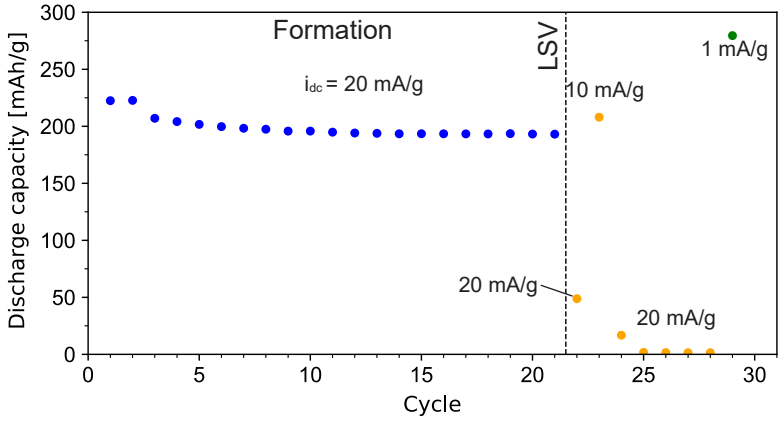

Figure C.8: Decrease in discharge rate capability following linear sweep voltammetry (LSV) for a 3D electrode with the geometry of 3D-M3 which was sintered at a lower temperature of 750 °C and for only 1 h. LSV was conducted at a scan rate of 0.1 mV/s starting from the open circuit potential until the maximum current of 5 A (1090 mA/cm^2) was reached.

D

Eliminating redox-mediated electron transfer mechanisms on a supported molecular catalyst enables CO_2 conversion to ethanol

Maryam Abdinejad*, Amirhossein Farzi*, Robin Möller-Gulland*, Fokko Mulder, Chengyu Liu, Junming Shao, Jasper Biemolt, Marc Robert, Ali Seifitokaldani, Thomas Burdyny

*These authors contributed equally to this work.

This appendix has been published as supplementary information in Nature Catalysis 7, 1109-1119 (2024), https://doi.org/10.1038/s41929-024-01225-1 [1].

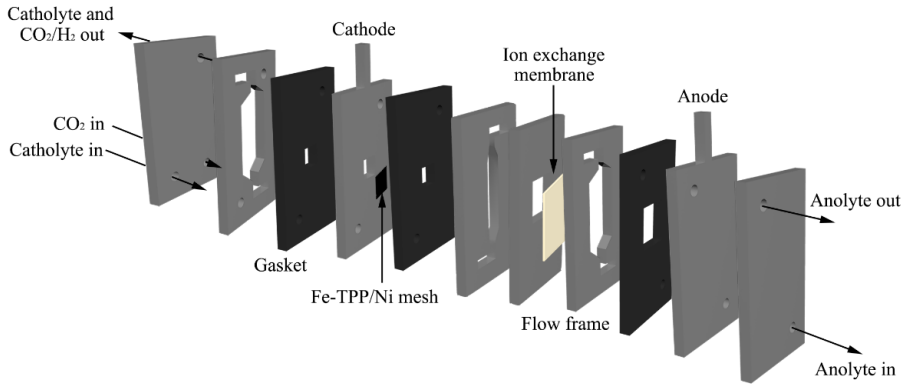

Figure D.1: Schematic illustration of the flow cell used for CO_2 electroreduction testing.

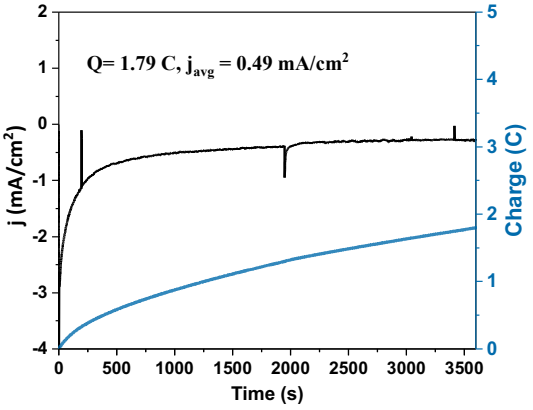

Figure D.2: CPE of a Fe-TPP/Ni foam (E = -0.30 V vs. RHE, t = 1 h) in CO-saturated 0.5 M $KHCO_3$ solution.

XANES

In all applied potentials shown in Figure D.4 and Table D.1, we attribute the pre-edge peak (7113.7 eV) to a similar energy peak in Fe(III), followed by a single broad transition peak associated with various octahedral and square-pyramidal Fe(III) compounds in Fe-TPP. This observation is consistent with findings from prior reports [2, 3]. However, due to deviations from calculated linear combination fittings, quantitatively distinguishing the trend becomes statistically challenging. Therefore, our approach focuses on visually assessing the trend in the graph. Upon closer inspection, the slight change resulting from further negative potentials can be summarized as the disappearance of the absorption drop at 7115 eV (attributed to Fe(III)) and an increased absorption in the pre-edge area, which aligns more closely with the absorption behavior of Fe(II), undergoing a very slight reduction. These findings are in line with observations reported in previous studies [4].

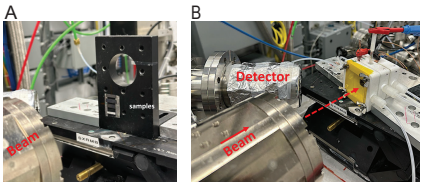

Figure D.3: The laboratory-based X-ray Absorption Near Edge Structure (XANES) Spectroscopy set-up: (A) ex-situ; and (B) in-situ.

For a deeper insight into the interfacial electronic properties of Fe-TPP with the Ni substrate, we compared the results with Fe-TPP deposited onto a carbon electrode at a comparable concentration. Figure D.6 and Table D.3 present the XANES comparison for Fe-TPP/Ni and Fe-TPP/C. Although there is an interaction between carbon and Fe-TPP, Ni has a much stronger influence on Fe-TPP compared to carbon as evidenced by a higher Fe(III) ratio to Fe(0). This observation suggests weaker molecule-substrate interactions between carbon and Fe-TPP, highlighting the significant impact of the local electronic properties of Fe-TPP.

The measurements were conducted at the Canadian Light Source (CLS) using a seven-element silicon drift detectors (SDD) array manufactured by

Table D.1: In-situ X-ray absorption near-edge spectroscopy (XANES) on Fe-TPP/Ni under various potentials of -0.1 to 3.0 V vs RHE.

Sample	Fe (0)	Fe (II)	Fe (III)	R-factor
Fe-TPP powder	0	11.7	88.3	0.0140
Fe-TPP (3 coats)	28.7	0	71.3	0.0232
-0.1 V	0	11.2	89.8	0.0148
-0.3 V	0	23.4	76.6	0.0132
-0.5 V	0	16.1	83.9	0.0059
-0.7 V	0	15.2	84.8	0.0048
-0.9 V	0	15.3	84.7	0.0039
-1.1 V	0	15.1	84.9	0.0036
-1.5 V	0	15.0	85.0	0.0036
-2 V	0	14.8	85.2	0.0038
-2.5 V	0	14.8	85.2	0.0037
-3.0 V	0	14.1	85.9	0.0039

Mirion Technologies. Energy steps with respect to the Fe K-edge were set at 2.0 eV intervals from -80 eV to -6 eV, and 0.35 eV intervals from -6 eV to 40 eV. Each sample underwent two scans, and the average absorptions at each energy level were reported. A dwell time of 1 second was used for each energy level within both mentioned ranges. During the in-situ tests, the gas diffusion layer was exposed to a CO_2-saturated chamber, and 0.5 M $KHCO_3$ was circulated in the anode and cathode chambers with two separate peristaltic pumps. In-situ scans were conducted once per applied potential.

Table D.2: Ex-situ X-ray absorption near-edge spectroscopy (XANES) on Fe-TPP/Ni with Fe-TPP with various loading.

Sample	Fe (0)	Fe (II)	Fe (III)	R-factor
Fe-TPP powder	0	11.7	88.3	0.0140
Fe-TPP/Ni (5 coat)	13.4	2.6	83.9	0.0165
Fe-TPP/Ni (3 coat)	28.7	0	71.3	0.0232
Fe-TPP/Ni (1 coat)	32.3	0	67.7	0.0258
Fe-TPP (1 diluted coat)	56.3	0	43.7	0.0572

Table D.3: X-ray absorption near-edge spectroscopy (XANES) comparison of Fe-TPP/Ni with Fe-TPP/C with one-layer loading.

Sample	Fe (0)	Fe (II)	Fe (III)	R-factor
Fe-TPP powder	0	11.7	88.3	0.0140
Fe-TPP/Ni	32.3	0	67.7	0.0258
Fe-TPP on CP	43.1	0	56.9	0.0398

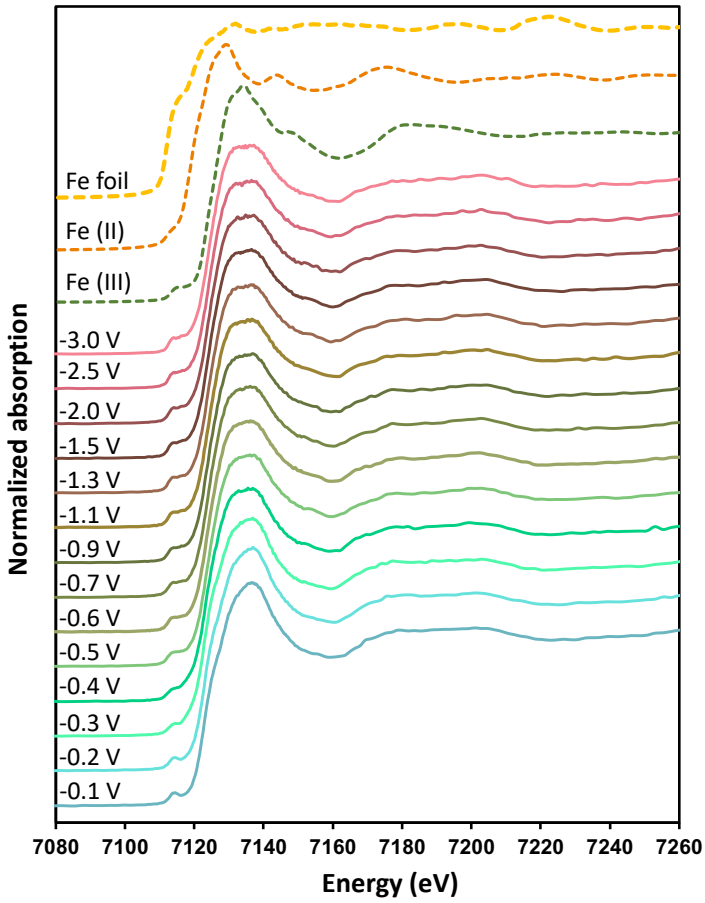

Figure D.4: In-situ X-ray absorption near-edge spectroscopy (XANES) on Fe-TPP/Ni catalyst at various potentials ranging from -0.1 to -3.0 V vs RHE.

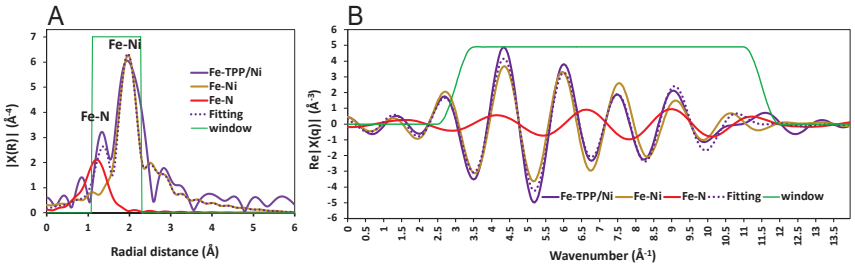

Figure D.5: Extended X-ray absorption fine structure (EXAFS) fittings of scattering paths, attributed to Fe-N and Fe-Ni interatomic distances in (A) R-space and (B) q-space with their corresponding fitting windows.

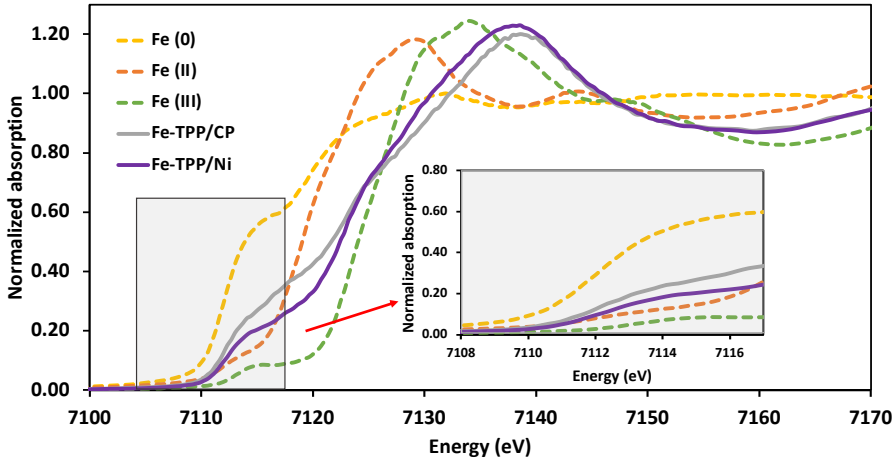

Figure D.6: A systematic comparison of in-situ X-ray absorption near-edge spectroscopy (XANES) on Fe- Fe-TPP/Ni with Fe-TPP with a similar loading of one-layer Fe-TPP coated onto the carbon electrode.

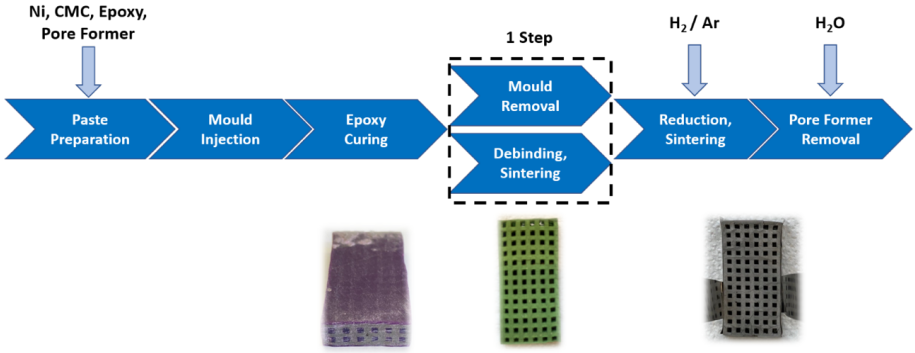

Figure D.7: Schematic of the 3D nickel electrode fabrication.

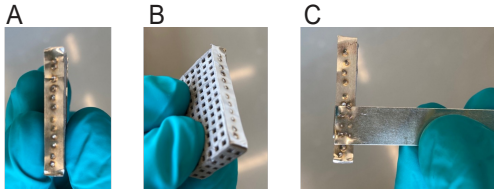

Figure D.8: Spot welding of nickel tabs onto the sintered 3D nickel electrode. (A, B) The nickel tab is first welded directly onto the side of the electrode. (C) Attaching the contact to the electrode.

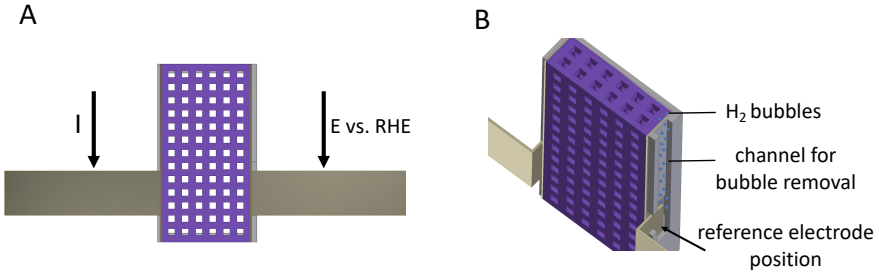

Figure D.9: (A) Two-point electrode connection allowing for measurements excluding contact resistances. (B) Reduction of noise in the reference electrode capillary by incorporating a bubble release channel in the electrode frame.

The major advantage of the presented 3D electrode is the improvement in electrode surface area that is in direct contact with the mixed phase flow consisting of the electrolyte and CO_2 bubbles (Figure D.10). As a result of the channels and the electrolyte flowing through rather than past the electrode, the electrode surface area in direct contact with gaseous CO_2 and electrolyte is increased significantly compared to an electrode geometry with no channels.

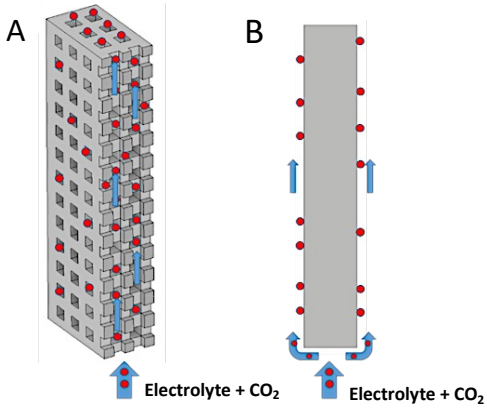

Figure D.10: Comparison of the mixed phase electrolyte and CO2 flow between (A) 3D electrode and (B) conventional (Non-3D) electrode.

To determine the increase in surface area of the 3D electrode compared to a Non-3D electrode, we first measured the electrode dimensions of the sintered electrode and adjusted the original CAD model in Autodesk Inventor accordingly (Figure D.11). In the process of the mould removal, debinding, and sintering the electrode shrinks by 20 % in width and height, and 15 % in thickness. With the adjusted model the geometric electrode surface area (40.49 cm^2) and volume excluding the channels (1.69 cm^3) can be calculated in Autodesk Inventor. Compared to an electrode geometry with no channels, the here discussed 3D electrode exhibits an increase in non-porous[1] surface area by a factor of 2.65.

[1]This does not include the internal surface area of the pores.

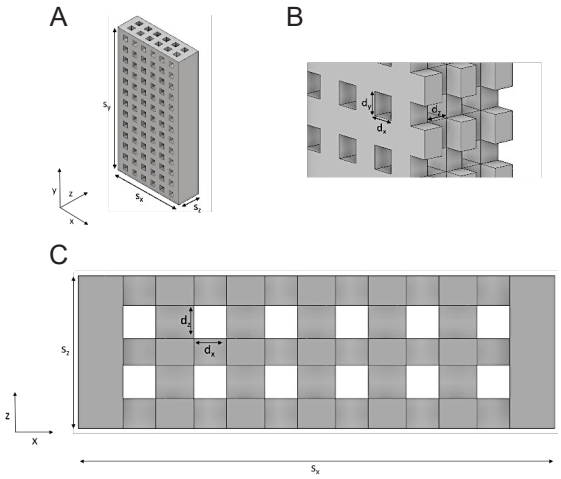

Figure D.11: Isometric view of the 3D electrode (A) and cut view of the 3D electrode showing the internal channel geometry (B, C). s_x = 32.3 mm, s_y = 16 mm, s_z = 5.1 mm, $d_x = d_y = d_z$ = 1.1 mm.

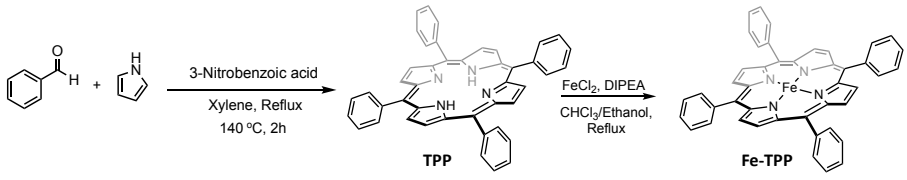

Scheme 1: Synthesis of tetraphenylporphyrin (TPP) followed by metallation reaction to form irontetraphenylporphyrin (Fe-TPP).

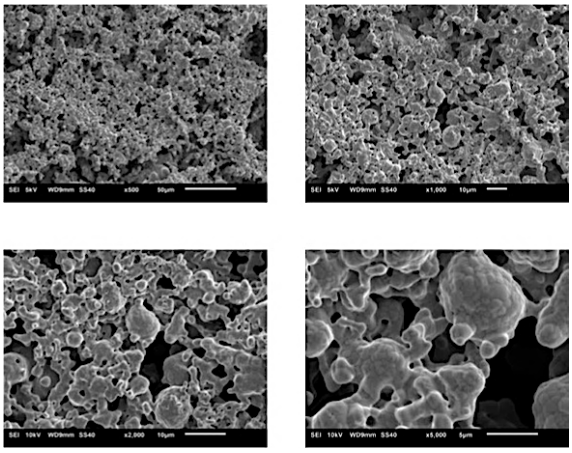

Figure D.12: Scanning electron microscopy (SEM) of the bare nickel electrode in magnifications of x500, x1000, x2000 and x5000.

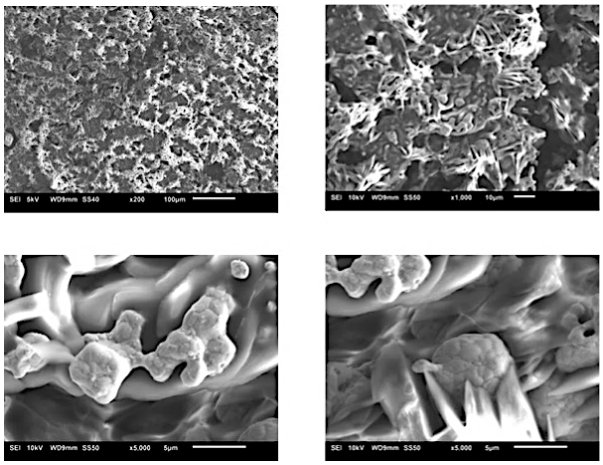

Figure D.13: Scanning electron microscopy (SEM) of the deposited Fe-TPP onto nickel electrode (Fe-TPP/Ni) in magnifications of x200, x1000 and x5000.

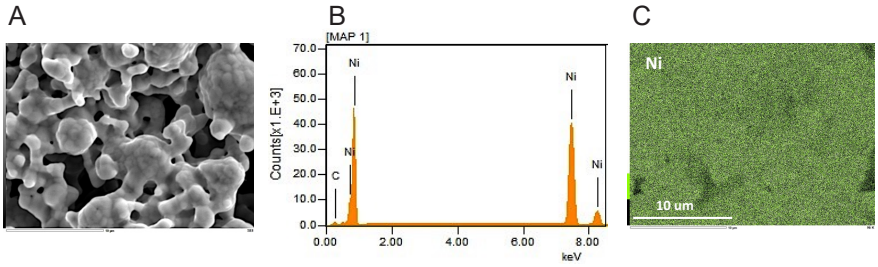

Figure D.14: (A) Scanning Electron Microscopy (SEM) of a bare 3D nickel electrode. (B) SEM mapping of elemental distribution. (C) Energy Dispersive X-rays Spectroscopy (EDX) of a bare 3D nickel electrode.

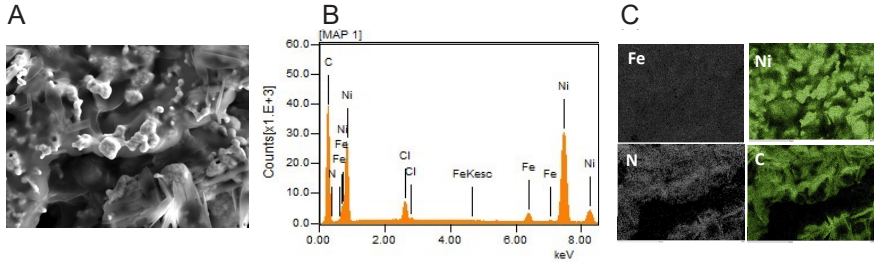

Figure D.15: (A) Scanning Electron Microscopy (SEM) of a Fe-TPP/Ni electrode. (B) SEM mapping of elemental distribution. (C) Energy Dispersive X-rays Spectroscopy (EDX) of Fe, Ni, N, and C.

XPS

The XPS survey shown in Figure D.16 A indicates the characteristic peaks of Ni, Fe, N, C and O elements in Fe-TPP/Ni. The Fe 2p core-level XPS spectra before deposition onto the nickel electrode exhibit two characteristic peaks belonging to Fe $2p_{1/2}$ at 722.98 eV and Fe $2p_{3/2}$ at 709.41 eV, respectively (Figure D.16 B). Notably, these peaks shifted to higher binding energies of 724.98 eV and 712.08 eV upon the deposition of Fe-TPP onto nickel (Figures D.16 B and D.17 A) [5, 6]. This phenomenon confirms the electronic interaction between Fe-TPP and Ni electrode surface.

The Ni 2p XPS spectra shown in Figure D.16 C display two spin-orbital doublets located at 853.2 (Ni $2p_{3/2}$), 871.0 (Ni $2p_{1/2}$) corresponding to characteristics of nickel metal (Ni(0))[7, 8]. The peaks at 856.1 (Ni $2p_{3/2}$), and 874.3 eV (Ni $2p_{1/2}$) can be assigned to $Ni(OH)_2$, providing a Ni^{+2} state, which is likely a surface passivation layer. The presence of NiO may also be present but is not disambiguated. Notably the Ni(0) peak disappears in the case of Fe-TPP/Ni. This can be attributed to either a partial charge transfer of oxidized nickel to Fe after deposition, resulting in a modification of the electronic structure and oxidation state of the nickel species; or the added Fe-TPP layer preventing the XPS from penetrating to the bulk nickel metal.

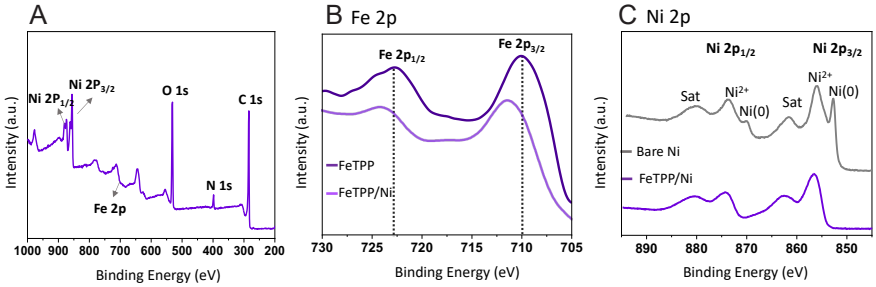

Figure D.16: (A) X-ray photoelectron spectra (XPS) survey of Fe-TPP/Ni electrode. The XPS comparison of (B) Fe 2p; and (C) Ni 2p before and after deposition of Fe-TPP onto nickel electrode.

The C1s spectra of Fe-TPP/Ni are attributed to the C=C (283.6 eV), C-O (284.7 eV), C=O (286.3 eV) bonds (Figure D.17 B). The characteristic N 1s peaks located at the binding energies of 400.12 (N-pyrrolic),

398.45 eV (N-pyridinic), and 402.1 eV (N-graphitic) (Figure D.17 C)[9, 10]. Considering the important role of pyridinic and pyrrolic nitrogen in the charge distribution between porphyrin ligand and metal, we compared the N 1s spectra before and after Fe-TPP deposition onto Ni. Figure D.18 illustrates a shift in both pyridinic and pyrrolic nitrogen to higher energy, which again suggests a great interaction between Fe-TPP and the Ni surface.

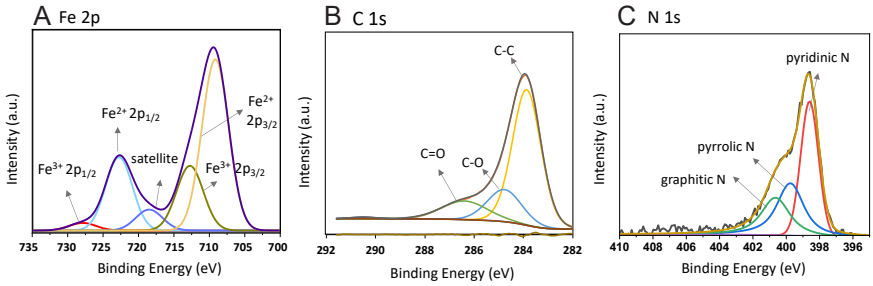

Figure D.17: X-ray photoelectron spectroscopy (XPS) characterization of Fe-TPP/Ni electrode including (A) Fe 2p, (B) C 1s; and (C) N 1s spectra.

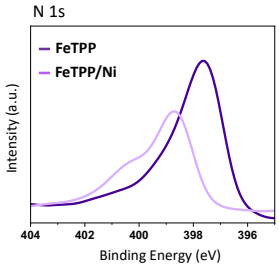

Figure D.18: X-ray photoelectron spectra (XPS) survey comparison of N 1s before and after deposition of Fe-TPP onto nickel electrode.

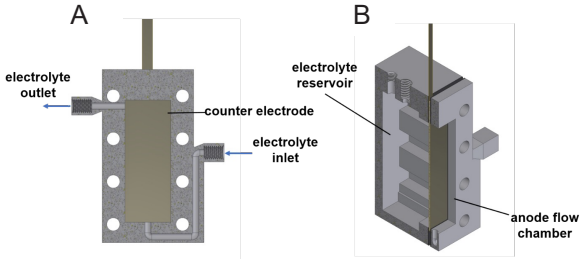

Figure D.19: Front (A) and isometric view (B) of the 3D printed anode electrolyte reservoir and anode flow chamber.

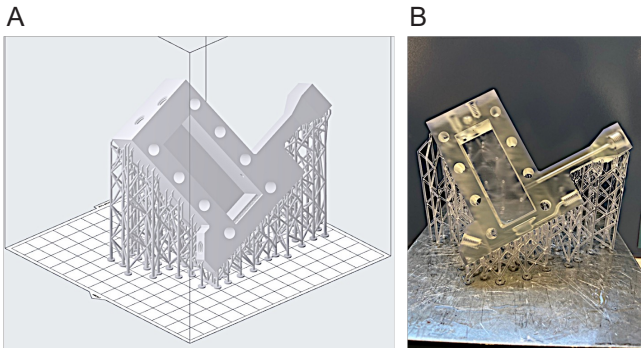

Figure D.20: 3D printing of the CO2RR electrolyser working electrode compartment. The cell is 3D printed in clear resin on a SLA Formlabs Form 2 3D-printer. (A) Set-up of supporting structure prior 3D printing in Formlabs' PreForm® software. (B) Completed 3D printed cell before support structure removal, washing and curing.

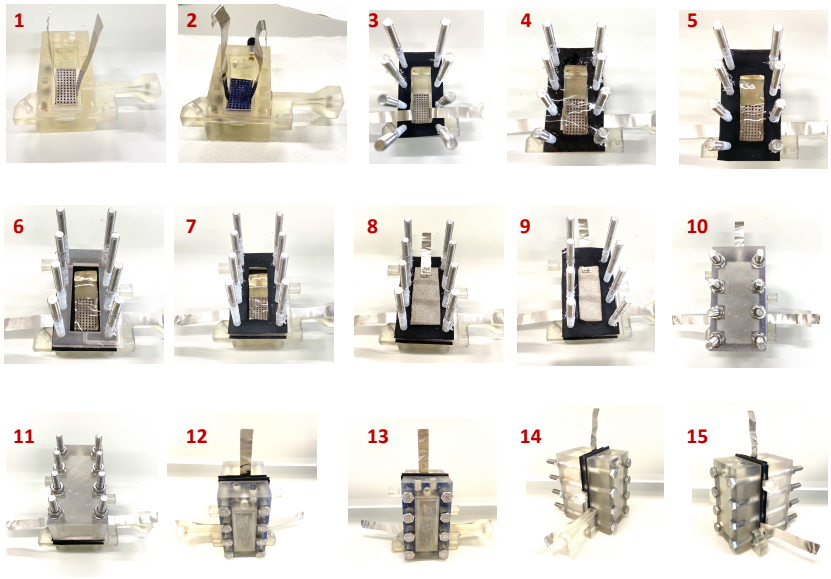

Figure D.21: Assembly of the electrolyser cell for the 3D electrodes.

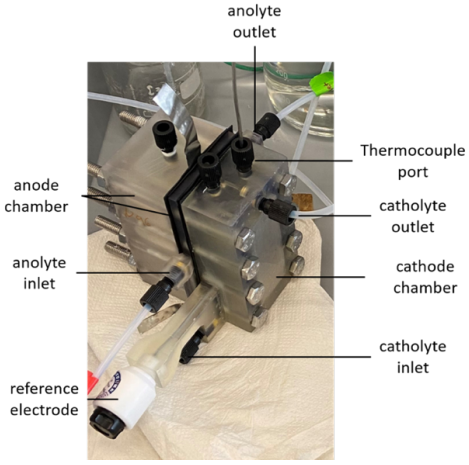

Figure D.22: Assembled CO_2 electrolyser for 3D electrodes.

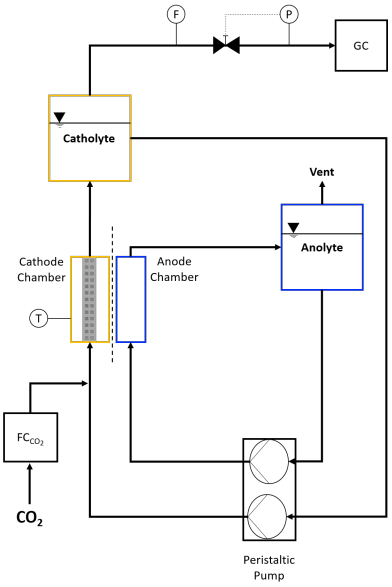

Figure D.23: Experimental set-up including the CO_2 flow controller (FC_{CO_2}), the flow meter at the reactor outlet (F), the temperature measurement in the cathode chamber (T) and the gas chromatograph (GC). The pressure of the cathode circuit is controlled via a pressure control (P) in front of the GC.

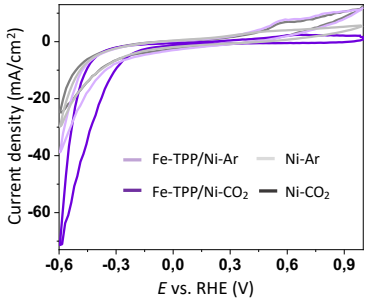

Figure D.24: Cyclic voltammetry (CV) comparison of bare nickel and Fe-TPP/Ni electrocatalysts under CO_2 and Ar with a scan rate of 100 mV/s in 0.5 M $KHCO_3$ with electrolyte flow.

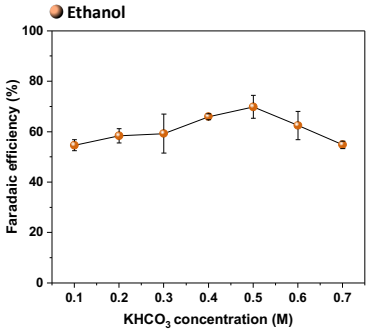

Figure D.25: Effect of $KHCO_3$ electrolyte concentration on ethanol selectivity.

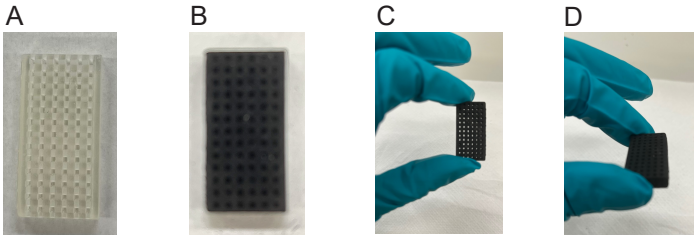

Figure D.26: Fabrication of the carbon black electrode by coating a 3D-printed template with carbon black. (A) Before coating, and after coating (B-D).

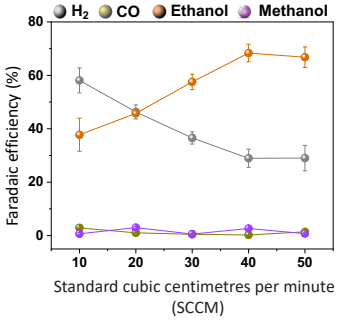

Figure D.27: CO_2 utilization and consumption for the CO_2 flow rates of 10-50 SCCM using Fe-TPP/Ni at -0.3 V vs. RHE.

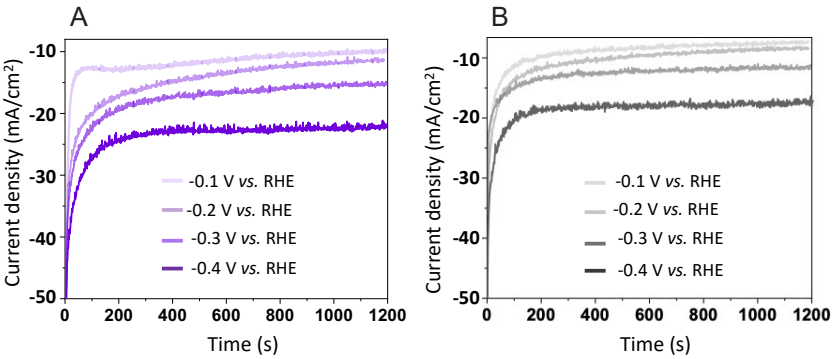

Figure D.28: Chronoamperometry of (A) Fe-TPP/Ni; and (B) bare nickel at -0.1, -0.2, -0.3, and -0.4 V vs. RHE with no electrolyte flow.

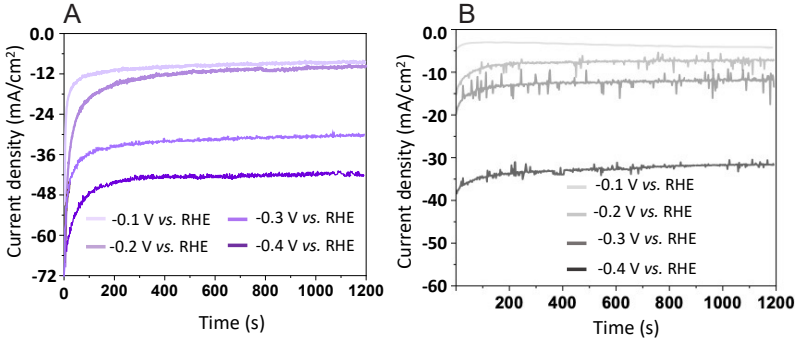

Figure D.29: Chronoamperometry of (A) Fe-TPP/Ni; and (B) bare nickel at -0.1, -0.2, -0.3, and -0.4 V vs. RHE with an electrolyte flow rate of 10 ml/min.

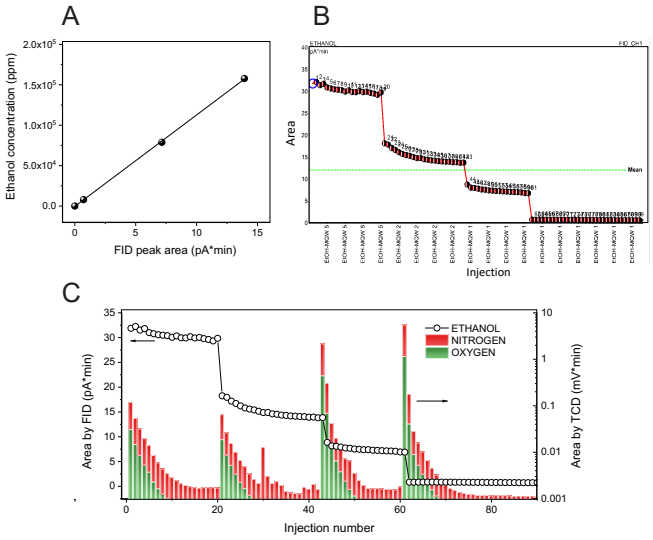

Figure D.30: (A) Calibration plots of Ethanol (in ppm) pervaporate vs. FID peak area; (B) Ethanol peak areas of the 92 GC injections as displayed by the GC-software Chromeleon®; and (C) Change of N_2 & O_2 concentration during the ethanol calibration, where the beaker was exposed to air while changing the concentration levels of the alcohol mixture.

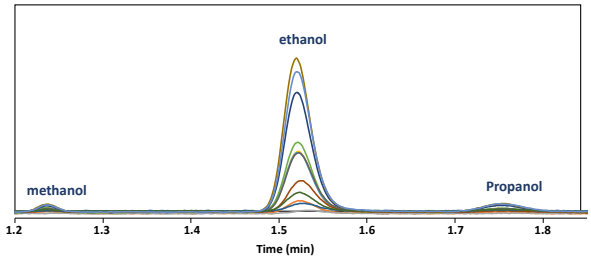

Figure D.31: Detected CO_2RR products using Gas Chromatography (GC) instrument.

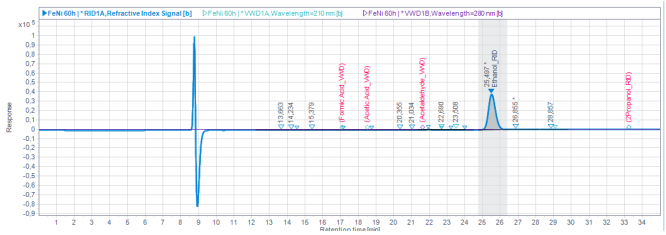

Figure D.32: Detected CO_2RR products using a High-Performance Liquid Chromatograph (HPLC)

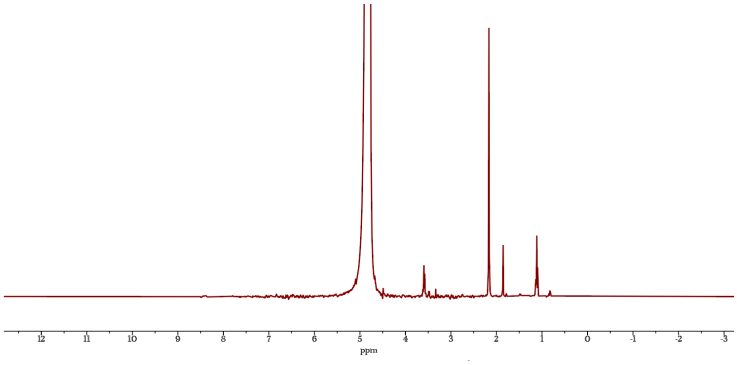

Figure D.33: An example of the proton Nuclear Magnetic Resonance (^{1}H NMR) spectrum of liquid products including ethanol at 1.17 and 3.64 ppm; trace amounts of methanol at 3.34 ppm, and propanol at 0.89, 1.54, and 3.56 ppm.

No reduced product was detected at -0.1 V vs RHE for either of the catalysts (Figure D.34). The formation of CO followed by ethanol as the major liquid product from Fe-TPP/Ni was first reliably identified at -0.2 V vs RHE with an FE of 37 %. The selectivity of ethanol was increased to 68 % at a more negative overpotential of -0.3 V vs RHE, which could be attributed to the increased electrochemical driving force [11]. At more negative potentials (-0.4 V vs RHE), the FE dropped to 32 %, and an increase in HERs was observed.

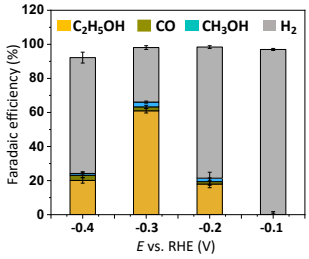

Figure D.34: Faradic efficiency (FE) of Fe-TPP/Ni after CO_2 electrolysis at -0.1, -0.2, -0.3, -0.4 V vs. RHE in 0.5 M $KHCO_3$ with no flow.

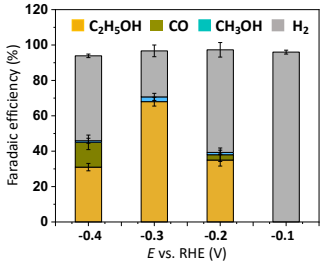

Figure D.35: Faradic efficiency (FE) of Fe-TPP/Ni after CO_2 electrolysis at -0.1, -0.2, -0.3, -0.4 V vs. RHE in 0.5 M $KHCO_3$ with electrolyte flow (10 ml/min).

Table D.4: Product analysis of the heterogeneous bare nickel, Fe-TPP/Ni, and Fe-TPP/C catalysts in H-cell under flow. The reported data are the average values of three separate measurements taken from four individual reaction runs at various potentials.

Compound	Electrolyte	V vs. RHE	j (mA/cm^2)	FE% (Ethanol)	FE% (Methanol)	FE% (CO)	FE% (H_2)	References
Ni	$KHCO_3$ (0.5 M)	-0.1	-0.35	0	0	0	98.7±1.5	Current work
	$KHCO_3$ (0.5 M)	-0.2	-0.8	0	0	0	99.3±1.3	Current work
	$KHCO_3$ (0.5 M)	-0.3	-14	0	0	8±0.5	91±2	Current work
	$KHCO_3$ (0.5 M)	-0.4	-32	0	0	14±2	85±2.4	Current work
	$KHCO_3$ (0.5 M)	-0.4	-32	0	0	14±2	85±2.4	Current work
Fe-TPP/Ni	$KHCO_3$ (0.5 M)	-0.1	-8	0	0	0	95±3.2	Current work
	$KHCO_3$ (0.5 M)	-0.2	-11	37±5.5	1.3±0.2	3±0.2	58±5.3	Current work
	$KHCO_3$ (0.5 M)	-0.3	-31	68±3.2	2.7±0.2	0	26±3.4	Current work
	$KHCO_3$ (0.5 M)	-0.4	-42	32±1	0.1±0.3	11±1	52±1.7	Current work
Fe-TPP/C	$KHCO_3$ (0.5 M)	-0.5	-6.7	-	-	28±3.1	67±4.7	Current work
	$KHCO_3$ (0.5 M)	-0.6	-7.4	-	-	52±3.2	48±1.6	Current work
	$KHCO_3$ (0.5 M)	-0.7	-7.9	-	-	43±3.9	55±2.8	Current work
	$KHCO_3$ (0.5 M)	-0.8	-8.2	-	-	31±1.6	69±3.7	Current work

To confirm the key role of the Fe-centered for product selectivity, control experiments on both metal-free porphyrin (TPP), and bare Ni, individually, were performed. As shown in Table D.4, no liquid products were found, neither with bare nickel nor Fe-TPP/C. We found that Fe-TPP/C complex undertook an electrocatalytic CO_2 reduction pathway only towards CO and H_2, i.e. very different from their iron analogues, illustrating the necessity of both Fe-TPP and 3D nickel electrode for the formation of ethanol.

DFT

The formation of C_{2+} products occur either through *CO dimerizes to form *OCCO at low overpotentials [12], to be converted to *OCCOH [13] through a hydrogenation reaction, or via *CO hydrogenation to form *CHO [14], which takes place at high overpotentials. It should be noted that the C-C coupling step is highly sensitive to the structure and morphology of the catalyst and should profit from high local density of C intermediates [15].

To understand the strength of the interaction between the Fe-TPP and the support, we looked into the adsorption energies calculated by DFT computations. The simulated supports need to be large enough, so the adsorbed Fe-TPP is not affected by the imaginary neighbours existing in the periodic boundary conditions applied in the DFT. Due to computational limitations, we had to modify the Fe-TPP molecule by substituting benzene cycles with a hydrogen atom (to reduce the size of the computations), as suggested in the literature [16, 17]. We optimized the modified Fe-TPP on graphene structure and the nickel surface. Results showed a significant difference in the adsorption distances. While the distance between Fe atom and the nickel surface is 2.00 Å, revealing a strong adherence and chemisorption, it increases to 3.92 Å on graphene, revealing a weak physisorption (Figures 5.1 A and 5.1 B). Charge delocalization plots (Figures 5.1 A and 5.1 B), show qualitatively the stronger interaction between the Fe-TPP molecule and nickel surface compared to that with graphene. There is a larger electron donation to the chemical bond between Fe and Ni, while the electronic structure of carbon atoms on graphene looks intact. Bader charge analysis exhibited only 0.061 increase in the oxidation state of Fe atom when exposed to the carbon. However,

the nickel surface donates more electron and decreases the oxidation state of Fe by 0.222, enabling the active site to donate more electron during the reduction reaction.

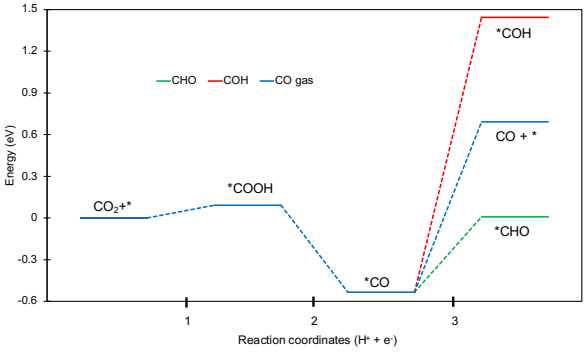

Figure D.36: Energy diagram of the protonation of mono-carbon species.

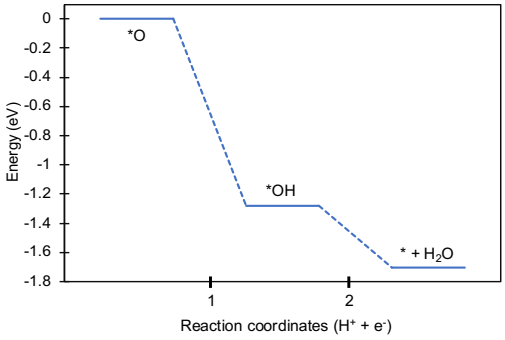

Figure D.37: Oxygen removal from the surface and site recovery reaction energy* stands for the catalytic site and *i corresponds to the adsorbed I species.

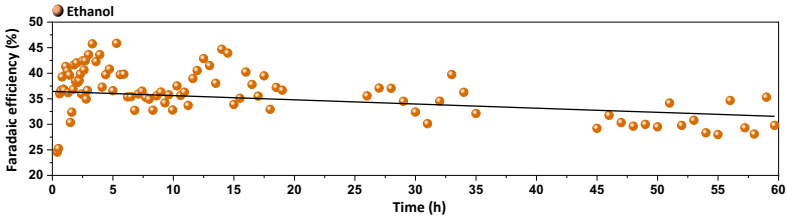

Figure D.38: Long-term stability test of Fe-TPP/Ni at a constant potential of -0.3 V vs. RHE in 0.5 M $KHCO_3$ with 10 SCCM CO_2 flow.

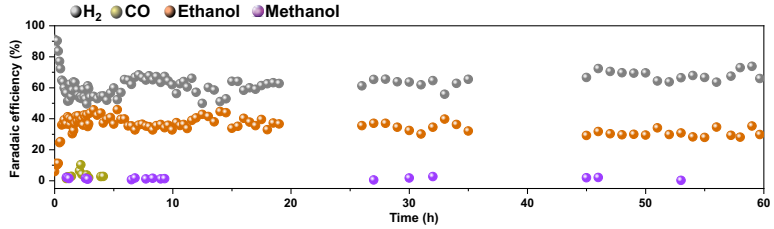

Figure D.39: Long-term stability test of Fe-TPP/Ni at a constant potential of -0.3 V vs. RHE in 0.5 M $KHCO_3$ under 10 SCCM CO_2 flow.

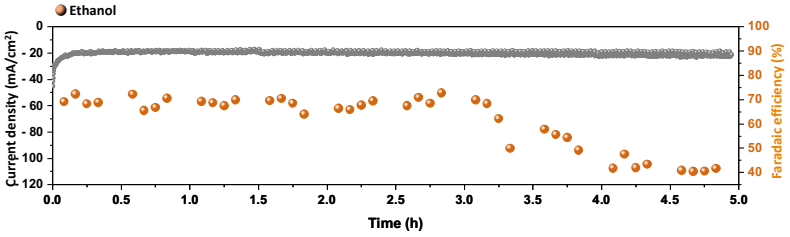

Figure D.40: Long-term stability test of Fe-TPP/Ni at a constant potential of -0.3 V vs. RHE in 0.5 M $KHCO_3$ under 40 SCCM CO_2 flow. Running a long stability test at a flow rate of 40 SCCM CO_2 is challenging due to the increased bubble formation under a high flow rate which leads to the detachment of the Fe-TPP from the Ni surface. As a result, there's a significant rise in hydrogen evolution reaction (HER), causing an increase in the cell pressure as well as a subsequent drop in Faradaic efficiencies.

XRD

The XRD was performed using a Bruker D8 Advanced diffractometer with Cu-Kα source (Cu radiationwavelength: Kα1(100) = 1.54060 Å, Kα2(50) = 1.54439 Å) and Lynxeye-XE-T position sensitive detector. Although the monolayer of deposited Fe-TPP through drop casting on the Ni electrode surface is not expected to be measurable with XRD, Fe-TPP was detected in some small regions of the highly porous nickel electrode, as shown in Figure D.41. This observation suggests slight aggregation phenomena occurring in certain areas of the electrode surface after the drop-casting process.

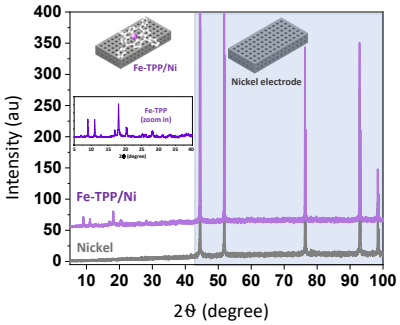

Figure D.41: Comparison of X-ray diffraction (XRD) patterns of Fe-TPP/Ni and bare Ni.

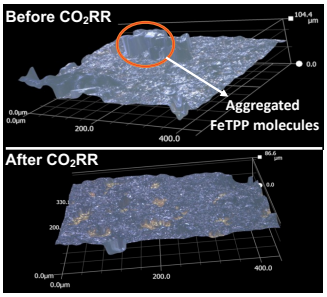

Figure D.42: 3D view of Fe-TPP/Ni electrode surface before and after 60h electrochemical CO_2RR taken using Keyence VHX7000 digital microscope and optical profiler.

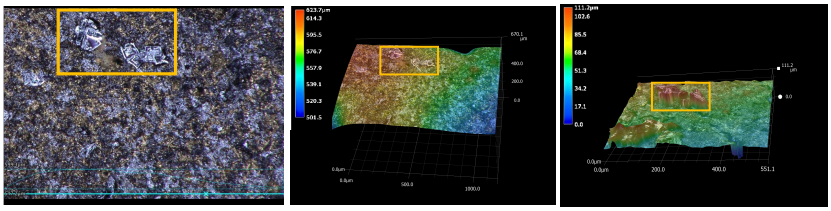

Figure D.43: Highlighted molecular aggregation on Fe-TPP/Ni electrodes. The images were taken with the Keyence VHX7000 digital microscope and optical profiler.

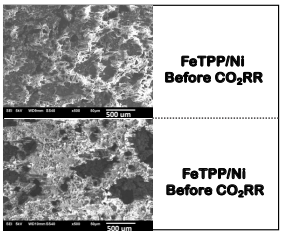

Figure D.44: Scanning Electron Microscopy (SEM) comparison before and after 62 hours of electrolysis.

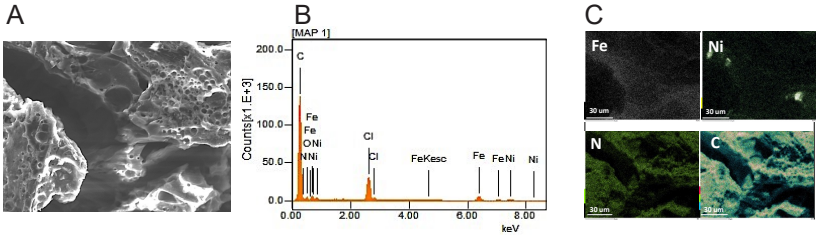

Figure D.45: (A) Scanning Electron Microscopy (SEM) of the Fe-TPP/Ni 3D electrode. (B) SEM mapping of elemental distribution. (C) Energy Dispersive X-rays Spectroscopy (EDX) of Fe, Ni, N, and C after 62 hours of electrolysis.

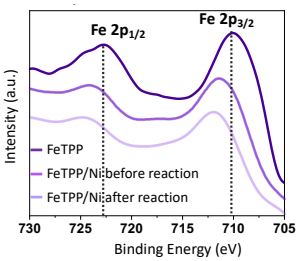

Figure D.46: X-ray photoelectron spectra (XPS) survey comparison of Fe 2p with Fe-TPP/Ni before and after 62 hours of electrolysis.

Tafel

Tafel slopes and electrochemical surface area (ECSA) were calculated to obtain additional insight into the reaction kinetics of each individual bare Ni and Fe-TPP/Ni catalyst towards the CO_2RR. Tafel analyses show a significantly higher exchange current and slightly lower slope for Fe-TPP/Ni compared to bare Ni. This suggests that the rate-determining step for ethanol formation may change with the Fe-TPP catalyst [18–20]. The temperature was measured and compared under Ar and CO_2 for the entire reaction, which shows a slight rise along with increasing the potential energy (Figure D.47). The cell was operated with no electrolyte flow and a CO_2 flow rate of 40 sccm. Each set potential is held for 10 minutes in order to allow for the current to stabilize. Tafel analyses comparison for electrocatalytic CO_2RR to ethanol on bare nickel and Fe-TPP/Ni, show a lower slope in the case of Fe-TPP/Ni. This suggests that the rate-determining step for ethanol formation may change with the Fe-TPP catalyst [18–20].

Electrochemically active surface area (ECSA)

ECSA of the bare nickel electrode and Fe-TPP/Ni was determined from the electrochemical double-layer capacitance (Figure D.49)[21]. Comparing the results, the ECSA of Fe-TPP/Ni is 1.5 fold larger than the ECSA of bare Ni. This could be due to the additional conductive molecular layer within the pores of the nickel electrode increasing the electrochemically active surface area. It was determined from the electrochemical double-

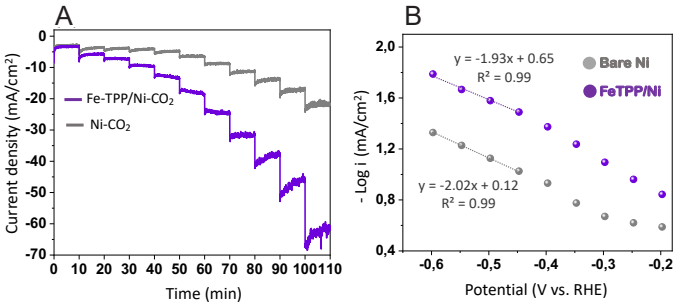

Figure D.47: (A) Tafel plot for the 3D nickel electrode (black) and the 3D nickel electrode loaded with Fe-TPP (purple) in 0.5 M $KHCO_3$; (B) Tafel slope comparison of bare Ni and Fe-TPP/Ni.

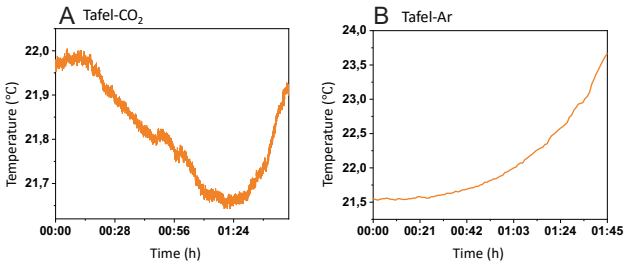

Figure D.48: Temperature measurement during Tafel experiment under (A) CO_2 and (B) Ar.

layer capacitance [21, 22]. First, a potential window between 0.1 V and 0.2 V vs. RHE was identified via cyclic voltammetry in which little to no Faradaic currents occur. Within this window, cyclic voltammograms at increasing scan rates were measured including a 10 s hold at each potential vertex. The resulting charging currents, I^+ and I^-, are measured at 0.15 V vs RHE for both the positive and negative sweeps, respectively. These are related to the scan rate ν and the double layer capacitance C_{DL} as follows[21, 23, 24]:

$$I^{+/-} = \nu \, C_{DL}^{+/-} \tag{D.1}$$

The slope of the capacitive current vs. the scan rate constitutes the

double layer capacitance and can be determined from a linear fit of the experimental data (Figure D.49 C). It is common practice to report the average double layer capacitance which is determined from the average of the absolute values of both the positive and negative potential sweeps[21, 25]:

$$\bar{C}_{DL} = \frac{C_{DL}^{+} + \left|C_{DL}^{-}\right|}{2} \tag{D.2}$$

The ECSA can then be estimated from the specific capacitance of the sample, C_s[21]:

$$ECSA = \frac{\bar{C}_{DL}}{C_s} \tag{D.3}$$

The specific capacitance C_s represents the capacitance per unit area of an ideally smooth surface of the studied material paired with an electrolyte. Technically, C_s has to be determined experimentally for each catalyst and electrolyte condition. While specific capacitances have been measured for nickel in various NaOH and KOH solutions, these values vary significantly depending on the electrolyte composition and concentration[21]. Moreover, to the best of our knowledge, there are no measurements of C_s available for the here discussed Fe-TPP. This is further exacerbated by the presence of dissolved CO_2, which warrants additional measurements of C_s specifically for the presented application. Overall, the double-layer capacitance increases from 136 mF before Fe-TPP loading to 194.5 mF following the loading procedure (~+ 43 %).

To arrive at an estimate for the roughness factor R and the volume specific surface area a_V of the sintered 3D nickel electrode, we use the average value of 40 μF/cm^2 reported by McCrory for alkaline solutions [21]. According to Equation D.2, this results in an electrochemically active surface area of 3402 cm^2 and 4850 cm^2 before and after Fe-TPP loading, respectively. The roughness factor R for the nickel electrode loaded with Fe-TPP is determined as the ratio of the electrochemically active surface area over the total non-porous[2] surface area $A_{tot,3D}$, which is calculated

[2]This does not include the internal surface area of the pores.

from the CAD model[3]:

$$R = \frac{ECSA}{A_{tot,3D}} = \frac{4850\ cm^2}{40.49\ cm^2} = 119.78 \tag{D.4}$$

The volume specific surface area a_V is defined as the electrochemically active surface area over the porous electrode volume which constitutes the pore volume V_p and the non-porous nickel volume V_{Ni}:

$$\begin{aligned} a_V &= \frac{ECSA}{V_p + V_{Ni}} = \frac{ECSA}{\frac{m_{H_2O}}{\rho_{H_2O}} + \frac{m_{Ni}}{\rho_{Ni}}} \\ &= \frac{4850\ cm^2}{1.531\ cm^3} = 3167.86\ \frac{cm^2}{cm^3} \\ &\approx 3.17 \times 10^5\ \frac{m^2}{m^3} \end{aligned} \tag{D.5}$$

Here, the pore volume is determined via the mass and density of absorbed water.

[3]Adjusted for the shrinkage measured after sintering.

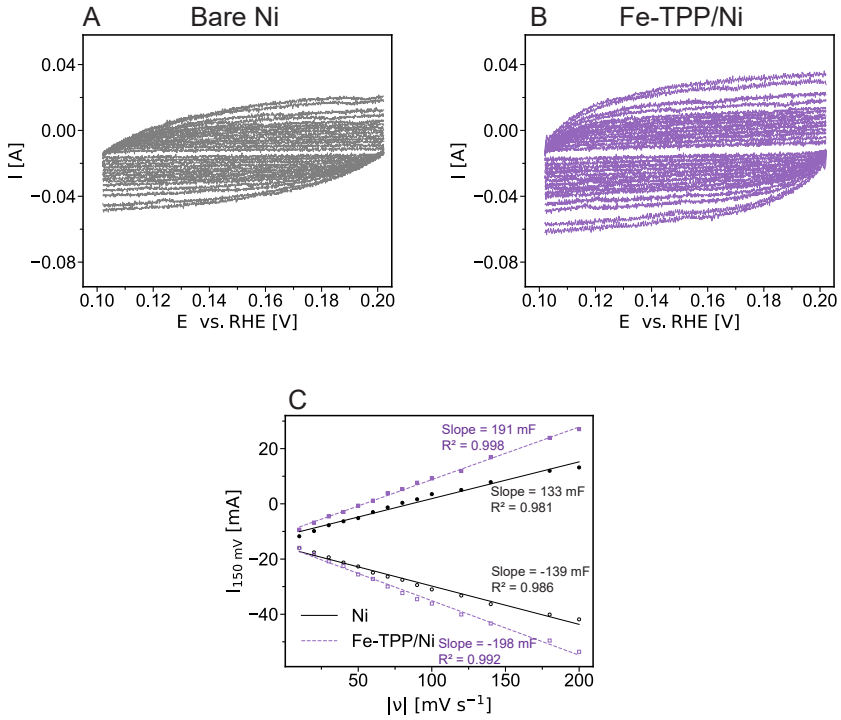

Figure D.49: Cyclic voltammograms in 0.5 M $KHCO_3$ with varying scan rates in a non-Faradaic potential region in order to estimate the electrochemically active surface area (ECSA) for a bare nickel electrode (A) and a nickel electrode loaded with Fe-TPP (B). (C) The double-layer capacitance C_{DL} is estimated from the slope of the anodic and the cathodic double-layer charging current measured at 0.15 V vs RHE vs. the scan rate. Scan rates of 10, 20, 30, 40, 50, 60, 70, 80, 90, 120, 140, 180 and 200 mV/s are applied between 0.1 V and 0.2 V vs. RHE.

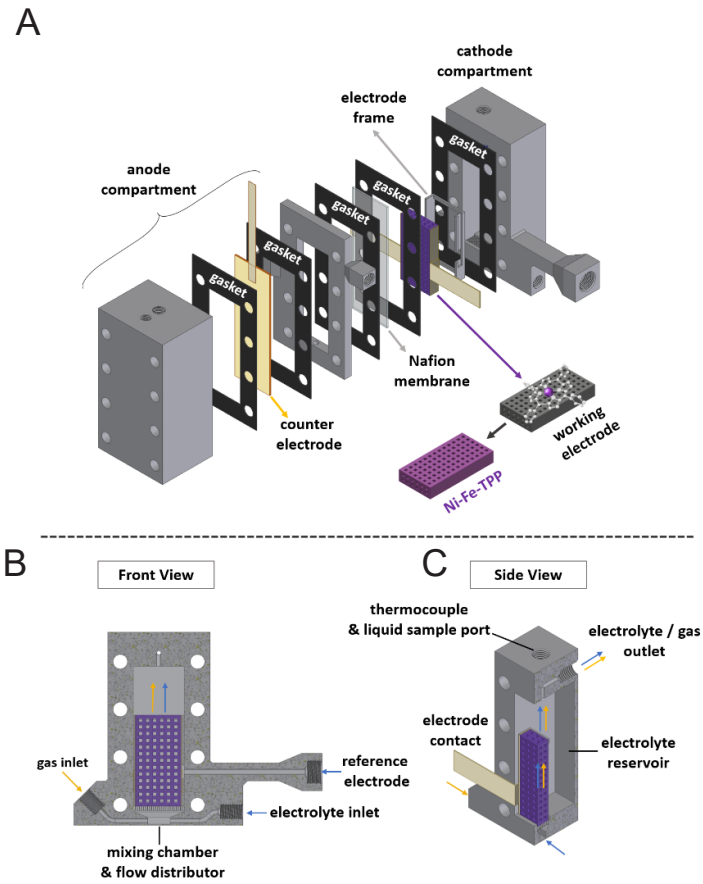

Figure D.50: Illustration of the electrolysis cell developed for the 3D electrodes. (A) Explosion view showing all components. Front (B) and isometric cut view (C) of the cathode compartment showing gas and electrolyte mixing before flowing through the electrode.

References

[1] M. Abdinejad, A. Farzi, R. Möller-Gulland, F. M. Mulder, C. Liu, J. Shao, J. Biemolt, M. Robert, A. Seifitokaldani, and T. Burdyny, *Eliminating redox-mediated electron transfer mechanisms on a supported molecular catalyst enables CO_2 conversion to ethanol,* Nature Catalysis **7**, 1109 (2024).

[2] S. Kim, D. Tryk, I. T. Bae, M. Sandifer, R. Carr, M. R. Antonio, and D. A. Scherson, *In situ extended X-ray absorption fine structure of an iron porphyrin irreversibly adsorbed on an electrode surface,* The Journal of Physical Chemistry **99**, 10359 (1995).

[3] C. Cartier, M. Momenteau, E. Dartyge, A. Fontaine, G. Tourillon, A. Bianconi, and M. Verdaguer, *X-ray absorption spectroscopy of carbonyl basket handle Fe (II) porphyrins: the distortion of the tetrapyrrolic macrocycle,* Biochimica et Biophysica Acta (BBA)-Protein Structure and Molecular Enzymology **1119**, 169 (1992).

[4] X. Lu, H. A. Ahsaine, B. Dereli, A. T. Garcia-Esparza, M. Reinhard, T. Shinagawa, D. Li, K. Adil, M. R. Tchalala, T. Kroll, *et al.*, *Operando elucidation on the working state of immobilized fluorinated iron porphyrin for selective aqueous electroreduction of CO_2 to CO,* ACS Catalysis **11**, 6499 (2021).

[5] T. Liu, A. Li, C. Wang, W. Zhou, S. Liu, and L. Guo, *Interfacial electron transfer of Ni_2P–NiP_2 polymorphs inducing enhanced electrochemical properties,* Advanced Materials **30**, 1803590 (2018).

[6] C. Liu, H. Zhu, Z. Zhang, J. Hao, Y. Wu, J. Guan, S. Lu, F. Duan, M. Zhang, and M. Du, *Binary nickel iron phosphide composites with oxidized surface groups as efficient electrocatalysts for the oxygen evolution reaction,* Sustainable Energy & Fuels **3**, 3518 (2019).

[7] D. Ripepi, B. Izelaar, D. D. Van Noordenne, P. Jungbacker, M. Kolen, P. Karanth, D. Cruz, P. Zeller, V. Pérez-Dieste, I. J. Villar-Garcia, *et al.*, *In situ study of hydrogen permeable electrodes for electrolytic ammonia synthesis using near ambient pressure XPS,* ACS Catalysis **12**, 13781 (2022).

[8] M. C. Biesinger, B. P. Payne, L. W. Lau, A. Gerson, and R. S. C. Smart, *X-ray photoelectron spectroscopic chemical state quantification of mixed nickel metal, oxide and hydroxide systems,* Surface and Interface Analysis **41**, 324 (2009).

[9] F. Buchner, K. Flechtner, Y. Bai, E. Zillner, I. Kellner, H.-P. Steinruck, H. Marbach, and J. M. Gottfried, *Coordination of iron atoms by tetraphenylporphyrin monolayers and multilayers on Ag (111) and formation of iron-tetraphenylporphyrin,* The Journal of Physical Chemistry C **112**, 15458 (2008).

[10] J. M. Gottfried, K. Flechtner, A. Kretschmann, T. Lukasczyk, and H.-P. Steinrück, *Direct synthesis of a metalloporphyrin complex on a surface,* Journal of the American Chemical Society **128**, 5644 (2006).

[11] X. Liu, J. Xiao, H. Peng, X. Hong, K. Chan, and J. K. Nørskov, *Understanding trends in electrochemical carbon dioxide reduction rates,* Nature Communications **8**, 15438 (2017).

[12] J. H. Montoya, C. Shi, K. Chan, and J. K. Nørskov, *Theoretical insights into a CO dimerization mechanism in CO_2 electroreduction,* The Journal of Physical Chemistry Letters **6**, 2032 (2015).

[13] E. Pérez-Gallent, M. C. Figueiredo, F. Calle-Vallejo, and M. T. M. Koper, *Spectroscopic observation of a hydrogenated CO dimer intermediate during CO reduction on Cu (100) electrodes,* Angewandte Chemie International Edition **56**, 3621 (2017).

[14] K. J. P. Schouten, Z. Qin, E. Perez Gallent, and M. T. M. Koper, *Two pathways for the formation of ethylene in CO reduction on single-crystal copper electrodes,* Journal of the American Chemical Society **134**, 9864 (2012).

[15] R. M. Arán-Ais, D. Gao, and B. Roldan Cuenya, *Structure-and electrolyte-sensitivity in CO_2 electroreduction,* Accounts of Chemical Research **51**, 2906 (2018).

[16] J. Shen, M. J. Kolb, A. J. Gottle, and M. T. M. Koper, *DFT study on the mechanism of the electrochemical reduction of CO_2 catalyzed by cobalt porphyrins,* The Journal of Physical Chemistry C **120**, 15714 (2016).

[17] F. Li, Y. C. Li, Z. Wang, J. Li, D.-H. Nam, Y. Lum, M. Luo, X. Wang, A. Ozden, S.-F. Hung, B. Chen, Y. Wang, J. Wicks, Y. Xu, Y. Li, C. M. Gabardo, C.-T. Dinh, Y. Wang, T.-T. Zhuang, D. Sinton, and E. H. Sargent, *Cooperative CO_2-to-ethanol conversion via enriched intermediates at molecule–metal catalyst interfaces,* Nature Catalysis **3**, 75 (2020).

[18] C.-T. Dinh, T. Burdyny, M. G. Kibria, A. Seifitokaldani, C. M. Gabardo, F. P. García de Arquer, A. Kiani, J. P. Edwards, P. De Luna, O. S. Bushuyev, C. Zou, R. Quintero-Bermudez, Y. Pang, D. Sinton, and E. H. Sargent, *CO_2 electroreduction to ethylene via hydroxide-mediated copper catalysis at an abrupt interface,* Science **360**, 783 (2018).

[19] S. Gao, Y. Lin, X. Jiao, Y. Sun, Q. Luo, W. Zhang, D. Li, J. Yang, and Y. Xie, *Partially oxidized atomic cobalt layers for carbon dioxide electroreduction to liquid fuel,* Nature **529**, 68 (2016).

[20] W. Ma, S. Xie, T. Liu, Q. Fan, J. Ye, F. Sun, Z. Jiang, Q. Zhang, J. Cheng, and Y. Wang, *Electrocatalytic reduction of CO_2 to ethylene and ethanol through hydrogen-assisted C–C coupling over fluorine-modified copper,* Nature Catalysis **3**, 478 (2020).

[21] C. C. L. McCrory, S. Jung, J. C. Peters, and T. F. Jaramillo, *Benchmarking heterogeneous electrocatalysts for the oxygen evolution reaction,* Journal of the American Chemical Society **135**, 16977 (2013).

[22] S. Trasatti and O. A. Petrii, *Real surface area measurements in electrochemistry,* Pure and Applied chemistry **63**, 711 (1991).

[23] P. Connor, J. Schuch, B. Kaiser, and W. Jaegermann, *The determination of electrochemical active surface area and specific capacity revisited for the system MnOx as an oxygen evolution catalyst,* Zeitschrift für Physikalische Chemie **234**, 979 (2020).

[24] S. P. Zankowski and P. M. Vereecken, *Electrochemical determination of porosity and surface area of thin films of interconnected nickel nanowires,* Journal of The Electrochemical Society **166**, D227 (2019).

[25] T. Kou, S. Wang, R. Shi, T. Zhang, S. Chiovoloni, J. Q. Lu, W. Chen, M. A. Worsley, B. C. Wood, S. E. Baker, *et al.*, *Periodic porous 3D*

electrodes mitigate gas bubble traffic during alkaline water electrolysis at high current densities, Advanced Energy Materials **10**, 2002955 (2020).

Acknowledgements

While this PhD has been one of the most rewarding experiences of my life, it was also certainly the most difficult. Without the support of my family, friends and colleagues you would not be holding this book in your hands.

Thank you, **Fokko**, for letting me join the team back in 2018. Even though I applied two weeks past the deadline and my profile did not really fit the description of the job posting, I am happy you still took a chance with me. I appreciate the freedom you gave me to pursue high risk projects and the trust you put in me to see them through (despite countless failures, a.k.a. learning experiences). Thank you also for your advice, all the work you put into the patent and the fast editing of my thesis chapters.
Ruud, thank you for your advice and feedback. Your input and perspective on my thesis and PhD in general were a great help.

Martin, you were one of the biggest sources of support for me throughout this journey. Since meeting you as a master student at UCLA, you have become one of the best researchers and engineers I know. Our daily discussions on our shared struggles in the lab and life and generally just derping around were essential and helped me through some difficult times. If you hadn't pushed me to keep trying to weld electrode contacts, my thesis would not be what it is today. I hope that our CVs will someday converge again. And never forget, if the bar doesn't bend, you just pretend.

Sanjana, you too were one of the biggest sources of support during this odyssey. Our coffee breaks never failed to recharge my batteries (pun intended). All the cute cat photos of Luna you shared with me were the catalyst for Cinta and me to get Miep and Vincent, which turned out to be one of the best decisions we could have made. I am also thankful for your support during the time we spent together working at Battolyser Systems.
Tushar, the BBQs and dinners you organized were amazing and helped

me take my mind off my experiments. I am looking forward to many more in the future.

Tom, I loved having you as an office mate at the beginning of my PhD. I'll never forget the heartfelt conversations we had about work and life during this time. You're not only a great researcher but also an amazing manager who always has his students' best interest at heart.

Maryam, Amirhossein, Fokko, Chengyu, Junming, Jasper, Marc, Ali and **Tom**, thank you for all the hard work you put into the ethanol paper (Chapter 5). Applying the electrodes I developed for the battolyser™ to CO_2 reduction was a great experience. **Maryam**, you were the driving force in turning our interesting results into an impactful paper. Thank you for taking me along for the ride. I wish you all the best for your journey in academia.

My office mates **Divya, Mark, Diana** and **Audrey**, you never failed to make me laugh no matter how hard my day was. Thank you for your open ears over the years and providing me with a safe space to vent. **Giorgio**, moving apartments, longboarding and just chatting about life with you was always great fun. **Kailun**, I was always happy when my German humor could make you laugh. **Dylan** and **Peter**, thanks for all the laughs. **Herman** and **Joost**, thank you for all your help in the lab and time spent researching, buying and setting up equipment that was essential for my experiments. My bachelor and master students **Loebna, Shubham, Jeannet** and **Arden**, thank you for all the effort you put into your projects. Especially at the beginning, your help was invaluable. **Audrey, Bernhard** and **Andrea**, it was great working on the battolyser™ together with you in a team. **Duco, Bart** and **Xiaohui**, thank you for all your help with SEM, XPS and XRD. Thanks to the entire **MECS** group, you do research that matters and keep it fun.

Mattijs, Pieter, Nate, Naila, Sanjana, Martijn, Stefano, Nick, Marco, Bas, Cas, Omar, Catriona, Sid, Aurian, Anesa, Kathleen, Nick, Thomas, Falco, Saeid and the entire team at **Battolyser Systems**, I learned a lot while working with you. Seeing the technology of the battolyser™ being scaled up was incredibly motivating for my own PhD work. What you have achieved so far is remarkable and I wish you lots of further success for the future.

Jet, my trusted hairdresser, thank you for all the great haircuts and even greater conversations over the past years. I'm looking forward to many more in the future.

Meine Freunde aus der Heimat, **Jan, Betül, Simon, Lara, Daniel, Anja, Gigi, Laura, Christoph, Oli** und **Kerstin**, vielen Dank für eure Unterstützung und Freundschaft der letzten Jahrzehnte. Ihr seit meine homebase auf die ich immer zählen kann.

The infamous Squid Squad, **Jeff, Kris, Jon, Ken, Christian, Fritz, Henry, Max** and **Ben**, and **Nanette**, the time spent with you in LA is amongst the fondest memories of my life. I am grateful to have you in my life. Seeing you guys find your way, both in your personal life and your career, has been a constant motivation for me during my PhD. I can't wait to see you all again soon. **Jeff**, your strength in helping me through some deep lows and celebrating the good times together means the world to me. **Nanette, Kris** and **Jeff**, thank you for integrating me in Loui's lab and beyond. The great time I had working with you was one of the main reasons why I decided to pursue a PhD.

My friends in Utrecht, **Lieke** and **Francisco**, thank you for all the fun times and delicious dinners that helped me recharge from everyday life as a PhD student.

Meine Physik- und Mathematiklehrer an der Europaschule Bornheim, **Herr Machholz, Herr Kittelmann** und **Frau Dittrich**, Sie haben mein Interesse an den Naturwissenschaften geweckt und gefördert. Ohne Sie hätte ich kein Maschinenbau studiert und wäre wahrscheinlich nicht in der Entwicklung elekrochemischer Energiespeichersysteme gelandet. Vielen Dank.

Meine Geschwister **Vivien, Mervyn** und **Jenni**, vielen Dank für eure Unterstützung während dieser fordernden Zeit. Meinen Neffen **Jan, Jonas** und **Oskar** möchte ich für ihre stete Inspiration danken. Ihr Wohlergehen in einer sich verändernden Welt, besonders im Hinblick auf den Klimawandel, hat mich tief motiviert und meine Arbeit maßgeblich geprägt.

Mama and **Papa**, thank you so much for all your support throughout my life and education. None of this would have been possible without you. Knowing that I can always fall back on you gives me strength and comfort for any further challenges I will face in the future.

Our sweet cats **Miep** and **Vincent**, thank you for your emotional support and all the laughs and comfort you bring us with your derpiness and near constant purring.

My dear **Cinta**, thank you for always being there for me. Having you by my side during our shared PhD journeys made all the difference. You were there to celebrate the highs, pick me up from the lows and cheer me up with our countless inside jokes. Living together with you and our sweet cats has been some of the best times of my life and the best part of coming to the Netherlands. T'estimo moltíssim i tinc moltes ganes del nostre futur junts.

Curriculum Vitae

Robin Möller-Gulland was born on the 17th of June 1990 in Cuxhaven, Germany. In 2010, he completed his mandatory military service as a ship's technician aboard the frigate Hamburg. He then obtained his Bachelor's degree in mechanical engineering at RWTH Aachen University in 2014. In the course of his Bachelor's, he gained practical experience through internships at Boll & Kirch Filterbau GmbH, Hydro Aluminium, and the Shell Technology Centre Hamburg, where he worked on the development of fuel additives. The topic of his Bachelor's thesis was the electrochemical cleavage of lignin to value-added chemicals in a membrane reactor. Robin then pursued a Master's degree in chemical engineering at RWTH Aachen University during which he continued his work on the electrochemical cleavage of lignin as a student research assistant at the chair for chemical process engineering. For his Master's thesis, Robin visited the group of Prof. Louis Bouchard at the University of California, Los Angeles (UCLA) where he worked on the visualization of gas-phase reactions via magnetic resonance imaging in 3D printed reactors. Following the completion of his Master's in 2016, Robin returned to UCLA and continued his Master's research as a staff research associate. In 2018, he joined Prof. Fokko Mulder's group in the group of Materials for Energy Conversion of Storage at the Delft University of Technology in order to pursue his PhD. Here, he worked on the development of 3D electrodes and cell concepts for an integrated battery-electrolyser and electrochemical CO_2 reduction. From May 2022 to September 2023, Robin worked as an electrode research engineer at Battolyser Systems in Schiedam. In September 2024, Robin rejoined Prof. Mulder's group as a postdoctoral researcher.

List of Publications

R. Möller-Gulland, J. Middelkoop, F. M. Mulder, *3D iron electrodes for hybrid battery and electrolysis application*, **submitted**.

R. Möller-Gulland, J. R. van Ommen, F. M. Mulder, *3D hybrid battery-electrolyser nickel electrodes: A theoretical analysis*, **submitted**.

R. Möller-Gulland, F. M. Mulder, *3D nickel electrodes for hybrid battery and electrolysis devices*, Cell Reports Physical Science, **accepted** (2024).

M. Abdinejad*, A. Farzi*, **R. Möller-Gulland***, F. M. Mulder, C. Liu, J. Shao, J. Biemolt, M. Robert, A. Seifitokaldani, T. Burdyny, *Eliminating redox-mediated electron transfer mechanisms on a supported molecular catalyst enables CO_2 conversion to ethanol*, Nature Catalysis (2024). *These authors contributed equally to this work.

R. Möller-Gulland, F. M. Mulder, *3D electrode for integrated battery and electrolyser application*, N2036627, filing date 21-12-2023, **patent pending**.